Optical studies of micron-scale flows : holographic microscopy, optical trapping and superhydrophobicity

Guido Bolognesi

Optical studies of micron-scale flows: holographic microscopy, optical trapping and superhydrophobicity

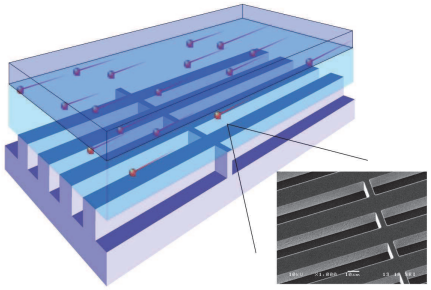

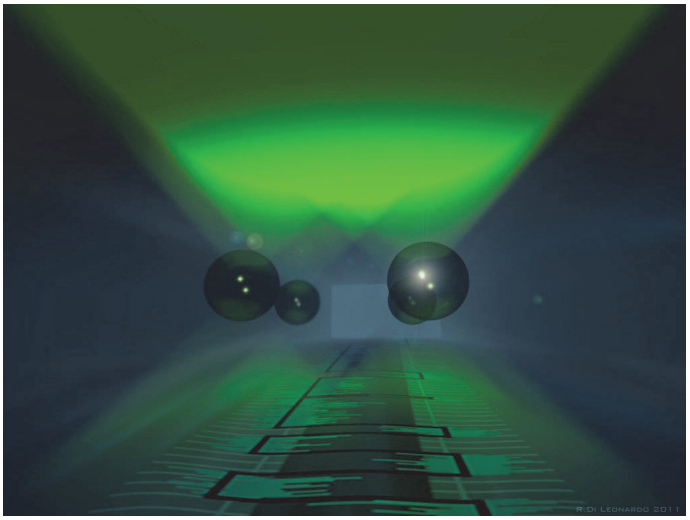

Ph.D. Guido Bolognesi

Printed in London, February 2012

“Al mio omonimo illustre”

SAPIENZA
UNIVERSITÀ DI ROMA

UNIVERSITÉ DE LYON

UNIVERSITÉ
FRANCO
ITALIENNE

UNIVERSITÀ DI ROMA "LA SAPIENZA" - UNIVERSITÉ CLAUDE BERNARD LYON 1

Optical studies of micron-scale flows: holographic microscopy, optical trapping and superhydrophobicity

DOTTORATO MECCANICA TEORICA ED APPLICATA
XXIV Ciclo

ÉCOLE DOCTORALE DE PHYSIQUE ET ASTROPHYSIQUE

Candidate
GUIDO BOLOGNESI

Tutor
Prof. CARLO MASSIMO CASCIOLA

Docenti Guida
Prof. LYDÉRIC BOCQUET
Dr. ROBERTO DI LEONARDO

Acknowledgements

As it is well known (to those who know it well), a doctorate is very long and structured process which requires the Ph.D. student to devote wholeheartedly to it. However, all his efforts would be useless without the help of several people he meets along the way. That's why it is a pleasure to thank those who made my thesis possible providing their support in a number of different ways.

I would like to thank Prof. Renzo Piva who suggested me to undertake the Ph.D. studentship and welcomed me in his research group with open arms. I am heartily thankful to my supervisor and director of the doctoral school of Theoretical and Applied Mechanics Prof. Carlo Massimo Casciola, who was (is and shall be) to me a mentor and a reference for all the researches and studies I did in the last three years. I am also greatful to all the members of the Fluid Dynamics Group in Rome, particularly to Mr. Alberto Giacomello for his cooperation and Dr. Mauro Chinappi, whose encouragement, support and friendship helped me so much.

I owe my deepest gratitude to my supervisor Dr. Roberto Di Leonardo who I consider a good friend as well as an excellent thesis director. Frankly, I feel extremely lucky to have the chance to work with him and to be part of his group. I would like to thank Prof. Giancarlo Ruocco (head of the Department of Physics) and all the members of the MicroPhysics group, particularly Mr. Silvio Bianchi and Mr. Lorenzo Cavallini.

I am very grateful to Prof. Lydéric Bocquet who accepted my proposal for a join international Ph.D. program and welcomed me in his fantastic group at the Laboratoire de Physique de la Matière Condensé et Nanostructures (LPMCN) at the University of Lyon. During my stay in France, he constantly provided me with help, suggestions and support. I would like to thank Prof. Jean-Louis Barrat and Prof. Alfonso San Migeul (heads of the LPMCN) and Prof. Elisabeth Charlaix and Prof. Christophe Dujardin (directors of the doctoral school of Physics and Astrophysics). I would like to show my gratitude to all the members of the Liquids and Interfaces group at LPMCN, especially to Dr. Christophe Pirat, Dr. Cécile Cottin-Bizonne and Dr. Christophe Ybert who I feel honored to work with.

Lastly and most importantly, I am very grateful to my family who always offered me encouragement, guidance and wholehearted support.

G.B.

Contents

Preface

Microfluidics is a very recent branch of science and technology. The development and the success, it has had in the last 15 years, is mainly due to the concept of lab-on-a-chip. Those miniaturized devices, integrating one or more laboratory functions, have aroused great interest among several research areas as physics, chemistry, biology and bioengineering. When a fluid is confined in a micro or nano scale structure, its behaviour is strongly affected by its interactions with the surrounding surfaces. In this context, the theme of fluid/solid slippage has been widely studied both theoretically and experimentally. Innovative technologies to enhance the surface slippage by specifically designing the solid interfaces have reportedly demonstrated to be an effective way to reduce the fluid/solid friction. To this end, superhydrophobic surfaces have increasingly attracted the interest of the scientific and technological community thanks to the large wall-slippage they present for liquid water. Though their behaviour has been extensively investigated through several theoretical and numerical methods, the experimental approaches are still indispensable to test and understand the properties of these surfaces. However, the lack of a general predicting model is also due to the fact that no one of the several existing experimental techniques has shown up as a very reliable one. Indeed, the reported measurements of slippage still depends on the specific adopted method, thwarting attempts to corroborate the proposed theoretical and numerical schemes. Therefore, it is evident that a more sensitive and effective experimental technique is still missing.

This thesis began and developed inside the wider project of setting up an innovative technique to investigate the fluid-solid slippage on superhydrophobic surfaces by means of optical tweezers. Even though this project is still going on, this work reports the steps performed along the long way towards this main goal and it consists of a collection of several researches involving different scientific fields as optics, microscopy, surface science, microhydrodynamics, microfluidics and microfabrication. Despite an apparent heterogeneity, all the experiments and simulations presented in this work share the common feature of investigating the physics of liquids con-

fined in micrometric structures. In this "micro-world", the balance between different forces is completely reversed compared to the macroscopic world and this results in stunning effects we have never experienced in our daily life. For example, in an inertia-less environment, where also the gravity has very weak effects, the force exerted by a light beam is enough to move a micrometric object. When the beam has an appropriate shape, an optical tweezer can be realized and the object can be even trapped. In a quite different context, interfacial interactions can results extremely strong and they can overcome buoyant forces or fluid shear stresses as in the case of the superhydrophobic surfaces. For this engineered surfaces, the mix of a suitable roughness and low energy interface results in surface forces able to trap nanometric and micrometric air bubbles inside the roughness. Consequently, when a liquid flows past such a surface, the liquid/air contact can strongly reduce the total friction on the whole surface.

The researches presented in this work can be separated in two main categories: i) holographic micromanipulation and microscopy, ii) superhydrophobicity. Accordingly, the thesis is divided in two Parts. In the first Part, holography is adopted to accomplish two completely different tasks. Projecting an hologram on a spatial light modulator, the light intensity of a coherent source is modified at will so that several optical traps are generated in the sample volume. In this scheme, the laser light is an input of the microscope system and it used as an active tool to manipulate micron-scale objects and investigate the surrounding fluid. On the other hand, illuminating the sample through a monochromatic plane wave generates an hologram, recorded on CMOS camera, that contains the information of the light intensity distribution in the entire sample volume. In this case, the coherent light is the output of the microscope system and provides a tool for three-dimensional visualization and analysis of the examined sample. In such a context, if we regard a trapped bead as a local probe of fluid properties, holographic optical trapping allows us to trap multiple particles at the same time and to freely move them throughout the sample volume. As an interesting application of holographic micromanipulation for microfluidics, in Chapter 1 we investigate the hydrodynamic interaction between two aligned micron-scale rods at several relative distances, highlighting a three-dimensional to two-dimensional crossover in the hydrodynamic coupling. To fully exploit the three-dimensional trapping capability of holographic tweezers, in Chapter 2 we present a custom digital holographic microscope for three-dimensional visualization, coupled to a holographic trapping system. Depending how the recorded holograms are processed, two different tracking techniques have been implemented: digital holographic microscopy and digital holographic tracking. Relying on the knowledge of the propagation function of a monochromatic light beam in a homogeneous isotropic medium, the intensity of the electromagnetic field recorded at the hologram plane can be back-propagated throughout the sample volume, so that the light intensity distribution is three-dimensionally reconstructed. This technique, called digital holography microscopy, is ideal for simultaneously tracking a large amount of beads and it can be implemented on graphic processing units for real-time applications. As an example, we visualize the motion of two holographically trapped beads simultaneously from three perpendicular viewing directions. Similarly, we apply this technique to monitor the flow of seeded water in a microfluidic channel from three perpendicular cross sections at the same time. When only few spherical probes have to be tracked with higher accuracy, a different method for hologram processing is chosen. In particular, fitting the experimental hologram to the theoretical predic-

tion of the Lorenz-Mie scattering theory provides a nanometric resolution tracking as well as high accuracy measurements of particle's radius and relative refractive index. We refer to this technique as digital holographic tracking. In Chapter 3 holographic optical tweezers and digital holographic tracking are combined together to realize a tool for high accuracy multipoint viscosity measurements. Furthermore, we also demonstrate as digital holographic tracking offers a quick and simple way to accurately characterize polymeric coated micro-bubbles used as ultrasound contrast agent.

The second Part of the thesis deals with the experimental characterization of the superhydrophobicity and slippage properties of silicon surfaces. In Chapter 4, micro particle image velocimetry is adopted to provide a reference standard characterization of microgrooved silicon superhydrophobic samples that would be very useful in view of a validation of holographic trapping measurements of fluid/solid slippage. However, what was initially conceived as a standard approach has revealed some interesting aspects that have been deeply investigated, as the role of the curvature and position of the liquid/air meniscus inside the microgrooves and the detrimental effect of the contamination of the liquid/air interface. A Section in the present work is dedicated to the description of the design and microfabrication process to realize microchannels equipped with a superhydrophobic wall. As regards microfabrication, in Chapter 5 we discuss an easy-to-implement and very cheap procedure to turn a silicon flat sample into a superhydrophobic surface via porosification. We analyze the wetting properties of the resulting surfaces by measuring the static contact angles and we probe the sensitivity of wettability to the process parameters. Those porous silicon superhydrophobic surfaces exhibit a mixing behaviour in between the two classical theoretical models for superhydrophobicity and, consequently, we propose a new model to justify the obtained results where water only partially fills in the surface micropores. Finally, relying on numerical studies presented in literature, we compute the expected slippage for the obtained surface roughness.

Demonstrating the capabilities of digital holographic microscopy and holographic tweezers to locally probe the fluid properties in terms of high accuracy measurements and high spatial resolution, the work presented in this thesis paves the way for superhydrophobicity characterization via holographic tweezers and digital holographic microscopy. Our main hope for the next future work is to set up an experimental apparatus where multiple holographically trapped beads can probe the local fluid/solid slippage of microgrooved and porous superhydrophobic surfaces. Once this technique will be implemented and accurately characterized, we firmly believe that it will play an important role in the future advances in the research studies on superhydrophobic surfaces.

Part I

Holographic micromanipulation and microscopy

Chapter 1

Holographic micromanipulation

Holographic techniques have demonstrated to be an effective and reliable technique for the simultaneous manipulation of several micron scale objects. The hologram, when displayed on a liquid crystal device, allows us to sculpt the wavefront of the incident laser beam and generate multiple traps when focusing through a microscope objective.

In the first part of the Chapter, we briefly report how the idea of optical trapping arose and we describe the working principle and the basic experimental set-up (Section 1.1). Subsequently, we introduce holographic optical trapping, starting off with its first implementations (Section 1.2), and we describe in more details the most used experimental configuration consisting of a spatial light modulator in a Fourier plane geometry (Section 1.3). Particularly, we discuss the working principle of the spatial light modulator and the algorithms used for generating digital holograms. A basic scheme of an holographic optical trapping set-up is described as well. We conclude this part reporting the most important applications of holographic micromanipulation techniques in microfluidics together with the future perspectives, with particular regards to the lab-on-chip technology (Section 1.4). The second part of the Chapter is dedicated to the study of hydrodynamic interactions between micron scale rods immersed in a liquid sample (Section 2). We develop simple theoretical (Section 2.2) and numerical models (Section 2.2) that predict a three-dimensional to two-dimensional crossover in the hydrodynamic coupling. The holographic micromanipulation of silica microrods allows us to experimentally verify such interactions and we find a remarkably good agreement between the experiment, the theory and the simulation.

1 Holographic Tweezers

1.1 A single beam optical trap: the optical tweezer

In our everyday life, we constantly see light interacting with solid objects and being reflected, refracted, transmitted and absorbed. This is indeed what happens when we wear our sunglasses or when we check our look in the mirror. On the other hand, what cannot be observed by a naked eye is that light can even exert extremely weak forces to those objects. The first scientist who hypothesized this behaviour was the astronomer Johannes Kepler in the seventeenth century. He justified the fact that the comet tails point away from the sun as the result of radiation pressure exerted by the sun itself. Nearly three centuries later James Clark Maxwell theoretically demonstrated the existence of this radiation pressure. However, optical forces are of the order of piconewtons for milliwatts of light power. Hence, we can detect them only if a high power and confined light beam impinges on very small objects. In 1970 Arthur Ashkin focused a laser light beam by a microscope objective in a liquid sample seeded with polystyrene particles and thereby he observed particles being pulled toward and pushed along the optical axis , see Ashkin (1970). By tuning the beam power, Ashkin and Dziedzic (1971) balanced the gravity force with the radiation pressure and let the beads levitating in the sample. Later, Ashkin and colleagues realized the first all-optical 3D trap adopting two counter-propagating beam, whereas in Ashkin et al. (1986) the first single beam optical trap was obtained by highly focusing a laser beam through a high numerical aperture (NA) objective. Ashkin gave it the name *optical tweezer*.

Depending on the size of the trapped object compared to the light wavelength λ, three different regimes exist and three corresponding theories can be used to model the optical forces. The simplest scenario is when the object size is much larger than λ and ray optics regime applies. In Figure 1.1 we show the simple case of two rays impinging on a dielectric sphere. When rays hit the sphere, they undergo multiple deflections due to refractions and reflections. For sake of clarity, in Figure 1.1 we report only the first reflection and the second and third refraction.

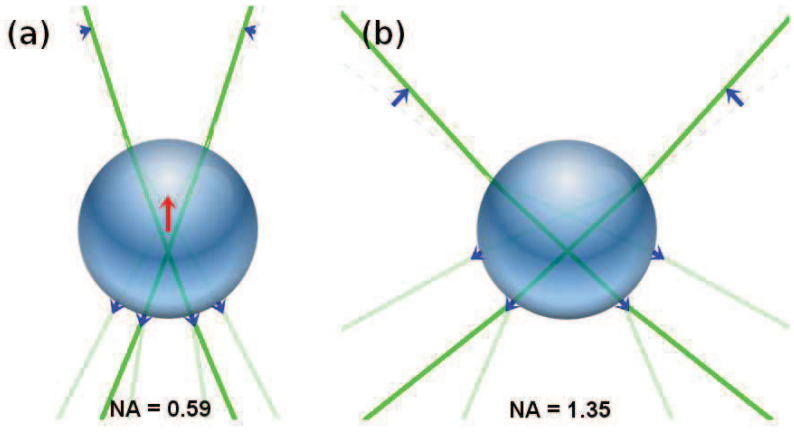

Figure 1.1: Ray optics model of optical trapping. Two rays impinge on a dielectric sphere and are reflected and refracted several times. For sake of clarity, only the first reflection and the second and third refractions are shown. (a) A low numerical aperture is not enough for the gradient force to balance the scattering one, which pushes away the particle. (b) A high numerical aperture is needed to generate an all-optical 3D stable trap.

As those rays carry momentum, the rate of change of momentum of refracted and reflected rays conveys an equal and opposite rate of change of momentum to the sphere. In Figure 1.1 the changes of momentum are represented by the blue arrows for each refracted or reflected components of the incident rays. The total change in light momentum flux produces a net force on the bead, represented by a red arrow. If we consider parallel incident rays, the momentum change is mostly along the light propagation direction and hence the bead is push downward this direction. This force is referred to as *scattering force*. As the ray beam is slightly convergent, as Figure 1.1(a), optical forces due to refracted light raise and push the bead toward the beam focus, contrasting the scattering force. When the interaction of light with the bead is addressed through the electromagnetic theory, it can be demonstrated that such force that pushes the particle toward the beam focus is proportional to the electric field gradient. Thus, even in the optics regime context we can refer to this force as *gradient force*. However, when the beam is only mildly convergent, the radiation pressure prevails and the bead is pushed away. In the case of a high focused beam, as in Figure 1.1(b), gradient forces are enough strong to balance the scattering forces and a 3D stable trap is obtained.

When the particle has a very small relative magnitude size with respect to λ, the Rayleigh regimes holds. Light can be no longer represented by rays but a simplified theory to predict the intensity of optical forces still exists. Indeed, the particle can be treated as an induced point dipole, since the electromagnetic field is uniform across it. The scattering forces results proportional to the Pointying vector of the incident field, while the gradient force is directed toward the light intensity gradient.

Unfortunately, in most of the applications the size of the trapped objects is the same order of magnitude of the light wavelength. In this intermediate regime, to which we refer as *Lorenz-Mie* regime, it's the most complicated for a theoretical model since no approximation can be used and the Maxwell equations have to be solved.

The experimental apparatus

As shown in Figure 1.2, the simplest optical tweezer set-up consists of a standard light microscope with a high numerical aperture (NA) objective and a single mode laser source. The laser beam is tightly focused by the objective so that the high light intensity gradient can stabilize the trap in the axial direction. To achieve the best performance in terms of trap quality, the laser focus has to be close to the specimen plane, since the whole of the optics of a conventional microscope is designed to reduce the aberrations near this plane. In order to improve the trap stiffness in the weaker direction, that is the axial one, the laser beam should slightly overfill the objective back-aperture. This ensures that laser is focused to a diffraction limited spot and the intensity gradient in the focal area is as intense as possible.

Other devices, in addition to this simple configuration, can be used to tune and handle the optical trap. For example, neutral density filter or half-wave plate are used to control the laser power and, thus, the optical force intensity. A motorized stage, or a piezoelectric one, can be used to move the trap in the xy plane of the sample, while the axial positioning of the trap is easily accomplished by changing the position of the microscope focus (for example, moving the objective up or down). On the other hand, to axially displace the center of the trap with respect to the actual focus of the objective, the divergence of the incoming light beam has to be modified.

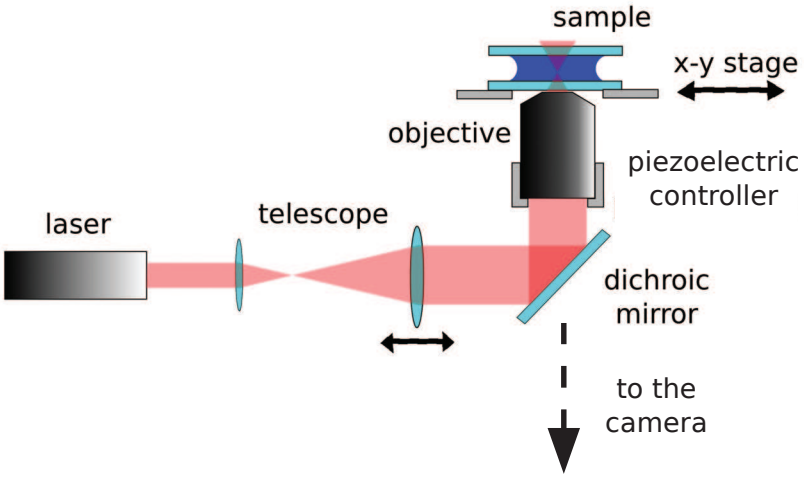

Figure 1.2: Scheme of a simple experimental set-up of an optical trapping system. A single mode laser beam, whose waist is adjusted through a telescope, overfills the back aperture of the microscope objective. The trap motion is accomplished moving the sample or the objective via a microscope stage or the telescope lenses.

1.2 Multiple optical traps: holographic optical trapping

It is automatic to ask how the experimental set-up reported in the previous Section can be improved to get multiple traps and independently move them throughout the sample. The simple case of two individual traps can be obtained adopting a pair of beam splitters and separate steering mirrors as shown by Misawa et al. (1992). To have more than two traps, instead, a single beam can be intermittently focused on different locations by a rapid scanning galvo-mirror or an acousto-optical deflector (AOD), see Visscher et al. (1993), Fällman and Axner (1997) and Vossen et al. (2004). Time-sharing several traps can produce very complicated trap schemes (e.g. Vossen et al. (2004) simultaneously trapped up to 100 particles) and, thanks to the high bandwidth of the AODs, it can be done at very fast refreshing speed (tens of MHz). However, neither of those systems allows an easy and simultaneous control of the axial position of the traps as holographic optical tweezers (HOTs) do.

The basic idea behind HOTs is to interpose, in the optical train between the laser source and the objective, a diffractive optical element (DOE) to "sculpt" the light phase and/or the light intensity distributions, so that we get the desired intensity distribution in the sample cell. Different system configurations can be set up depending both on the specific device acting as a DOE and on the method used to generate the light intensity pattern in the sample.

Fournier et al. (1995) relied on the Fresnel diffraction of a periodic binary phase grating, illuminated by a quasi-plane wave, in order to form self-images of that grating in planes that are evenly spaced along the direction of propagation. That is the so-called Talbot effect and it reportedly resulted as an effective way for the generation of large and periodic 3D arrays of traps. For instance, by placing the sample in the Fresnel region of a spatial light modulator (see the next Section) and relying on the Talbot effect, Schonbrun et al. (2005) managed to trap in three-dimensions hexagonal arrays of micron sized silica beads.

Friese et al. (1996) used computer generated phase holograms to convert the Gaussian (TEM_{00}) mode of their laser source into a Laguerre-Gaussian mode (LG_{03}) that, after being focused by a 100x microscope objective, could trap and rotate mi-

cron sized absorbing CuO particles. Since the Laguerre-Gaussian mode are propagation invariant solution of the Helmholtz equation, there is no specific constraint relating the positions of the DOE plane and the objective image plane.

Another way to implement HOTs is to place the DOE in a plane conjugate to the objective image plane. This image plane geometry has been adopted by Eriksen et al. (2002) where a spatial light modulator was used in phase modulation mode with a phase-contrast filter in the Fourier plane. This scheme allows a very easy computation of the holograms, generating the desired traps' structures, because of the straightforward relation between the image plane and the DOE plane. Nevertheless, the axial positioning is more problematic and should rely on the radiation pressure of counter-propagating beam.

However, in the most common implementation of HOTs, the diffractive element plane is conjugate to the back focal plane of the objective, so that the complex amplitudes in the DOE plane and in the trapping plane form a Fourier transform pair. Moreover, in most of the cases the diffractive element is a spatial light modulator. This scheme was reported for the first time by Dufresne and Grier (1998), where a commercial diffractive element was used to generate a 4×4 array of traps, while Curtis et al. (2002) implemented it by means of a spatial light modulator. After these seminal papers, a large amount of studies have been conducted in the following fifteen years, demonstrating as the Fourier-plane holographic approach, combined with the spatial light modulators, is so far the most effective way to generate multiple traps since they allow an easy, high and flexible individual positioning of traps that can be arranged even in very generic and complicated manners.

The set-ups that were used for the experiments reported in this thesis are equipped with a reflective phase-only spatial light modulator working in the Fourier plane geometry. The details of such a configuration as well as the working principle of a spatial light modulator are described in the following Section.

1.3 Fourier plane holography using a spatial light modulator

Spatial light modulators

Liquid crystal phase-only spatial light modulators (SLMs) are very similar to standard liquid crystal screens, where defined voltages are locally applied at the nodes (i.e. the pixels) of a squared grids lying on a thin liquid-crystal layer. Thus, the liquid crystal molecules align along the external electric field, varying their optical properties. In SLM for phase-only modulation, the local relative refractive index depends on the liquid crystals' orientation of the corresponding pixel, so that, as light pass through, it undergoes a well defined phase shift. Modulating the pixels' voltages over the entire screen, it is possible to deform the wavefront of the outgoing light beam at will. The liquid crystals for SLM can be either nematic or ferroelectric. Nematic SLM has a larger number of bit; usually 8 bit, that is, each pixel can assume 256 different phase values. On the other hand, their update rate is pretty low (typically 60 Hz). The ferroelectric SLMs are quite faster as their update rate can be even of tens of kilohertzs. This is because only two phase levels are available. On the contrary, a two-level system limits the diffraction efficiency of the device as well as its adaptability to the several existing algorithms for computer hologram generation. Even if ferromagnetic SLMs have been used for holographic trapping purpose, the nematic SLMs are the usual choice.

In order to reduce the limitation due to a low update rate, the nematic liquid

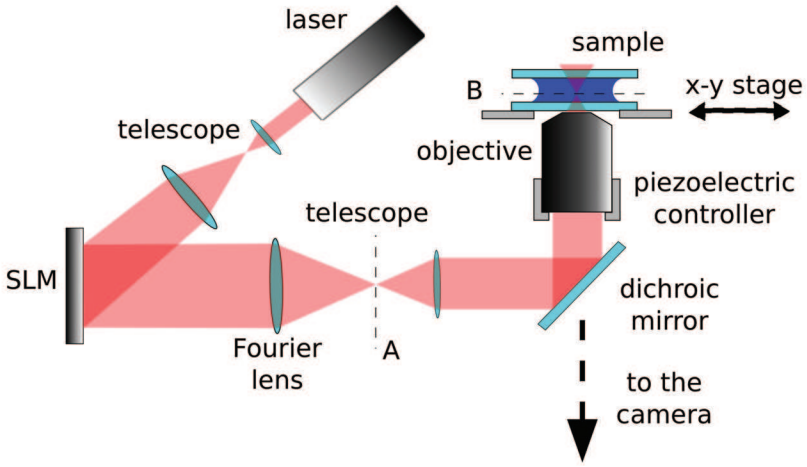

Figure 1.3: Scheme of the experimental set-up of an holographic trapping system. The system is the same of Figure 1.2, expect for the presence of the diffractive element, that in this case is a reflective spatial light modulator.

layer has to be as thin as possible. Indeed, the delay in the reorientation of liquid crystals grows with the square of the thickness because of inertia. For this reason, reflective SLMs are usually preferred as the light pass through the nematic layer twice and thus the layer thickness required (which depends on the maximum working light wavelength) is halved compared to the transmissive SLMs. However, reflective SLMs are more sensitive to planar imperfections of the SLM display, resulting in a deterioration of the quality of the traps. Nevertheless, tailored holograms can be computed and displayed on the device to correct both these beam distortions and all of the remaining aberrations in the optics, getting small point spread function and more efficients traps in terms of stiffness and symmetry, as shown by Love (1997) and Wulff et al. (2006).

The experimental apparatus

In Figure 1.3, a simple scheme of a HOT set-up equipped with a reflective, programmable spatial light modulator (SLM) is shown. The first telescope expands the laser beam to fit the SLM screen, since the trapping efficiency improves when the entire displayed hologram is illuminated by the laser. Moreover, this allows distributing the laser power on the whole screen, thereby reducing the risk of boiling the liquid crystals when high light intensity is used. The SLM and the back focal plane of the objective are coupled by another telescope in a 4f-lens geometry, so that the beam waist is reduced to slightly overfill the objective entrance pupil. Such a configuration assures that the light field in the trapping plane is the Fourier transform of the light field in the SLM plane. Furthermore, the 4f-lens geometry lets the SLM steer the light beam avoiding it to walk off of the entrance pupil of the objective. It's worth noting that the plane A between the telescope lenses is conjugate to the trapping plane B. Therefore, we can see on the former plane a magnified image of the light pattern generated by the SLM and thus we can modify it by spatial filtering. For instance, the part of light that is simply reflected by the SLM and it is not affected by any projected hologram comes out along the zeroth diffraction order of the device. Basically, we would like the generated trapping light pattern not to interfere with this undeflected spot. Hence, the desired output of the

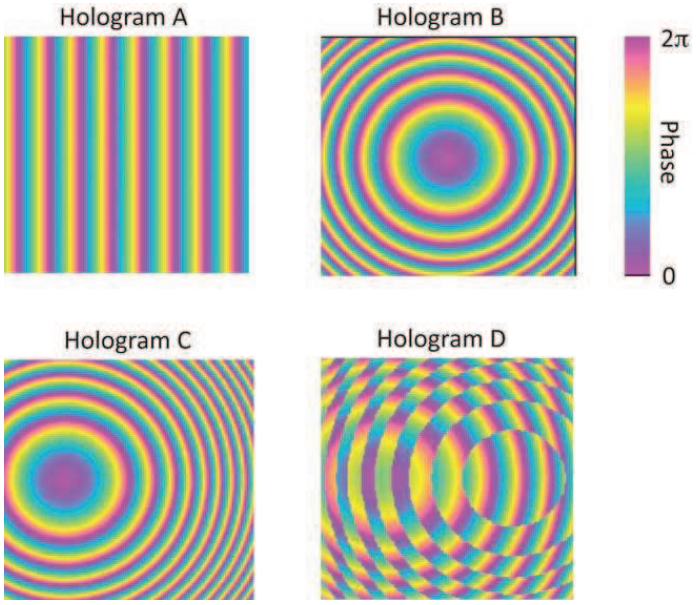

Figure 1.4: Simple holograms to move one ore two traps in the sample volume. Hologram A displaces the trap in the x-direction, whereas hologram B displaces the trap in the z-direction. To simultaneously displace the trap both in x and z direction, the modulo 2π addition of A and B has to be calculated as in hologram C. The complex addition of A and B generates two traps whose centers lie on the x axis (hologram D). Figure reproduced from Padgett and Di Leonardo (2011).

SLM is shifted on the first diffraction order and the downstream optics is aligned along that direction. Ultimately, placing an iris in the plane B we filter out all the diffraction orders but the first. At the end of the optical train, there is the trapping lens, namely a high numerical aperture microscope objective. Recently, Zwick et al. (2009) has obtained three-dimensional stable optical trap even with low numerical aperture lens by positioning a mirror on the opposite side of the sample with respect to the objective. By accurately positioning two traps, defocused to each other so that they form respectively the beam and the counter-propagating beam, Thalhammer et al. (2011) has shown that is possible to trap and manipulate particles and living organism almost 100 μm in size at very large working distance .

Algorithms for computer generated hologram design

Let's first introduce the algorithm used for positioning a single trap throughout the sample volume. In order to shift light away from the zeroth diffraction order, we can use a very simple hologram, namely a blaze diffraction grating, that allows displacing the trap center in the focal plane, as shown by hologram A in Figure 1.4. The position and the distance from the zeroth order spot is set by the pitch of the grating and its angular orientation. The axial displacement of a single trap is obtained by adding pixel by pixel, modulo 2π, the parabolic phase shift of a Fresnel lens. Therefore, a suitable combination of gratings and lens allows us to position in 3D the trap center (see holograms B and C in Figure 1.4). We can extent such an algorithm to the case of multiple traps by simply taking the argument of the complex addition of individual holograms, as for hologram D in Figure 1.4. The "gratings and lenses" algorithm is thus a computationally fast and easy-to-implement approach for hologram design of even complex trap arrangement, as reported by Reicherter et al.

(2006). A simplified version of the algorithm is to split the SLM screen in multiple regions as many as the desired traps and display the individual hologram separately. In this manner, the traps can be individually controlled and the whole hologram has no longer to be recalculated at any display refresh. On the other hand, this algorithm has some drawbacks. First the light power is not equally distributed to the different traps and part of light is directed towards unwanted ghost traps. To overcome this limitation as well as to get a fine positioning of the light spots, the algorithm requires further iterations. However, the most important limitation is that this approach does not permit to generate complex shaped traps as line and ring traps. A more general and effective way for hologram computation is the algorithm proposed by Gerchberg and Saxton (1972) that provides the suited hologram to be displayed on a phase-only SLM in order to generate a close approximation to any chosen intensity distribution on the trapping plane. However, this method has no direct control on the phase distribution of the resulting trap pattern but this is not limiting its applications since in most of the cases we are interested in the intensity distribution only. The Gerchberg-Saxton algorithm is based on iterative Fourier transform calculations back and forth between the SLM plane and the trapping plane, so it can results somehow slow. However, this problem has been brilliantly overcome by Bianchi and Di Leonardo (2010) using modern graphics processing units since their parallel architecture is well-suited for performing such calculations and thus the real time hologram generation by Gerchberg-Saxton algorithm is now possible.

1.4 HOTs: microfluidic applications and perspectives

In the last twenty years nano and micro technologies have undergone continuous development letting be possible the realization of very complex and advanced micro-scale devices as the so-called lab on a chip. Those miniaturized systems, integrating one or more laboratory functions, have aroused great interest among several research areas as physics, chemistry, biology and bioengineering. Despite technologies as soft-lithography and two photon polymerization have led to the fabrication of complicated 3D micro structures as complex pattern surface and micro-sized objects (e.g. gears, levers, pumps, valves, etc.), the path along the miniaturization of actuating systems, that can coherently move those objects to accomplish a well-defined task, is still long. In this context, since light carries both linear and angular momentum and it can be easily focused and shaped at will in those micrometric devices, holography technique is a natural candidate as an actuating system being able to exert forces and torques on micron-scale objects. In 1994, it was demonstrated as light can be used to drive a miniature windmill, etched from silicon dioxide, because of the scattering forces acting on its asymmetric blades, see Higurashi et al. (1994). In addition, if a spiral phase term is added to the trapping hologram displayed on the SLM so that a helically phased doughnut beam is generated, light carries an optical angular momentum that, when transferred to a particle, causes it to spin. For example, this approach has been used by Friese et al. (2001) to set into rotation microgears by spinning a nearby birefringent particle and, in 2006, a couple of optically rotating spheres in a narrow channel served as an optical microfluidic pump or valve to set a flow in a microfluidic channel or to stop it, see Leach et al. (2006).

HOTs have also reportedly demonstrated to be an effective multipoint measurement system when several trapped colloids are used as probes sensing the surrounding environment (e.g. fluid, nearby structures, etc.). The simplest model for a

trapped particle immersed in a fluid is that one of a damped harmonic oscillator, where the trap is modeled as a linear elastic element, while the surrounding fluid acts as the system damper. Tracking the particle position, we can study the Brownian dynamics of the trapped objects and thus we can infer the local properties of the sample environment which affect such a dynamics. That concept led to the realization of the photonic force microscope by Rohrbach et al. (2004) where the displacements of a trapped bead as it is scanned around the sample are mapped into a force field in order to study surface forces, molecular binding forces, entropic and viscoelastic forces of single molecules, and small variations in particle flow, local diffusion, and viscosities. Indeed, particle dynamics depends on its mobility and, thus, the latter can be measured by the power spectra of particle motion, or its mean square displacements or the exponential decay response when an intermittent optical trap induces a step function velocity of the bead relative to the fluid. That approach has allowed Pesce et al. (2005) and Yao et al. (2009) to measure the local rheological properties of the surrounding fluid. As demonstrated by Keen et al. (2009), HOTs permit to extend this measurements simultaneously over different points of the sample volume. In Chapter 3, we present an experimental method to perform high accuracy multi-point viscosity measurements where HOTs are coupled with a digital holographic microscope. The recorded holograms, analyzed through digital holographic tracking technique, provide both the mobility and the particles' size. Hence, we achieve a very precise and accurate viscosity measurement that is independent by the individual probe size, see Bolognesi et al. (2011).

Since HOTs give the possibility to arrange a set of particle in a very precise, controlled and reproducible configuration, they have also been applied to locally maps fluid flow in precise points of the sample, using spherical beads as velocity probes. Indeed, as shown by Di Leonardo et al. (2006), as the traps are continuously turned on and off, the mean displacements of particles can be tracked and the corresponding velocity vectors of the background fluid flow can be deduced. The same configuration has been extensively exploited to investigate the hydrodynamic interactions of networks of particles. To this respect, experimental results were found in very good agreement with the hydrodynamic theory that predicts how the dynamics of an individual spherical particle is affected by all the surrounding particles as well as the sample cell walls. Only recently the hydrodynamic interaction studies has been extended by Di Leonardo et al. (2011) to the case of non spherical objects, as micro-scale rods. In the next Section, we reported the experiment where the hydrodynamic coupling of two micron sized silica parallel rods are investigated at different relative distances, highlighting the existence of a three-dimensional to two-dimensional cross-over in the hydrodynamic interaction.

HOTs have also been extensively applied for fundamental researches in colloidal science. For instance, the blinking tweezer has been used to deeply understand several aspects of electrostatic interactions between colloids such as the many body effects by Merrill et al. (2009), non polar solvent by Sainis et al. (2008) and confinement by Han and Grier (2003). Another fascinating issue addressed by HOTs is that one of non-equilibrium systems as the case of Brownian motors, reported by Astumian (1997), where non-equilibrium fluctuations can bias the Brownian motion of a particle when an asymmetric external potential is applied, see Faucheux et al. (1995). In lab-on-chip devices, the surface to volume ratios are so high that the surface forces may have a dominant role in those systems. Indeed, such forces can even drive a flow as in the case of thermocapillary effect that raises when a thermal gra-

dient is established at a fluid/solid interface. A holographically shaped light beam impinging on a solid surface can generate a well-controlled thermal spatial gradient at the interface and thus it can be used, for instance, to achieve active controlled droplet routing in microfluidic channels, see Cordero et al. (2008). Similarly, light thermal gradient can directly induce the particle motion by means of thermophoresis, which in an appropriate configuration can lead to reversible self-assembly of large 2D crystal due to long range hydrodynamic attractions between colloids, as demonstrated by Weinert and Braun (2008) and Di Leonardo et al. (2009).

In the most of the current applications of optical trapping for microfluidics, a microscope apparatus is still required. Thus, even though the microfluidic device occupies a few millimeters on a chip, a microscopy system is necessary to make it work. Therefore, the future research for HOTs applications in microfluidic system should be focused on embedding such a technique on the microscopic device, so that a fully integrated lab-on-a-chip could be finally available. However, this research direction has already been undertaken by several groups providing integrated systems for both imaging and trapping, see Cui et al. (2008) and Guck et al. (2001). In this context, driving light into the lab-on-a-chip by optical fibers seems a very promising solution, as discussed by Di Leonardo and Bianchi (2011a). Particularly, by appropriately shaping light at the entrance of the fiber through a spatial light modulator, it has been recently demonstrated that particles can be holographically trapped and displaced in the sample without any mechanical movement of the fiber being required, see Čižmár and Dholakia (2011). A similar approach has been proposed by Di Leonardo and Bianchi (2011b) to perform endoscopic fluorescence microscopy and micromanipulation via a multi-mode fiber.

2 Hydrodynamic interactions between two parallel micron scale rods

2.1 Introduction

Flagella, microtubules, nanotubes, and nanowires are a few examples of the rich variety of fundamental roles that slender bodies have in physics, chemistry, and biology. They all share the same geometrical feature of being "slender", that is, having a linear dimension which is much larger than the other two. As a consequence of that they are all expected to have a similar physical behavior in those situations where only shape matters, such as in microhydrodynamics. The Stokes drag force on a thin nanotube and a thicker microrod will be very similar. The drag primarily depends on the body length, while the thickness only appears in logarithmic terms, see Happel and Brenner (1991). While there is a huge amount of work on single slender body dynamics, especially in the context of bacterial motility, see Lighthill (1975), investigation of hydrodynamic interactions between slender bodies is almost only limited to the phenomenology of synchronization, see Reichert and Stark (2005) and Polin et al. (2009). One reason could be that, as opposed to spheres, which have been studied extensively, as reported by Crocker (1997), Meiners and Quake (1999) and Di Leonardo et al. (2007), hydrodynamic couplings between anisotropic bodies are a complex function of both relative distance and orientation.

Optical tweezers can be used to trap and move one-dimensional (1D) objects, see Tan et al. (2004), Maragó et al. (2008) and Maragó et al. (2010). In particular, holographic optical trapping has been shown by Carberry et al. (2010), Plewa et al.

(2004), Agarwal et al. (2005), Simpson and Hanna (2010) and **?** to be an ideal tool for full 3D micromanipulation of microrods and nanotubes. Such capabilities offer a unique opportunity for trapping and orienting slender bodies in a well defined relative configuration, and directly probe their coupled dynamics. In the following Section, we provide a direct measurement of hydrodynamic coupling between a pair of parallel aligned silica microrods optically trapped in blinking holographic tweezers. We found a crossover from 3D behavior at large distances, to a 2D logarithmic behavior, when the distance falls below the rod's length. Experimental data are in excellent agreement with finite element analysis (FEA) and can be very well reproduced by a simplified theoretical approach.

2.2 Microrods as lines of Stokes singularities

Let's now consider the hydrodynamic interaction between two arbitrarily oriented microrods of length L_1 and L_2 and diameters a_1 and a_2. We can model the microrods as very prolate spheroids with semi-major axis $L_1/2$ and $L_2/2$ and eccentricities e_1 and e_2, respectively. The choice of the prolate spheroid is due to the fact that for such a shape the disturbance field in a generic ambient flow is analytically known, see Kim and Karrila (1991). The external force $\mathbf{F}_1$ is applied on the center of the particle 1 and similarly the particle 2 experiences the force $\mathbf{F}_2$. Since the Stokes equations are linear, in a quiescent flow the resulting particle velocities $\mathbf{U}_1$ and $\mathbf{U}_2$ can be written as[1]

$$\begin{aligned} \mathbf{U}_1 &= \mathbf{M}_{11} \cdot \mathbf{F}_1 + \mathbf{M}_{12} \cdot \mathbf{F}_2 \\ \mathbf{U}_2 &= \mathbf{M}_{21} \cdot \mathbf{F}_1 + \mathbf{M}_{22} \cdot \mathbf{F}_2 \end{aligned} \tag{1.1}$$

where $\mathbf{M}_{11}$ and $\mathbf{M}_{22}$ are the body second-rank mobility tensors and $\mathbf{M}_{21}$ and $\mathbf{M}_{12}$ are the coupling second-rank tensors, that account for the hydrodynamic interaction between those objects. These formulae can be lumped in a compact mobility matrix formulation:

$$\mathsf{U} = \mathsf{M}\mathsf{F} \tag{1.2}$$

where $\mathsf{U} = [\mathbf{U}_1, \mathbf{U}_2]$, $\mathsf{F} = [\mathbf{F}_1, \mathbf{F}_2]$ and the mobility matrix is

$$\mathsf{M} = \begin{bmatrix} \mathbf{M}_{11} & \mathbf{M}_{12} \\ \mathbf{M}_{21} & \mathbf{M}_{22} \end{bmatrix} \tag{1.3}$$

Once we set the external forces $\mathbf{F}_i$, we can derive the velocities $\mathbf{U}_i$ by the method of reflections that provides an approximate solution when those particles are widely separated. Such a problem is also referred to as a *mobility* problem and through Eq.(1.2) leads to the determination of both the mobility and coupling tensors. Even though the method of reflections is at our disposal for well separated particles, the obtained velocity fields are still quite accurate when particle are fairly close together. Indeed, as it is shown below, the higher order reflections in mobility problems consist of dipole-dipole interactions that are pretty weak.

The zeroth order approximation in the method of the reflections is the superposition of the fields produced by the isolated particles: $\mathbf{v}_1(\mathbf{x})$, $\mathbf{v}_2(\mathbf{x})$. At great distance from the particle, the velocity field can always be expressed as a multipole expansion, irrespective of the particular shape of the object. In this case, the field

[1] Such formulas hold as long as the rotational and translational degrees of freedom of the system can be decoupled.

is obtained as a Taylor series of the Oseen tensor $\mathcal{G}(\mathbf{x}-\boldsymbol{\xi})$, expanded about the particle center, $\boldsymbol{\xi}=0$,

$$\mathbf{v}(\mathbf{x}) = \sum_{n=0}^{\infty} \frac{(-1)^n}{n!} \mathbf{L}^{(n)} \cdot \frac{\mathcal{G}(\mathbf{x})}{8\pi\mu} \tag{1.4}$$

where

$$\mathbf{L}^{(n)} = \int_{\mathcal{S}} [(\boldsymbol{\sigma}\cdot\hat{\mathbf{n}})\xi_{k_1}\dots\xi_{k_n}]\,\mathrm{d}S \frac{\partial}{\partial x_{k_1}}\dots\frac{\partial}{\partial x_{k_n}} \tag{1.5}$$

and $\boldsymbol{\xi}\in\mathcal{S}$ and $\mathcal{S}$ is the object surface. The coefficients of the expansion, namely the moments of the surface traction $\boldsymbol{\sigma}\cdot\hat{\mathbf{n}}$, are analytically known for particular shapes as, for instance, the sphere and the ellipsoid. Alternatively, the solution is given by an appropriate distribution of a collection of singularities over a particular region. Such a method is referred to as the *singularity* method and the region over which the singularities are located is called the *image system*. For a prolate spheroid, the image system is the line segment between the foci of the generating ellipse and the intensity of the singularities are analytically known. However, for deriving a simple expression for the velocities $\mathbf{v}_i(\mathbf{x})$ we use neither the multipole expansion approach nor the singularity method. We rather rely on the slender body theory that provides very simple but still effective formulae. Moreover the silica microrods used in our experiments are closer to needle-like particles than prolate spheroids and thus such a theory fits perfectly with this problem. At a first order approximation, a slender body can be modeled as a line distribution of lowest order singularities, i.e. the Stokeslet $\mathcal{G}(\mathbf{x})$ and the potential dipole $\mathcal{D}(\mathbf{x})$. Therefore, the velocity fields $\mathbf{v}_1(\mathbf{x})$ and $\mathbf{v}_2(\mathbf{x})$ can be written as

$$\mathbf{v}_i(\mathbf{x}) = \frac{\mathbf{F}_i}{8\pi\mu L_i}\cdot\int_{-L_i/2}^{L_i/2}\left(\mathcal{G}(\mathbf{x}-\boldsymbol{\xi}) + \left(\frac{a_i^4}{6a_i^2+L_i^2}-\frac{a_i^2}{2}\right)\mathcal{D}(\mathbf{x}-\boldsymbol{\xi})\right)\mathrm{d}\xi \quad , \quad i=1,2 \tag{1.6}$$

where $\boldsymbol{\xi}$ now varies along the particles' axis. The coefficient of the potential dipole is chosen in order to satisfy the boundary condition at the particle surface. This approach is thus very similar to the singularity solution for a prolate spheroid, truncated at the lowest order singularity. The resulting zeroth order approximation for the particles' velocities is

$$\mathbf{U}_i^{(0)} = \mathbf{v}_i(\mathbf{x}_p) = \mathbf{M}_{ii}\cdot\mathbf{F}_i \quad , \quad \mathbf{x}_p\in S_i \quad , \quad i=1,2 \tag{1.7}$$

and S_i represents the surface of particle i. Therefore, we get the particle mobilities as

$$\mathbf{M}_{ii} = \frac{1}{8\pi\mu L_i}\int_{-L_i/2}^{L_i/2}\left(\mathcal{G}(\mathbf{x}_p-\boldsymbol{\xi}) + \left(\frac{a_i^4}{6a_i^2+L_i^2}-\frac{a_i^2}{2}\right)\mathcal{D}(\mathbf{x}-\boldsymbol{\xi})\right)\mathrm{d}\xi \quad , \quad i=1,2 \tag{1.8}$$

The first order of reflection involves the velocity field $\mathbf{v}_{ij}(\mathbf{x})$ that is produced by the object j when is immersed in a ambient flow given by the zeroth order field $\mathbf{v}_i(\mathbf{x})$ of the object i. Such a field can be obtained as a multipole expansion where the multipole moments are given by the Faxèn law. Since $\mathbf{v}_1$ and $\mathbf{v}_2$ produce exactly the prescribed forces $\mathbf{F}_1$ and $\mathbf{F}_2$, the particle motions obtained by the subsequent reflections $\mathbf{v}_{12}$ and $\mathbf{v}_{21}$ are force-free and torque-free, thus the leading order term in the multipole expansion is a stresslet $\mathcal{S}$

$$\mathbf{v}_{ij}(\mathbf{x}) = \left(\mathcal{S}_j^{(1)}\cdot\lambda\right)\cdot\frac{\mathcal{G}(\mathbf{x}-\mathbf{x}_j)}{8\pi\mu}+\dots \quad , \quad i,j=1,2 \quad \text{and} \quad i\neq j \tag{1.9}$$

The stresslet intensity and the resulting translational and rotational velocities of the particles are given by the Faxèn law for a prolate spheroid, see Kim and Karrila (1991). Herein, we only report the translational velocities

$$\mathbf{U}_i^{(1)} = \frac{1}{e_i L_i} \int_{-e_i L_i/2}^{e_i L_i/2} \left\{ 1 + \left[\left(\frac{e_i L_i}{2} \right)^2 - \xi^2 \right] \frac{1 - e_i^2}{4 e_i^2} \nabla^2 \right\} \mathbf{v}_j(\boldsymbol{\xi}) \mathrm{d}\xi \tag{1.10}$$

with $i, j = 1, 2$ and $i \neq j$. Therefore, to the first reflection order, the particle linear velocities are

$$\mathbf{U}_i = \mathbf{U}_i^{(0)} + \mathbf{U}_i^{(1)} = \mathbf{M}_{ii} \cdot \mathbf{F}_i + \mathbf{U}_i^{(1)} \quad , \quad i = 1, 2 \tag{1.11}$$

Comparing this expression to Eq.(1.1), it results that the hydrodynamic coupling term can be approximate as the particle velocity due to the first reflection field:

$$\mathbf{M}_{ij} \cdot \mathbf{F}_j = \mathbf{U}_i^{(1)} \quad , \quad i, j = 1, 2 \quad \text{and} \quad i \neq j \tag{1.12}$$

Substituting Eq.(1.10) and Eq.(1.6) into the last expression and neglecting the potential dipole term, we have

$$\mathbf{M}_{ij} = \frac{1}{e_i L_i} \int_{-e_i L_i/2}^{e_i L_i/2} \left\{ 1 + \left[\left(\frac{e_i L_i}{2} \right)^2 - \xi_2^2 \right] \frac{1 - e_i^2}{4 e_i^2} \nabla^2 \right\} \int_{-L_j/2}^{L_j/2} \frac{1}{L_j} \frac{\mathcal{G}(\boldsymbol{\xi}_i - \boldsymbol{\xi}_j)}{8\pi\mu} \mathrm{d}\xi_i \mathrm{d}\xi_j \tag{1.13}$$

with $i, j = 1, 2$ and $i \neq j$. In the case of a very prolate spheroid, the eccentricity e_i tends to unity, thus we get the simplified formula for the coupling terms

$$\mathbf{M}_{ij} = \frac{1}{8\pi\mu L_i L_j} \int_{-L_i/2}^{L_i/2} \int_{-L_j/2}^{L_j/2} \mathcal{G}(\boldsymbol{\xi}_i - \boldsymbol{\xi}_j) \mathrm{d}\xi_i \mathrm{d}\xi_j \tag{1.14}$$

with $i, j = 1, 2$ and $i \neq j$. From the last equation, it's evident that $\mathbf{M}_{ij} = \mathbf{M}_{ji}$ and, hence, the matrix M is symmetric. We conclude noting that such a property can also be demonstrated as a consequence of the Lorenz reciprocal theorem.

Parallel interacting rods: 3D to 2D crossover

We now consider the simple case of two parallel microrods of length L and diameter $2a$, located at distance of d, as shown in Figure 1.5. We introduce a reference system with coordinate versors $\{\hat{\mathbf{e}}_x, \hat{\mathbf{e}}_y, \hat{\mathbf{e}}_z\}$ where $\hat{\mathbf{e}}_y$ is parallel to the microrods' axes of symmetry and $\hat{\mathbf{e}}_x$ lies on the transverse direction joining the particle centers: $\mathbf{x}_1$ and $\mathbf{x}_2$. We limit our investigation to the translational motion along the transverse direction, i.e. the x axis. Let's now compute the transverse mobility M_{11}^{xx} of the isolated microrod by the xx component of Eq.(1.8), assuming $\mathbf{x}_p = \mathbf{x}_i + a\hat{\mathbf{e}}_x$ and

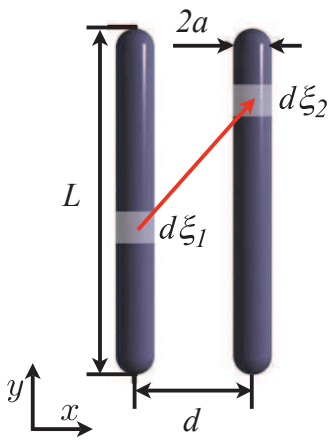

Figure 1.5: Scheme of two parallel aligned microrods providing the geometrical parameters of the investigated configurations.

$\boldsymbol{\xi} = \mathbf{x}_i + \xi\hat{\mathbf{e}}_y$:

$$\begin{aligned} M_{11}^{xx} =& \frac{1}{8\pi\mu L}\int_{-L/2}^{L/2}\left(\mathcal{G}^{xx}(a\hat{\mathbf{e}}_x - \xi\hat{\mathbf{e}}_y) + \left(\frac{a_i^4}{6a_i^2+L_i^2} - \frac{a_i^2}{2}\right)\mathcal{D}^{xx}(a\hat{\mathbf{e}}_x - \xi\hat{\mathbf{e}}_y)\right)\mathrm{d}\xi = \\ =& \frac{1}{8\pi\mu L}\int_{-L/2}^{L/2}\left(\frac{a^2}{\sqrt{(a^2+x^2)^3}} + \frac{1}{\sqrt{a^2+x^2}}\right)\mathrm{d}\xi + \\ &+ \frac{1}{8\pi\mu L}\int_{-L/2}^{L/2}\left(\frac{a_i^4}{6a_i^2+L_i^2} - \frac{a_i^2}{2}\right)\left(\frac{3a^2}{\sqrt{(a^2+x^2)^5}} - \frac{1}{\sqrt{(a^2+x^2)^3}}\right)\mathrm{d}\xi = \\ &= \frac{1}{8\pi\mu L}\left[\frac{\sqrt{4\varepsilon^2+1}}{6\varepsilon^2+1} - 2\log\left(\frac{2\varepsilon}{\sqrt{4\varepsilon^2+1}+1}\right)\right] \end{aligned} \tag{1.15}$$

and, thus,

$$M_{11}^{xx} = \frac{1}{8\pi\mu L}\left(1 + 2\log(\varepsilon^{-1})\right) + o(\varepsilon^2) \tag{1.16}$$

where $\varepsilon = a/L$. Similarly the coupling term M_{12}^{xx} along the transverse axis is obtained by the xx component of Eq.(1.14), assuming $\boldsymbol{\xi}_1 = \mathbf{x}_1 + \xi_1\hat{\mathbf{e}}_y$ and $\boldsymbol{\xi}_2 = \mathbf{x}_2 + \xi_2\hat{\mathbf{e}}_y$. We recall that $\mathbf{x}_2 - \mathbf{x}_1 = d\,\hat{\mathbf{e}}_y$ and, hence, we have

$$\begin{aligned} M_{12}^{xx} =& \frac{1}{8\pi\mu L^2}\iint_{-L/2}^{L/2}\mathcal{G}^{xx}(d\hat{\mathbf{e}}_y + (\xi_2-\xi_1)\hat{\mathbf{e}}_x)\mathrm{d}\xi_1\mathrm{d}\xi_2 \\ =& \frac{1}{8\pi\mu L^2}\iint_{-L/2}^{L/2}\left(\frac{d^2}{\sqrt{(d^2+(\xi_2-\xi_1)^2)^3}} + \frac{1}{\sqrt{d^2+(\xi_2-\xi_1)^2}}\right)\mathrm{d}\xi_1\mathrm{d}\xi_2 \end{aligned} \tag{1.17}$$

Working out the double integration, we finally get the hydrodynamic coupling between the two parallel rods

$$M_{12}^{xx} = \frac{1}{8\pi\mu L}\log\left[\frac{L+\sqrt{L^2+d^2}}{\sqrt{2L^2+d^2-2L\sqrt{L^2+d^2}}}\right] \tag{1.18}$$

When the two rods are much farther apart than their length, the propagator reduces obviously to the Oseen tensor component

$$M_{12}^{xx}(d \gg L) = \frac{1}{4\pi\mu d} \tag{1.19}$$

Indeed the Oseen tensor (i.e. the Stokeslet) represents the first term in the multipole expansion of the Stokes flow produced by a given force spatial distribution. The Stokeslet propagates the perturbation of a zero-dimensional point force and therefore does not depend on particle shape and orientation. For spherical beads it provides a remarkably good description of couplings down to interparticle distances of about 2.5 radii, as demonstrated by Crocker (1997) **?** and Di Leonardo et al. (2007). We conclude that when the microrods are enough far apart, they basically interact as they were simple spheres. More interestingly, for separations that are much smaller than the rods length, the interacting term has the following logarithmic expression

$$M_{12}^{xx}(d \ll L) = \frac{1}{4\pi\mu L} \log\left(\frac{2L}{d}\right) \tag{1.20}$$

This equation is very similar to what was observed by Di Leonardo et al. (2008) for hydrodynamic coupling in two-dimensional thin liquid layers. In other words, microrods interact like point particles in 3D when they are very far away, and then like point particles in 2D at short distances. The crossover distance is determined by the most important length in the problem, that is, the rod's length. Such a finding is not surprising when one realizes that at short distances the problem reduces to the idealized two-dimensional case of infinitely long cylinders, where the finite length of the two rods is only responsible for edge effects.

Despite the presented model seems to provide good interpolation between the two limiting cases, higher order singularities in the slender body description of the isolated flow field $\mathbf{v}_i(\mathbf{x})$ might be needed when evaluating the flow very close to the particle surfaces. In particular, a line distribution of source doublets restores the correct boundary conditions on the surface of an infinite cylinder of radius a, see Lighthill (1975) and Batchelor (1970). However, that will only contribute to the produced flow with a rapidly decaying term of order $(a/d)^2$, which amounts to less than one percent at the closest distance configuration examined in our experiments. To be definitely sure that our theoretical framework accurately describes the hydrodynamic interactions between two rods, we test it with a finite element analysis simulation, as presented in the next Section.

2.3 Finite element analysis

Through a three-dimensional finite element analysis (FEA), implemented on a commercial software platform (COMSOL®), the system of stationary Stokes equations are solved for the simple geometry of two parallel rods in order to extract the particle mobilities as well as the hydrodynamic couplings: M_{11}^{xx}, M_{12}^{xx}.

The geometric model consists of two cylinders of length L and radius a at distance d. The cylinder axes are parallel to the y direction and lie on the x, y plane, as shown in Figure 1.6(a). The origin of the reference system $\{x, y, z\}$ is set on the midpoint of the segment joining the cylinders' centers, so that the geometry is symmetric with respect to the reference planes. Since in FEA the solution domain is necessarily closed, finite size effects on rods' dynamics are reduced by having the two cylinders

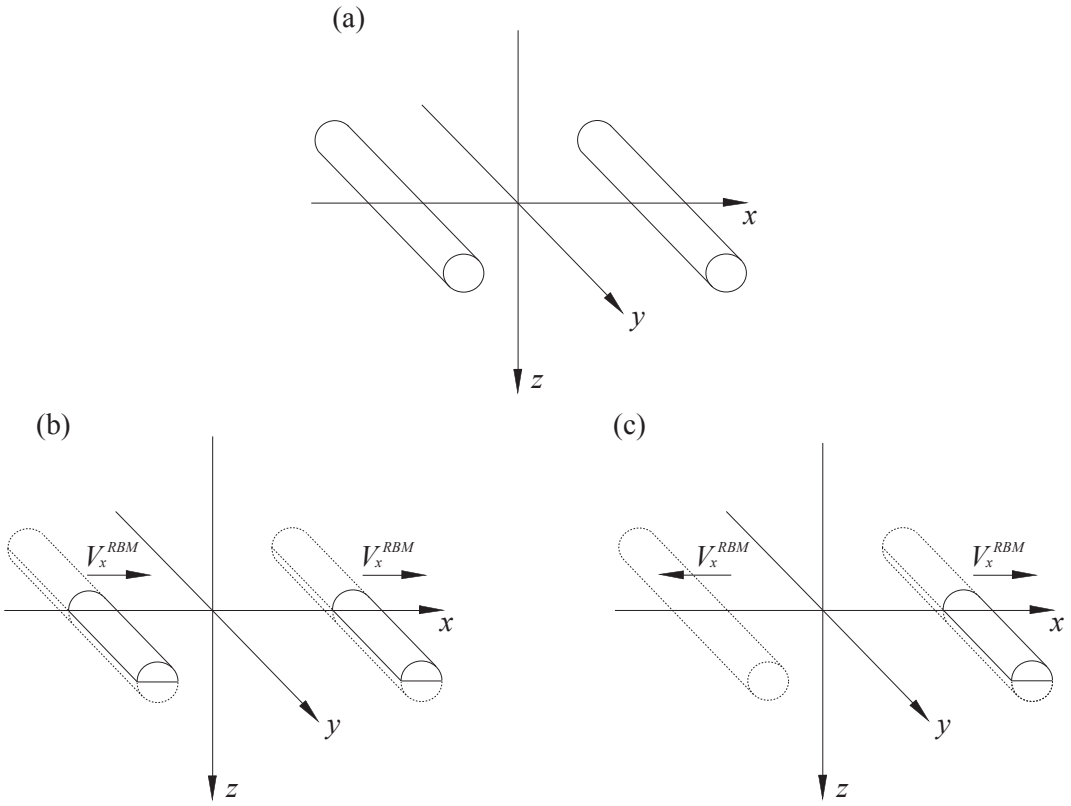

Figure 1.6: Geometrical model of the finite element analysis. (a) The whole geometry model. (b) The reduced model for the rigid body motion simulation. The geometry and the boundary conditions are symmetric with respect to x, y and x, z planes and so only one quarter (solid lines) of the whole geometry is simulated. The remaining part (dashed lines) is recovered imposing the symmetric boundary conditions on the x, y and y, z planes. (c) The reduced model for the relative motion simulation. A new plane of symmetry is added, namely the y, z plane. Only one octave of the geometry is considered.

inside a fluid sphere of radius $100L$. The particles' motion is prescribed by setting the appropriate boundary conditions. Once the velocity field is computed on the nodes of the finite elements, the resulting forces exerted on the particles are determined by numerically integrating the stress tensor on the cylinder surfaces. As opposed to the mobility problem, the resistance forces are now unknown and they have to be determined. That is the reason why we refer to this problem as a *resistance problem*. Because of the linearity of the Stokes equations, in a resistance problem we can relates the particles' velocities $\mathbf{U}_1$,$\mathbf{U}_2$ to the particles' forces $\mathbf{F}_1$,$\mathbf{F}_2$ as follows:

$$\begin{aligned} \mathbf{F}_1 &= \mathbf{R}_{11} \cdot \mathbf{U}_1 + \mathbf{R}_{12} \cdot \mathbf{U}_2 \\ \mathbf{F}_2 &= \mathbf{R}_{21} \cdot \mathbf{U}_1 + \mathbf{R}_{22} \cdot \mathbf{U}_2 \end{aligned} \tag{1.21}$$

where $\mathbf{R}_{11}$ and $\mathbf{R}_{22}$ are the particle second-rank resistance tensors and $\mathbf{R}_{21}$ and $\mathbf{R}_{12}$ are the second-rank coupling tensors. In the particular case of two aligned microrods, the transverse direction x, see Figure 1.6(a), is an eigenvector of both the resistance and the coupling tensors and, consequently, Eq.(1.21) can be projected on the x axis and rewritten as

$$\begin{aligned} F_1^x &= R_{11}^{xx} U_1^x + R_{12}^{xx} U_2^x \\ F_2^x &= R_{21}^{xx} U_1^x + R_{22}^{x} U_2^x \end{aligned} \tag{1.22}$$

Adopting the matrix formulation, we get

$$\mathsf{F}^x = \mathsf{R}^{xx}\mathsf{U}^x \tag{1.23}$$

where $\mathsf{U}^x = [U_1^x, U_2^x]$, $\mathsf{F}^x = [F_1^x, F_2^x]$ and the transverse resistance matrix is

$$\mathsf{R}^{xx} = \begin{bmatrix} R_{11}^{xx} & R_{12}^{xx} \\ R_{21}^{xx} & R_{22}^{xx} \end{bmatrix} \tag{1.24}$$

For the same reason, we can project the Eq. (1.1) of the mobility problem along the transverse direction

$$\begin{aligned} U_1^x &= M_{11}^{xx} F_1^x + M_{12}^{xx} F_2^x \\ U_2^x &= M_{21}^{xx} F_1^x + M_{22}^{x} F_2^x \end{aligned} \tag{1.25}$$

and, thus,

$$\mathsf{U}^x = \mathsf{M}^{xx}\mathsf{F}^x \tag{1.26}$$

where the transverse mobility matrix is

$$\mathsf{M}^{xx} = \begin{bmatrix} M_{11}^{xx} & M_{12}^{xx} \\ M_{21}^{xx} & M_{22}^{xx} \end{bmatrix} \tag{1.27}$$

Comparing Eq.(1.26) and Eq.(1.23), we get $\mathsf{M}^{xx} = (\mathsf{R}^{xx})^{-1}$, and thus

$$M_{11}^{xx} = \frac{R_{11}^{xx}}{(R_{11}^{xx} - R_{12}^{xx})(R_{11}^{xx} + R_{12}^{xx})} \qquad M_{12}^{xx} = \frac{-R_{12}^{xx}}{(R_{11}^{xx} - R_{12}^{xx})(R_{11}^{xx} + R_{12}^{xx})} \tag{1.28}$$

where we have used the symmetric condition of the resistance matrix $R_{12}^{xx} = R_{21}^{xx}$ and we have assumed $R_{11}^{xx} = R_{22}^{xx}$ since we are dealing with two identical particles.

To determine the hydrodynamic couplings, we perform two different simulations. In the first case, the rigid body motion (RBM) is considered and the same velocity V_x^{RBM} is assigned to both rods, see Figure 1.6(b). In order to improve the quality of the numerical solution, we exploit the symmetry of the problem in terms of geometry and boundary conditions with respect to the x, y and x, z plane. Therefore, we only considered the geometry in the semi-spaces: $z > 0$, $y > 0$, see Figure 1.6(b). Once the system of equation is solved, we integrate the stress tensor over both the particle surfaces and we get the average total force F_x^{RBM} exerted by the fluid on the rods when they rigidly move. Hence, according to Eq. (1.23), the fluid resistance to the rigid body motion is equal to the sum of the particle resistance and the coupling term

$$\frac{F_x^{RBM}}{V_x^{RBM}} = \frac{1}{M^{RBM}} = R_{11}^{xx} + R_{12}^{xx} \tag{1.29}$$

where M^{RBM} represents the transverse mobility of the rigid body motion. In the second case, as shown in Figure 1.6(c), we study the relative motion (RM) between the rods, setting two opposite velocities on the cylinder surfaces: $U_1^x = V_x^{RM}$ and $U_2^x = -V_x^{RM}$. We can now exploit an additional degree of symmetry of the system, since the new boundary conditions are symmetric with respect to all the references planes. Therefore we can simulate just one-octave of the whole geometry, see Figure 1.6(c), and, thus, only one rod has to be considered, particularly the rod lying in the semi-space $x > 0$. Integrating the stress on the particle surface, we get the total force F^{RM} that, according to Eq. (1.23), is related to V^{RM} as follows

$$\frac{F_x^{RM}}{V_x^{RM}} = \frac{1}{M^{RM}} = R_{11}^{xx} - R_{12}^{xx} \tag{1.30}$$

d (μm)	Simulated (μm/pN·s)	Theoretical (μm/pN·s)	Rel.Err. (%)
4.82	38.34	34.69	-9.5
7.75	37.58	34.69	-7.8
12.45	38.15	34.69	-9.1
20.00	38.35	34.69	-9.6

Table 1.1: Comparison between simulated and theoretical values of particle mobilities at several interparticle distances. The rod's length is 11μm, while the diameter is 300nm. The fluid viscosity is set to 1×10^{-3} Pa·s.

d (μm)	Simulated (μm/pN·s)	Theoretical (μm/pN·s)	Rel.Err. (%)
4.82	12.4	11.3	-9.6
7.75	8.8	8.3	-6.1
12.45	5.6	5.8	-2.7
20.00	4.1	3.8	-7.1

Table 1.2: Comparison between simulated and theoretical values of hydrodynamic couplings. The rod's length is 11μm, while the diameter is 300nm. The fluid viscosity is set to 1×10^{-3} Pa·s.

and M^{RM} is the mobility of the relative motion. Hence, the fluid contrasts the relative motion proportionally to the difference of the particle resistance and the coupling term. Combining Eq.(1.29), Eq. (1.30) and Eq. (1.28), we can estimate the microrod mobility M_{11}^{xx} and the hydrodynamic coupling M_{12}^{xx} using the following relations

$$M_{11}^{xx} = \frac{M^{RBM} + M^{RM}}{2} \qquad M_{12}^{xx} = \frac{M^{RBM} - M^{RM}}{2} \tag{1.31}$$

Thus, the coupling term (particle mobility) is given by the half difference (sum) between the rigid motion mobility and the relative motion mobility.

As an example, in Table 1.1 and Table 1.2 we respectively report the particle mobilities and the coupling terms for two microrods (11μm in length and 300nm in width) computed at several particle distances d and we compared the results with the theoretical predictions, presented in the previous Section. As expected, the calculus of the single transverse mobilities is not affected by the particles' distance and for both the mobilities and the hydrodynamic couplings the simulations and the theoretical predictions show a very good agreement.

2.4 Experimental results

In this Section we report how we used the holographic optical trapping technique to manipulate and place a couple of micron scale rods in the parallel configuration as described in the previous Section. Studying the free Brownian motion of the rods, when the traps are intermittently turned off, we infer the magnitude of the hydrodynamic interactions. As we investigate the dependence of the hydrodynamic coupling on the particles' distance, we find again the crossover between the 3D and the 2D regimes that has already been pointed out in the theoretical study of the

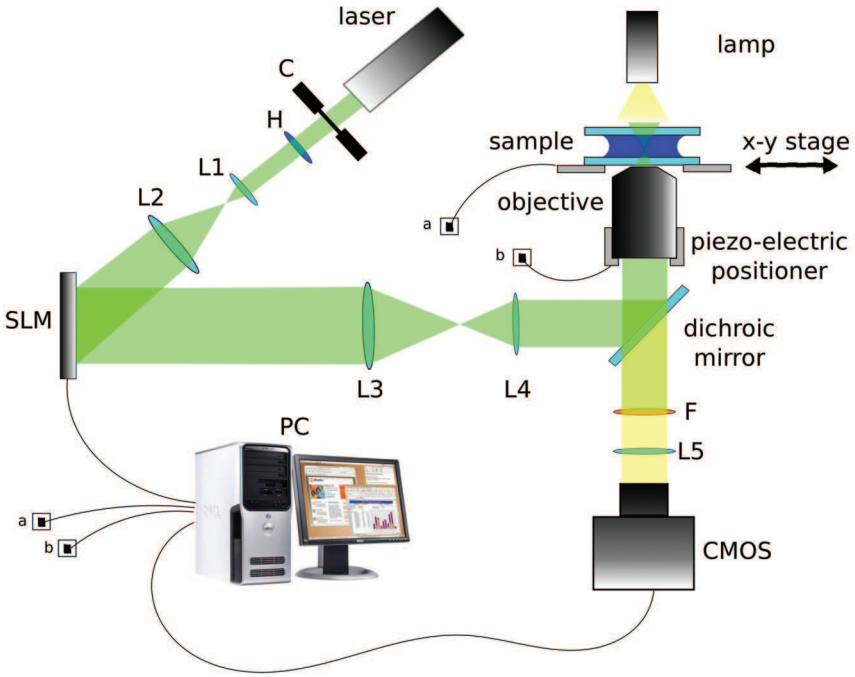

Figure 1.7: Scheme of the blinking holographic trapping system used to determine the hydrodynamic coupling between two aligned microrods. The details are reported in the text.

problem.

The experimental apparatus

We used an experimental apparatus, whose schematic view is shown in Figure 1.7, very similar to that one described in Section 1.3. A Gaussian mode TEM00 cw laser beam (Laser Quantum Opus, 2.5W) with wavelength $\lambda = 532\,\mathrm{nm}$ is expanded through the lenses $L1$ (focal length 20mm) and $L2$ (focal length 220mm) to match the screen of the reflective phase-only spatial light modulator (Holoeye LCR-2500). The screen of the SLM is 19.6 mm in width and 14.6 mm in height and the nematic liquid crystal screen size is 1024×768 pixels. The pixel size is $19\,\mu\mathrm{m}$. Before hitting the SLM screen, the beam passes through the chopper C, in order to generate blinking optical traps. Since the SLM has best performances when the incident light is vertically polarized we introduce the half-wave plate H to set the polarization of the light to the correct direction. The SLM is controlled by the PC as if it were a second monitor. The holograms projected on such a monitor are 8 bit gray level images of 768×768 pixels, since this is the area of the SLM screen actually illuminated by the laser. The holograms are generated by a weighted Gerchberg-Saxton algorithm running on a graphics processing unit (NVIDIA GPU GTX 480). For further details about the algorithm the reader is referred to the work of Di Leonardo et al. (2007a) and Bianchi and Di Leonardo (2010). A second telescope with lenses L3 (focal length 500 mm) and L4 (focal length 200 mm) shrinks the beam waist to match the back aperture of the oil immersion high numerical aperture objective (Nikon Plan

Apo 100x, NA 1.4) mounted on a Nikon TE2000-U inverted microscope. The beam is directed toward the objective through a dichroic mirror which also prevents the portion of beam reflected by the sample to reach the CMOS camera (PROSILICA GCS-1280). The weak portion of the reflected beam that is transmitted by the dichroic mirror is ultimately stopped by the filter F. The positioning of the objective relative to the sample is accomplished by the xy stage (Prior ProScan II) and the piezo-electric positioning system (Mipos 100 PL SG), addressed by the PC. While the piezo-electric controller lets us finely set the position of the focal plane in the sample, the coarse positioning is obtained by manually tightening or loosening the screw of the kinematics where the objective is placed. The sample is illuminated by a 100W halogen lamp whose light is collected by the objective and the tube lens (L5, focal lens 200mm) to be consequently focused on the camera plane.

The silica microrods

The silica microrods were realized by a standard sol-gel chemistry. This method has reportedly demonstrated to be an effective way of producing uniform distribution of silica particles with an accurate control of both shape and size. The details of the process used for fabricating those silica microrods are extensively explained by Carberry et al. (2010) and Akkopru and Durucan (2007). Thus we herein report just a summary of the protocol. 2.08 g tetraethyl orthosilicate was added to a stirred solution of 1.75 g ethanol (38 mmol), 0.36 g H_2O (2 mmol) and 0.3 ml 1 molar HCl (0.3 mmol). Following the procedures reported by Masuda et al. (1998), a mold with a pore diameter of 300 nm and a pore depth of 15μm, made of a self-ordered nanoporous anodic aluminium oxide (AAO), was prepared and immersed in the solution after it had been stirred for 10 min. When the gelation was completed, the AAO, filled with the silica gel, was covered by silicon oil and heated to 60° for 24 h. The template was subsequently removed by chemical etching with a mixture of 1.8 g chromium(VI)oxide, 7.1 g 85% phosphoric acid and 91.1 g deionized water at 50° for 48 h. The final suspension containing the silica microrods was neutralized and cleaned by several successive centrifugation steps. In Figure 1.8(a) is shown one of those rods immersed in distilled water, while in Figure 1.8(b) there is a couple of aligned rods constrained by four traps. The frames were recorded through the microscope system described in the previous Section.

Measurements of hydrodynamic interactions between microrods

The hydrodynamic coupling can be determined from monitoring the Brownian motion of the rods. The chance of observing two rods, occasionally aligned in parallel at some given distance, clearly makes the problem practically impossible to approach experimentally by simple video microscopy observations. However, holographic tweezers provide an ideal tool to directly verify our theoretical and numerical results by trapping and orienting two slender objects in well defined and reproducible relative configurations.

We used holographic tweezers to manipulate the silica microrods described in the previous Section. The rods are dispersed in deionized water and samples are held in a sealed glass chamber at room temperature (22 ± 2°C). Each rod is held in two traps independently and dynamically reconfigurable, as shown in Figure 1.8(b). The two rods can be aligned and moved at different distances. In order to avoid boundary effects we move the rods at the highest distance above the cover slip before

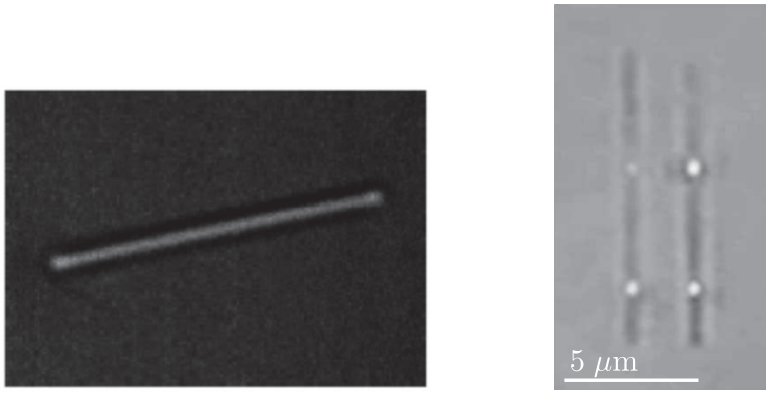

(a) (b)

Figure 1.8: Digital images of silica microrods in a distilled water sample. (a) A single rod. (b) A couple of aligned rods constrained in such a configuration by four holographic traps (the bright spots).

spherical aberrations start to make trapping unstable. This usually corresponds to a height of about 30 μm which is large enough to make the flow produced by image singularities weak compared to direct hydrodynamic couplings. Using a chopper on the trapping beam, we periodically release the rods every 1/15 s and subsequently start recording bright field images at 300 fps for 1/30 s. Five thousand frames were collected for each distance point. Even in the presence of a small local heating due to trapping beams, heat will diffuse away in a few microseconds once trapping light is switched off. Thus, no local viscosity variation due to temperature raising has to be considered when the free Brownian motions of the rods are analyzed.

We limit ourselves to the computed case of center of mass dynamics of parallel aligned rods. The horizontal x coordinate of each rod is obtained by fitting the 1D intensity profile obtained by binning recorded images over the y direction. Alternative approaches like image spatial moments, as reported by Phillips et al. (2011), tend to be very noisy in our case where a short exposure time was needed to guarantee a high enough frame rate. We have experimentally verified that our rods have a rotational diffusion coefficient of about 0.02 rad^2/s. That means that the mean squared angular displacement during acquisition time is about $\pi/100$. It is therefore safe to neglect rotational-translational coupling, see Doi and Edwards (1988) and Han et al. (2006), and project on the x axis the mobility problem with stochastic forces

$$\begin{bmatrix} \dot{x_1}(t) \\ \dot{x_2}(t) \end{bmatrix} = \mathsf{M}^{xx} \cdot \begin{bmatrix} \eta_1(t) \\ \eta_2(t) \end{bmatrix} \tag{1.32}$$

where η_1 and η_2 are stochastic forces with zero average and correlation:

$$\langle \eta_i(0)\eta_j(t)\rangle = 2k_bT(\mathsf{M}^{xx})^{-1}_{ij}\delta(t) \tag{1.33}$$

This is a coupled Langevin equation leading to a displacement covariance matrix, see Aguirre (1972):

$$\langle (x_i(t) - x_i(0))(x_j(t) - x_j(0))\rangle = 2k_bT(\mathsf{M}^{xx})_{ij}t \tag{1.34}$$

Diagonal terms represent the mean squared displacements of the two rods. The corresponding diffusion coefficients provide a direct measurement of single particle mobilities. On the other hand, hydrodynamic couplings are easily extracted from

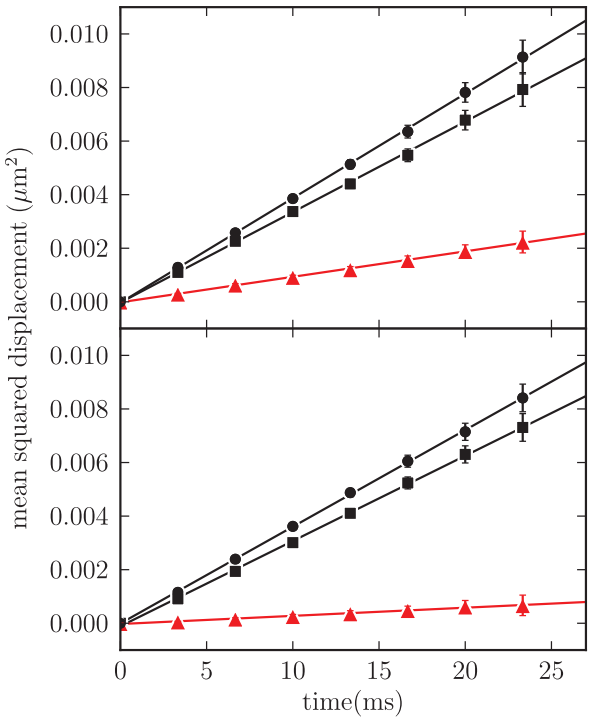

Figure 1.9: Mean squared displacements of freely diffusing rods starting off a parallel aligned configuration. The top and bottom panel refer, respectively, to interparticle distances of 3.5 and 20 μm. Solid circles and squares represent the mean squared displacements of the two single rods, while solid triangles are the mean cross displacements. Linear fits are reported as solid lines.

the diffusion coefficients of the off-diagonal terms. In Figure 1.9 we report the two single particle mean squared displacements together with the crossed term for interparticle distances of 3.5 and 20 microns. Diffusion coefficients can be easily extracted by fitting with a straight line. Single particle diffusion coefficients do not show a systematic dependence on interparticle distance and their deviations are mainly attributable to small differences in rod lengths. Indeed, microrods in our sample have an average length of 10.5 μm with a standard deviation of 8%. Tracking single rod Brownian motion, we extract an average transverse mobility of 42 μm/pN. Such a value can be reproduced by slender body theory, as in Eq.(1.16), using an average rod thickness of about 200 nm, which is well compatible with the nominal pore size (300 nm) used for the rod's growth. Turning now to hydrodynamic couplings, the diffusion coefficient of crossed terms directly provides a measure of M_{12}^{xx} through Eq.(1.34). We found an excellent agreement with theoretical and numerical predictions as shown in Figure 1.10. To give an idea of the sensitivity of theoretical predictions to experimental parameters we report as a gray shaded area the range of theoretical curves corresponding to the given uncertainties in viscosity ($0.95 \pm 0.05 \times 10^{-3}$ Pa·s) and rod lengths ($10.5 \pm 0.8 \mu$m). The rods diameter has a much larger uncertainty; however, coupling values are expected to be much less affected by the actual rod thickness than the single rod mobilities. In particular, the results in Figure 1.10 are expected to remain valid even in the case of a vanishing rods thickness, as could be the case for single walled carbon nanotubes, microtubules, or short straight DNA segments. The same is also true for spheres where, while mobilities diverge with the inverse sphere radius, couplings converge to the finite

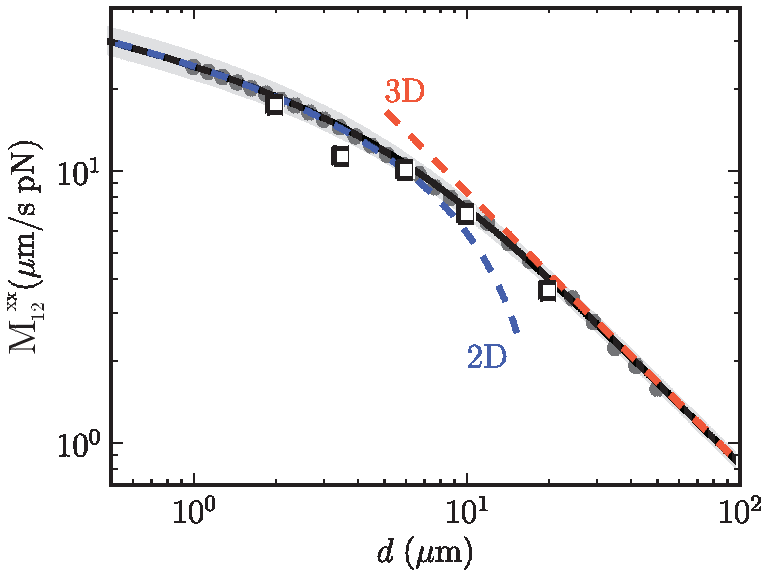

Figure 1.10: Hydrodynamic coupling between rods as a function of their distance. The solid line represents the theory in Eq.(1.18). Solid circles are numerical results from finite element analysis. Experimental data are reported as open squares (error bars are within symbol size). Dashed lines represent the long Eq.(1.19) and short Eq.(1.20) distance limiting behaviors.

large distance limit in Eq. (1.19) at all distances. However, single rod mobilities diverge only logarithmically with radius, see Eq.(1.16) and also Batchelor (1970). As a consequence, when our rods are placed at a distance of 2 μm and forced in the same x direction, they move with a speed that is about 3 times larger than when forced in the opposite direction. That factor would remain as big as about 2 when the radius is shrunk down to 5 nm.

2.5 Conclusions

We have directly measured hydrodynamic interactions between freely diffusing microrods. We demonstrated by direct experimental observation and numerical FEA that two parallel aligned microrods interact like point particles in 3D when they are much farther apart than their length, and like point particles in 2D for short distances. We also derived a simple analytical expression that reproduces very well both experimental and numerical data. Although the validity of our results is expected to hold even for much thinner, and interesting objects, like nanotubes or microtubules, an experimental investigation of hydrodynamic coupling in those systems remains an open and challenging problem. Using digital holographic microscopy (see the next Chapter) may also allow us to extend the above investigations to the full 3D rotational and translational coupled dynamics.

References

Agarwal, R., Ladavac, K., Roichman, Y., Yu, G., Lieber, C., and Grier, D. (2005). Manipulation and assembly of nanowires with holographic optical traps. *Optics Express*, 13(22):8906–8912.

Aguirre, T. (1972). Brownian motion of n interactiong particules. 1. extension of the einstein diffusion relation to the n-particule case. *J. Chem. Phys*, 57:2098.

Akkopru, B. and Durucan, C. (2007). Preparation and microstructure of sol-gel derived silver-doped silica. *Journal of sol-gel science and technology*, 43(2):227–236.

Ashkin, A. (1970). Acceleration and trapping of particles by radiation pressure. *Physical Review Letters*, 24(4):156–159.

Ashkin, A. and Dziedzic, J. (1971). Optical levitation by radiation pressure. *Applied Physics Letters*, 19(8):283–285.

Ashkin, A., Dziedzic, J., Bjorkholm, J., and Chu, S. (1986). Observation of a single-beam gradient force optical trap for dielectric particles. *Optics letters*, 11(5):288–290.

Astumian, R. (1997). Thermodynamics and kinetics of a brownian motor. *Science*, 276(5314):917.

Batchelor, G. (1970). Slender-body theory for particles of arbitrary cross-section in stokes flow. *Journal of Fluid Mechanics*, 44(03):419–440.

Bianchi, S. and Di Leonardo, R. (2010). Real-time optical micro-manipulation using optimized holograms generated on the gpu. *Computer Physics Communications*, 181(8):1444–1448.

Bolognesi, G., Di Leonardo, R., and Bianchi, S. (2011). Digital holographic tracking of microprobes for multipoint viscosity measurements. *Optics Express*, 19(17):–.

Carberry, D., Simpson, S., Grieve, J., Wang, Y., Sch
"afer, H., Steinhart, M., Bowman, R., Gibson, G., Padgett, M., Hanna, S., et al. (2010). Calibration of optically trapped nanotools. *Nanotechnology*, 21:175501.

Čižmár, T. and Dholakia, K. (2011). Shaping the light transmission through a multimode optical fibre: complex transformation analysis and applications in biophotonics. *Optics Express*, 19(20):18871–18884.

Cordero, M., Burnham, D., Baroud, C., and McGloin, D. (2008). Thermocapillary manipulation of droplets using holographic beam shaping: Microfluidic pin ball. *Applied Physics Letters*, 93:034107.

Crocker, J. (1997). Measurement of the hydrodynamic corrections to the brownian motion of two colloidal spheres. *Journal of Chemical Physics*, 106(7):2837–2840.

Cui, X., Lee, L., Heng, X., Zhong, W., Sternberg, P., Psaltis, D., and Yang, C. (2008). Lensless high-resolution on-chip optofluidic microscopes for caenorhabditis elegans and cell imaging. *Proceedings of the National Academy of Sciences*, 105(31):10670.

Curtis, J., Koss, B., and Grier, D. (2002). Dynamic holographic optical tweezers. *Optics Communications*, 207(1-6):169–175.

Di Leonardo, R. and Bianchi, S. (2011a). Hologram transmission through multi-mode optical fibers. *Optics Express*, 19(1):247–254.

Di Leonardo, R. and Bianchi, S. (2011b). A multi-mode fiber probe for holographic micromanipulation and microscopy.

Di Leonardo, R., Cammarota, E., Bolognesi, G., Schäfer, H., and Steinhart, M. (2011). Three-dimensional to two-dimensional crossover in the hydrodynamic interactions between micron-scale rods. *Physical Review Letters*, 107(4):044501.

Di Leonardo, R., Ianni, F., and Ruocco, G. (2007a). Computer generation of optimal holograms for optical trap arrays. *Optics express*, 15(4):1913–1922.

Di Leonardo, R., Ianni, F., and Ruocco, G. (2009). Colloidal attraction induced by a temperature gradient. *Langmuir*, 25(8):4247–4250.

Di Leonardo, R., Keen, S., Ianni, F., Leach, J., Padgett, M., and Ruocco, G. (2008). Hydrodynamic interactions in two dimensions. *Physical Review E*, 78(3):031406.

Di Leonardo, R., Keen, S., Leach, J., Saunter, C., Love, G., Ruocco, G., and Padgett, M. (2007b). Eigenmodes of a hydrodynamically coupled micron-size multiple-particle ring. *Physical Review E*, 76(6):061402.

Di Leonardo, R., Leach, J., Mushfique, H., Cooper, J., Ruocco, G., and Padgett, M. (2006). Multipoint holographic optical velocimetry in microfluidic systems. *Physical review letters*, 96(13):134502.

Doi, M. and Edwards, S. (1988). *The theory of polymer dynamics*, volume 73. Oxford University Press, USA.

Dufresne, E. and Grier, D. (1998). Optical tweezer arrays and optical substrates created with diffractive optics. *Review of Scientific Instruments*, 69:1974.

Eriksen, R., Daria, V., and Gluckstad, J. (2002). Fully dynamic multiple-beam optical tweezers. *Optics Express*, 10(14):597–602.

Fällman, E. and Axner, O. (1997). Design for fully steerable dual-trap optical tweezers. *Applied optics*, 36(10):2107–2113.

Faucheux, L., Bourdieu, L., Kaplan, P., and Libchaber, A. (1995). Optical thermal ratchet. *Physical review letters*, 74(9):1504–1507.

Fournier, J., Burns, M., and Golovchenko, J. (1995). Writing diffractive structures by optical trapping. In *Proceedings of SPIE*, volume 2406, page 101.

Friese, M., Enger, J., Rubinsztein-Dunlop, H., and Heckenberg, N. (1996). Optical angular-momentum transfer to trapped absorbing particles. *Physical Review A*, 54(2):1593.

Friese, M., Rubinsztein-Dunlop, H., Gold, J., Hagberg, P., and Hanstorp, D. (2001). Optically driven micromachine elements. *Applied Physics Letters*, 78:547.

Gerchberg, R. and Saxton, W. (1972). Optik (stuttgart) 35. *View Record in Scopus— Cited By in Scopus (1114)*, page 237.

Guck, J., Ananthakrishnan, R., Mahmood, H., Moon, T., Cunningham, C., and Käs, J. (2001). The optical stretcher: a novel laser tool to micromanipulate cells. *Biophysical Journal*, 81(2):767–784.

Han, Y., Alsayed, A., Nobili, M., Zhang, J., Lubensky, T., and Yodh, A. (2006). Brownian motion of an ellipsoid. *Science*, 314(5799):626.

Han, Y. and Grier, D. (2003). Confinement-induced colloidal attractions in equilibrium. *Physical review letters*, 91(3):38302.

Happel, J. and Brenner, H. (1991). *Low Reynolds number hydrodynamics: with special applications to particulate media*, volume 1. Kluwer Academic Print on Demand.

Higurashi, E., Ukita, H., Tanaka, H., and Ohguchi, O. (1994). Optically induced rotation of anisotropic micro-objects fabricated by surface micromachining. *Applied physics letters*, 64(17):2209–2210.

Keen, S., Yao, A., Leach, J., Di Leonardo, R., Saunter, C., Love, G., Cooper, J., and Padgett, M. (2009). Multipoint viscosity measurements in microfluidic channels using optical tweezers. *Lab Chip*, 9(14):2059–2062.

Kim, S. and Karrila, S. (1991). *Microhydrodynamics: principles and selected applications*. Butterworth-Heinemann Boston.

Leach, J., Mushfique, H., di Leonardo, R., Padgett, M., and Cooper, J. (2006). An optically driven pump for microfluidics. *Lab Chip*, 6(6):735–739.

Lighthill, M. (1975). Mathematical biofluidynamics. siam.

Love, G. (1997). Wave-front correction and production of zernike modes with a liquid-crystal spatial light modulator. *Applied optics*, 36(7):1517–1520.

Maragó, O., Bonaccorso, F., Saija, R., Privitera, G., Gucciardi, P., Iati, M., Calogero, G., Jones, P., Borghese, F., Denti, P., et al. (2010). Brownian motion of graphene. *ACS nano*.

Maragó, O., Jones, P., Bonaccorso, F., Scardaci, V., Gucciardi, P., Rozhin, A., and Ferrari, A. (2008). Femtonewton force sensing with optically trapped nanotubes. *Nano letters*, 8(10):3211–3216.

Masuda, H., Yada, K., and Osaka, A. (1998). Self-ordering of cell configuration of anodic porous alumina with large-size pores in phosphoric acid solution. *Japanese journal of applied physics*, 37:L1340–L1342.

Meiners, J. and Quake, S. (1999). Direct measurement of hydrodynamic cross correlations between two particles in an external potential. *Physical review letters*, 82(10):2211–2214.

Merrill, J., Sainis, S., and Dufresne, E. (2009). Many-body electrostatic forces between colloidal particles at vanishing ionic strength. *Physical review letters*, 103(13):138301.

Misawa, H., Sasaki, K., Koshioka, M., Kitamura, N., and Masuhara, H. (1992). Multibeam laser manipulation and fixation of microparticles. *Applied physics letters*, 60(3):310–312.

Padgett, M. and Di Leonardo, R. (2011). Holographic optical tweezers and their relevance to lab on chip devices. *Lab Chip*.

Pesce, G., Sasso, A., and Fusco, S. (2005). Viscosity measurements on micron-size scale using optical tweezers. *Review of scientific instruments*, 76:115105.

Phillips, D., Carberry, D., Simpson, S., Sch
"afer, H., Steinhart, M., Bowman, R., Gibson, G., Padgett, M., Hanna, S., and Miles, M. (2011). Optimizing the optical trapping stiffness of holographically trapped microrods using high-speed video tracking. *Journal of Optics*, 13:044023.

Plewa, J., Tanner, E., Mueth, D., and Grier, D. (2004). Processing carbon nanotubes with holographic optical tweezers. *Optics Express*, 12(9):1978–1981.

Polin, M., Tuval, I., Drescher, K., Gollub, J., and Goldstein, R. (2009). Chlamydomonas swims with two gears in a eukaryotic version of run-and-tumble locomotion. *Science*, 325(5939):487.

Reichert, M. and Stark, H. (2005). Synchronization of rotating helices by hydrodynamic interactions. *The European Physical Journal E: Soft Matter and Biological Physics*, 17(4):493–500.

Reicherter, M., Zwick, S., Haist, T., Kohler, C., Tiziani, H., and Osten, W. (2006). Fast digital hologram generation and adaptive force measurement in liquid-crystal-display-based holographic tweezers. *Applied optics*, 45(5):888–896.

Rohrbach, A., Tischer, C., Neumayer, D., Florin, E., and Stelzer, E. (2004). Trapping and tracking a local probe with a photonic force microscope. *Review of scientific instruments*, 75:2197.

Sainis, S., Germain, V., Mejean, C., and Dufresne, E. (2008). Electrostatic interactions of colloidal particles in nonpolar solvents: Role of surface chemistry and charge control agents. *Langmuir*, 24(4):1160–1164.

Schonbrun, E., Piestun, R., Jordan, P., Cooper, J., Wulff, K., Courtial, J., and Padgett, M. (2005). 3d interferometric optical tweezers using a single spatial light modulator. *Optics Express*, 13(10):3777–3786.

Simpson, S. and Hanna, S. (2010). Holographic optical trapping of microrods and nanowires. *JOSA A*, 27(6):1255–1264.

Tan, S., Lopez, H., Cai, C., and Zhang, Y. (2004). Optical trapping of single-walled carbon nanotubes. *Nano Letters*, 4(8):1415–1419.

Thalhammer, G., Steiger, R., Bernet, S., and Ritsch-Marte, M. (2011). Optical macro-tweezers: trapping of highly motile micro-organisms. *Journal of Optics*, 13:044024.

Visscher, K., Brakenhoff, G., and Krol, J. (1993). Micromanipulation by multiple optical traps created by a single fast scanning trap integrated with the bilateral confocal scanning laser microscope. *Cytometry*, 14(2):105–114.

Vossen, D., van der Horst, A., Dogterom, M., and van Blaaderen, A. (2004). Optical tweezers and confocal microscopy for simultaneous three-dimensional manipulation and imaging in concentrated colloidal dispersions. *Review of scientific instruments*, 75:2960.

Weinert, F. and Braun, D. (2008). Observation of slip flow in thermophoresis. *Physical review letters*, 101(16):168301.

Wulff, K., Cole, D., Clark, R., DiLeonardo, R., Leach, J., Cooper, J., Gibson, G., and Padgett, M. (2006). Aberration correction in holographic optical tweezers. *Opt. Express*, 14(9):4170–4175.

Yao, A., Tassieri, M., Padgett, M., and Cooper, J. (2009). Microrheology with optical tweezers. *Lab on a Chip*, 9(17):2568–2575.

Zwick, S., Haist, T., Miyamoto, Y., He, L., Warber, M., Hermerschmidt, A., and Osten, W. (2009). Holographic twin traps. *Journal of Optics A: Pure and Applied Optics*, 11:034011.

Chapter 2

Holographic microscopy

Due to the coherent nature of the laser light, the scattered beam from an object contains the information about the three-dimensional light distribution in the working volume. As this scattered light interferes with a reference beam, a two-dimensional fringe pattern, called the *hologram*, is generated. By appropriately handling the recorded hologram, we can optically or digitally reconstruct the whole three-dimensional virtual image of the examined object. Generating magnified holograms of micrometric scale objects by means of a microscope objective and recording them on a digital device is the basic working principle of the digital holographic microscopy. Once the holograms are stored on a computer, they are numerically processed to reconstruct a three-dimensional view of light field in the sample volume. The simplest image processing is to back-propagate the light waves by means of the impulse response function of the Helmholtz equation, ruling the light propagation within the approximation of the scalar diffraction theory. Particularly, this propagation function assumes a very simple expression when the light field is reconstructed on a plane parallel to the initial one. However, the method can also be extended to the case of an arbitrarily tilted reconstruction plane.

In the first part of this Chapter, we introduce the basic concepts of analog and digital holography (Section 1.1) together with a description of the digital holographic microscopy in the so-called Gabor configuration (Section 1.2). Next, we report the most important and recent applications of digital holographic microscopy in microfluidics (Section 1.3). In the second part, we propose a fast implementation of the real-time back-propagation between parallel planes by exploiting the parallel architecture of the modern graphics processing units (Section 2.1). Then, we extend the algorithm to the propagation between arbitrarily oriented planes (Section 3.2), and we demonstrate the high speed capabilities of this method by tracking the motion of two holographically trapped beads at the same time from three perpendicular viewing directions (Section 3.3). The potentialities for microfluidics of this real-time reconstruction scheme are also shown by using the digital holographic microscopy as a flow visualization technique. Particularly, we present the real-time monitoring of a fluid flow, seeded with polystyrene micro-beads, over the three cross sections of a microfluidic channel (Section 3.4).

1 Digital holographic microscopy

1.1 Analog and digital holography

The depth perception is an essential visual ability for the living beings who move and interact with each other and with the external objects in a three-dimensional world. Two eyes, mildly displaced with respect to each other, give us two slightly different perspectives that, once combined together, provide a three-dimensional visualization. Nevertheless, when we take a picture or we record a video, this 3D effect disappears and the world is flattened on a two-dimensional medium (that could be the photo-printing paper or the computer/TV monitor). Clearly, in the recording process a part of the information has been lost and the recorded "reality" is somehow altered, since it looks like to be two-dimensional.

As in the macroscopic world, in the microscopic one we experience the same drawbacks when we record a scene through a camera and a bright-field microscope. For instance, in the previous Chapter, we have shown how holographic optical tweezers (HOTs) allows the three-dimensional micromanipulation of several objects throughout the sample volume. Such manipulation can also be performed in real-time when the computer hologram generation relies on the computational power of the moder graphic processing units (GPUs). Unfortunately, the standard bright-field microscopy gives us only a two-dimensional perspective and the information about what is out of focus is unavoidably lost, unless the focal plane scans the entire sample volume. This limits the advantages offered by HOTs since we can manipulate several trapped objects in any 3D configurations but we cannot simultaneously visualize all of them. In order to exploit the whole potentiality of such a technique, we would like to visualize and track even those objects that are manipulated outside the depth of field of the microscope system.

The research of a viable and effective method for 3D visualization and tracking of micron-scale objects is still a stimulating open issue, as shown by the several new approaches proposed in the last few years, see Lee and Grier (2007), Lee et al. (2007), Bowman et al. (2010) and Fung et al. (2011). Even though there are already well-established techniques as the back focal plane interferometry, see Ghislain and Webb (1993) and Allersma et al. (1998), or the fluorescence microscopy, see Florin et al. (1996) and Sasaki et al. (1997), enabling a nanometric three-dimensional tracking of micrometric objects, for such methods the axial tracking and visualization range is limited to the depth of field of the imaging system. Furthermore, relying on principles of stereomicroscopy, a novel interesting approach for 3D visualization of multiple holographically trapped objects has been recently introduced by Bowman et al. (2010). Despite the excellent performances in terms of bandwidth and tracking accuracy, the axial tracking range is still limited to the order of ten microns.

In such a context, holography has demonstrated to be a reliable way for recording and reconstructing three-dimensional scenes of both macroscopic and microscopic environments. When objects are illuminated by a laser source and the scattered light (*object beam*) interferes with an undisturbed *reference beam*, the resulting image is an interference pattern, named the *hologram*. Since the interference fringes and speckles on the hologram plane depend on the three-dimensional distribution of the light field and, thus, on the position, orientation and shape of the scattering objects in the illuminated volume, the hologram inherently contains the 3D information that was lost in the standard bright-field microscopy. Thus, we use the world *holography*, that, derived from Greek, means *whole script*, as the information of the wavefield on the

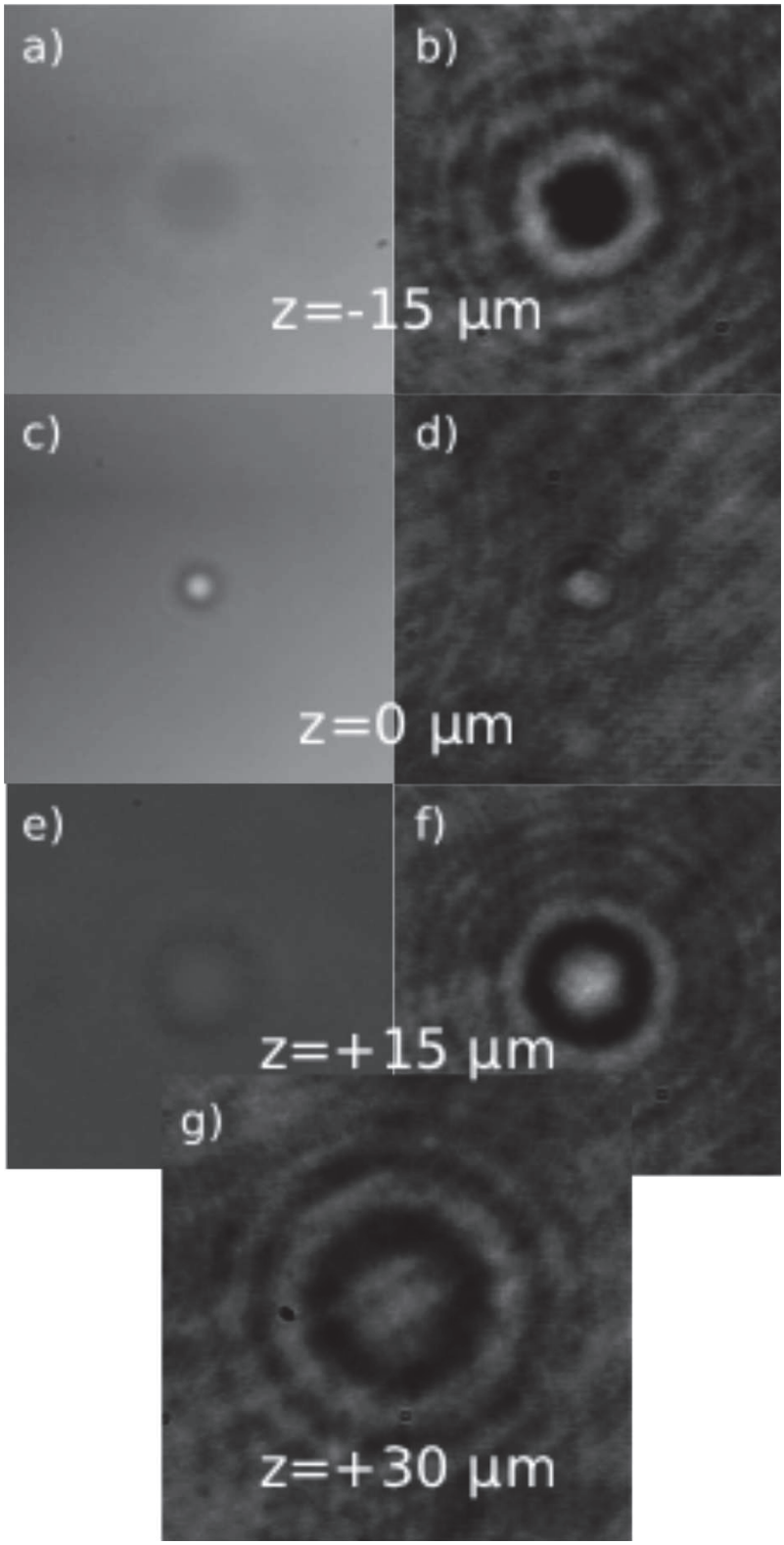

Figure 2.1: Visualization of a 2.07 μm diameter silica bead immersed in DI water in both bright-field and holographic microscopy. We assume that the origin $z = 0$ of the optical axis is at the plane in which the particle is in focus. Bright-field images and holograms are recorded at several focal planes: $z = 15\,\mu$m (a and b), $z = 0\,\mu$m (c and d), $z = 15\,\mu$m (e and f), $z = 30\,\mu$m (g). The last holograms demonstrates the long axial tracking range of holographic microscopy.

entire sample volume is *written* on a two-dimensional image. A direct comparison between standard bright-field microscopy and holographic microscopy is shown in Figure 2.1 where the bright-field images and holograms of a silica bead immersed in DI water are reported for several focal plane positions.

Holography was invented in 1948 by Dennis Gabor while he was attempting to improve the resolution of the electron microscope. He realized that the diffraction pattern of the electron beam contained the whole information of the electron wave, as its amplitude and phase. He applied this imaging principle to the visible light and because of holography in 1971 he was awarded the Nobel Prize in Physics. However, in order to be fully developed and applied this technique had to wait for the invention and realization in the 1960s of a powerful coherent source of light, namely the laser, so that an high quality interference contrast could be achieved.

A standard analog holographic set-up basically consists of a recording medium (e.g a photographic plate) and coherent laser source that is split into two directions by means of a beam splitter. One part of the beam is directed toward the object where it is consequently scattered and reflected to the recording device. The second wave acts a reference beam, directly illuminating the recording target. The interference pattern is then fixed on the medium by chemical development. To reproduce the image of the objects that have generated the hologram, the developed medium is illuminated by a reference wave (equal to the previous reference beam but propagating in the opposite direction), thereby the original object wave is reconstructed and an observer can see its virtual image, exhibiting all effects of perspectives. In Gabor setup, the propagation directions of both the reference beam and the object beam are parallel to the optical axis and perpendicular to the photographic plate. In such a configuration, named *in-line holography*, in the reconstruction step the undiffracted reconstruction wave (zeroth order), the virtual image and the twin image overlap along the optical axis. In order to spatially separate each one of those reconstructed waves, Leith and Upatnieks (1962) and Leith and Upatnieks (1964) used an off-axis reference wave so that they eliminated the problem of the zero-order and twin images.

Despite the further improvements the analog holography underwent in the following decades, such an implementation obviously precludes any possibility to perform real-time operations. Substituting the recording medium with a digital device made a breakthrough in the development of this technique. In the so-called *digital holography* we can get rid of the development step and, thus, of all the facilities required for that process, simply replacing them with a computer and a digital camera. The recording process can be performed at video rates, i.e. orders of magnitude faster than in the analog holography. In addition, since the diffraction theory accurately describes the propagation of light in an homogeneous medium, the reconstruction of light volume distribution can be totally performed via numerical processing, speeding up this step as well. Moreover, any operation to improve the quality of the reconstructed hologram (e.g. suppression of the twin images, optical phase unwrapping, aberration compensation) can also be performed by computer, avoiding doing it physically through additional and cumbersome optics. The first usage of computer in holography was to generate artificial holograms by numerical methods in order to print them on a photograph plate and to optically reconstruct the light volume distribution. This technique is referred to as computer generated holography, see Lee (1978) and Bryngdahl and Wyrowski (1990). Kronrod et al. (1972a) and Kronrod et al. (1972b) performed the first numerical hologram reconstruction starting

off sampled images of in-line and Fourier holograms recorded on a photographic medium. The full digital recording and processing of holograms were however realized much later by Schnars and Jüptner (1994). In the following years, the same authors applied digital holography in several optical techniques as interferometry, see Schnars (1994), shearopgraphy and speckle photography, see Schnars and Jüptner (1994a). Indeed, one of the most important achievements due to the digital holography with respect to the analog one is that we can implement all those different techniques simply modifying the way the holograms are numerically processed without any additional changes in the recording process and optical set-up. For a complete review of the principles and techniques of digital holographic microscopy we refer the interested reader to the work of Kim (2010).

1.2 Digital Gabor holographic microscopy

Digital holography has been extensively used as a microscopy technique by using an objective lens to form on the hologram plane (i.e. camera plane) a magnified image of the object. In that technique, called digital holographic microscopy (DHM), once the hologram is stored in the computer, by appropriately setting the pixel size and the wavelength in the reconstruction algorithm, the magnified image of the object can be reconstructed. Such a configuration, where the object or its magnified image is close to the hologram plane, is called *image plane holography*. This is very useful especially in the case of low coherent laser source, as the distance between the object and the focal plane is small compared to the coherent length of the laser. This technique is particularly preferred for microscopy applications since a low coherence source allows the reduction of spurious interference noise due to scattering objects in the optical system that are not within the coherence length, see Dubois et al. (1999), thereby resulting in hologram with higher contrasted speckles and lower background noise.

Even though off-axis holography can separate the zeroth order from the holographic representation of the objects, it results in low resolution images and, thus, for microscopy applications the in-line configuration is often chosen. In this respect, several methods have been introduced to reduce the zeroth order and twin effects in the reconstructed image. For example, a high-pass filter in the Fourier domain with the cut-frequency close to zero has been proved to highly attenuate the effect of the DC component (zeroth order). In order to completely remove the twin image artifacts, the phase-shifting multi-exposure method has been proposed by Pedrini et al. (1998) and improved by Monaghan et al. (2009). In that case, multiple holograms of the same object are recorded controlling the phase of the reference beam and varying it in the range of $[0, 2\pi]$, so that both amplitude and phase of the recorded hologram can be determined. Indeed, when even the phase of the hologram is known, in the reconstruction process there are no ambiguities and only the object beam is reproduced.

Nevertheless, phase-shifting multi-exposure method requires additional optics to accurately control the phase of the reference beam and it is quite difficult to use it when we handle systems with fast dynamics as, for instance, a biological sample. When digital holographic microscopy is adopted as a 3D visualization and tracking system in the research fields of microfluidics, biology and colloid science, the in-line holography is often used and implemented in a very simple way, that is eliminating the reference beam. In fact, even if the incoming light is not split into two separate beams, it can still act as both the reference wave and the object

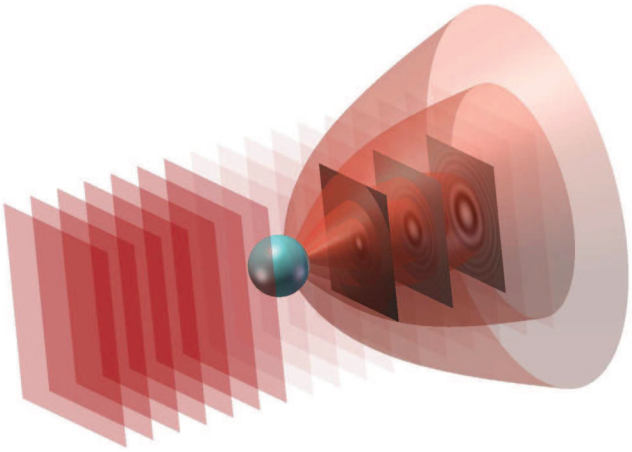

Figure 2.2: Schematic representation of the hologram generation of a spherical particle in Gabor holography configuration. Only a part of the incoming plane wave is scattered by the bead (conical wavefronts), while the rest of the light passes undisturbed. The interference between the two of them generates the hologram, made of a pattern of concentric dark and bright fringes. The longer is the distance between the hologram plane and the object and the larger are the radii of the concentric interference rings.

wave. The resulting hologram is generated by the interference of the part of light that is scattered by the objects with the part of light that passes through the sample without being modified. That was exactly the configuration adopted by Gabor in its first experiments on holography, and for that reasons it's called *Gabor holography*. In Figure 2.2 we report a scheme of the hologram generation in Gabor configuration for a spherical particle illuminated by a monochromatic plane wave.

Clearly, this method is effective as long as the objects in the volume sample do not excessively perturb the illuminating beam. That is what happens if the refractive indices of the objects are close to the refractive index of the surrounding medium or the object density in the illuminated volume is low. For such reasons, digital Gabor holography has been extensively applied in particle image analysis, see Sheng et al. (2006), Lebrun et al. (2003), Murata and Yasuda (2000) and Meng et al. (2004). In addition, as the holograms are produced by microscopic particles, that weakly scatters the incoming light, the problems of twin images and zeroth order effect are less important since even those artifacts are weaker than what it would have been if an independent reference wave had been used. The Gabor holography is the ideal solution also in the case of holographic optical trapping, see Lee and Grier (2007), as the trapped objects have refractive indices slightly higher than the surrounding medium and so the incoming beam is only mildly perturbed by the trapped particles. In fact, with a relative refractive index less than unity the gradient force reverses its direction and it pushes the particle away from the beam focus. Conversely, for high refractive index particles, the scattering force is too strong and the stabilizing gradient force cannot balance it. Furthermore, the particle density in the sample is usually limited in order to avoid distortion of the trapping laser. Finally, setting up a digital holographic microscope for Gabor holography on an existing HOTs setup requires only minor changes to the original configuration. In the next Section, we describe our custom digital holographic microscope equipped with a holographic

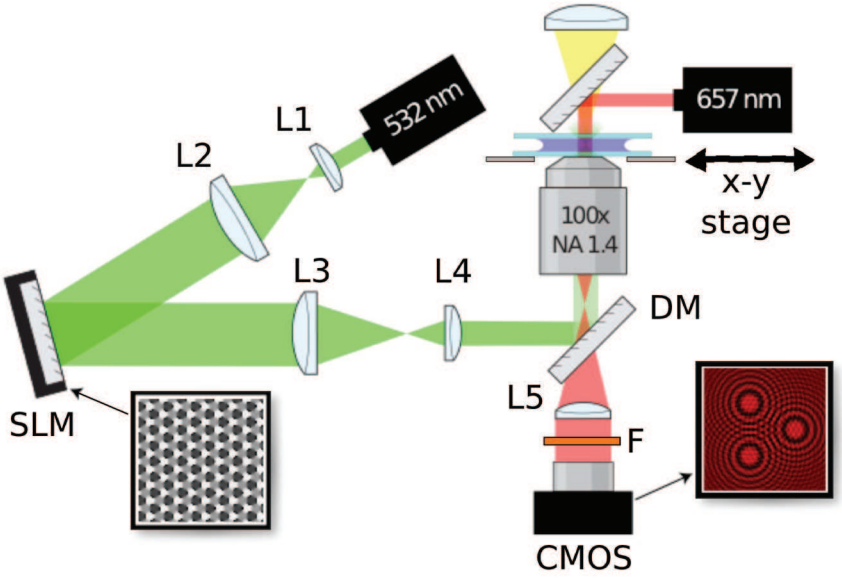

Figure 2.3: Schematic view of our digital holographic microscope/tweezers system. Sample illumination can be switched between white light and a collimated diode laser ($\lambda = 657\,\text{nm}$).

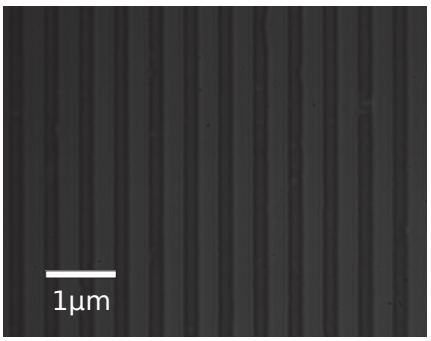

Figure 2.4: Bright-field image of a resolution test target made of 2000 lines per millimetres.

trapping system.

The experimental apparatus

We completely designed and realized a custom microscope system, whose a schematic drawing is shown in Figure 2.3. A 100x numerical aperture 1.4 oil immersion objective (Nikon Plan Apo), placed on a linear translation stage for manual focusing, collects either the collimated light of a diode laser ($\lambda = 0.657\ \mu\text{m}$) or the light coming out a tungsten-halogen fiber lamp (Thorlabs OLS1-EC). In the bright-field configuration, since the incoherent light coming out the fiber is spatially inhomogeneous, to evenly illuminate the sample we adopt the Köhler illumination by means of a set of additional lenses and diaphragms that are removed when the microscope works in the holography mode. The objective is coupled with a tube lens (L5, focal lens 200mm) to image the focal plane on the CMOS camera (PROSILICA GC-1280) plane. The CMOS sensor is an array of 1280×1024 pixels, whose size is $6.75\ \mu\text{m} \times 6.75\ \mu\text{m}$. A filter F placed in front of the camera prevents the trapping laser to achieve the camera plane, so that the hologram is generated by the collimated illuminating laser only. The specimen's positioning is controlled by a mo-

torized microscope stage (Märzhäuser SCAN IM). The magnification of the whole optical train has been determined using a resolution test target made of 2000 lines per millimetres. By focusing that target in the bright-field mode (Figure 2.4) we count the number of pixels per line and we get the magnification factor, that for our system is a 67.51 nm per pixel. That factor is perfectly in agreement with the magnification of the objective and the camera pixel size.

The holographic optical trapping system is very similar to that one introduced in Section 2.4 of Chapter 1. A reflective phase-only spatial light modulator (Holoeye LCR-2500) is used in the Fourier geometry. The Gaussian mode TEM00 of a cw DPSS laser (Coherent Verdi 3W, $\lambda = 532\,\text{nm}$) is expanded by lenses $L1$ (focal length 35 mm) and $L2$ (focal length 200 mm) to match the SLM screen. Subsequently, the laser beam is shrunk by a second telescope made of lens L3 (focal length 400 mm) and $L4$ (focal length 200 mm). Finally, the trapping laser is directed toward the objective through a dichroic mirror (DM). This experimental apparatus has been used to perform the experiments presented in both this Chapter and the following one.

1.3 DHM: microfluidic applications and perspectives

Digital holographic microscopy has been extensively applied for three-dimensional tracking of micrometric particles immersed in fluid samples. Measuring the position and the motion of those particles has been used in colloid science to measure and characterize the dynamics of colloidal systems. For instance, the nature (e.g. electrostatic, interfacial, hydrodynamic, etc.) and the intensity of the forces acting on the interacting particles can be determined by tracking the particle motion. On the other hand, when the net force on the micron-scale particles is negligible, they can be considered as passive tracers, and their motion provide information about the three-dimensional structure of the surrounding fluid flow.

In both cases, one limitation of such a 3D tracking is that the accuracy of the measured particle position is not the same in all directions. Particularly, the tracking along the optical axis is always less accurate than the tracking along the perpendicular directions. In fact, by considering the diffraction pattern of a point source, it can be demonstrated that the resolution is equal to $1.22\,\lambda\,(2d/a)$, where λ is the laser wavelength, d is the distance between the in-focus plane of the object and the hologram plane and a is the object size. The corresponding depth-of-focus, i.e. the axial depth over which the image remains nearly in focus, is proportional to d^2/λ. For the case of 2 μm diameter particles illuminated by a red laser ($\lambda \sim 600\,\text{nm}$), this results in a depth-of-focus of about ten microns. In order to improve the axial detection, different configurations have been proposed as recording multiple viewing, see Gopalan et al. (2008), Lu et al. (2008), Malkiel et al. (2003) and Soria and Atkinson (2008), or minimizing the root mean square value of the imaginary part of the reconstructed hologram, see Pan and Meng (2003). Another widespread solution is to detect the point of minimum intensity (or maximum intensity if the DC component of the recorded hologram has been suppressed) along the axis of the reconstructed particle trace, as shown by Kim and Lee (2007), Satake et al. (2005), Sheng et al. (2006), Sheng et al. (2007), Sheng et al. (2008) and Sheng et al. (2009). In our experiment, we adopted this latter approach and in Section 2.2 we discuss the precision and the accuracy of such a method applied to the tracking of micron-sized spherical beads. For an extensive review on the several solutions proposed to cope with the problem of the depth-of-field as well as a detailed overview of the

applications of DHM in fluid dynamics we refer to Katz and Sheng (2010).

To measure the displacement of particles from the reconstructed hologram, both the correlation based analysis and the individual particle tracking have been reported. As shown in the following Sections, we relied on the first approach for the visualization of the flow profile in a rectangular cross section microchannel (see Section 3.3), while we used the second one to probe the local viscosity of a confined fluid (see Chapter 3). In literature, several methods have been used to determine the particle velocities and trajectories. A tracking algorithm based on the concept of match probability between two consequent holograms has been proposed by Baek and Lee (1996) and used by Kim and Lee (2007) to calculate the flow field in a microtube. Sheng et al. (2008) have proposed a more complicated two-step scheme. First the planar velocity projections are obtained by a standard two-dimensional particle image velocimetry. Secondly, in order to obtain the 3D velocity vector, they used several criteria to determine which, among the particle traces located within a spherical volume around the first exposure of each particle, was the most likely second exposure. Those criteria were the deviation from first step analysis predictions, the similarities in particle size, volume and intensity distribution and many others. Gopalan et al. (2008) relied on several Lagrangian criteria to track crude-oil droplets and neutrally buoyant particles. For more details about these methods we directly refer the readers to the cited references.

By back-propagating recorded in-line holograms, Van Oostrum (2011) analyzed the phase behavior of dilute colloidal dispersions. Measuring the radial distribution function of silica coated porous Titania particles dispersed in a solution of Cyclo-Hexyl Chloride, he observed ordering and formation of long-ranged crystal even at very low volume fraction, due to the small amount of ions in that solution and the resulting high Debye screening length. Similarly, he studied the sedimentation profiles of Titania/silica particles and he compared the experimental results to the theoretical predictions of the Boltzmann distribution, that describes the balance between the gravity force and the Brownian diffusion. Furthermore, he applied the back-propagating algorithm to detect the positions and the orientations of silica micro rods in ethanol solution. This technique would allow us to extend the measurement of the hydrodynamic interactions, presented in the previous Chapter, to all the translational and rotational coupling terms. Tracking the motion of spherical beads by a DHM-HOTs system, Roichman et al. (2008) highlighted the effects of the nonconservative component of the optical forces on the dynamics of the trapped objects. In that case, the particle detection was performed by fitting the experimental hologram to the prediction of Lorenz-Mie scattering theory (see Chapter 3).

DHM has also proved as a reliable method to study the dynamics of biological systems as for instance the characterization of the swimming motion of living cells and the related flow fields. By attaching a mirror to one sample wall, it's possible to simultaneously record two perpendicular views using an in-line holographic set-up. Such a configuration has been adopted by Malkiel et al. (2003) to study the behaviour as well as the generated 3D flows of a swimming copepod. The flow field was determined by tracking the motion of polystyrene particles surrounding the copepod. That study showed as this animal was able to generate a downward feeding current through a sinking motion of its body, periodically interrupted by short hops upward. From the 3D velocity distribution, the copepod relative weight and its thrust were also measured. Sheng et al. (2007) performed a very interesting study on the predation strategies of some marine dinoflagellates. Mixing those animals with

the organisms they prey on, they found out that the predators cluster around their prey and, depending on the distance from the prey, they accordingly modify their swimming motion. It is worth noting that by reconstructing the light distribution in the sample volume they were able to visualize the location and the shape of the longitudinal flagellum of the dinoflagellates, albeit this 200 nm diameter flagellum is smaller that the resolution limit of the microscope objective.

Right from the beginning of DHM, several methods have been proposed in order to improve both the recording and reconstruction step. This improvement process has never been interrupted, and, particularly, in the last few years a lot of new approaches for hologram-analysis procedures have been introduced. Therefore, it is likely that in the following years the research on DHM will still be focused on that issue. With regards to tracking motion and trajectories, 3D correlation-based analysis of in-line holograms were recently performed using the complex amplitude field by Ooms et al. (2008), as opposed to the intensity distribution. Therein strategies to suppress directional ambiguity and bias error are also investigated. A very important contribution in developing new strategies of computer hologram processing for particle detection, tracking and characterization has come from Grier and coworkers. Lee and Grier (2007) analyzed the holograms of spherical dielectric beads fitting them to the theoretical hologram predicted by the Lorenz-Mie scattering theory (see Chapter 3). A nanometric three-dimensional position of beads was achieved together with a high accurate detection of the bead size and relative refractive index. Later on, through the same technique Cheong et al. (2009a) implemented a label-free holographic flow cytometry system, enabling the detection of molecular scale coatings on the beads' surfaces. Moreover, Dixon et al. (2011b) extended the method to also measure the 2D particle velocity, accounting for the blurring that occurs as the spherical particle moves during the camera's exposure time. In the so-called holographic particle streak velocimetry, the 2D velocity is inferred through the angular variance of the hologram radial intensity. Very recently, the same authors have also introduced a novel implementation of the back-propagation algorithm, claiming nanometric 3D tracking resolution together with the suppression of the twin image, see Dixon et al. (2011a). That result is achieved by deconvolving the volumetric reconstruction with an optimal kernel derived from the Rayleigh-Sommerfeld propagator.

2 Digital reconstruction between parallel planes

2.1 The algorithm

In the context of the scalar diffraction theory, see Saleh et al. (1991), a monochromatic light wave can de described as a complex scalar field. As we explained in the previous Section, the hologram generation is due to the interference of the object beam e_s and the reference beam e_0, so that the resulting intensity pattern is

$$I = |e_0 + e_s|^2 = |e_0|^2 + 2\mathcal{R}\{e_0 e_s^*\} + |e_s|^2 \tag{2.1}$$

where $\mathcal{R}\{\cdot\}$ stands for the real part of a complex number. In the case of the optical reconstruction, the same reference wave $e_0 = A_{e_0}\exp(i\varphi_0)$, that was used to generate the recorded hologram, irradiates the developed photographic plate, so that, the reconstructed light field f can be written as

$$f = e_0 I = (A_{e_0}^2 + |e_s|^2)e_0 + A_{e_0}^2 e_s + A_{e_0}^2 \exp(2i\varphi_0)e_s^* \tag{2.2}$$

The first term is the reference wave (zeroth order) multiplied by a complex factor. The second term is the reconstructed object wave, forming the virtual image, times a real constant that only affects the image brightness. Lastly, the remaining term produces a distorted real image of the object, namely the twin image.

When that procedure is performed via digital reconstruction, the illumination with a reference beam is replaced by simulating the light propagation through the point-spread function of the Helmholtz equation for an optically homogeneous and isotropic medium. Therefore, the complex light field in the volume is reconstructed by considering the hologram pixels as source points with intensity equal to their grey-values while the corresponding phases (when they are not recorded) are conventionally set to zero.

Within such a framework, we now consider the propagation of the electromagnetic field in an homogeneous and isotropic medium from an "input plane" to an "output plane" parallel to the input one. Let us introduce a reference coordinate system $\{x, y, z\}$, with the origin on the input plane and the z axis perpendicular to both the input and the output planes. Denoting as $f(x, y)$ and $g(x, y)$ the complex field at the input and the output planes, respectively, it results that

$$g(x,y) = \iint f(x',y')h(x-x',y-y',d)dx'dy' \tag{2.3}$$

where $h(x - x', y - y', d)$ is the impulse-response function of the Helmholtz equation, evaluated at the point (x, y, d) when the point source is located at $(x', y', 0)$. The function h is also called the Rayleigh-Sommerfeld propagator and its analytical expression is

$$h(x,y,z) = \frac{1}{2\pi}\frac{\partial}{\partial z}\left(\frac{\exp(-ik\sqrt{x^2+y^2+z^2})}{\sqrt{x^2+y^2+z^2}}\right) \tag{2.4}$$

To save computing time, sometimes might be convenient to adopt simpler expressions for the propagation function as those provided by the Fresnel and the Fraunhofer diffraction theory. In image plane holography, that we implemented in our digital holographic microscope, the scattering objects are enough close to the hologram plane that the aforementioned approximations do not hold and, thus, hereafter we will only refer to the Rayleigh-Sommerfeld propagation function.

Rather then perform the double convolution integral of Eq.(2.3), it is worth rewriting that expression in term of Fourier components of the considered fields. Indeed, the complex amplitude on the input plane $f(x, y)$ can be regarded as a superposition of plane waves:

$$f(x,y) = \iint F(\nu_x,\nu_y)\exp\left[-i2\pi(\nu_x x+\nu_y y)\right]d\nu_x d\nu_y \tag{2.5}$$

where $F(\nu_x, \nu_y)$ is the Fourier transform of $f(x, y)$, and ν_x and ν_y are the spatial frequencies. $F(\nu_x, \nu_y)$ is also called the angular spectrum of the complex field $f(x, y)$. Carrying out the Fourier transform of Eq.(2.3) and appealing to the convolution theorem, we get the complex amplitude on the output plane as

$$g(x,y) = \iint H_d(\nu_x,\nu_y)F(\nu_x,\nu_y)\exp\left[-i2\pi(\nu_x x+\nu_y y)\right]d\nu_x d\nu_y \tag{2.6}$$

where $H_d(\nu_x, \nu_y)$, namely the Fourier transform of $h(x, y, d)$, is the transfer function between two parallel planes at a distance d and it assumes the following expression

$$H_d(\nu_x,\nu_y) = \exp\left[-i2\pi d\sqrt{\frac{1}{\lambda^2}-\nu_x^2-\nu_y^2}\right] \tag{2.7}$$

Such an approach is referred to as the angular spectrum method, since it involves the calculation of the angular spectra of the recorded and the reconstructed holograms. As opposed to the convolution method, the angular spectrum method leads to an expression for the reconstructed hologram $g(x, y)$ that can be very easily implemented on a computer through the discrete Fourier formalism.

In the context of in-line holography, the incident wave can be modelled as a plane wave with amplitude e_0 and a constant phase profile in the (x, y) plane. Using $e_s(x, y)$ as the scattered wave, the recorded intensity at the camera (hologram) plane can be expressed as:

$$I(x, y) = |e_0 + e_s(x, y)|^2 \simeq |e_0|^2 + 2\mathcal{R}\{e_0^* e_s(x, y)\} \tag{2.8}$$

The term $|e_s(\mathbf{x}, \mathbf{y})|^2$ is neglected since the amplitude of the scattered wave is usually smaller than the incident wave. In order to suppress the zeroth order component, we remove the contribution of the reference wave, so the input hologram $f(x, y)$ to back-propagate is

$$f(x, y) = I(\mathbf{x}, \mathbf{y}) - |e_0|^2 \simeq 2\mathcal{R}\{e_0^* e_s(\mathbf{x}, \mathbf{y})\} \tag{2.9}$$

Thus, the Fourier transform of the complex amplitude in the output plane is obtained as

$$G(\nu_x, \nu_y) = F(\nu_x, \nu_y) H_{-d}(\nu_x, \nu_y) \tag{2.10}$$

yielding

$$G(\nu_x, \nu_y) = e_0^* E_s(\nu_x, \nu_y) H_{-d}(\nu_x, \nu_y) + e_0 E_s^*(-\nu_x, -\nu_y) H_{-d}(\nu_x, \nu_y) \tag{2.11}$$

where $E_s(\nu_x, \nu_y)$ is the Fourier transform of $e_s(\mathbf{x}, \mathbf{y})$. Except for a constant phase shift, the first term in Eq.(2.11) is the reconstructed scattered field at a distance d from the focal plane, while the second term is the artifact due to the twin image that barely affects the image when d is large enough.

The presented algorithm can be simply implemented through the discrete Fourier transform (DFT) formalism. Let's denote the digital hologram recorded by the camera at the pixel (m, n) as I_{mn}, where the indices m and n represent, respectively, the row and the column of that pixel on the $M \times N$ sensor array of the camera. First, we compute the DFT of the recorded signal as

$$\tilde{I}_{pq} = \sum_{m=0}^{M-1} \sum_{n=0}^{N-1} I_{mn} \exp\left(\frac{-2\pi i p m}{M}\right) \exp\left(\frac{-2\pi i q n}{N}\right) \tag{2.12}$$

where the normalization factor $1/(NM)$ has been omitted. In order to subtract the reference field contribution as in Eq. (2.9), in principle we have to separately record the reference (or background) wave e_0, that is the recorded hologram when no one of the scattering objects, we are interested in, is in the field of view of the camera. However, such an operation is not always possible and for sure it would complicate the recording procedure. So we can rely on the average value of the recorded hologram $I(x, y)$ as a good approximation of e_0. Thus, we get the input hologram $f(x, y)$ by suppressing the DC component of the angular spectrum $\tilde{I}_{pq}$, that is $\tilde{I}_{00} = 0 + i\,0$. Subsequently, we perform the element by element multiplication of $\tilde{I}$ and $\tilde{H}$, where $\tilde{H}$ is the discretized transfer function, obtained by sampling the

continuous one, Eq. (2.7), on a $M \times N$ grid. Finally, the discretized field on the output plane is determined by taking the inverse discrete Fourier transform

$$g_{mn} = \sum_{p=0}^{M-1} \sum_{q=0}^{N-1} \tilde{I}_{pq} \tilde{H}_{pq} \exp\left(\frac{2\pi i p m}{M}\right) \exp\left(\frac{2\pi i q n}{N}\right) \tag{2.13}$$

The presented algorithm is the simplest one that can be devised by using the angular spectrum method. However, by considering the structure of the transfer function we can slightly modify it in order to reduce the amount of calculations and, consequently, the computing time. In fact, the function $H_d(\nu_x, \nu_y)$ is a loss pass filter that exponentially attenuate the amplitudes corresponding to the frequencies (ν_x, ν_y) lying outside the circle of radius $1/\lambda$, that is $\nu_x^2 + \nu_y^2 > 1/\lambda^2$. Therefore, we can shrink the size of $M \times N$ arrays to work only with those frequencies lying inside that circle. This approximation corresponds to neglect the near field effects and this is correct since in our configuration the distance between the focal plane and the closest scattering object is at least ten times the light wavelength and thus the evanescent waves are clearly negligible.

To get multiple views of the samples on several parallel planes in real-time, we rely on the parallel computing capability of the modern graphics processing unit (GPU), as recently reported by Shimobaba et al. (2010). We implemented the algorithm purely in CUDA C and used a combination of Python and C as host-code to perform initialization and provide a GUI (Graphical User Interface) for our applications. The package CUFFT from nVidia (2011) has been used to compute the fast Fourier transform. Such a package is highly optimized for CUDA architectures and it can also be used as a drop-in replacement for software packages like FFTW. For further details of the CUDA based implementation we refer the interested reader to the work of Cavallini (2011). The computational performances of the implemented algorithm are excellent when compared to the previous implementations, as Shimobaba et al. (2010), and allow the reconstruction of holograms on parallel planes at rate of few kHz.

2.2 Example of digital reconstruction

Using the experimental apparatus described in Section 1.2, we report an example of digital hologram reconstruction of an actual recorded hologram on several parallel planes. We prepared a sample putting a drop of distilled water seeded with 2.07 μm diameter silica beads between a 2.54cm$\times$6.0cm microscope slide and a 18mm$\times$18mm cover slip. The chamber was sealed by pouring transparent nail varnish along the cover slip edges. Focusing inside the liquid sample and cropping the field of view of the camera with a region of 1024×1024 pixels, we recorded a hologram, whose actual size is 69.12 μm$\times$ 69.12 μm, as shown in Figure 2.5. By back-propagating this frame we can refocus to an arbitrary parallel plane, thus obtaining the light distribution on the whole sample volume. Figure 2.6 shows the intensity of the back-propagated holograms in Figure 2.5 for different values of the distance d from the focal plane. It is worth noting that the brightness and the contrast of a digital recorded hologram depend on recording parameters as the beam light intensity, the camera exposure time, and the camera response function. For a digital reconstructed hologram displayed on a monitor, we have also to account for the linear function that maps the floating point values of the light intensity in Eq.(2.3) onto the discretized 8 bit interval of the output device. Therefore, when particles are brought into focus,

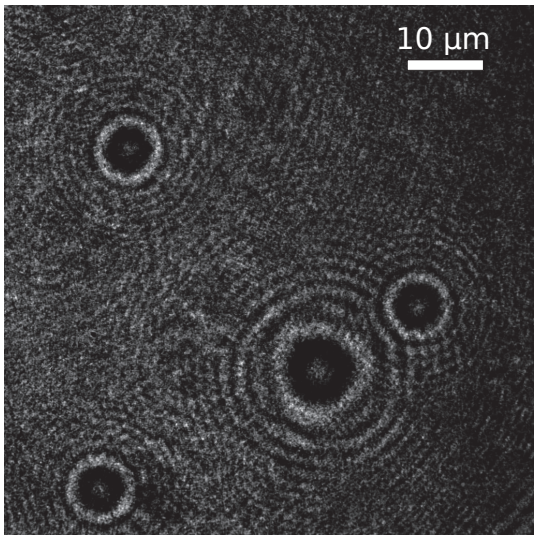

Figure 2.5: Recorded hologram of a 2.07 μm diameter beads dispersed in distilled water.

as in Figure 2.6 e), due to the high pixel values around the particle centers, the resulting image is made of small bright spots in an otherwise dark background. To control this effect and modify the image contrast, usually a thresholding function as the following is introduced

$$v(i) = \begin{cases} \frac{i - v_{min}}{v_{max} - v_{min}} & \text{if} \quad v_{min} < i < v_{max} \\ 0 \quad \text{otherwise} \end{cases} \tag{2.14}$$

where i is the actual intensity value and $v(i)$ is the corresponding pixel gray level. Varying the thresholds v_{max} and v_{min}, we can modify the reconstructed hologram contrast. This is very useful when the real-time back-propagation is used for a quick inspection of the volume sample. By adequately setting the thresholds, indeed, we can quickly have a clear overview of the particle distribution.

2.3 Particle tracking

As already introduced, several schemes have been proposed to determine the position of a spherical bead when imaged through an in-line holographic set-up. Determining the projection of particle center on the camera plane, namely the x and y, can be carried out with the standard 2D tracking schemes of digital video microscopy. We will not discuss such methods and we only refer the interested reader to the work of Crocker and Grier (1996). Herein we limit to report the results of Lee and Grier (2007) and Cheong et al. (2010) that claim an accuracy for in-plane holographic tracking of about ten nanometers. Such value is comparable to that one obtained for in-plane tracking in digital bright field microscopy.

Conversely, the axial tracking of particle center is less straightforward. The simplest way to identify the particle axis position is to locate the intensity peak of the reconstructed object beam. Even if that is a very simple strategy, it also easy to predict that the peak position does not correspond to the particle center. Indeed, as the sphere is illuminated by a plane wave, it acts as lens and it focuses the light further downstream. Therefore, the intensity peak method introduces a systematic error in particle center detection, equal to the particle's focal distance. In the ray

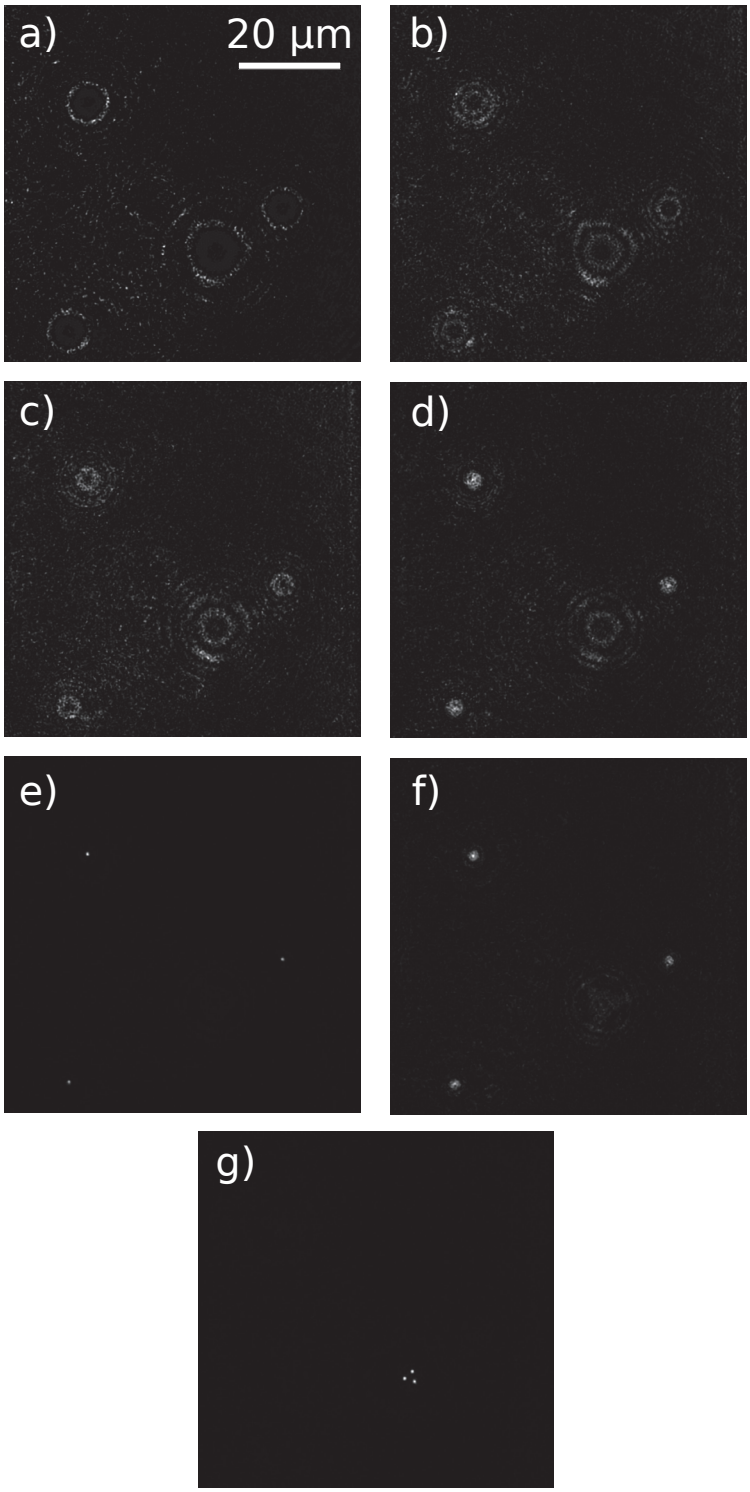

Figure 2.6: Reconstructed holograms on a series of parallel planes at several distances from the focal plane. The original recorded hologram is shown in Figure 2.5.

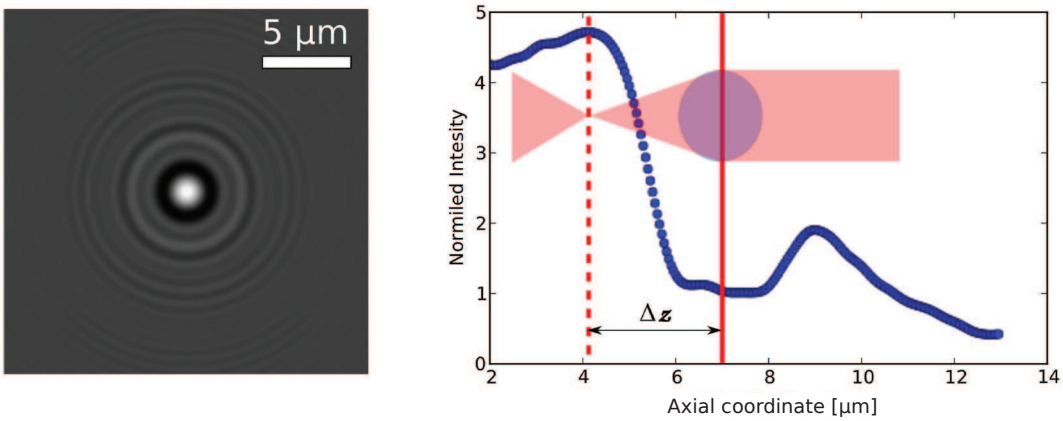

Figure 2.7: On the left, a theoretical hologram of a 2 μm diameter silica bead immersed in pure water, computed through the Lorenz-Mie scattering theory. On the right, the reconstructed light intensity along a line parallel to the optical axis and passing through the particle center. The particle center (solid line) is shifted by Δz with respect to the intensity peak (dashed lined), due to the lens effect.

optics regime, the distance between the particle center and its focus is analytically known but, unfortunately, this estimate is no longer valid when the particle size and the wavelength of the incoming light are of the same order of magnitude, as in the most of the experimental cases.

In order to quantify this systematic error and, thus, estimate the accuracy of the axial tracking scheme, we appeal to the Lorenz-Mie scattering theory, that provides us with the analytical solution of the Maxwell equations for a homogeneous and isotropic dielectric sphere illuminated by a linearly polarized plane wave (see Chapter 3). On the left panel, Figure 2.7 shows the Lorenz-Mie hologram for a silica bead (refractive index 1.46) immersed in pure water (refractive index 1.33). The bead diameter is 2.0 μm while the vacuum laser wavelength is 657 nm. Since the hologram intensity is proportional to the incoming beam intensity, for convenience, we have assumed a unitary amplitude of the reference wave e_0. The particle is arbitrarily located at the center of the image and the distance z between the particle center and the hologram plane is 7 μm. On the right panel of the same Figure, we plot the intensity profile against the distance along the z axis. For each axial position, the corresponding intensity value has been estimated through a Gaussian-weighted average over a grid of 9×9 pixels centered at the origin of the sphere. The solid red line represents the actual axial position of the simulated dielectric sphere while the dashed line locates the intensity peak. Therefore, the lens effect of the particle (shown as inset) introduces a systematic error on the particle detection comparable with the particle size. In the examined case, the distance Δz between the intensity peak and the particle center is about one-half the bead diameter. This distance represents the axial tracking accuracy. In Table 2.1 we report the computed accuracies Δz for two common particle materials, namely silica and polystyrene, and several bead diameters. In this Table, the dependence of the accuracy on the relative distance z between the focal plane and the particle center is investigated as well. The accuracy has the same order of magnitude of the particle radius and it mildly depends on the particle material, size and distance from the focal plane.

In the experimental hologram there is always a certain amount of background noise (e.g. the speckles due to unwanted scattering objects as impurities in the

Silica, $n = 1,46$				Polystyrene, $n = 1,57$			
z [μm]	$2a$ [μm]	Δz [μm]	$\Delta z/2a$	z [μm]	$2a$ [μm]	Δz [μm]	$\Delta z/2a$
15	1.0	0.63	0.6	15	1.0	0.63	0.6
	2.0	1.83	0.9		2.0	1.73	0.9
35	1.0	0.63	0.6	35	1.0	0.72	0.7
	2.0	2.14	1.1		2.0	2.14	1.1
	5.0	6.06	1.2		5.0	4.73	0.9
55	1.0	0.23	0.2	55	1.0	0.43	0.4
	2.0	2.44	1.2		2.0	2.54	1.3
	5.0	6.96	1.4		5.0	5.35	1.0
75	5.0	8.06	1.6	75	5.0	9.95	2.0

Table 2.1: Accuracies Δz of the axial tracking of spherical particle, based on the back-propagation of holograms. Particle center is identified with the local maxima of the light intensity of the reconstructed holograms. Due to the lens effect of the tracked spherical bead, the intensity peak is at a finite distance Δz from the particle center. We use the Lorenz-Mie scattering theory to predict the quantity Δz for silica and polystyrene spherical beads immersed in pure water. We also investigate the sensibility of Δz on particle radius a and distance z from the focal plane.

Silica, $n = 1,46$				Polystyrene, $n = 1,57$			
z [μm]	$2a$ [μm]	Δz [μm]	$\Delta z/2a$	z [μm]	$2a$ [μm]	Δz [μm]	$\Delta z/2a$
15	1.0	5.9	0.6%	15	1.0	2.7	0.3%
	2.0	5.4	0.3%		2.0	3.2	0.2%
35	1.0	10.14	1.0%	35	1.0	5.4	0.4%
	2.0	5.97	0.3%		2.0	2.3	0.1%
	5.0	34.1	0.7%		5.0	3.1	0.06%
55	1.0	22.7	2.3%	55	1.0	12.0	1.2 %
	2.0	7.1	0.4%		2.0	4.9	0.2%
	5.0	58.2	1.2 %		5.0	2.3	0.05%
75	5.0	8.3	0.2%	75	5.0	4.7	0.1%

Table 2.2: Precisions Δz of the axial particle tracking by back-propagation of synthetic holograms. Particle center is identified with the local maxima of the light intensity of the reconstructed holograms. Δz quantifies the dependence of the position of the intensity peak on the background noise and, thus, it estimates the precision of the measurements. Hologram synthetic generation is shown in Figure 2.8.

sample or dust on the optics, electronic noise of the camera, etc.) that affects the measured positions. Because of the random variation of the background noise, even if the particle were completely at rest, the particle tracking analysis would not provide constant values. Those measurements would oscillate, instead, around a mean value and the amplitude of those oscillations represents the precision or the reproducibility of the measurement. We can estimate it appealing again to the Lorentz-Mie scattering theory for synthetic hologram generation. Such holograms are obtained multiplying the computer generated Lorentz-Mie holograms by the recorded experimental holograms of an empty (particle free) sample. The former represents the known signal and the latter the background noise. A schematic representation of

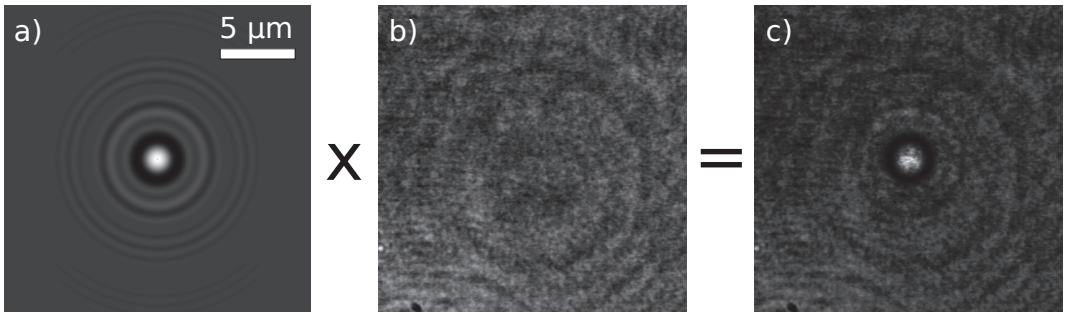

Figure 2.8: Generation of synthetic holograms. The theoretical hologram a) is multiplied by the experimental background hologram b), the latter being normalized by its mean value. The result is the synthetic hologram c).

the synthetic hologram generation is shown in Figure 2.8. Keeping constant the position of the particle in the theoretical hologram, we determine its axial position for different background holograms. Finally, the standard deviation of the measured axial positions provides the precision of the axial tracking method. Table 2.2 shows the estimated precisions for the same particle materials, sizes and distances used for the accuracy analysis. The axial positions are evaluated using two hundred recorded background holograms.

In conclusion, comparing the standard tracking schemes for digital video microscopy with the in-line holography tracking method based on the back-propagation algorithm, it has been demonstrated by Lee and Grier (2007) and Cheong et al. (2010) that those approaches share almost the same in-plane tracking accuracy and resolution. As opposed to the bright-field microscopy, digital holography provides the axial position of the illuminated particles and, herein, we have investigated the accuracy and the precision of the axial tracking. Ultimately, we have shown how the back-propagation algorithm enables the particle localization with nanometric precisions but very low accuracy. When only spherical colloids are considered (that is the case in the most of the applications), the theoretical prediction of the Lorenz-Mie theory allows us to compensate the systematic error due to the lens effect of the bead. Nevertheless, when objects with more complicated (or even unknown) shapes have to be tracked, the compensation procedure will be more tricky and not always viable. Finally, it's worth noting that if we are interested in the relative displacement of one particle or the relative motions between more particles, as a first approximation we can assume that the distance between the intensity peak and the object center is constant and thus the systematic error can be automatically canceled out.

3 Digital reconstruction between two arbitrarily tilted planes

3.1 Introduction

Back-propagating the object beam on parallel planes enables us to reconstruct the light field throughout the sample volume. If we desire to inspect the sample from a viewing direction not parallel to the optical axis, the entire volume will have to be scanned in several planes and, subsequently, by processing the stack of reconstructed holograms, we will determine the hologram on the desired tilted plane. That is

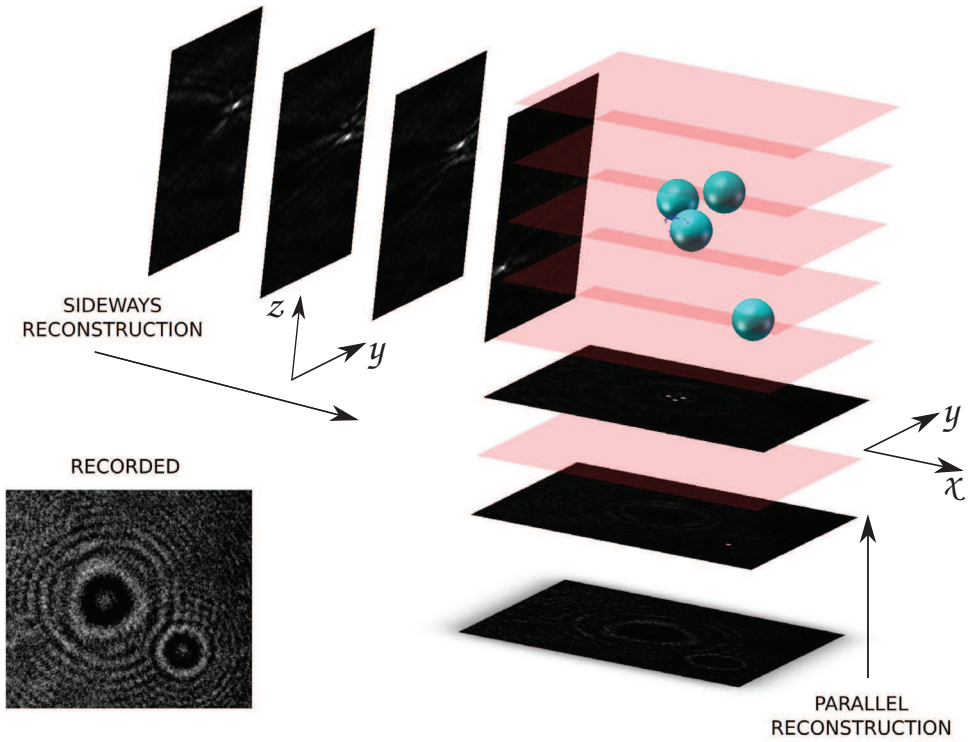

Figure 2.9: Digital reconstruction between arbitrarily oriented planes. A set of spherical beads is illuminated by a plane wave. The recorded hologram is propagated on planes both parallel and perpendicular to the focal plane x, y. This offers a side view of the sample, providing a quick overview of the beads' arrangement.

also the case for other three-dimensional microscopy techniques, as for instance the confocal microscopy.

Nevertheless, it will be very useful if we can propagate the light field directly to any arbitrarily oriented plane, thereby avoiding the scan process that is quite time consuming. As an example, Figure 2.9 schematically shows four beads illuminated by a monochromatic plane wave and the corresponding reconstructed holograms parallel to the image plane xy. Propagating the light between titled planes provide us with a direct access to a perpendicular viewing direction. For instance, we can see the beads' arrangement through a side view, parallel to the optical axis z, thereby enabling a quick inspection of the three-dimensional beads' distribution. The first algorithm for back-propagating a coherent light beam between arbitrarily oriented plane has been proposed by Tommasi and Bianco (1992), using the angular spectrum rotation method. Further implementations and developments of this algorithm were provided by Delen and Hooker (1998), Matsushima et al. (2003), De Nicola et al. (2005) and Akhter and Kim (2010).

Basically following the original idea, we now present a new implementation that leads to strongly speed up the hologram reconstruction between arbitrarily tilted planes, enabling real-time image processing (Section 3.2). To prove the 3D visualization capabilities of this method, we demonstrate that it allows the real-time microscopic inspection of particle distribution over three mutually orthogonal planes at the same time (Section 3.3). Particularly, we show how the proposed technique is extremely useful when coupled to holographic optical tweezers providing an inter-

active visual feedback on the 3D arrangement of trapped beads. As an additional straightforward application, we use such technique for real-time monitoring of fluid flow over three orthogonal cross sections of a microfluidic channel (Section 3.4).

3.2 The algorithm

As we consider the propagation between two arbitrarily oriented planes, the Rayleigh-Sommerfeld propagator $H_d(\nu_x, \nu_y)$, introduced in Section 2.1, should be replaced by a new propagation function. Instead of deriving its analytical expression, as reported by Tommasi and Bianco (1992), we rather discuss a numerical approach to reconstruct the scattered field. Let us choose a reference system $\{x, y, z\}$, with the x, y plane lying on the input plane, see Figure 2.10. We decompose the complex amplitude $f(x, y)$ on the input field through a discrete Fourier transform:

$$f(x,y) = \sum_{m,n} F_{m,n} \exp\left[-i2\pi(\nu_m x + \nu_n y)\right] \tag{2.15}$$

where $\nu_m = m/Nu$ and $\nu_n = n/Nu$ are the discrete spatial frequencies. The two indices n, m go from 0 to $N-1$, while u is the spatial step that, in our case, is given by the magnification times the camera pixel size. The field in the whole 3D sample volume will be:

$$U(\mathbf{R}) = \sum_{m,n} F_{m,n} \exp(-i\mathbf{K}_{m,n} \cdot \mathbf{R}) \tag{2.16}$$

where

$$\mathbf{K}_{m,n} = (2\pi\nu_m, 2\pi\nu_n, 2\pi\sqrt{\lambda^{-2} - \nu_m^2 - \nu_n^2}) \tag{2.17}$$

In those formulas, the three-dimensional position vector is represented by $\mathbf{R} = (x, y, z)$ while the dot denotes the inner product. Let us now introduce a new coordinate system $\{\xi, \eta, \zeta\}$ with ξ and η lying on the output plane. Denoting vectors in the new coordinate system with primed letters, we can rewrite the field as:

$$U(\mathbf{R}') = \sum_{m,n} F'_{m,n} \exp(-i\mathbf{K}'_{m,n} \cdot \mathbf{R}') \tag{2.18}$$

where

$$\mathbf{K}'_{m,n} = (2\pi\nu'_m, 2\pi\nu'_n, 2\pi\sqrt{\lambda^{-2} - \nu'^2_m - \nu'^2_n}) \tag{2.19}$$

In the most general case, coordinate transformation between the two reference systems will imply a translation $\mathbf{R}_{OO'}$ and a rotation $\mathbf{M}$ so that

$$\mathbf{R} = \mathbf{M} \cdot \mathbf{R}' + \mathbf{R}_{OO'} \tag{2.20}$$

Substituting such a relation into Eq.(2.16) and comparing to Eq.(2.18), we get

$$F'_{m,n} = F_{m,n} \exp(-i\mathbf{K}_{m,n} \cdot \mathbf{R}_{OO'}) \tag{2.21}$$

$$\mathbf{K}'_{m,n} = \mathbf{M}^T \cdot \mathbf{K}_{m,n}. \tag{2.22}$$

Substituting $\zeta = 0$ in Eq.(2.18), we can now write the field on the output plane as

$$g(\xi,\eta) = \sum_{m,n} F'_{m,n} \exp\left[-i2\pi(\nu'_n \xi + \nu'_m \eta)\right] \tag{2.23}$$

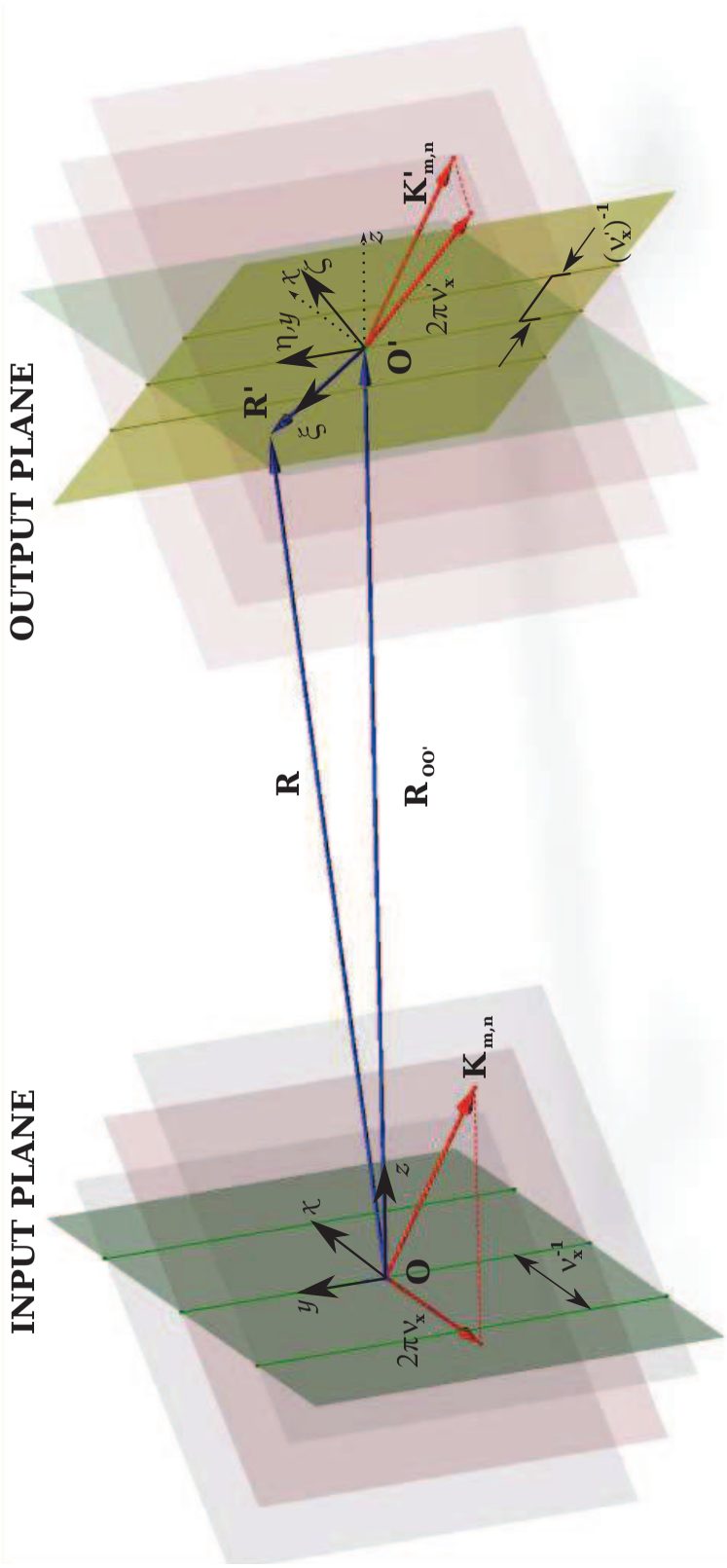

Figure 2.10: Scheme of the propagation of a plane wave between two tilted planes. The signs and the symbols are discussed in the text.

This equation shows how the m,n-component of the input signal, with amplitude $F_{m,n}$ and frequencies ν_m, ν_n, when propagated to a tilted plane, will contribute to the reconstructed field with a phase shifted amplitude $F'_{m,n} = F_{m,n}\exp(-i\mathbf{K}_{m,n}\cdot\mathbf{R}_{OO'})$ and new frequencies ν'_m, ν'_n. As an example, in Figure 2.10 a single plane wave component $\mathbf{K}_{m,n}$ is considered. We represent the simple case of an output plane rotated with respect to the y axis. The in-phase planar wavefronts intersect the input plane in straight lines evenly distributed at a distance $1/\nu_x$. Due to the relative rotation, the same wavefronts intersect the output planes in evenly distributed straight lines but less far apart (namely, $1/\nu'_x$). Hence, we can visually understand how the same plane wave results in different Fourier components when the input and output planes are rotated with respect to each other. However, since those new frequencies ν'_m, ν'_n are not evenly distributed, the fast Fourier transform (FFT) algorithm cannot be directly applied to compute Eq.(2.23). For this reason, we introduce a new set of spatial frequencies $\nu'_p = p/Nu, \nu'_q = q/Nu$ lying on a square grid. Instead of computing the exact values of the corresponding complex amplitudes $G_{p,q}$ and the Jacobian of the frequency transformation, we approximate them through a nearest interpolation method by mapping the old frequencies ν'_m, ν'_n into the new ones ν'_p, ν'_q and summing over the corresponding complex amplitudes $F'_{m,n}$:

$$G_{p,q} = \sum_{m,n} F'_{m,n}\Theta\left(\frac{1}{2u} - |\nu'_p - \nu'_m|\right)\Theta\left(\frac{1}{2u} - |\nu'_q - \nu'_n|\right) \tag{2.24}$$

where Θ is the Heaviside function. The field on the output plane can now be expressed as a discrete Fourier transform on an equally spaced grid of spatial frequencies:

$$g(\xi,\eta) = \sum_{p,q} G_{p,q}\exp\left[-i2\pi(\nu'_p\xi + \nu'_q\eta)\right] \tag{2.25}$$

Tommasi and Bianco (1992) presented the angular spectrum rotation method in terms of continuum Fourier transform and, thus, the Jacobian of the frequency rotation transform Eq.(2.22) explicitly appears in the field on the tilted output plane. Consequently, its value has to be worked out, unless small tilt angles are considered. Furthermore, the problem of not-evenly spaced rotated frequencies was overcome through a linear interpolation methods. Conversely, we have directly presented the algorithm through the discrete Fourier transform formalism. In this context, the new complex amplitudes $G_{p,q}$ on the output plane are expressed by Eq.(2.24) that performs two steps in one: a nearest-neighbor approximation of the new amplitudes as well as an approximation of the Jacobian of the transformation between the input and the output spatial frequency coordinates. This results in a strong speed-up of the algorithm compared to the former implementations reported in literature.

The algorithm is implemented on a CUDA-based GPU (GeForce GTX470). The first step is to compute the FFT of the recorded image through the CUDA package CUFFT [nVidia (2011)]. To subtract the contribution of the incident wave as shown in Eq.(2.9), we set to zero the DC component of the Fourier transform. Then we perform the following steps: (i) each plane-wave gets propagated up to the reconstruction plane through a phase-shift $\exp[-i\mathbf{K}_{m,n}\cdot\mathbf{R}_{\mathbf{OO'}}]$ as in Eq.(2.23); (ii) we compute the new frequencies ν'_m, ν'_n as the (ξ,η) components of the rotated wavevector $\mathbf{M}^T\cdot\mathbf{K}_{m,n}$ divided by 2π; (iii) we implement Eq.(2.24) to compute the new complex amplitudes $G_{p,q}$ by an histogram procedure with weights $F'_{m,n}$. The final reconstructed image is then obtained by performing an inverse FFT as in Eq.(2.25).

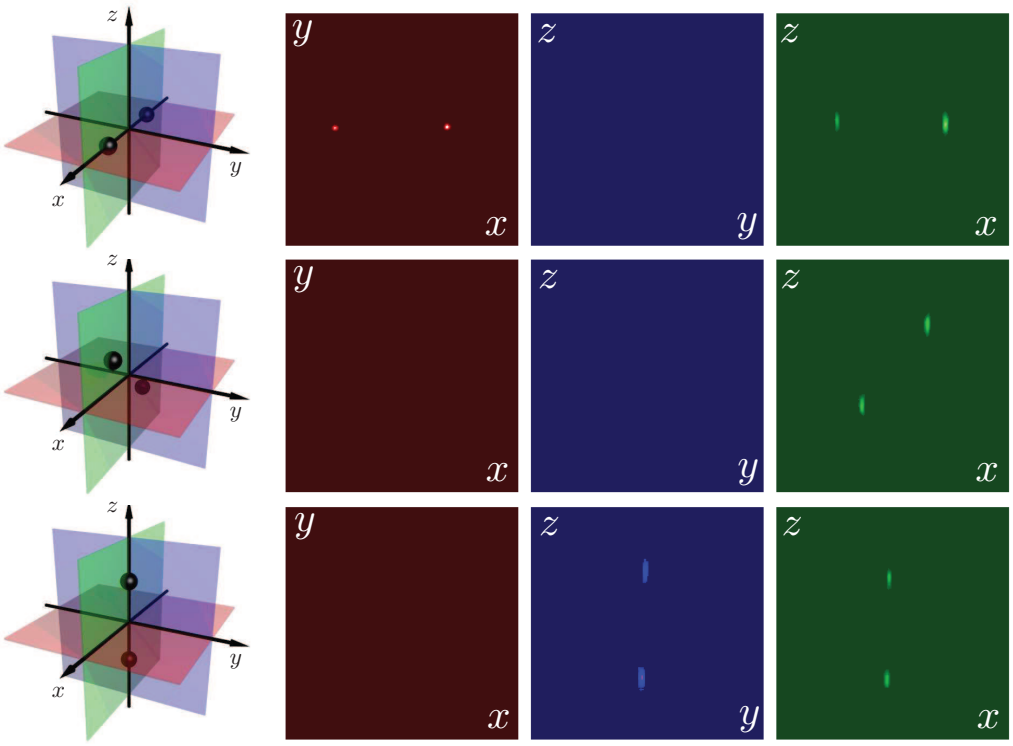

Figure 2.11: An 3×3 array of images showing simultaneous reconstructions over three mutually orthogonal planes at three different times. A 3D scheme of the corresponding bead arrangement is also shown on the left. In the (z, x) plane (third column), the beads are always on focus and two bright spots rotate with respect to the plane center. On the remaining planes (first and second columns), the spots appear only when particles intersect the (y, x) and (z, y) planes as in the first and third row, respectively.

3.3 Real time 3D tracking of trapped beads

We now demonstrate the high speed capabilities of our algorithm by following in real-time 3D trajectories of two 2.07 μm diameter silica beads, simultaneously on three orthogonal planes. We used the experimental apparatus described in Section 1.2. The sample cell is assembled by placing a cover slip on top of a microscope slide, using two 60 μm diameter nylon wires as spacers and sealing with transparent nail varnish. The chamber is filled with a dispersion of 2.07 μm diameter silica microspheres (Bangs Laboratories, Inc.) in distilled water. Considering the reference frame (x, y, z) with the z axis lying on the optical axis, we placed two trapped beads along x axis. Then we tracked beads' motion while performing a full rotation in the (x, y) plane, followed by a full rotation in the (x, z) plane, see Figure 2.11. Image processing of the reconstructed holograms, like contrast enhancement and thresholding, are also performed in real-time, so that the intensity peaks can be easily detected (i.e. the bright spots in Figure 2.11). Moreover, we can artificially increase the depth of field by averaging over a stack of N evenly spaced parallel reconstruction planes. For example, in Figure 2.11, we set a depth of field of 2 μm, by averaging over 10 planes. Such operation prevents tracked beads to suddenly disappear from the selected view plane because of their Brownian motion and possible misalignment between bead rotation axis and coordinates axis. Tracked microspheres

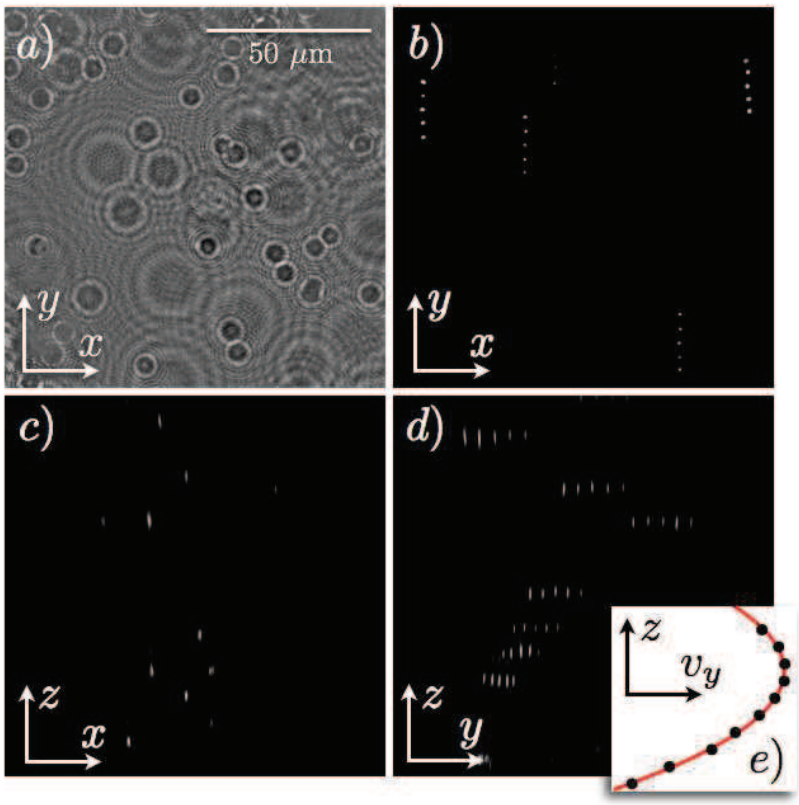

Figure 2.12: Simultaneous orthogonal views of tracers in a micro channel flow. (a) Raw hologram; (b),(c),(d) reconstructed images over three orthogonal cross sections. For sake of clarity, only 115 μm×115 μm cropped regions are shown. To enhance flow visualization we have superimposed five frames with a time interval of 0.2 s. Panel e) shows in black circles the average velocity profile extracted from yz reconstructions together with the theoretical parabolic behavior as a red line.

appear as prolate spheroids with major (z) and minor (x, y) axis measuring respectively 1.35 μm and 0.4 μm full width at half maximum. High computational speed of our algorithm allows us to perform reconstructions of a single plane at about 1 kHz.

3.4 Real time flow visualization

The presented technique can be also very useful in microfluidic applications, allowing real-time flow visualization. Indeed, we applied the back-propagation algorithm between tilted planes to follow the trajectories of polystyrene beads dispersed in distilled water and flowing in a micro channel. The experimental apparatus is the same we used to track the motion of the rotating beads, but the trapping laser is now turned off. The sample consists of a rectangular cross section channel (Ibidi U-SLIDE I LUER), which is 200 μm in height along the optical z axis, 5 mm in width along the x axis and 5 cm in length along the y axis. A flow of distilled water seeded with 2 μm diameter polystyrene beads (Bangs Laboratories, Inc.) is established via hydrostatic pressure along the y direction. Back-propagating the raw recorded holograms on the x, y plane (Figure 2.12a), we can follow the flow at the same time over three orthogonal planes: one perpendicular to the z axis, as the

focal plane but at a different height in the channel (Figure 2.12b), one perpendicular to the y axis (Figure 2.12c) and one perpendicular to the x axis (Figure 2.12d). To enhance the flow visualization we have superimposed five frames with a time interval of 0.2 s. In the y, z plane, we can clearly observe how particles' speed varies along the z direction. Particularly, higher speeds correspond to higher distances from the wall, that is located approximately at the bottom of the image. Image contrast enhancement and thresholding are also performed in real-time to facilitate beads' detection. Due to the high aspect ratio of the channel rectangular cross section, we have a planar flow parallel to the y, z plane. Hence, we set a depth of field of 20 μm by averaging over 66 equally spaced planes, thereby we brought to focus at the same time several particles floating on different planes. That provides a better statistics when the cross-correlation analysis is performed to detect the velocity profiles. In the inset of Figure 2.12, we show a part of the experimental velocity profile, measured through the cross-correlation techniques (see Chapter 4), compared to the theoretical prediction of the one-dimensional Poiseuille flow.

3.5 Conclusions

In summary, we have demonstrated the possibility of performing real-time digital holographic microscopy on multiple and arbitrarily oriented planes. This approach offers 3D real-time visualization capabilities that will be extremely useful in many applications where a fast and general 3D inspection of the sample is needed. Even if the back-propagation approach has a lower resolution than other 3D tracking schemes, (e.g. Lorenz-Mie fitting of hologram or back focal plane interferometry), it has no limitation in terms of maximum number and/or specific shape of tracked objects. Hence, our technique is the most suited for those contexts where many complex shaped objects (e.g. cells, bacteria, microrods, etc.) have to be tracked throughout the sample. In addition, we totally rely on software hologram processing and no additional hardware devices are required. Therefore, the proposed method can be easily implemented on any standard optical microscope, once the bright field illumination is replaced by a coherent light source. A well-improved implementation combined with an optimized code for graphics processing unit allows us to process 1024x1024 holograms at a rate of more than 1kHz. This is even about hundreds of times faster than recently reported real-time schemes where only back-propagation to parallel planes is accomplished. Among others, for instance, there is the work of Shimobaba et al. (2008) where a rate of 24 fps for 512x512 holograms is reported and the one of Trujillo et al. (2010) where a rate of 32 fps for 1024x1024 holograms is demonstrated.

As an application of our technique we tracked in real-time two trapped beads on three perpendicular planes while they are manipulated by a holographic trapping system. Thus, DHM coupled with HOT makes the optical 3D manipulation of micro-objects easier and more interactive since a real-time access to the sample volume simultaneously from many viewing directions is now possible. Moreover, we applied the angular spectrum rotation method to perform flow visualization by tracking particle motion over the three cross sections of a microfluidic channel. It will be important to investigate the possibility of extending our technique to the real-time tracking of complex shaped objects, like motile cells, or for real-time inspection of larger organisms across multiple sections.

References

Akhter, N. and Kim, K. (2010). Reconstruction of digital hologram of small particles on arbitrarily tilted plane using digital holography. *Optics Communications*.

Allersma, M., Gittes, F., deCastro, M., Stewart, R., and Schmidt, C. (1998). Two-dimensional tracking of ncd motility by back focal plane interferometry. *Biophysical journal*, 74(2):1074–1085.

Baek, S. and Lee, S. (1996). A new two-frame particle tracking algorithm using match probability. *Experiments in Fluids*, 22(1):23–32.

Bowman, R., Gibson, G., and Padgett, M. (2010). Particle tracking stereomicroscopy in optical tweezers: Control of trap shape. *Optics Express*, 18(11):11785–11790.

Bryngdahl, O. and Wyrowski, F. (1990). I digital holography-computer-generated holograms. *Progress in Optics*, 28:1–86.

Cavallini, L. (2011). Digital holographic microscopy of multiple and arbitrarily oriented image planes. MSc Thesis in Physics.

Cheong, F., Krishnatreya, B., and Grier, D. (2010). Strategies for three-dimensional particle tracking with holographic video microscopy. *Opt. Express*, 18(13):13563.

Cheong, F., Sun, B., Dreyfus, R., Amato-Grill, J., Xiao, K., Dixon, L., and Grier, D. (2009). Flow visualization and flow cytometry with holographic video microscopy. *Optics Express*, 17(15):13071–13079.

Crocker, J. and Grier, D. (1996). Methods of digital video microscopy for colloidal studies. *Journal of Colloid and Interface Science*, 179(1):298–310.

De Nicola, S., Finizio, A., Pierattini, G., Ferraro, P., and Alfieri, D. (2005). Angular spectrum method with correction of anamorphism for numerical reconstruction of digital holograms on tilted planes. *Optics Express*, 13(24):9935–9940.

Delen, N. and Hooker, B. (1998). Free-space beam propagation between arbitrarily oriented planes based on full diffraction theory: a fast fourier transform approach. *JOSA A*, 15(4):857–867.

Dixon, L., Cheong, F., and Grier, D. (2011a). Holographic deconvolution microscopy for high-resolution particle tracking.

Dixon, L., Cheong, F., and Grier, D. (2011b). Holographic particle-streak velocimetry. *Optics Express*, 19(5):4393–4398.

Dubois, F., Joannes, L., and Legros, J. (1999). Improved three-dimensional imaging with a digital holography microscope with a source of partial spatial coherence. *Applied optics*, 38(34):7085–7094.

Florin, E., Hörber, J., and Stelzer, E. (1996). High-resolution axial and lateral position sensing using two-photon excitation of fluorophores by a continuous-wave nd: Yag laser. *Applied physics letters*, 69:446.

Fung, J., Martin, K., Perry, R., Kaz, D., McGorty, R., and Manoharan, V. (2011). Measuring translational, rotational, and vibrational dynamics in colloids with digital holographic microscopy. *Optics Express*, 19(9):8051–8065.

Ghislain, L. and Webb, W. (1993). Scanning-force microscope based on an optical trap. *Optics letters*, 18(19):1678–1680.

Gopalan, B., Malkiel, E., and Katz, J. (2008). Experimental investigation of turbulent diffusion of slightly buoyant droplets in locally isotropic turbulence. *Physics of Fluids*, 20:095102.

Katz, J. and Sheng, J. (2010). Applications of holography in fluid mechanics and particle dynamics. *Annual Review of Fluid Mechanics*, 42:531–555.

Kim, M. (2010). Principles and techniques of digital holographic microscopy. *SPIE Reviews, Volume 1, id. 018005 (2010).*, 1(1):8005.

Kim, S. and Lee, S. (2007). Measurement of 3d laminar flow inside a micro tube using micro digital holographic particle tracking velocimetry. *Journal of Micromechanics and Microengineering*, 17:2157.

Kronrod, M., Merzlyakov, N., and Yaroslavskii, L. (1972a). Computer synthesis of transparency holograms. *Soviet Physics Technical Physics*, 17:329.

Kronrod, M., Merzlyakov, N., and Yaroslavskii, L. (1972b). Reconstruction of a hologram with a computer. *Soviet Physics Technical Physics*, 17:333.

Lebrun, D., Benkouider, A., Coëtmellec, S., and Malek, M. (2003). Particle field digital holographic reconstruction in arbitrary tilted planes. *Opt. Express*, 11(3):224–229.

Lee, S. and Grier, D. (2007). Holographic microscopy of holographically trapped three-dimensional structures. *Opt. Express*, 15(4):1505–1512.

Lee, S., Roichman, Y., Yi, G., Kim, S., Yang, S., Van Blaaderen, A., Van Oostrum, P., and Grier, D. (2007). Characterizing and tracking single colloidal particles with video holographic microscopy. *Optics Express*, 15(26):18275–18282.

Lee, W. (1978). Iii computer-generated holograms: Techniques and applications. *Progress in Optics*, 16:119–232.

Leith, E. and Upatnieks, J. (1962). Reconstructed wavefronts and communication theory. *JOSA*, 52(10):1123–1128.

Leith, E. and Upatnieks, J. (1964). Wavefront reconstruction with diffused illumination and three-dimensional objects. *JOSA*, 54(11):1295–1301.

Lu, J., Fugal, J., Nordsiek, H., Saw, E., et al. (2008). Lagrangian particle tracking in three dimensions via single-camera in-line digital holography. *New Journal of Physics*, 10:125013.

Malkiel, E., Sheng, J., Katz, J., and Strickler, J. (2003). The three-dimensional flow field generated by a feeding calanoid copepod measured using digital holography. *Journal of experimental biology*, 206(20):3657.

Matsushima, K., Schimmel, H., and Wyrowski, F. (2003). Fast calculation method for optical diffraction on tilted planes by use of the angular spectrum of plane waves. *JOSA A*, 20(9):1755–1762.

Meng, H., Pan, G., Pu, Y., and Woodward, S. (2004). Holographic particle image velocimetry: from film to digital recording. *Measurement Science and Technology*, 15:673.

Monaghan, D., Kelly, D., Pandey, N., and Hennelly, B. (2009). Twin removal in digital holography using diffuse illumination. *Optics letters*, 34(23):3610–3612.

Murata, S. and Yasuda, N. (2000). Potential of digital holography in particle measurement. *Optics & Laser Technology*, 32(7-8):567–574.

nVidia (2011). Cufft pacakge. `http://developer.nvidia.com/cufft`.

Ooms, T., Koek, W., and Westerweel, J. (2008). Digital holographic particle image velocimetry: eliminating a sign-ambiguity error and a bias error from the measured particle field displacement. *Measurement Science and Technology*, 19:074003.

Pan, G. and Meng, H. (2003). Digital holography of particle fields: reconstruction by use of complex amplitude. *Applied optics*, 42(5):827–833.

Pedrini, G., Fröning, P., Fessler, H., and Tiziani, H. (1998). In-line digital holographic interferometry. *Applied optics*, 37(26):6262–6269.

Roichman, Y., Sun, B., Stolarski, A., and Grier, D. (2008). Influence of nonconservative optical forces on the dynamics of optically trapped colloidal spheres: the fountain of probability. *Physical review letters*, 101(12):128301.

Saleh, B., Teich, M., and Saleh, B. (1991). Fundamental of photonics.

Sasaki, K., Tsukima, M., and Masuhara, H. (1997). Three-dimensional potential analysis of radiation pressure exerted on a single microparticle. *Applied physics letters*, 71:37.

Satake, S., Kunugi, T., Sato, K., Ito, T., and Taniguchi, J. (2005). Three-dimensional flow tracking in a micro channel with high time resolution using micro digital-holographic particle-tracking velocimetry. *Optical review*, 12(6):442–444.

Schnars, U. (1994). Direct phase determination in hologram interferometry with use of digitally recorded holograms. *JOSA A*, 11(7):2011–2015.

Schnars, U. and Jüptner, W. (1994a). Digital recording and reconstruction of holograms in hologram interferometry and shearography. *Applied optics*, 33(20):4373–4377.

Schnars, U. and Jüptner, W. (1994b). Direct recording of holograms by a ccd target and numerical reconstruction. *Applied Optics*, 33(2):179–181.

Sheng, J., Malkiel, E., and Katz, J. (2006). Digital holographic microscope for measuring three-dimensional particle distributions and motions. *Applied optics*, 45(16):3893–3901.

Sheng, J., Malkiel, E., and Katz, J. (2008). Using digital holographic microscopy for simultaneous measurements of 3d near wall velocity and wall shear stress in a turbulent boundary layer. *Experiments in fluids*, 45(6):1023–1035.

Sheng, J., Malkiel, E., and Katz, J. (2009). Buffer layer structures associated with extreme wall stress events in a smooth wall turbulent boundary layer. *Journal of Fluid Mechanics*, 633:17–60.

Sheng, J., Malkiel, E., Katz, J., Adolf, J., and Belas, R. (2007). Digital holographic microscopy reveals prey-induced changes in swimming behavior of predatory dinoflagellates. *Proceedings of the National Academy of Sciences*, 104(44):17512.

Shimobaba, T., Masuda, N., Ichihashi, Y., and Ito, T. (2010). Real-time digital holographic microscopy observable in multi-view and multi-resolution. *Journal of Optics*, 12:065402.

Shimobaba, T., Sato, Y., Miura, J., Takenouchi, M., and Ito, T. (2008). Real-time digital holographic microscopy using the graphic processing unit. *Optics express*, 16(16):11776–11781.

Soria, J. and Atkinson, C. (2008). Towards 3c-3d digital holographic fluid velocity vector field measurementtomographic digital holographic piv (tomo-hpiv). *Measurement Science and Technology*, 19:074002.

Tommasi, T. and Bianco, B. (1992). Frequency analysis of light diffraction between rotated planes. *Optics letters*, 17(8):556–558.

Trujillo, C., Restrepo, J., and Garcia-Sucerquia, J. (2010). Real time numerical reconstruction of digitally recorded holograms in digital in-line holographic microscopy by using a graphics processing unit. *Photonics Letters of Poland*, 2(4):pp–177.

Van Oostrum, P. (2011). *Using Light Scattering to Track, Characterize and Manipulate Colloids*. PhD thesis, Universiteit Utrecht.

Chapter 3

Digital holographic tracking

Since the origin of digital holography, the computer generation of artificial holograms of ideal objects has been investigated. In principle, to predict the electromagnetic field, and thus the hologram, produced by a known object when it is illuminated by a coherent laser source, would require to solve the entire system of Maxwell equations. Practically, this task can be addressed relying on simplified light scattering models and/or via numerical solutions. Nevertheless, in the very simple case of a dielectric sphere immersed in an isotropic and homogeneous medium, the Maxwell equations can be analytically solved, as demonstrated by Gustav Mie in 1908. As the theoretical hologram is compared to the experimental one, digital holographic microscopy turns out to be an ideal tool for three-dimensional tracking of microspheres while simultaneously allowing a full and accurate characterization of their main physical properties such as: radius and refractive index.

The fundamentals of this technique, to which we refer as digital holographic tracking, are presented in Section 1.2. Then we report a detailed analysis of the tracking and sizing capabilities in terms of precision and accuracy of the method in relation to the primary sources of error (Section 1.3). As long as several beads are holographically trapped and their motion is accurately tracked, they act as local sensors of the physical/chemical properties of the surrounding fluid, as discussed in Section 2.1. Next, we exploit the sizing and tracking capabilities of digital holographic tracking (Section 2.2) to set-up a multipoint viscosity measurement system with an estimated accuracy less than 3%. We finally applied digital holographic tracking technique to the characterization of the radius and shell thickness of lipidic microbubbles (Section 3.1).

1 Digital Holographic Tracking

1.1 Introduction

In most of the cases the 3D spatial reconstruction of a hologram is obtained by direct numerical back propagation. Nevertheless, DHM has been shown to provide a powerful tool for fast 3D particle tracking especially when using spherical probes. In that case object reconstruction can be achieved by fitting the recorded hologram to the superposition of forward propagated Mie scattering patterns. This approach was introduced by Lee et al. (2007) and subsequently recalled by Cheong et al. (2010), Cheong et al. (2009a), Cheong et al. (2009b) and Xiao and Grier (2010). Such a technique, hereafter referred to as Digital Holographic Tracking (DHT), allows to track spherical colloids in a 3D space with a supposed resolution of nanometers while simultaneously measuring the mean radius a and the relative refractive index m with high but not yet well characterized accuracy. After discussing the working principle of the technique (Section 1.2), we quantify the actual precision and accuracy of DHT in relation to the primary sources of error (Section 1.3).

1.2 Hologram analysis by Lorenz-Mie scattering theory

As discussed in the previous Chapter, when a plane monochromatic wave impinges on a dielectric sphere, the scattered light interferes with the incident beam resulting in a fringe pattern, the hologram. A magnified image of the interference pattern is projected on a CMOS camera by the microscope objective. Comparing the experimental hologram with the predictions given by Lorenz-Mie theory, we can extract particle's 3D position together with its radius and relative refractive index. Let us assume the incident light is approximately a linearly polarized plane wave $\mathbf{E}_i(\mathbf{r}) = \exp(jk\mathbf{r}\cdot\hat{\mathbf{z}})\hat{\mathbf{x}}$, where the spatial vector position is denoted as $\mathbf{r}$, $\hat{\mathbf{z}}$ is the unit vector in the direction of beam propagation and $\hat{\mathbf{x}}$ is the unit vector in the direction of beam's polarization. The light field scattered by a dielectric sphere particle is $E_i\,\mathbf{f}(\mathbf{r}-\mathbf{r}_p, a, m)$, where $\mathbf{f}$ is an analytically known function of the spatial position relative to the particle's center $\mathbf{r}_p$, as well as of the particle's radius a and refractive index relative to the medium m. As reported by Bohren and Huffman (2010), such a function can be expressed as a infinite series of linear combinations of the vector spherical harmonics $\mathbf{N}_{e1n}$, $\mathbf{M}_{o1n}$:

$$\mathbf{f}(\mathbf{r}-\mathbf{r}_p, a, m) = \sum_{n=1}^{\infty} \frac{i^n(2n+1)}{n(n+1)}(i\alpha_n\mathbf{N}_{e1n} - \beta_n\mathbf{M}_{o1n}) \tag{3.1}$$

The vector spherical harmonics are calculated through the associate Legendre functions of the first kind, first order and degree n, whereas the spherical Bessel functions of the first and third kind compares in the expression of both the vector spherical harmonics and the coefficients α_n and β_n. As suggested by Wiscombe (1980), a good approximation of the scattered field is obtained when the series in Eq.(3.1) is truncated at $n_c = ka + 4.0(ka)^{1/3} + 2.0$, where k is the wavevector amplitude of the illuminating laser in the working medium. The resulting theoretical light intensity, normalized by $|\mathrm{E}_i|^2$, is

$$I_{th}(\mathbf{r}, \mathbf{r}_p, a, m) = 1 + 2\alpha\mathcal{R}\{\exp(jk\mathbf{r}\cdot\hat{\mathbf{z}})\hat{\mathbf{x}}\cdot\mathbf{f}(\mathbf{r}-\mathbf{r}_p, a, m)\} + \alpha^2 f(\mathbf{r}-\mathbf{r}_p, a, m)^2 \tag{3.2}$$

where the parameter α is used to adjust the scattering efficiency relative to the ideal case ($\alpha = 1$).

In practice, recorded holograms always suffer from a mainly multiplicative "background" noise due to scattering from unwanted objects inevitably found within the sample environment and in the whole optical path outside of the sample chamber. Such a background noise can be partially corrected by dividing the recorded hologram by a previously recorded empty field of view image. The resulting pattern provides the experimental normalized intensity I_{exp}. We fit the obtained holograms I_{exp} to I_{th} using a Levenberg-Marquardt nonlinear least-squares minimization algorithm with the five free parameters: $\mathbf{r}_p = (x_p, y_p, z_p)$, a and m. A considerable speed up in chi squared evaluations is achieved exploiting the computational power of a CUDA based graphic processing unit (nVidia GTX260). The computation of I_{th} is very expensive since it involves the evaluation of the aforementioned special functions which are expressed as recursive series and hence not suited for parallelization. However, special functions are evaluated as a function of radial distance only. To speed up the computation, we tabulate them once on a 1D array an then use linear interpolations. Our software can analyze 23 particle's hologram per second (i.e. real time analysis). When the radius and the relative refractive index are previously calibrated, we can reduce the fitting parameters with a speed up of 50% (i.e. 35 fps).

1.3 Primary sources of error: a detailed study of the precision and accuracy of the method

Even though DHT has demonstrated to be as an effective tool for high accuracy 3D particle tracking and sizing, before the work of Bolognesi et al. (2011) there was no detailed study about the precision and the accuracy of this technique. In this paragraph, we discuss the main sources of error that affect the result of the fit to the theoretical Mie hologram. Then, following the synthetic hologram based method, presented in Section 2.3 of Chapter 2, we test the three-dimensional particle tracking and sizing capabilities of the DHT in terms of precision and accuracy.

First of all, possible laser intensity variation during the elapsed time between the acquisition of the hologram to be analyzed and the background hologram can affect the quality of the fit. In order to account for those laser intensity variations, we introduce in the expression of the theoretical hologram I_{th} a multiplicative factor β which can be inferred by minimizing the whole error $\sum_i \chi_i^2$:

$$\beta = \frac{\sum_i I_{th}(x_i) I_{exp}(x_i)}{\sum_i I_{exp}(x_i)^2} \tag{3.3}$$

where the sum is performed over all pixels. However, small variations in the empty field of view hologram can occur over time and dividing by a previously recorded background could result in significant errors at the required levels of accuracy. For example, we report in Figure 3.1 a typical time correlation function $c(t)$ of recorded empty field background fluctuations:

$$c(t) = \frac{1}{N} \sum_i \left\langle \delta b_i(0) \delta b_i(t) \right\rangle \quad \text{with} \quad \delta b_i(t) = b_i(t) - \langle b_i \rangle \tag{3.4}$$

where $b_i(t)$ is the intensity on the i^{th} camera pixel normalized by the full array average, N is the total number of pixels and $\langle \cdot \rangle$ represents time averages. At the beginning, the correlation function suddenly decreases of about 20% due to the intrinsic sensor noise of the camera. Then a slower decay is observed on a few minutes time scale.

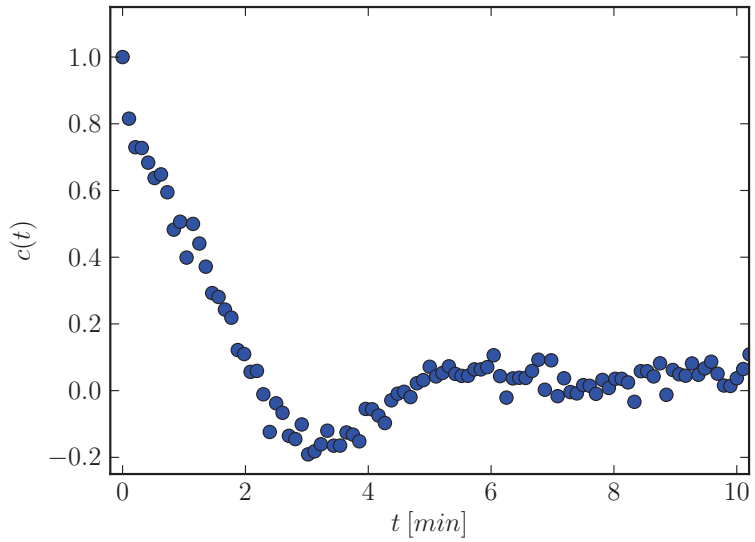

Figure 3.1: The correlation function $c(t)$ of background fluctuations is plotted as a function of time. It vanishes in approximately two minutes.

It is also worth noting that when approaching a precision level in the fitting parameters of about one percent other, usually negligible, imperfections in the actual hologram recording, such as camera distortions and discretization, may affect performance. For example, one would expect to find an α parameter that is smaller than the ideal value of 1 since Mie theory doesn't account for the effect of bead nanoscale roughness or absorption. On the contrary we noticed that a value greater than 1 by a few tens of percent is usually needed to get the best fit. This is an artifact due to distortions in the CMOS. In particular, we found that the response function of our camera is given by a straight line shifted by a constant offset:

$$I_g = IbT_s - c \tag{3.5}$$

where I is the light intensity on the camera, T_s is the exposure time, I_g is the pixel gray level and b and c are two positive parameters depending on the camera properties. Such parameters can be experimentally evaluated by imaging with different shutters a beam with fixed intensity. In our case we found a value for c of about 38 over a dynamic range of 255. Taking into account the camera's response and neglecting quadratic scattering terms, the recorded normalized intensity I_g will be:

$$I_g = 1 + 2\alpha'\mathcal{R}\{\exp(jk\mathbf{r}\cdot\hat{\mathbf{z}})\hat{\mathbf{x}}\cdot\mathbf{f}\} \qquad \text{where} \quad \alpha' = \frac{\alpha|E_i|^2}{|E_i|^2 - b} \tag{3.6}$$

which explains why the measured value of α' is larger than the true α. If recorded images are correctly linearized, we always obtain α values smaller than one.

Previously reported precisions of DHT by Lee et al. (2007), Cheong et al. (2009a) and Cheong et al. (2010) are of few nanometers for the Cartesian coordinates (x, y and z), and a one part per thousand error for the particle radius a and relative refractive index m. Although precision can be easily measured experimentally, accuracy is less easily accessible due to the lack of an independent, high resolution, determination of bead size, and refractive index. Regarding probe position, one could think of tracking a nanopositioned bead to get a direct estimate of accuracies. Unfortunately, accurate nanopositioning is usually achieved by having a bead that is stuck

Accuracies	A	B	C
$x, y\ [nm]$	0.09	1.9	6.0
$z\ [nm]$	0.7	13	23
$a\ [nm]$	0.2	2.7	2.2
$m\ [\%]$	0.002	0.04	0.04

Precisions	B	C
$x, y\ [nm]$	1.7	1.7
$z\ [nm]$	8.5	8.2
$a\ [nm]$	2.0	2.1
$m\ [\%]$	0.04	0.03

Table 3.1: Estimated accuracies and precisions of position, radius and relative refractive index measurements. A: no background noise, B: correlated background fluctuations, C: uncorrelated background fluctuations.

on a fixed support, like a cover slip, rigidly connected to a piezo-stage. However DHT heavily relies on the assumption of a spherical and homogeneous bead that is embedded in an optically homogeneous medium. The presence of a nearby glass surface would produce a hologram that wouldn't agree with Mie theory. For this reason we now proceed to evaluate accuracy and precision using synthetic "experimental" holograms obtained as follows:

1. Compute a set of theoretical normalized intensities I_{th} of a Brownian moving particle.
2. Record a time series of true background holograms I_{bg} with an empty field of view.
3. Obtain time series of synthetic noisy Mie interference patterns $I_{sim} = I_{th} I_{bg}$.
4. Emulate the camera discretization to 256 gray levels.

We can now fit our synthetic dataset made of 4000 simulated holograms based on about a 8 minute long time series of experimental backgrounds, which we also used to work out the correlation function $c(t)$ shown in Figure 3.1. Resulting accuracies, shown in Table 3.1, are computed as the standard deviation of the absolute errors. We performed this calculation for three different cases in order to discriminate between different sources of error.

Case A: We skip steps ii) and iii) imposing $I_{sim} = I_{th}$ so that the fitted interference pattern is noiseless but discretized to 256 levels. This case shows that the camera discretization is sufficient to set the accuracy limit to values that (except for m) are much higher than the floating point precision which is expected for a noiseless image.
Case B: We compute the normalized holograms dividing I_{sim} by a background recorded few seconds earlier. This means that the background image is still very correlated and thus we obtain a low noise normalized hologram. That case gives an estimate of the best accuracy we can achieve in a real experiment.
Case C: We compute the normalized holograms dividing I_{sim} by a background recorded eight minutes earlier. In that case the background is already in the low correlated regime (see Figure 3.1).

In order to estimate the precision of the system, we repeated the same procedure starting off the same theoretical Mie pattern (ideally fixed bead). The standard deviations of fitted parameters are reported in Table 3.1, where we skipped the case (a), since it's meaningless.

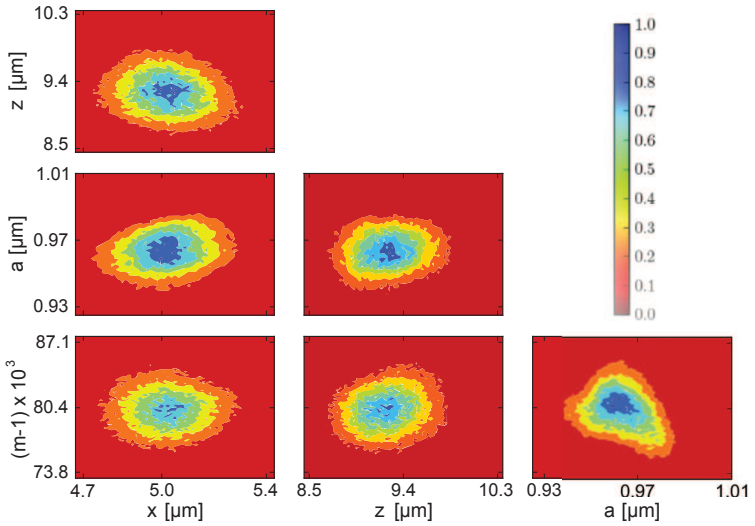

Figure 3.2: Mutual dependences between the adjustable parameters. Tracking the free Brownian motion of a single 2.07 μm diameter silica bead over 2000 frames, the contour plot of the normalized two-dimensional histograms of the measured parameters' pairs are shown. Only the most significant parameters' pairs are considered. A significant mutual dependence appears only for the couple radius/relative refractive index, where a slight anti-correlation is observed.

Furthermore, we also checked if there are any significant correlations between the adjustable parameters while tracking the Brownian motion of single actual 2.07 μm diameter silica bead. As shown in Figure 3.2, no significant mutual dependence between parameters appears, except for the radius and the relative refractive index for which a weak anti-correlation is observed (the slope of the regression line is $-0.07\,\mu m^{-1}$).

The above analysis shows that tracking performance is mainly deteriorated by the background noise. As it has been proposed by Dubois et al. (1999), a partially coherent source helps reducing the artifacts that are visible when using a fully coherent illumination. In addition, carefully cleaning sample and optics can also substantially reduce background inhomogeneities.

2 Multipoint viscosity measurements

2.1 Introduction

As discussed in Chapter 1, holographic tweezers allow a full 3D, dynamic and contactless micromanipulation of samples in micro environments. A straightforward application of that in lab on chip technology is the use of trapped beads as a multipoint sensor of physical/chemical properties of surrounding fluid, as demonstrated in several works by Di Leonardo et al. (2006), Mushfique et al. (2008), Valentine et al. (1996), Pesce et al. (2005), Buosciolo et al. (2004), Bishop et al. (2004), Yao et al. (2009), andKlauke et al. (2006). There are many different situations in physics and biology where monitoring fluid properties such as viscosity at many positions simul-

taneously can be of extreme importance, see Weihs et al. (2006). For instance, cell environments can be highly inhomogeneous in time and space due to time varying concentration gradients of macromolecules around cell membranes.

The basic principle of a holographic multipoint sensors is that a suspended object will experience forces that depend on fluid properties such as viscosity and temperature. The analysis of resulting trajectories can be then used to extract local fluid properties. The accuracy of such light driven sensors relies clearly on the available spatial and temporal resolutions of tracking probe particles. However particle shape and size will also play a role and assuming a perfect, monodisperse nominal radius can introduce an important source of error when comparing data from different probes. An ideal tracking tool should then provide a high spatial and temporal resolution combined with simultaneous accurate particle sizing capabilities. As demonstrated by Lee and Grier (2007), DHT can provide those requirements and we now show that it allows multipoint viscosity measurement with a superior accuracy to other proposed tracking schemes. Although higher spatial and temporal resolutions can be achieved using quadrant photodiodes in back focal plane interferometry, see Pesce et al. (2005), Buosciolo et al. (2004), Allersma et al. (1998), Fischer and Berg-Sørensen (2007), Atakhorrami et al. (2006) and Meiners and Quake (1999), they require additional accurate calibration and result cumbersome when tracking more than two particles. Multi particle tracking is usually performed using video microscopy at the cost of a worse spatial and temporal resolution. Both back focal plane tracking and video microscopy give no direct information on particle's size. Bead sizing is only available after a delicate calibration procedure that requires moving the probe at different distances from a fixed wall and then fitting the corresponding mobility values to Faxén formulas, as reported by Keen et al. (2009) and Schäffer et al. (2007). Moreover, such a procedure relies on the assumption of a homogeneous viscosity which prevents accurate multipoint viscosity measurements in inhomogeneous media. On the other hand, DHM provides an all-optical size determination which can be obtained from one single snapshot and results in an even better accuracy. In addition, as shown by Schnars and Jüptner (1994), axial tracking is available over a much larger range. As a demonstration of the peculiar features of DHT, we use a system of four probe beads in blinking holographic tweezers, see Crocker (1997), as a multipoint viscosity sensor. When the particle sizing capabilities of DHT are exploited, accuracy and precision of viscosity measurements are improved by a factor of at least four when compared to other techniques relying on position tracking alone.

2.2 Simultaneous viscosity measurement of a water sample in four different points

Keen et al. (2009) have shown that, using holographic optical tweezers, multiple beads can be trapped in target points to map viscosity. However, the behaviour of a bead inside a fluid is significantly influenced by its dimensions and by hydrodynamic interactions with other bodies. For example, due to the short working distance of high numerical aperture objectives, we usually observe particles that are a few tens of micrometers distant from the cover slip wall. In such a case, the diffusivity D of a spherical bead due to Brownian motion is dependent on the radius a and on the distance h from the wall according to Faxén correction formulas, see Faxén (1922),

Happel and Brenner (1991) and Leach et al. (2009):

$$D = \frac{k_B T}{6\pi\eta a}\left(1 - \frac{9}{16}\left(\frac{a}{h}\right) + O\left(\frac{a^3}{h^3}\right)\right) \tag{3.7}$$

We can use for example the measured value of D to get viscosity if we know particle size a and height h. A relative error on a will produce a relative error on η of $\delta a/a$, while an uncertainty on h contributes a relative error on η of about $(9/16)(a/h)(\delta h/h)$. For instance, for a 1 μm radius bead floating at about 10 μm from a solid wall, if we are interested in getting a viscosity value with a one percent accuracy then we should know particle height within 1 μm and particle size within 10 nm (1%). Highly uniform microspheres are commercially available with a typical size variation that is at best about 5%, therefore much bigger than what DHT can provide. Therefore, as already stated by Buosciolo et al. (2004) and Keen et al. (2009), bead radius uncertainty is a major source of systematic error on tweezers based viscosity measurements.

As a demonstration of DHT capabilities for multipoint viscosity measurements, we test our technique in an homogeneous medium (distilled water) whose rheology properties are well known, and evaluate the agreement of the local measured viscosities to the expected value. Using the experimental apparatus described in Section 1.2 of Chapter 2, we holographically trap four 2.07 μm silica beads (Bangs Laboratories Inc.). We place them on the vertices of a 8 μm$\times$8 μm square that lies on a plane parallel to the objective focal plane and ten microns above the cover slip wall. Using a chopper, located between the lenses L3 and L4 (see Figure 2.3), we periodically release the probes from the traps and record their free Brownian motion for 62.5 ms, before traps are switched on again and particles are reset to the same starting positions. Acquisition frame rate is set to 160 Hz and 8 frames per release are processed. Particles displacements in the z directions were 260 nm at most. Therefore we can safely neglect any variation of Faxén correction. Working with freely diffusing tracers has the advantage that hydrodynamic interactions on single particle diffusivities can be easily neglected. In particular, Crocker (1997) experimentally verified that, due to hydrodynamic interaction with neighboring beads, single particle diffusivities are only affected by a correction which is at most of order $(a/r)^4$, with a particle radius and r interparticle distance. In our geometry (where $r/a \sim 8$) that hydrodynamic correction is only expected to affect diffusivities, and hence viscosities, on the level of a few part over a thousand (namely, 8^{-4}). Another advantage of blinking tweezers for viscosity measurement is that data acquisition is only performed in the absence of laser light. Even in the presence of a small local heating due to trapping beams, that will diffuse away in a few microseconds once trapping light is switched off.

The measured mean square displacement (MSD) in the x coordinate is fitted by:

$$\langle \big(x(t) - x(0)\big)^2 \rangle = 2D_x t - \frac{2}{3} D_x T_s \tag{3.8}$$

where $\langle\cdot\rangle$ represents averaging over both time origin and the ensemble of recorded trajectories. The second term is an effect due to the finite exposure time T_s of the camera (2.5 ms in the present case) that affects the measure of the MSD, as extensively discussed by Savin and Doyle (2005). Measured MSDs and their best fit to Eq.(3.8) are shown in Figure 3.3. In Figure 3.4 a recorded hologram and its corresponding best fit are compared. Black circles are the normalized radial

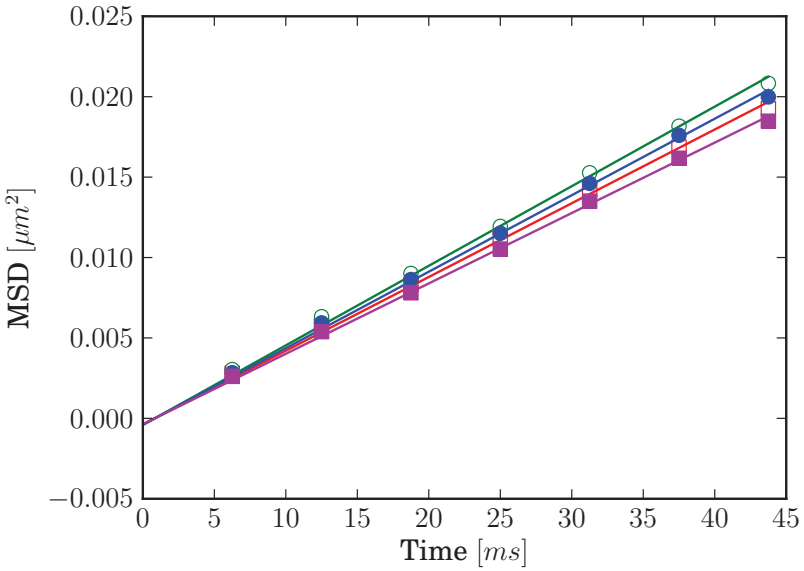

Figure 3.3: Mean square displacements of all particles along the x direction averaged over 10000 trajectories. Experimental data (squares and circles) are fitted to Eq.(3.8) (solid lines). The size of error bars is smaller than symbols size.

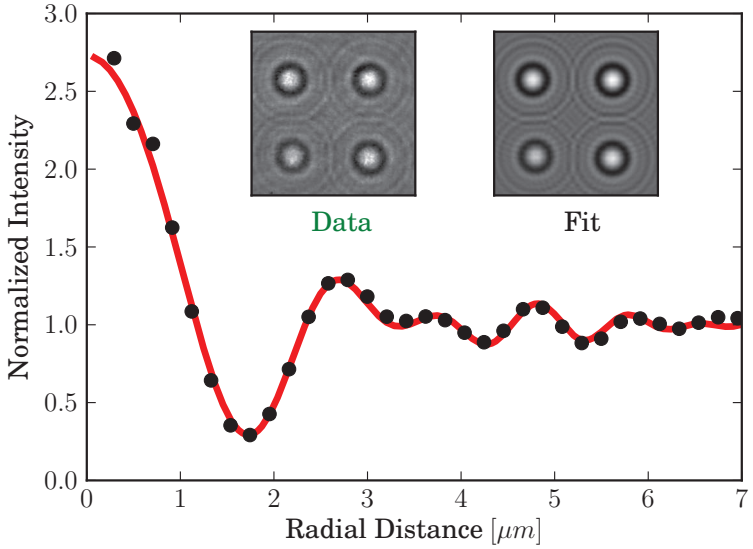

Figure 3.4: Experimental (solid circles) and best fit (solid line) normalized radial intensities. Experimental and theoretical holograms are shown as insets.

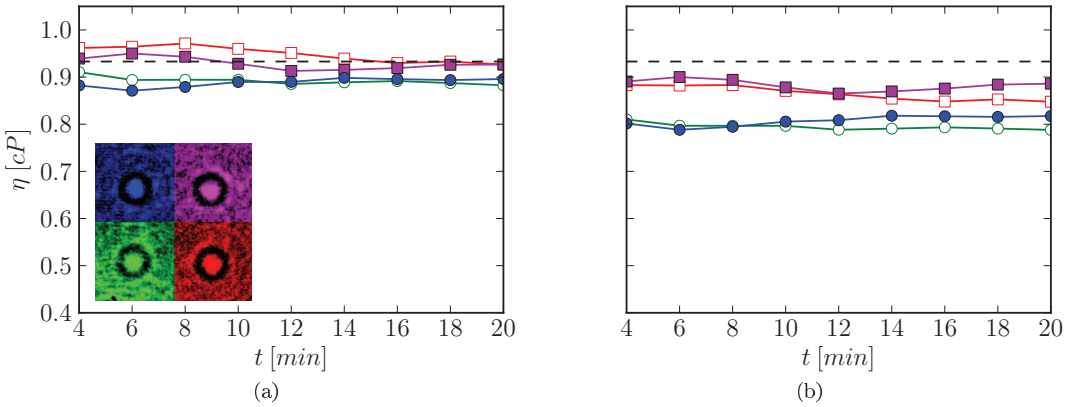

Figure 3.5: Viscosity measured at the vertices of a $8\mu m \times 8\mu m$ square tracking for a time t the free Brownian motion of four $2.07\mu m$ diameter silica beads (shown in inset). In plot (a), viscosity is inferred using the measured radii of particles, while in plot (b) the nominal radius is adopted. The dotted line shows the predicted viscosity for water at $23° C$. Both accuracy and precision of viscosity measurement improve when the radius of the tracked probes can be measured.

Particles	1	2	3	4
Radius $[\mu m]$	0.961 ± 0.006	0.997 ± 0.012	0.979 ± 0.008	0.940 ± 0.007
Rel. Refr. Index	1.081 ± 0.001	1.075 ± 0.001	1.072 ± 0.001	1.074 ± 0.001
Viscosity [cP]	0.90 ± 0.024	0.93 ± 0.025	0.93 ± 0.025	0.88 ± 0.024

Table 3.2: Radius, relative refractive index and measured viscosity for the four particles. Brownian motion is averaged over 80000 frames. Water viscosity at room $T = 23°$ C is 0.93 cP.

intensities showing an excellent agreement to the theoretical best fit reported as a solid line.

The viscosity measurements for the four particles are plotted in Figure 3.5 as a function of the time interval over which the MSDs are averaged. Left and right panels refer respectively to viscosity determinations using measured or nominal probe radius, that is $1.04 \pm 0.10 \mu$m. It is evident that assuming a uniform probe size results in artificial local viscosity inhomogeneities which are much reduced when the single probe sizing capabilities of DHT are exploited. Moreover, we found that probes radii are systematically smaller than the nominal one (see Table 3.2), so that even when averaging over different probes the measured viscosity will always be affected by a systematic error. The mean accuracy on viscosity is 2.7%, that is about four times better than the mean accuracy (10.5%) resulting from assuming in Eq.(3.7) the nominal values for the beads' radii instead of the measured ones. Such an accuracy of about 10% is comparable with that one obtained in former viscosity measurements performed with HOTs by Keen et al. (2009) and back focal plane interferometry by Pesce et al. (2005) and Buosciolo et al. (2004). Another advantage of DHT is that any probe contamination, such as small particles stuck to the probes, can be easily spotted when the bead hologram doesn't match the theoretical scattering pattern of a perfect Mie sphere. Hence, low accurate viscosity measurements obtained from those probes can be rejected.

When comparing position accuracies, back focal plane interferometry provides better performances allowing for subnanometer accuracies while in our implemen-

tation of DHT the estimated accuracy is limited by background noise to a few nanometers. However, when one is interested in measuring viscosity through diffusion coefficients, the required accuracy on position tracking has to be small when compared to the largest root mean squared displacement. For example in our case Brownian motion is tracked up to a root mean squared displacement of about 140 nm (see Figure 3.3). In those conditions a tracking accuracy of even 10 nm would be enough for 1% viscosity determinations, always provided one has simultaneous access to precise particle size. A low background noise is essential to get the higher tracking accuracy that is necessary when, relying on the ever increasing CMOS frame rates, fast viscosity changes have to be detected.

2.3 Conclusions

Simultaneously measuring the local viscosity in four different points of the water sample volume, we have demonstrated as DHT provides an ideal tool for multipoint sensing with holographic tweezers, allowing at the same time precise and individual probe sizing. Estimated tracking accuracy is better than standard video microscopy but still worse than the subnanometer capability of back focal plane interferometry. Nevertheless, DHT allows to track multiple probes over a much higher axial range while probe size is readily available together with position and relative refractive index from fitting of a single snapshot. This is in contrast to other tracking techniques, where probe size is not directly available but has to be deduced from multiple acquisitions taken at different distances from a fixed wall. Using the reliable probe sizes, provided by the DHT technique, we achieved a mean viscosity accuracy of 2.7% that is four times smaller than what is obtained using nominal bead size.

3 Characterization of lipidic microbubbles

3.1 Measurements of bubble radius and shell thickness: a preliminary study

In this last section, we describe the preliminary results of the application of DHT to characterize the physical properties of lipidic bubbles. Particularly, we analyzed a sample of air-filled poly(vynil-alcohol) (PVA)-based microbubbles, prepared according to the procedure described by Paradossi et al. (2002). In the last years, gas-filled microbubbles have attracted the attention of many researchers because of their potential applications as drag delivery systems and ultrasound contrast agents. Due to their lower density and their ability to carry therapeutic gases, the lipidic walls play a fundamental role and, thus, their properties have been reportedly investigated. A confocal laser scanning microscope was used by Cavalieri et al. (2005) to characterize the poly(vynil-alcohol) (PVA)-based microbubble radius as well as the shell thickness. Higher resolution radius and thickness measurements together with an estimate of the lipidic wall density were then reported by Fernandes et al. (2008) via scanning transmission X-ray microscopy analysis.

We are now investigating the possibility to perform the same measurements via DHT analysis, that could give access to the same information of the cited studies but with a simpler, cheaper and faster technique. Those microbubbles can be modeled as a core-shell structure, made of two homogeneous materials (namely, the gas and the lipidic wall) with different refractive indices. The Lorenz-Mie scattering theory can be slightly modified to account for such an additional homogeneous shell structure

by simply replacing the expressions of the coefficients α_n, β_n of Eq.(3.1), see Bohren and Huffman (2010). In such a scheme, two additional fitting parameters have to be considered: the shell thickness and its relative refractive index.

Previous analysis of core-shell structures via DHT were reported by Cheong et al. (2009a). Relying on the classical Mie model of a homogeneous dielectric sphere, the authors detected the presence of a avidin molecular layer binded to biotinylated polystyrene spheres by comparing the measured averaged radius and refractive index to those of plain polystyrene spheres. However, in that case no layer thickness measurement was available. On the contrary, Van Oostrum (2011) took into account the scattering contribution of both the core and the shell structures to measure the shell thickness of 1 μm diameter silica coated polystyrene beads. The nominal value of the silica coating thickness was 82 nm. The authors concluded that, since those beads were too small and the difference between the refractive indices of those materials were too weak, the particle scattering has not enough specific features to characterize simultaneously the radius, the thickness and the two refractive indices.

Using the experimental apparatus, described in Section 1.2 of Chapter 2, we recorded the holograms produced by microbubbles freely moving in a sample of distilled water. Figure 3.6 and Figure 3.7 show the recorded holograms and the corresponding fits for four different bubbles at several distances from the focal plane. The values of the fitting parameters are reported in the plots where the azimuthally averaged normalized intensity of the experimental holograms and the theoretical ones are compared. As opposed to the case of 1 μm diameter silica coated polystyrene spheres, the *scattering fingerprint* of those bubbles is quite specific and leads to a reliable measurement of the external bubble radius, the shell thickness and the two relative refractive indices. The measured values are in good agreements with the results obtained through the confocal and X-ray microscope techniques by Cavalieri et al. (2005) and Fernandes et al. (2008). However, to gain a better insight in the capabilities of this novel technique for microbubble characterization and to determine its stability, resolution and accuracy, we are currently working to extent the presented analysis to a higher number of bubbles that have also undergone to different fabrication and storage processes.

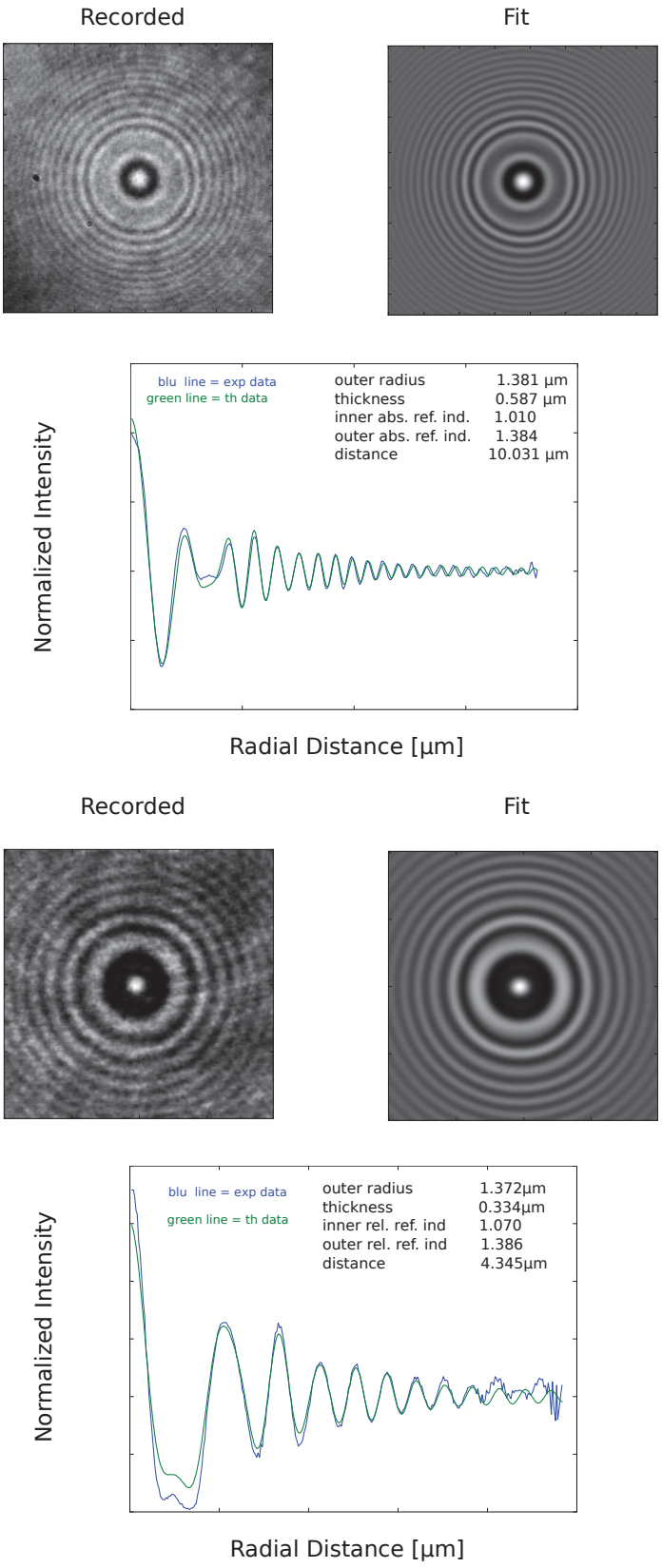

Figure 3.6: In the top panel, the recorded hologram (on the left) of an air-filled poly(vynil-alcohol) (PVA)-based microbubble and the corresponding fitting hologram (on the right) generated by a coated spherical bead. In the bottom panel, azimuthally averaged normalized intensity of the experimental (blue solid line) and the theoretical (green solid line) holograms are compared.

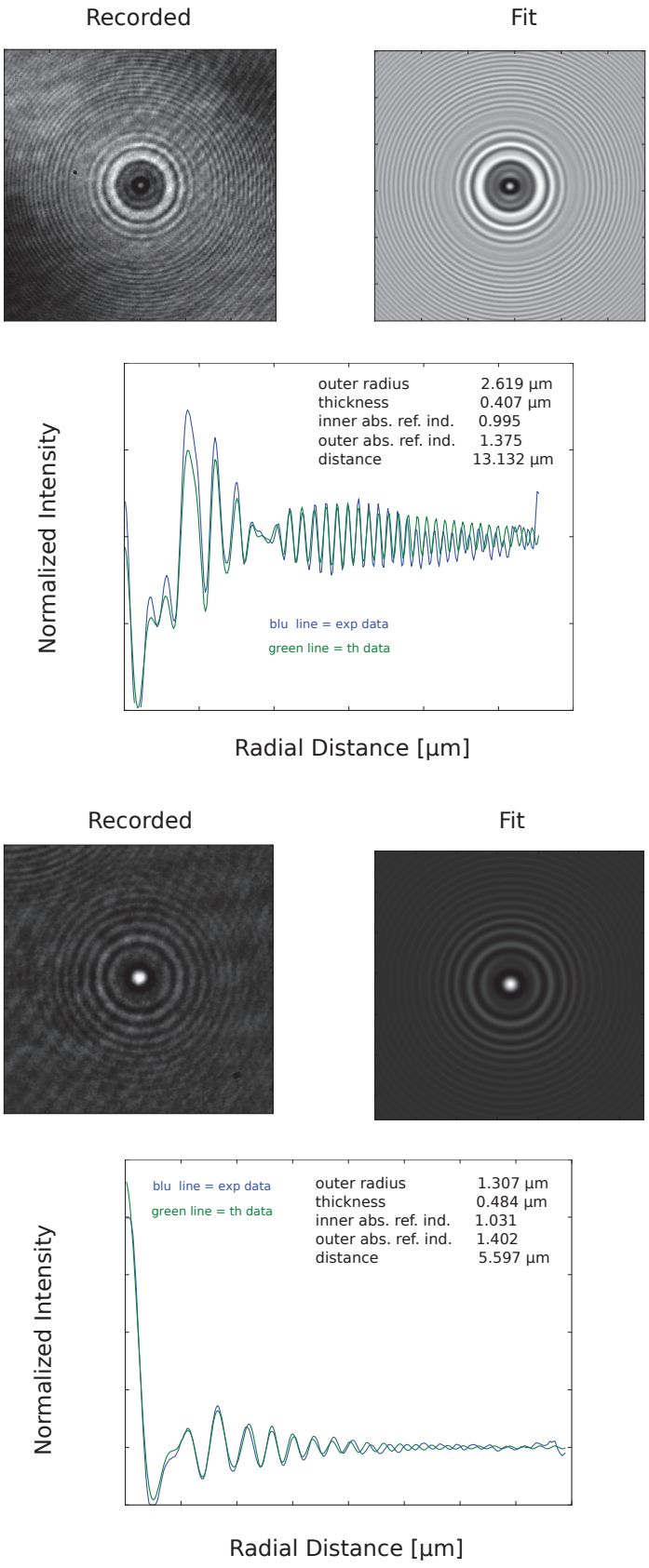

Figure 3.7: In the top panel, the recorded hologram (on the left) of an air-filled poly(vynil-alcohol) (PVA)-based microbubble and the corresponding fitting hologram (on the right) generated by a coated spherical bead. In the bottom panel, azimuthally averaged normalized intensity of the experimental (blue solid line) and the theoretical (green solid line) holograms are compared.

References

Atakhorrami, M., Sulkowska, J., Addas, K., Koenderink, G., Tang, J., Levine, A., MacKintosh, F., and Schmidt, C. (2006). Correlated fluctuations of microparticles in viscoelastic solutions: quantitative measurement of material properties by microrheology in the presence of optical traps. *Physical Review E*, 73(6):61501.

Bishop, A., Nieminen, T., Heckenberg, N., and Rubinsztein-Dunlop, H. (2004). Optical microrheology using rotating laser-trapped particles. *Physical review letters*, 92(19):198104.

Bohren, C. and Huffman, D. (2010). Absorption and Scattering of Light by Small Particles (Wiley, 1983).

Bolognesi, G., Bianchi, S., and Di Leonardo, R. (2011). Digital holographic tracking of microprobes for multipoint viscosity measurements. *Optics Express*, 19(20):19245–19254.

Buosciolo, A., Pesce, G., and Sasso, A. (2004). New calibration method for position detector for simultaneous measurements of force constants and local viscosity in optical tweezers. *Optics Communications*, 230(4-6):357–368.

Cavalieri, F., El Hamassi, A., Chiessi, E., and Paradossi, G. (2005). Stable polymeric microballoons as multifunctional device for biomedical uses: Synthesis and characterization. *Langmuir*, 21(19):8758–8764.

Cheong, F., Krishnatreya, B., and Grier, D. (2010). Strategies for three-dimensional particle tracking with holographic video microscopy. *Optics Express*, 18(13):13563–13573.

Cheong, F., Sun, B., Dreyfus, R., Amato-Grill, J., Xiao, K., Dixon, L., and Grier, D. (2009a). Flow visualization and flow cytometry with holographic video microscopy. *Opt. Express*, 17(15):13071–13079.

Cheong, F., Xiao, K., and Grier, D. (2009b). Technical note: Characterizing individual milk fat globules with holographic video microscopy. *J. Dairy Sci*, 92(1):95–99.

Crocker, J. (1997). Measurement of the hydrodynamic corrections to the Brownian motion of two colloidal spheres. *Journal of Chemical Physics*, 106(7):2837–2840.

Di Leonardo, R., Leach, J., Mushfique, H., Cooper, J., Ruocco, G., and Padgett, M. (2006). Multipoint holographic optical velocimetry in microfluidic systems. *Physical review letters*, 96(13):134502.

Dubois, F., Joannes, L., and Legros, J. (1999). Improved three-dimensional imaging with a digital holography microscope with a source of partial spatial coherence. *Applied optics*, 38(34):7085–7094.

Faxén, H. (1922). Der Widerstand gegen die Bewegung einer starren Kugel in einer zhen Flssigkeit, die zwischen zwei parallelen ebenen Wnden eingeschlossen ist. *Annalen der Physik*, 373(10):89–119.

Fernandes, P., Tzvetkov, G., Fink, R., Paradossi, G., and Fery, A. (2008). Quantitative analysis of scanning transmission x-ray microscopy images of gas-filled pva-based microballoons. *Langmuir*, 24(23):13677–13682.

Fischer, M. and Berg-Sørensen, K. (2007). Calibration of trapping force and response function of optical tweezers in viscoelastic media. *Journal of Optics A: Pure and Applied Optics*, 9:S239.

Happel, J. and Brenner, H. (1991). *Low Reynolds number hydrodynamics: with special applications to particulate media*. Kluwer Academic Print on Demand.

Keen, S., Yao, A., Leach, J., Di Leonardo, R., Saunter, C., Love, G., Cooper, J., and Padgett, M. (2009). Multipoint viscosity measurements in microfluidic channels using optical tweezers. *Lab on a Chip*, 9(14):2059.

Klauke, N., Monaghan, P., Sinclair, G., Padgett, M., and Cooper, J. (2006). Characterisation of spatial and temporal changes in ph gradients in microfluidic channels using optically trapped fluorescent sensors. *Lab Chip*, 6(6):788–793.

Leach, J., Mushfique, H., Keen, S., Di Leonardo, R., Ruocco, G., Cooper, J., and Padgett, M. (2009). Comparison of Faxéns correction for a microsphere translating or rotating near a surface. *Physical Review E*, 79(2):26301.

Lee, S. and Grier, D. (2007). Holographic microscopy of holographically trapped three-dimensional structures. *Optics Express*, 15(4):1505–1512.

Lee, S., Roichman, Y., Yi, G., Kim, S., Yang, S., Van Blaaderen, A., Van On the contrary, Oostrum, P., and Grier, D. (2007). Characterizing and tracking single colloidal particles with video holographic microscopy. *Optics Express*, 15(26):18275–18282.

Mushfique, H., Leach, J., Yin, H., Leonardo, R., Padgett, M., and Cooper, J. (2008). 3D mapping of microfluidic flow in laboratory-on-a-chip structures using optical tweezers. *Analytical chemistry*, 80(11):4237–4240.

Paradossi, G., Cavalieri, F., Chiessi, E., Ponassi, V., and Martorana, V. (2002). Tailoring of physical and chemical properties of macro-and microhydrogels based on telechelic pva. *Biomacromolecules*, 3(6):1255–1262.

Pesce, G., Sasso, A., and Fusco, S. (2005). Viscosity measurements on micron-size scale using optical tweezers. *Review of Scientific Instruments*, 76:115105.

Savin, T. and Doyle, P. (2005). Role of a finite exposure time on measuring an elastic modulus using microrheology. *Physical Review E*, 71(4):41106.

Schäffer, E., Nørrelykke, S., and Howard, J. (2007). Surface forces and drag coefficients of microspheres near a plane surface measured with optical tweezers. *Langmuir*, 23(7):3654–3665.

Schnars, U. and Jüptner, W. (1994). Direct recording of holograms by a CCD target and numerical reconstruction. *Applied Optics*, 33(2):179–181.

Valentine, M., Dewalt, L., and Ou-Yang, H. (1996). Forces on a colloidal particle in a polymer solution: a study using optical tweezers. *Journal of Physics: Condensed Matter*, 8:9477.

Van Oostrum, P. (2011). *Using Light Scattering to Track, Characterize and Manipulate Colloids*. PhD thesis, Universiteit Utrecht.

Weihs, D., Mason, T., and Teitell, M. (2006). Bio-microrheology: a frontier in microrheology. *Biophysical journal*, 91(11):4296–4305.

Wiscombe, W. (1980). Improved mie scattering algorithms. *Applied optics*, 19(9):1505–1509.

Xiao, K. and Grier, D. G. (2010). Multidimensional Optical Fractionation of Colloidal Particles with Holographic Verification. *Physical review letters*, 104(2):028302.

Yao, A., Tassieri, M., Padgett, M., and Cooper, J. (2009). Microrheology with optical tweezers. *Lab on a Chip*, 9(17):2568–2575.

Part II

Superhydrophobic surfaces

Chapter 4

Direct flow measurements on superhydrophobic surfaces

In the lab-on-a-chip technology, one of the most important issue is the very high hydrodynamic resistance the liquid experiences as it flows in a network of micrometric channels. The high surface to volume ratio of those microfluidic chips and the sticky boundary condition at the liquid/solid interface, that is still valid at the micrometer length scale, result in high pressure drops that often impose the lab-on-a-chip to be connected to compressors and pumping systems thousands of times bigger than the chip itself. In this respect, superhydrophobic surfaces have been demonstrated as an effective tool to relax the constraint of no-moving liquid at the channel walls, thereby promoting pressure drop reductions of tens of percents, compared to a plain surface.

In the first part of the Chapter, we introduce the working principle of the superhydrophobic surfaces, namely the Lotus effect (Section 1.1). Then, we give an overview of the most important applications of those surfaces for microfluidics, followed by the research outlook and perspectives in this field (Section 1.2). Finally, in Section 1.3 we report the most recent experiments where those surfaces have provided significant interface friction reduction for laminar flows in micrometric channels. The second part of the Chapter is dedicated to the description of the direct flow measurements conducted on a silicon microgrooved superhydrophobic surface by micro particle image velocimetry. After describing the experimental apparatus (Section 2.2), we present the procedure to fabricate the microchannels equipped with the superhydrophobic surface (Section 2.3). In Section 2.4, we discuss the acquisition and analysis of the particle image velocimetry images, that provide us with the velocity field throughout the scanned sample volume. By fitting to a one-dimensional laminar flow between a sticky and a slippery surface, we work out the global effective slip length (Section 2.5). Finally, we compare it to the theoretical predictions, that overestimate the friction reduction, and we investigate the causes of such a discrepancy (Section 2.6).

1 Superhydrophobic surfaces

1.1 The Lotus effect

Everyone knows by common experience of everyday life the different behaviours a liquid water drop undergoes when it's put in contact with a solid surface. The liquid can either totally spread on the surface, as for the rainwater hitting the buildings' and roads' concrete, or it can only partially wet the solid interface, having the shape of a spherical end cup, as it occurs when the rainwater touches our umbrella. Those distinct behaviours depend on the wetting properties of the liquid/solid system and the configuration, corresponding to the low total free energy, is the one preferred by the liquid drop. The angle formed by the liquid/air meniscus and the solid interface, called *contact angle*, macroscopically characterizes the wettability of the system. In fact, balancing the surface tensions at the triple contact line, the contact angle θ can be related to the surface energies at the three interfaces: solid/air (γ_{sa}), solid/water (γ_{sw}) and water/air (γ_{wa}) via the Young's relation:

$$\gamma_{sa} = \gamma_{sw} + \gamma_{wa} \cos\theta \tag{4.1}$$

When the water completely wets the interface or partially wets it with a contact angle less than 90°, the solid surface is hydrophylic. On the other hand, if the drop shape is bigger than half of a sphere (namely, the contact angle exceeds 90°), the surface is hydrophobic. As the contact angle passes the limit of 150°, the surfaces is usually referred to as a *superhydrophobic* surface (SHS). These three cases are summarized in Figure 4.1.

The first experimental observations of contact angles higher than 150° trace back at the beginning of the 20th century, where contact angles of about 160° and 180° have been reported by Ollivier (1907) and Coghill and Anderson (1923), respectively. During that century, the topic of superhydrophobicity received limited attention by the scientific community, until when in the 1990s the working principle of the so-called *Lotus effect* was explained by Neinhuis and Barthlott (1997). The remarkable property of the Lotus leaves is the self-cleaning ability. As a water drop falls on the leaf surface, it easily rolls down and take away all the dust particles that cross its way. The micrometer-sized protrusions on the leaf, covered in hydrophobic wax crystalloids, promote the superhydrophobicity of the surface as well as the instability of water drop, whose contact line cannot be pinned on the leaf surface and, hence, it easily moves because of gravity. As a dust particle comes in contact with the rolling

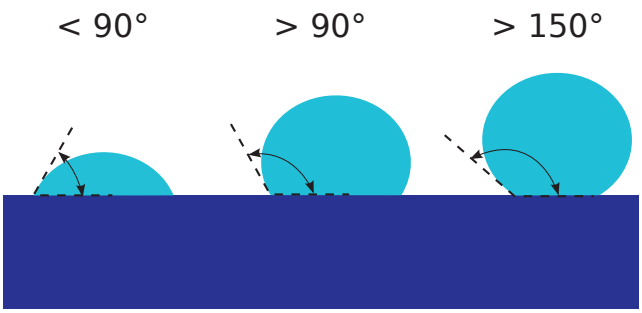

Figure 4.1: Contact angles (CA) of liquid drops on a flat solid surface for three different cases: hydrophilic surface (CA< 90°), hydrophobic surface (CA> 90°), superhydrophobic surface (CA> 150°).

Figure 4.2: Schematic representation of the Wenzel state: water filling the roughness cavities, and the Cassie state: air bubbles trapped inside the cavities.

water drop, it is trapped at the liquid/air interface because of the capillarity forces. Consequently, the Lotus leaf always appears very well clean and dust-free.

However, theoretical models, that justifies the superhydrophobic effect as a combination of suitable surface roughness and low-surface-energy materials, have already been introduced more than half a century before. Wenzel (1936) proposed that the liquid at the superhydrophobic interface fills in completely the roughness surface profile. The variation in the contact angle of a rough surface with respect to a perfectly smooth one is ascribed to the larger solid/liquid interface. According to the Wenzel model, the contact angle θ_W is given by

$$\cos\theta_W = r\cos\theta \ , \tag{4.2}$$

where r is the ratio of the actually wetted area to the projected area of the surface and θ is the contact angle on the smooth surface having the same surface composition. Even though high contact angles can be achieved in the Wenzel state, the contact angle hysteresis is quite large, since the contact line is pinned along the peaks and the protrusions of the roughness profile. As opposite to the Wenzel model, Cassie and Baxter (1944) considered the effects of air bubbles trapped within the pores and cavities of the roughness and they assumed that the liquid is in contact with the solid only at the peaks of the roughness. The resulting contact angle θ_C is

$$\cos\theta_C = -1 + \phi_s(1+\cos\theta) \tag{4.3}$$

where ϕ_s is the solid fraction of the interface, i.e. the ratio of solid-liquid area to whole droplet base. In this scenario, the air/liquid interface also reduces the contact angle hysteresis, since the contact line can be pinned along the solid fraction only. Consequently, the truly superhydrophobic state is the Cassie state. Moreover, as the liquid flows past the surface, the air bubbles reduce the total hydrodynamic resistance since a no-shear boundary condition holds where the liquid is in contact with the air pockets. This friction reduction is quantified by the effective slip length b, defined by assuming the average slip velocity v_s at the superhydrophobic interface proportional to the average shear stress τ:

$$v_s = \frac{b}{\eta}\tau \tag{4.4}$$

where η is the fluid viscosity. For rough hydrophobic surfaces, the onset of the Cassie state or the Wenzel state depends on the surface wettability, the static pressure in the water as well as in the air pockets and the geometry of the surface features. The transition from the Cassie state to the Wenzel state is one of the most important limitation of the superhydrophobic surface and it has been recently tackled by

Lee and Kim (2011), who proposed a surface structure allowing the restoration of a gas pocket from a wetted state and introduced a self-controlled gas generation mechanism to keep the Cassie state even under high liquid pressure.

In the last two decades, the research on SHSs has developed exploiting the working principle and the structures of the natural SHSs, available in the plant and animal worlds, in order to fabricate artificial synthetic ones. Some important examples in this field are provided by Mock et al. (2005), Otten and Herminghaus (2004), Gao and Jiang (2004) and Parker and Lawrence (2001). The interested reader can find in Li et al. (2007) a detailed review of the several processes reported in literature to fabricate those surfaces. At the same time, several numerical and experimental studies have been conducted on those artificial SHSs and compared to the theoretical predictions of the Cassie and Wenzel models. The large amount of papers recently published on this topics is highly motivated by the potential functional applications of these surfaces in different realms. In the next section we report the most important ones for microfluidics and lab-on-a-chip technology. A review on SHSs is beyond the scope of this work and for more details we refer the reader to the work of Rothstein (2010).

1.2 SHSs: microfluidic applications and perspectives

The drag reduction capability of the SHS is one of the most important feature of such surfaces. To test and characterize this property, different experiments have been conducted so far and in Section 1.3 we provide an overview of the recent experimental studies that focus on the friction reduction induced by SHSs for laminar flow in microchannels. Nevertheless, there is still a manifold of other applications of those surfaces for microfluidics. In this section we recall some of them, but for a complete review of the subject we refer the reader to the work of Zhang et al. (2008).

Since a SHS reduces the wall friction of a water flow, the same phenomenon can be exploited to reduce the drag force experienced by a moving object surrounded by water. Shi et al. (2007) fabricated superhydrophobic coatings of gold threads and confirmed a reduction of about 2 times of the drag force contrasting the object motion. They also suggested that this is the mechanisms used by water striders whose superhydrophobic legs allow them to move very fast on the water surface. Further studies on water striders, as in Gao and Jiang (2004), pointed out as a superhydrophobic interface provides extra supporting force, letting those animals float on the water surface. The additional thrust is due to the combination of the vertical component of the surface tension and the buoyancy forces provided by the air trapped in the surface cavities.

SHSs have also demonstrated to be an effective mean to control the motion of liquid droplets. Due to the Maxwell force and the charge induced change of the contact angle, Washizu (1998) and Torkkeli et al. (2001) reported the actuation of a water droplet on SHS by electrostatic methods. In addition, an electric field can also promote the droplet vertical motion and Takeda et al. (2002) showed how to make a water droplet jump on a SHS by applying a vertical electric field. Nevertheless, the electric potentials, required to activate the droplet motion, are very high and this interdicts applications in several fields, as for instance in the chemical and biological areas, due to the negative side effects of the electric heating. Consequently, alternative activation principles have been studied, as for instance the magnetic field as reported in Guo et al. (2006).

Considering a water flow in a hydrophilic channel, the border between an hydrophilic and a superhydrophobic surface can prevent the fluid to go ahead, due to the high jump in the surface tension. This is the working principle of the microfluidic fishbone-shaped valves designed by Lu et al. (2007). The authors demonstrated how superhydrophobic valves can effectively stop the flow of protein solution in order to prevent the non-specific binding. Those valves outperformed the plain capillary valves, that resulted to be quickly deteriorated under the same working conditions.

Very promising results can be obtained when SHS technology and surface-driven flow technique are coupled together. As theoretically and numerically demonstrated by Huang et al. (2008), this synergetic effect is basically due to the fact that in such a case the slip velocity V_s increases by a factor of $(1 + b/\lambda)$, where b is the hydrodynamic slip length and λ is the typical length scale of the interfacial region where the surface-transport phenomenon occurs. Since λ is of the order of nanometers, the amplification factor can practically be of order ten to hundreds or even more. For flat surfaces, such amplification does not depend on the nature of external field (electric potential, solute concentration, temperature) which promotes the transport. Conversely, when this process takes place on patterned hydrophobic surfaces in Cassie state the nature of the physical quantity varying on the macroscopic length scale along the flow direction is crucial. Further details about surface-driven flows on SHSs are reported in Appendix A, where we also describe some preliminary experimental tests to verify this giant amplification of the surface-transport effects. Even though the adopted experimental configuration was not the best one to highlight the desired effects, we hit on unexpected and very interesting phenomena leading to particle trapping inside surface roughness when the SHS is the Wenzel state and a salt concentration gradient is established. The experimental methods and the results are described in Appendix A.

It is well known that, for microfluidics at very low Reynolds number, mixing is a very challenging task. In the absence of specific mixing techniques, the mixing rate is ruled by the molecular diffusion and thus it occurs on a time scale much longer than what it could be needed in the applications. Using hydrophobic microridges tilted with respect to the flow direction, Ou et al. (2007) demonstrated both numerically and experimentally the onset of a secondary flow that effectively reduce the mixing length by stretching and folding the fluid elements. Compared to a smooth microchannel, the mixing improved by more than an order of magnitude. The authors also verified that the presented method was more efficient than other existing mixing techniques, as the hydrophilic grooved surface in Wenzel state proposed by Stroock et al. (2002), with respect to which a twofold increase in the mixing rate was reported. Another sensitive issue, especially in the microelectronic applications, is the heat transfer at the micrometer scale length. The feasibility of SHSs for increasing the heat transfer rate has been investigated via numerical simulations by Maynes et al. (2008). A pattern of alternating microribs and microgrooves was reported to increase the heat transfer rate up to 30 %, but this simulations have yet to be confirmed by experiments.

In biology, the superhydrophobicity has been used to reduce the adhesion of microorganism onto solid wall. Roach et al. (2006) reported sensitive reduction of protein adhesion at superhydrophobic wall, despite the surfactant role played by the proteins that promote the extension of the effective liquid/solid contact area. Ostuni et al. (2001) exploited the impossibility for cells to adhere on microbubbles, thereby obtaining a cell patterning on a SHS consisting of a regular lattice of microwells.

Due to this anti-cell adsorption properties, SHSs have also attracted the attention for their potential application in clinical therapy. The adherence of platelet to biocompatible SHSs has been investigated by Sun et al. (2005) and Toes et al. (2002), getting opposite results. Thus, that issue has not been fully understood and more experimental tests would be necessary to shed a new light on the problem.

In the work of Zhai et al. (2006) and Garrod et al. (2007), patterns of superhydrophobic and hydrophilic regions have been effectively engineered to promote in specific areas the condensation of water droplets that are subsequently collected and directed toward a defined target. The authors were inspired by the natural example of the Namib desert Stenocara beetle, whose back is made of hydrophilic hills and superhydrophobic channels. As long as the water from the fogs is collected on the hills, the water droplets are then conveyed to the beetle's mouth via the superhydrophobic channels, as explained by Parker and Lawrence (2001).

Although the studies of using the SHSs for drag reduction in the laminar flow inside microchannels have been extensively addressed only in the last decade, the fundamental properties of such flows have been understood. Nevertheless, there is still a lot of work to do and a series of challenges have still to be overcome. To date, only few attempts of SHS optimization in term of slippage property and Cassie state stability have been proposed and only a small subset of possible pattern geometries has been investigated. In this respect, the Achilles heel of those surfaces is the fact of being too fragile since the liquid/air interface cannot be maintained under large static pressures. Moreover, the hydrophobic coating used to promote the Cassie state are often damaged by the continuous water contact, as it occurs for the silane layers, and the superhydrophobic state cannot last as long as needed even at low liquid pressures. As shown in this Chapter, the outcomes of several experimental works not always overlap with the theoretical predictions and even when similar surface structures are examined, the results can be quite different. Most probably, there are still some factors to be identified and adequately controlled in order to fully understand the flow behaviour past SHSs.

In this respect, after discussing the state of the art of the experimental characterization of SHS, we report the direct flow visualization on a SHS with microgrooves parallel to the flow direction. The measured effective slip length is an order of magnitude lower than the theoretical predictions and this could be due to possible uncontrolled factors as the influence of meniscus shape and position with respect to the microribs' tops as well as the presence of polymer contaminants that promote an additional friction at the liquid/air interface.

1.3 Experimental characterization of laminar flows on SHSs: state of the art

Ou et al. (2004) were among the first to experimentally investigate the reduction of hydrodynamic resistance for a laminar flow in microchannel fitted with a superhydrophobic wall. Measuring the pressure drop as a function of the flow rate for a series of microchannel geometries and SHS designs (namely, microposts and microridges), they detected pressure drop reductions up to 40%, corresponding to apparent slip lengths larger than 20 μm. Supported by a good agreement between the experimental results and the predictions of analytical theory, they identified the shear-free interfaces as the responsible of the reduced interface friction. Focusing on the microridges geometry, Ou and Rothstein (2005) used the micro Particle Image velocimetry (μPIV) to probe the flow kinematics at length scales well below that of

the regular pattern of the examined SHSs. Whereas velocities vanish identically at the solid/liquid interfaces, the slip velocities at the center of the air/liquid interfaces were greater than 60% of the average velocity along the entire microchannel. Simultaneously, they also monitored the pressure drop in the channel and they found out a direct correlation between the increase in the pressure drop reduction and the increase in the slip velocity at the air/liquid interface. Davies et al. (2006) performed numerical simulation and pressure drop measurements for SHSs consisting of ribs and cavities parallel to the flow direction. They investigated the reductions in the friction factor as a function of the no-shear fraction and they also highlighted the dependence of the effective slip length on the laminar flow Reynolds number. Furthermore, in their simulations they accounted for the coupling between the liquid phase in the channel and the vapor phase in the cavities and they consequently deduced the global impact of the vapor cavity depth on the overall frictional resistance.

Choi et al. (2006) were the first to adopt and experimentally investigate a nanoscale grating pattern with 60 nm wide ridges spaced 180 nm apart. They compared the performances of both smooth and superhydrophobic surfaces via a custom flowmeter and they found slip length of $100 \div 200$ nm, corresponding to $20\ \% \div 30\ \%$ reduction of pressure drop in a 3 μm high channel when the flow is parallel to the nanogrates. According to the theoretical prediction, the measured slip length is halved for flow transverse to the ridge direction. Choi and Kim (2006) devised a nanostructured SHS, minimizing the liquid/solid contact area. Using the black silicon method, they created a needle-like structures on a silicon wafer, made of $1 \div 2$ nm tall nanoposts, spaced $0.5 \div 1$ μm. The authors claimed dramatic slip effects of 20 μm for water flow and 50 μm for 30 wt% glycerin. However, Bocquet et al. (2006) casted doubt on those measurements, performed with a cone-and-plate rheometer system, whose uncertainty in the slip length detection can be of the same order as the reported values. Subsequently, Lee et al. (2008) engineered SHSs by varying the pitch and the gas fraction of micropost and microridge pattern to maximize the slip length and to obtain samples that delay the Wenzel transition until the theoretical limit. Using such SHSs, they reported a slip length of about 200 μm, a value well beyond the experimental error of the shear rheometer, used to perform the measurements. In a very good agreement with the predictions of theory and simulations, the experiments also showed that at very low solid fractions the micropost geometry outperforms the microridge one for the same solid fraction.

Joseph et al. (2006) relied on μ-PIV measurements to determine the flow profile with submicrometric resolution on a SHS made of a random arrays of bundled carbon nanotubes. Slip length of a few microns were obtained as long as the Cassie state is maintained. Determining the average separation of the nanobundles via scanning electron microscopy, they experienced a linear dependence of the slip length on the post separation, in line with the theoretical predictions. They also verified that, as the Wenzel transition was induced, a vanishing slip length was recovered. Truesdell et al. (2006) simultaneously measured the force on a SHS, consisting of a cylinder with circumferential grooves parallel to the flow direction, and the velocity field close to that surface. The laminar flow was established between the SHS and an outer concentric rotating cylinder. A decrease of 20% in the flow resistance was detected and justified by the reduced effective solid/liquid contact area.

In all of the discussed works, the SHSs have demonstrated to be an effective mean to reduce the hydrodynamic resistance in microchannel where a laminar flow

occurs. Conversely, Steinberger et al. (2007) reported for the first time an anti-lubricant effect promoted by the air pockets trapped in the surface cavities. Performing nanorheology measurements of the boundary shear-driven flow on a surface with a square lattice of circular holes, they identified the liquid/air menisci as the responsible of the higher friction, compared to a flat surface. That finding has a paramount role in the fabrication microfluidic systems designed for reduction of wall friction, since the meniscus curvature can highly deteriorate the benefits introduced by a shear-free interface.

Byun et al. (2008) compared the μ-PIV measurements at a hydrophilic glass wall, a hydrophobic polydimethylsiloxane (PDMS) wall and a PDMS SHS consisting of microgrooves fabricated along vertical walls. The no-slip boundary condition was detected at the glass interface, whereas finite slip length of 2 μm was measured at the flat PDMS wall and a slip length ranging from 0.5 μm to 5.4 μm at the SHS was inferred, depending on the examined pattern geometry. Since the surface pattern was located on the vertical wall, they had optical access to the liquid/air interface profile and they reported a liquid meniscus protruding inside the SHS cavities, so that a wavy flow was created beyond the grooves. Finally, Tsai et al. (2009) investigated via μ-PIV the global effective slip length of a laminar flow on a hydrophilic PDMS flat surface and a series of PDMS and polyvinylidene fluoride (PVFD) surfaces with longitudinal microridges with different sizes and a constant solid fraction of 0.5. A vanishing slip length within the experimental error has been measured on the flat surface. As regards the microstructured surfaces, an effective slip length of a few micrometers have been determined. According to the theoretical results, the slip length increased with the microgroove width, due to a larger shear-free area. However, the surface resulted less slippery than the theoretical prediction of a periodic pattern of no-slip and no-shear slabs. The confined geometry of the channel and the bending of meniscus interface have been identified as the causes of such a discrepancy. Consequently, this work experimentally verified the important role played by the curvature of the meniscus in laminar microflows over hydrophobic microridges.

2 Characterization of water slippage on a microgrooved surface by means of μ-PIV

2.1 Introduction

In this section, we characterize the water flow past a superhydrophobic silicon surface made of a series of microgrooves and microribs parallel to the flow direction. We rely on micro particle image velocimetry measurements to locally investigate the flow behaviour at scale length lower than the typical size of the surface roughness profile. Exploiting the reflective properties of the flat surface at the top of the microribs, we devise a new procedure to detect with nanometric resolution the reference solid wall, with respect to which the global effective slip length is calculated. The measured total friction reduction on the examined SHS is about one order of magnitude lower than the theoretical prediction of Philip (1972). Thus, we further investigate the water flow at the liquid/solid and liquid/air interfaces, tracing the local effective slip length in the direction perpendicular to the microgrooves. In addition, we introduce a novel approach to identify the position and the shape of the liquid/air meniscus by post-processing the μ-PIV images and we directly relate those measurements to

the global effective slip length.

2.2 The experimental apparatus

The μ-PIV system as well as the driver and acquisition softwares were designed and provided by R&D Vision. A schematic view of the set-up is shown in Figure 4.3. An inverted optical microscope (Nikon Eclipse TE 2000-U), fitted with a water immersion microscope objective ($\times$60 NA 1.2), is placed on an optical breadboard (Melles Griot), that is mounted on an optical table support (Melles Griot), thereby isolating the system from external vibrations. The light beam of a DPSS laser is guided by a multimode fiber from the laser source (Cni MLL532, 400mW at 532 nm) to the acousto-optic-modulator AOM (AA Optoelectronics MT80). After the laser being collimated at the fiber exit, the beam waist is adjusted through a telescope (lenses L1 and L2). The light is then directed via a dichroic mirror (DM) to the microscope, passing through the tube lens $L3$ and the objective. The sample is placed on a manual xy stage and a flow control system (Fluigent MFCS-Flex) supplies the microchannel with a constant water flow. The axial displacement of the objective is performed via a stepper motor driven by an external controller (Marzhäuser Tango Desktop). The red fluorescent light of the excited colloids is collected and imaged on the CCD camera plane (Allied Vision Technologies). The image is recorded by a sensor array of 640×480 pixels, whose size is $7.4\,\mu$m$\times 7.4\,\mu$m. The resulting magnification scale factor is thus $0.123\,\mu$m per pixel. To prevent the reflected laser beam from reaching the camera sensor, a filter F is placed in front of the camera aperture. The laser source, the acousto-optic-modulator and the camera are triggered by a pulse generator (provided by R&D Vision), that is driven by a personal computer. The PC also controls the CCD camera, the microfluidic control system and the objective axial positioning. By removing the dichroic mirror DM, the standard bright field illumination of the Nikon microscope can be used via a beam splitter BM to visually inspect the microchannel.

2.3 Fabrication of the microfluidic channels

We now describe the fabrication process used to make the microfluidic channels adopted in our experiments. The superhydrophobic walls of the channels are clearly the core of these devices and they are also the most complicated part to produce. Since the realisation and the design of the first electronic chips go back to the early 1950s, a wide know-how has been developed in the nano and microfabrication of electronic miniaturized devices. Due to this half-century of experience, the fabrication of nano and microfluidic devices often relies on the same techniques and materials used for the electronic ones. Consequently, the silicon is widely used for microfluidic applications. However, realizing few prototypes of high-quality microstructured silicon surfaces can be a very expensive process, since it requires the access to high-technology facilities and equipments that are not always available in a physics laboratory. This is particularly true when very strict tolerances for the geometry of the surface roughness are requested. As we aim for a high-accuracy determination of the effective slippage over regularly microstructured silicon surfaces, these measurements can be strongly affected by any geometry defect. For this reason, we relied on the cleanroom facilities and expertise of the Institute for Nanotechnology at the University of Twente, that provides us with two silicon superhydrophobic surface (Si-SHS) samples.

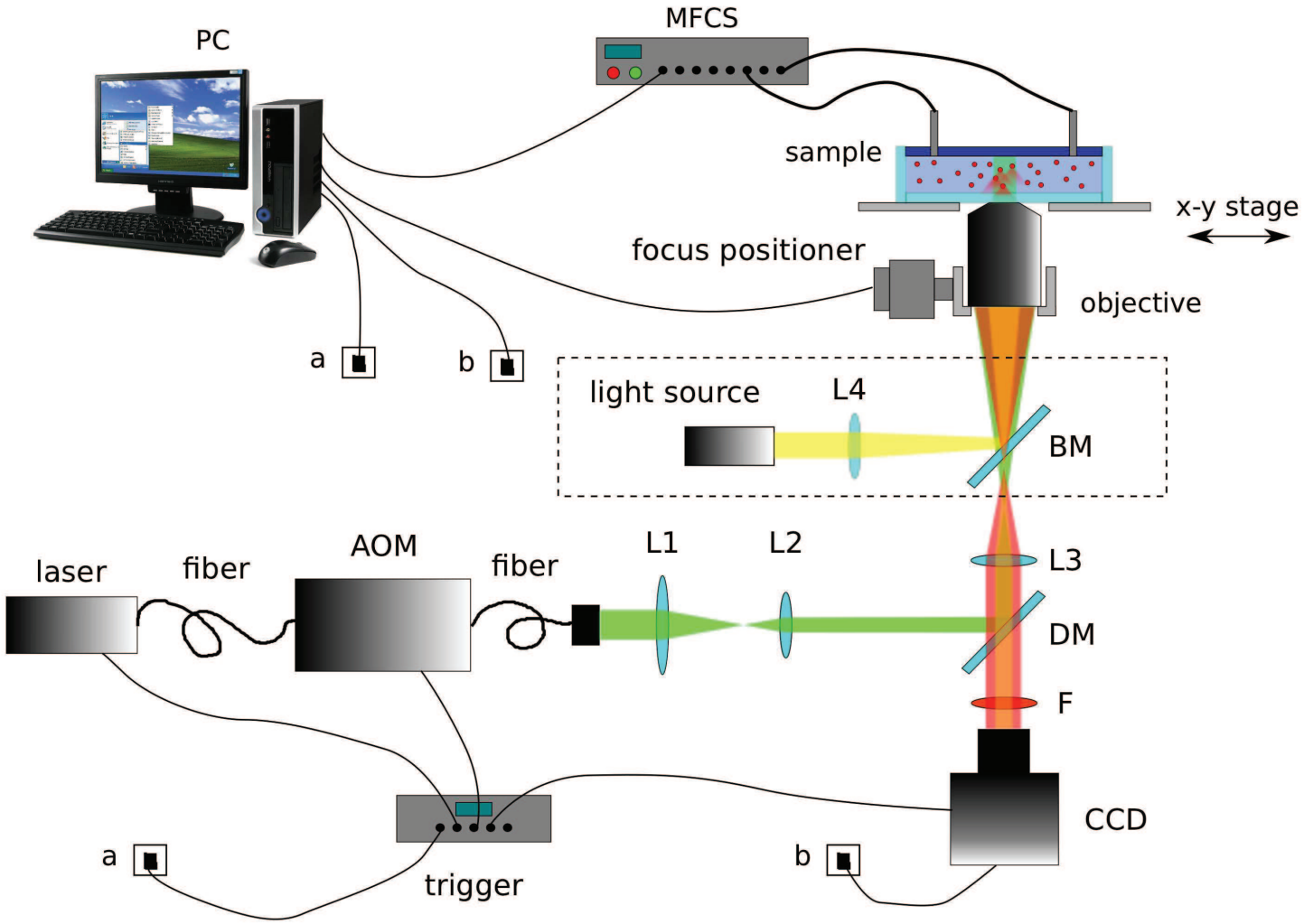

Figure 4.3: Scheme of the μ-PIV set-up. In the dashed rectangle, there are the additional elements used for the bright field illumination. The details of the apparatus are discussed in the text.

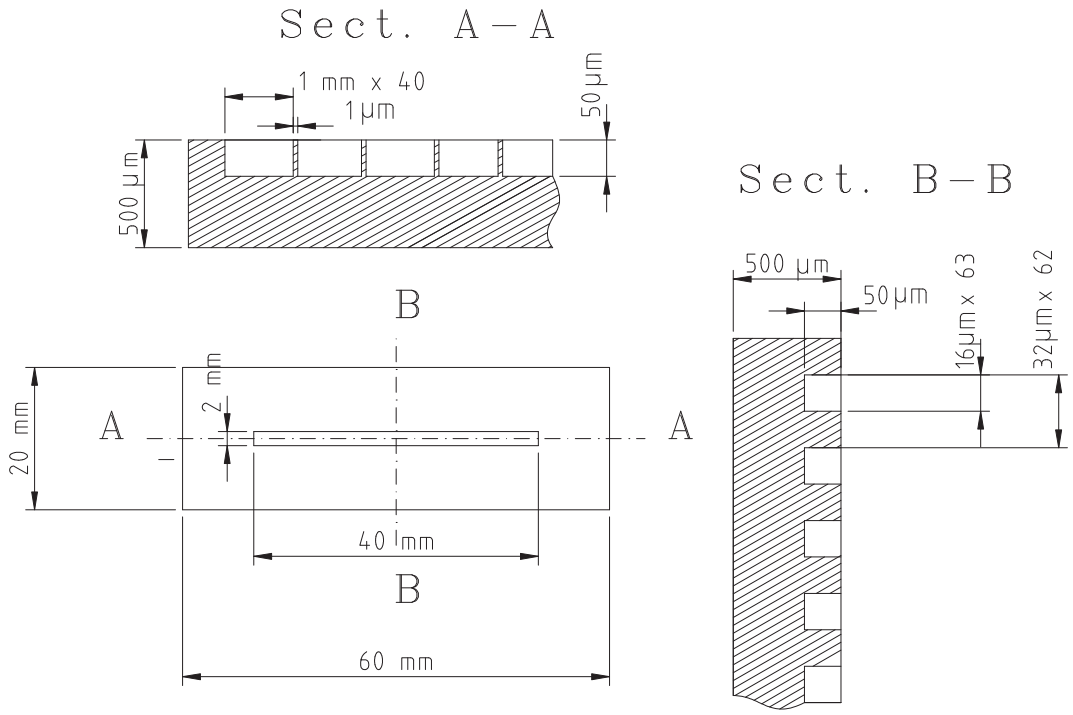

Figure 4.4: CAD drawings of the frontal and lateral views of the examined superhydrophobic surface, made of 20 mm×60 mm×0.5 mm silicon slice. A pattern of parallel microgrooves and microribs, shown in section B-B, is realized on a 2 mm×40 mm centered rectangular area. The microgrooves are evenly separated by 1 μm thick transverse walls, 1 mm far apart (section A-A).

Those surfaces were realised through the standard procedures of photolithography and plasma etching. Basically, a CAD drawing made of opaque and transparent regions was printed on a lithographic mask and thus transfered, via exposure to ultra-violet light, onto a photoresist film, stuck to the silicon surface. Therefore, the following plasma process etches only the exposed areas of the surface that are not protected by the patterned photoresist. Figure 4.4 shows a scheme of one of those Si-SHS[1]. The Si-SHS consists of a 20 mm×60 mm silicon slice, 0.5 mm in thickness. Only a central 2 mm×40 mm rectangular area was processed to obtain a regular pattern of grooves. The section B-B shows the cross-sections of the rectangular grooves that are 50 μm in depth and 16 μm in width. In all, there are 63 grooves, evenly separated by a distance of 16 μm. The seeded water is supposed to flow parallel to the axial direction of the grooves while the air is trapped inside them (see Figure 4.5). As discussed in Section 1.1, if the Si-SHS undergoes a Wenzel transition, the longitudinal grooves are filled in by water. If it occurs in a groove at a certain axial position, we would like to prevent the transition taking place in the whole groove length. Thus, each groove is split lengthwise in forty shorter grooves via 1 μm thick transverse walls (see section A-A). These walls are 1 mm far apart from each other and they act as bulkheads thereby confining the Wenzel transition to a small area rather then involving the entire channel length. As the oxide silicon is not enough hydrophobic (see Chapter 5), a regular micrometric roughness is not sufficient to get the superhydrophobic behaviour. To avoid the liquid completely wetting the

[1]It's worth noting that since the surface geometry has features at very different length scales, the cross-section views are not drawn to scale.

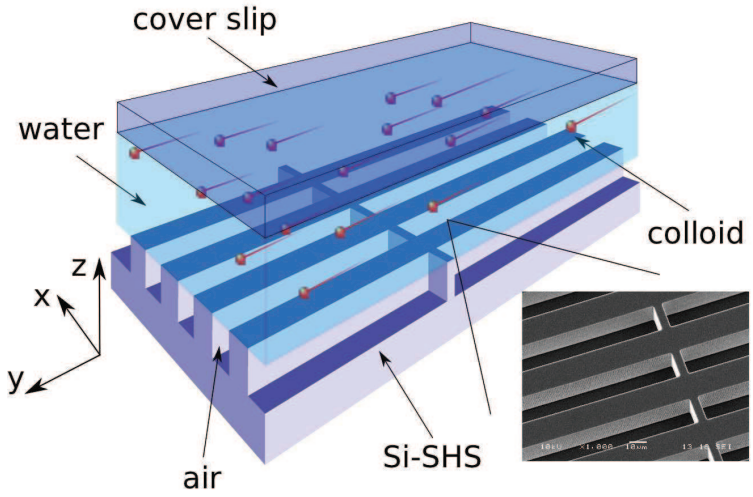

Figure 4.5: Three dimensional reconstruction of the microchannel. The ultrapure water and the fluorescent colloids flow in the direction parallel to the microgrooves. In the inset an image of the used Si-SHS realized through a scanning electroscope microscope.

grooves, the silicon surface is silanized via physical vapor deposition, adopting the following procedure. The sample is rinsed in ethanol and ultrapure Milli-Q water and dried in a oven at 60°C for 30 min. The surface is then activated in oxygen plasma by a Reactive Ion Etching (RIE) process. Finally the sample is put in a desiccator with few drops of 1H,1H,2H,2H-Perfluorooctyltrichlorosilane; 97% (ABCR). The vacuum is then established in the chamber by means of a mechanical compressor and the sample is left exposed to silane vapors for 12 hours.

The design of the microfluidic channel was centered around the described superhydrophobic surface sample. We choose the rectangular cross-section of the channel to have a high aspect-ratio, so that the liquid motion can be modelled as a unidimensional flow, far away from the shorter edges. This leads to simplified μ-PIV measurements of the flow field since the velocity is invariant (periodic) under translation parallel to the flow (transverse) direction. In addition, the channel height should be comparable with the spatial period of the surface roughness (that is 32 μm), in order to get remarkable deviation of the velocity profile from the case of a sticky silicon surface. In order to comply with these specifics, we cover by spin-coating a 25.4 mm$\times$60 mm microscope cover slip, about 170 μm thick, with a thin film of Polydimethylsiloxane (PDMS) (RTV-615). As we change the rotational speed of the spin-coater, the resulting thickness varies due to the different balance between centrifugal and viscous forces. In Table 4.1, we show the average thickness, measured via a mechanical profilometer, corresponding to different rotational speeds. Subsequently, through a metallic razor blade, we manually engrave the channel in

Angular Velocity [rpm]	Thickness [μm]
2000	60$\pm$5
3000	40 ± 5
5000	20 ± 5

Table 4.1: PDMS (RTV-615) film thickness corresponding to the angular velocity of the spin-coater. The PDMS film is spin-coated on a microscope cover slip and the thickness is measured via a mechanical profilometer.

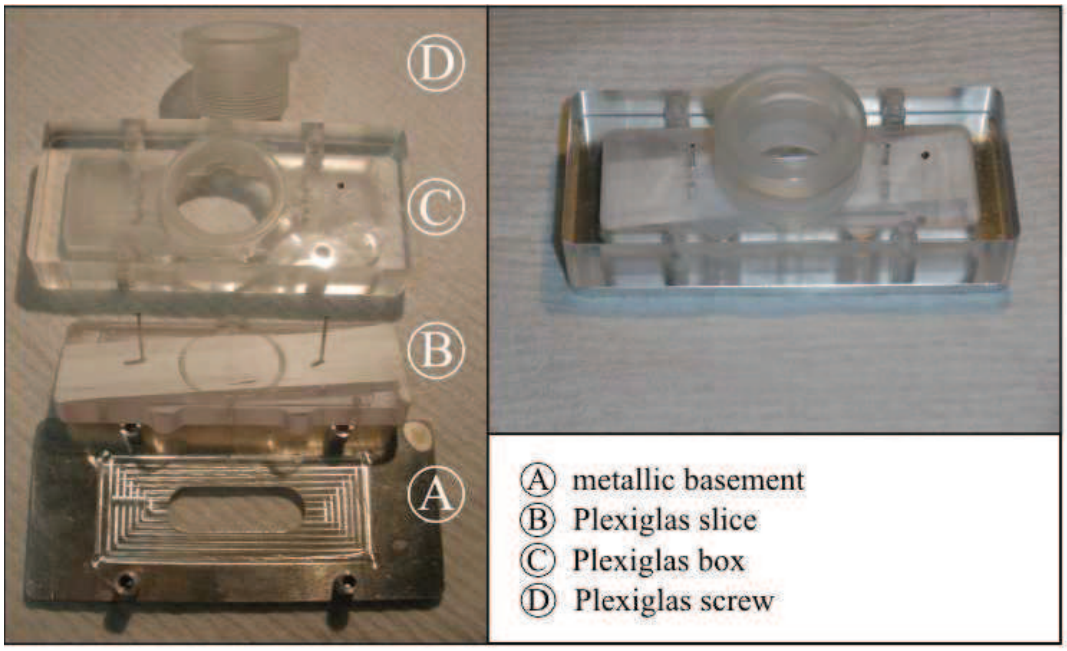

Figure 4.6: Custom pressing device used to seal the microchannel. On the left panel, the components of the device are shown. The PDMS coated cover slip is placed on the metallic base A. The superhydrophobic silicon slice is pressed against the cover slip by the Plexiglas element B via the Plexiglas screw D. This screw twists on the Plexiglas frame C, that is fixed to the metallic base. On the right panel a view of the assembled device is shown.

the PDMS film by removing a centered rectangular area. The resulting groove has the same size as the patterned region on the silicon slice, that is 2 mm×40 mm. Once the coated cover slip is sealed to the silicon surface, we obtain a rectangular cross-section microchannel with a high aspect ratio ($\simeq 40$). The engraving of the PDMS film can be easily performed manually since there are no strict dimensional and parallel constraints. Indeed, as regards the fluid flow, the leading dimension is the channel height (fixed by the angular velocity) while the width and the length are responsible for edge effects that are completely negligible once the flow measurement is carried out far away from the edges. To this respect, it is worth noting we tested several PDMS silicons and the RTV-615 gave the best results in terms of properness and sharpness of the manual cut.

The final step is to devise a method to seal the two parts of the channel, namely the silicon surface and the PDMS coated glass. The most common procedure involves a chemical exposure of both surfaces to a oxygen plasma, readily followed by a mechanical contact between the PDMS film and the silicon. This can be obtained by manually pressing against each other the two surfaces for tens of seconds. The chemical bonding is then stabilized by warming the sample on a hot plate for a few minutes. This procedure is easy, effective and irreversible. Indeed the sealing is assured by the covalent chemical bonds between the PDMS and the silicon oxide and, hence, there is no possibility to separate the two surfaces again. Since we prefer to avoid an irreversible bonding, we devised an alternative way to reversibly seal the channel as many time as needed. This approach gives us the chance to perform an unlimited number of measurements on the same surface sample, which is always well cleaned and re-silanized. Apart from reducing the costs of the experiment materials, this guarantees that the μ-PIV measurements are always conducted in very proper

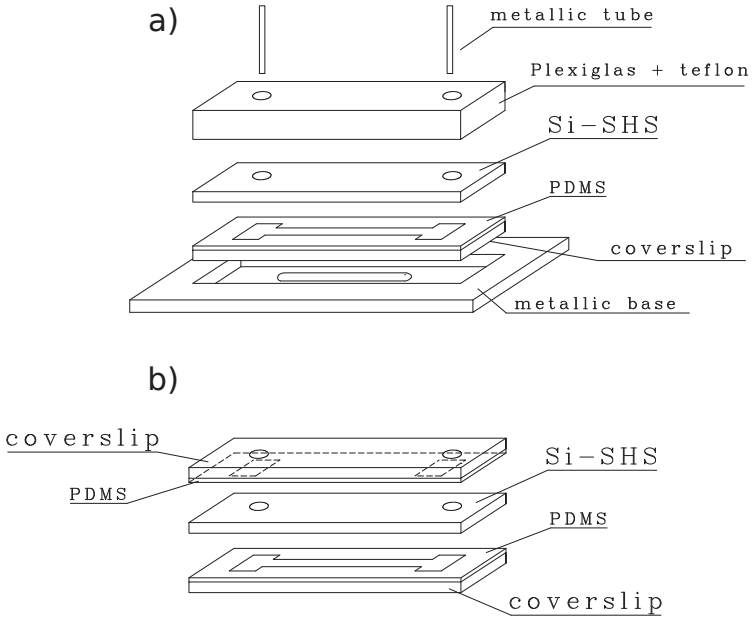

Figure 4.7: Scheme of the microchannel assemblage through the pressing device of Figure 4.6. a): The Si-SHS is sandwiched between the Plexiglas slice, acting as a piston, and the PDMS coated cover slip. The latter is placed on the groove of the metallic base, tailored to the cover slip size. b): An additional PDMS coated cover slip is placed on the top of the Si-SHS. Two reservoirs are engraved on the PDMS film at the channel inlet and outlet.

channel. Indeed, also the PDMS coated cover slip is cleaned and, because of its low fabrication cost, it is frequently replaced by a new one. In addition, since we used the same Si-SHS in all the measurements instead of replacing it with nominally identical samples, we can rule out any dependence of the results on the Si-SHS samples' differences, that may occur because of geometric tolerances, possible physical and chemical defects and so on. We sealed the channel by pressing against each other the two surfaces. To apply the pressure, we used the device shown in Figure 4.6. Basically, it consists of an open Plexiglas box (C) with a metallic base (A). The latter has a central rectangular groove having the same width, length and height of the cover slip and it is fitted with a central aperture. The PDMS coated glass is placed on the metallic base whose groove allows an easy and precise centering of the cover slip in the device. The aperture provides an optical access to the channel. The aperture's size and shape were designed according to the microscope objective's dimensions and they are a compromise between a wide optical access and a sufficient mechanical stiffness of the base. This one is fixed to the Plexiglas box (C) via four lateral screws located on the longest edges of the device. As shown in Figure 4.7(a), the Si-SHS is placed over the cover slip so that the superhydrophobic pattern is right in face of the channel engraved in the PDMS film. A Plexiglas slice (B), about 1 cm thick, is placed inside the box (C) and act as a piston pressing the Si-SHS against the cover slip via the Plexiglas screw (D). Such a slice is covered by a Teflon film to prevent leakages. The channel inlet and outlet are supplied with liquid flow via two metallic tubes that pass both through the box (C) and the slice (B). Therefore, the inlet and outlet holes have to be made on the Si-SHS. To drill the Si-SHS, we used a standard vertical drilling machine (Dremel) with 1.2 mm diameter diamond drill bits. An appropriate drilling procedure is followed in order to obtain proper holes and to avoid cracking the silicon surface, that is

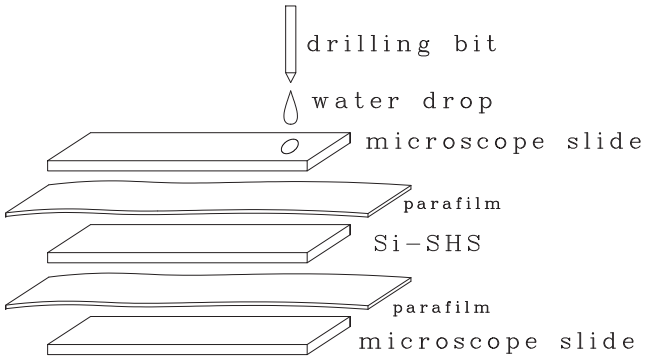

Figure 4.8: Scheme of the procedure adopted to properly drill the silicon slice, avoiding that the Si-SHS cracks. The Si-SHS is sandwiched between two microscope slides. Two parafilm slices are bonded between the microscope and silicon slides by warming the system through a hot plate. The compliance of the parafilm prevents that stress concentration occurs on the silicon surface while drilling. A water droplet is used as cooling to limit the temperature raise.

very fragile. Figure 4.8 shows a simple scheme of the preparation of the sample to be drilled. The silicon surface was sandwiched between two microscope slides, 1 mm in thickness, and two parafilm slices. The different pieces were stuck together in a sort of "sandwich" by warming it through a hot plate until the parafilm was about to melt. Due to the compliance of the parafilm slices, the pressure exerted by the drilling bit was homogeneously redistributed throughout the silicon sample, avoiding stress concentrations and cracks. Moreover, to preserve both the Si-SHS and the drilling bit, the temperature raise due to the friction between them had to be limited by supplying the contact area with a few drops of water.

Finally, in order to relax the constraint of a precise alignment between the holes on the Si-SHS and those on the Plexiglas slice, we put on the Si-SHS an additional drilled and PDMS coated cover slip, where two rectangular reservoirs had been engraved, as shown in Figure 4.7(b). Usually, two reservoirs were also engraved at the ends of the channel. The whole assembled device is shown in Figure 4.6b. The metallic tubes, coming out the device, were then connected to a control flow system (Fluigent MFCS-8), allowing a fine control on the input and the output pressures.

2.4 Image acquisition and analysis

Once the channel is fabricated as described in the previous Section and the whole device is assembled, the inlet tube is connected to a glass syringe, containing a solution of ultrapure Milli-Q water seeded with red fluorescent 0.3 μm diameter colloids (Thermo Scientific Fluoro-Max), 0.02% in solid concentration. Then the liquid is pumped to the channel by manually applying a very weak pressure at the syringe piston. At the aperture of the metallic base, we can visually follow the liquid/air meniscus advancing through the channel and we consequently adjust the applied pressure (and hence the meniscus speed) in order to prevent the formation of air bubbles between the cover slip and the silicon surface. Indeed, those trapped bubbles can be responsible of time flow variations that badly affect the velocity profile measurements. In addition, once bubbles are formed inside the channel, it's very difficult to remove them, due to the high hydrophobicity of the silicon surface, and, thus, it's absolutely necessary to avoid their formation right from the

Measur.	N **Images/plane**	**Axial Step** $[\mu m]$	**Init. Pos.** $[\mu m]$	**Fin. Pos.** $[\mu m]$
A	3200	0.3	-4.0	$+34.7$
	4000	0.1	-4.0	$+6.0$
B,C	3200	0.3	-11.8	-4.0
	4000	0.1	-3.9	$+6.0$
	3200	0.3	$+6.3$	$+35.1$

Table 4.2: Acquisition parameters of the examined channel scans: A, B and C. For each acquisition we list the number N of recorded frames per plane, the axial step of the scan and the initial and final axial positions. The Si-SHS is located around $z = 0$.

channel filling. Unfortunately, we don't have an optical access to the whole sample and sometimes the possible presence of hidden bubbles is determined only by the following data analysis that reveals a non constant fluid flow during the scan.

Subsequently, the channel inlet and outlet are connected via flexible tubes (inner diameter $300\,\mu$m) to the reservoirs of the flow control system that allows us to finely control the inlet and outlet pressures. The pressure difference between the reservoirs is set around 5mbar. As a constant flow is established, we scan the channel height by recording N frames at M evenly spaced focal planes. The acquisition has a constant frame rate of 200 fps, thus any two consecutive frames are time separated by 5 ms. Since the frames are evenly spaced over time, we have $N - 1$ couples of images that contribute to estimate the velocity field at the selected plane. While the camera sensor is exposed to the incoming light, the pulse generator triggers the laser and the acousto-optic-modulator, so that the light beam illuminates the sample for $10\,\mu$s. The whole acquisition is controlled by a commercial software (Hiris Automate, R&D Vision). Usually we record $N = 3000 \div 4000$ frames per plane while the axial step of the scan is about $100 \div 300$ nm. The number M of total planes analysed is about $140 \div 200$ and the whole acquisition takes approximately one hour and half. Despite a single scan lasts so long, the Si-SHS proves to be very stable, remaining in the Cassie states for several hours. On the contrary, the flow rate might not be constant throughout the scan, due to events as the detachment and the passage of air bubbles that temporarily disturb the flow. These events are the more likely, the longer the acquisition is. Therefore we perform a quick preliminary analysis of each scan, determining the velocity field at a reduced set of scanned planes by means of the commercial software DirectPIV for PIV-image analysis, provided by R&D Vision. If at this level of analysis a flow variation is detected, the whole acquisition is rejected.

In the present work, we report and discuss the results for three experiments that have shown the most stable liquid flow. The acquisition parameters, as the number of recorded images per plane, the axial step and the initial and final axial positions, are listed in Table 4.2 for the three examined cases: A, B and C. We introduce a reference coordinate system (see Figure 4.5) with the z coordinate parallel to the optical axis and positively oriented from the Si-SHS to the cover slip. The z axis origin is always chosen close to the silicon solid interface. As explained in the next section, the reflective power of the silicon surface can be exploited to the detect the channel wall position and hence the channel scan starts few micron below that surface. Furthermore, to get high accuracy wall detection, we scan the volume close to the Si-SHS with a scan step of $0.1\,\mu$m, that is otherwise set to $0.3\,\mu$m. The number

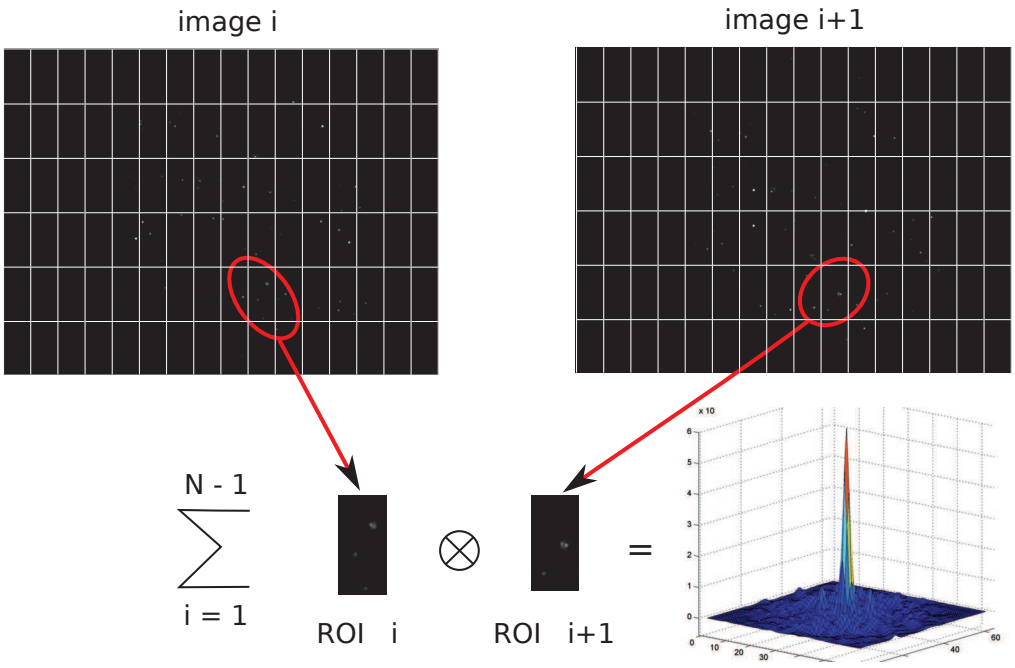

Figure 4.9: Scheme of the correlation-based algorithm used to determine the in-plane flow velocity. Once the images are divided in overlapping interrogation windows, for each one of them the correlation function averaged over $N-1$ image pairs is worked out. The peak of those functions determine the image displacements and, hence, the corresponding fluid velocities.

N of images per plane, over which the average velocity profile is worked out, was chosen so that the Brownian motion component of the colloids can be neglected. Indeed, the Brownian velocity component of the particles, averaged on N frames, can be estimated as $\bar{V}_b = \sqrt{2Dt}/\sqrt{N}t$, where D is the particle diffusion coefficient and t is the elapsed time between two consecutive frames (that is 1/200). If we assume that $\bar{V}_b$ should be less than 1% of the minimum detectable flow velocity V_{min}, we get

$$N > \frac{2D}{t}\frac{10^4}{V_{min}^2} \tag{4.5}$$

For $V_{min} \simeq 30\ \mu$m/s, it results $N \geq 3200$. Consequently, in examined cases, we choose $N = 3200$ and $N = 4000$.

The μ-PIV image analysis are performed by the standard correlation-based PIV evaluation algorithm, that is implemented via a Matlab code. A scheme of the algorithm is shown in Figure 4.9. First, each frame is divided in small overlapping regions of interest (ROIs), also called interrogation windows. They are 3.94 μm (32 pixels) in width (x direction) and 7.87 μm (64 pixels) in height (y direction), while the overlap in both directions is 50%. Therefore, the centers of these interrogation windows are placed at the nodes of a 16 μm$\times$32 μm rectangular grid. Secondly, the cross correlation function $\Phi_i(m,n)$ between the corresponding ROI, centered in (x_m, y_n), of two consecutive images $(i, i+1)$ is worked out. This function has a peak at the position of the most probable particle image displacement in the examined ROI. Nevertheless, there are also lower sub-peaks due to the noise or mismatch of the images. If the particle density is low or the noise is high, some of those sub-peaks could increase and even exceed the main peak. In such a case, if the velocity

were estimated by the correlation function of a single image pair, we would get an erroneous value. Since the main peak of $\Phi_i(m,n)$ is always at the same position for all the recorded image pairs, whereas the sub-peaks have random position and intensity, in order to get a more accurate velocity estimate, we average the correlation function over the $N-1$ recorded image pairs. The resulting averaged correlation functions is, thus, written as

$$\Phi_{avg}(m,n) = \sum_{i=1}^{N-1} \frac{1}{N} \Phi_i(m,n) \tag{4.6}$$

An example of the averaged function $\Phi_{avg}(m,n)$ in shown in the lower inset of Figure 4.9 Averaging the correlation functions rather than the velocity vectors results in a more accurate determination of the velocity field, since $\Phi_{avg}(m,n)$ is less affected by possible errors due to the Brownian motion, background noise and low particle density. The peak position of $\Phi_{avg}(m,n)$ relative to the window center defines the mean displacement of the fluid on the examined ROI. Once the displacement is divided by the elapsed time between two consecutive frames (that is 5 ms), we get the 2D velocity vector, that is assigned to the window center. This procedure is iterated for all the scanned planes, thereby getting the velocity field in the sample volume given by the objective field of view times the scanned height.

2.5 Results and discussion

Detection of the solid/liquid interface

The accuracy of the slip length measurement is strictly dependent on the accuracy of the localization of the solid wall, relative to which the slip length is computed. In this respect, Joseph et al. (2006) have proposed an easy and reliable method based on the detection of the colloids unavoidably stuck to the solid wall. By scanning through the optical axis the fluorescent light intensity emitted by the stuck colloids and fitting to a Lorentzian curve, they detected the particle centers and thus, considering the nominal particle radius, the wall position as well. When this procedure is implemented with a piezoelectric focus positioning system with a resolution of 10 nm and using colloids $100 \div 200$ nm in diameter, the wall detection resolution is

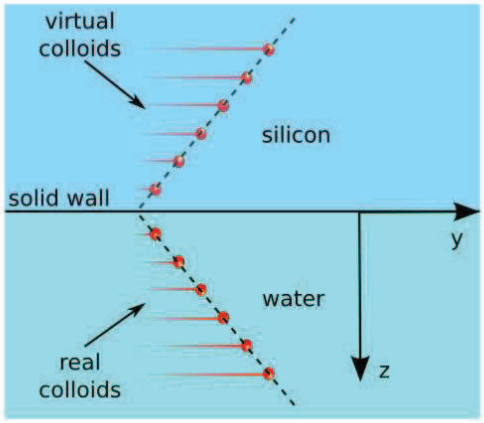

Figure 4.10: The silicon solid surface acts as a mirror. By determining the position of the symmetry axis of the velocity profiles of the real and virtual colloids, the solid wall is located with nanometric resolution.

about 30 nm. Even though this approach is easy to implement and provides a nanometric measurement of the wall position, it has the drawback of being dependent on the individual particle size. Indeed, the wall position accuracy is limited by the knowledge of particle radius, that may be different from the nominal one due to the colloids polydispersity.

We now present a novel approach for high accuracy detection of the wall position based on the reflective power of the silicon wall. The fluorescent light reaching the liquid/silicon solid interface is partially absorbed and partially reflected. The reflected part is a few tens of percents of the incident light and thus it is still enough to be collected by the objective and imaged onto the camera plane. Figure 4.10 schematically shows how this mirror effect of a flat silicon surface can be exploited to locate the wall position. For sake of simplicity, in Figure 4.10 the origin of the $\{y, z\}$ reference system lies on the liquid/solid interface. As the objective focal plane is placed inside the channel ($z > 0$), we visualize the real images of the colloids. On the other hand, when we focus on a plane outside the channel ($z < 0$), we detect the virtual images of the colloids, whose velocity is exactly the same of the corresponding real images. In the case of a perfectly flat interface, this results in a symmetric velocity profile, as shown in Figure 4.10, and the axis of symmetry locates the position of the reflective surface.

In Figure 4.11 we plot the experimental velocity profile (case C of Table 4.2) as a function of the axial coordinate z. Since the velocity field is invariant under translation in the flow direction y, hereafter all the reported experimental velocities are averaged along that direction. The profile shown in Figure 4.11 is obtained as a transverse slice, 3.94 μm thick (namely, the ROI width), of the measured velocity field. Particularly, only those interrogation windows centered at the transverse position $x = 9.9\ \mu$m are now considered. We can clearly observe that focusing on the virtual images of the colloids ($z < 0$) results in a velocity profile, beyond the solid interface ($z \simeq 0$), symmetric with respect to the solid wall. Consequently, we can determine the wall position at the examined x coordinate by fitting the experimental profile to a one-dimensional Poiseuille velocity profile plus the specular reflection at the solid wall, that can be written as follows

$$V(z; z_g, z_w, v_{max}) = \begin{cases} A(z - z_g)(z - z_w) & \text{if} \quad z > z_w \\ A(z - z_w)(z - (2z_w - z_g)) & \text{if} \quad z \leq z_w \end{cases} \tag{4.7}$$

where

$$A = -\frac{4V_{max}}{(z_w - z_g)^2}$$

We assume as fitting parameters the wall and cover slip positions, respectively z_w and z_g, and the maximum velocity V_{max}. The solid red line in Figure 4.11 represents the fitting curve while the black dashed line shows the resulting wall position. The theoretical model and the experimental data are in a very good agreement. We notice that the minimum theoretical particle motion that can be detected is the one corresponding to a displacement of 1 pixel between two consecutive frames. This corresponds to a particle velocity of 25 μm/s.

Considering the velocity profiles at N_x transverse positions x_i, we can iterate the fitting procedure and determine the whole interface profile $z_{w,i}$, as shown in Figure 4.12. The black empty circles, evenly spaced $\Delta x = 1.97\ \mu$m (16 pixels) apart, represent the fitted wall position $z_{w,i}$. Since the ROIs have an overlap of 50%, each $z_{w,i}$ has to be considered as an average over a transverse segment $[x_i - \Delta x; x_i + \Delta x]$,

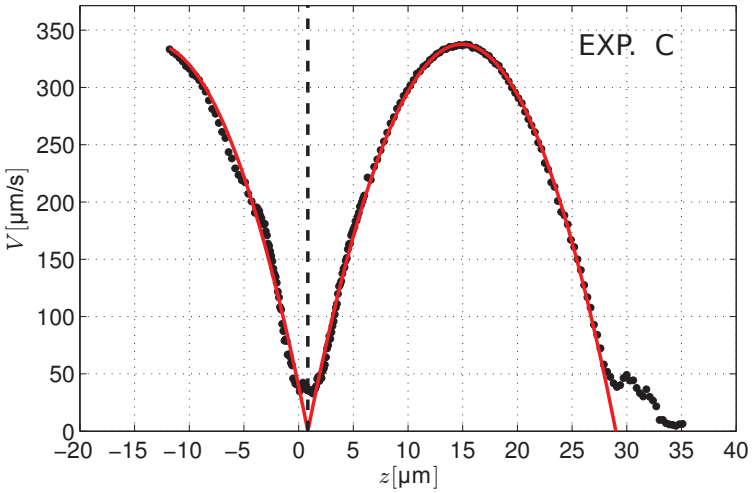

Figure 4.11: Measured velocity profile (solid circles) for the case C on a vertical slice, 3.94μm thick, and the fitting curve (solid line) to a 1D Poiseuille profile. The dashed line identifies the solid wall.

that is centered in x_i and is $2\Delta x = 3.95\ \mu$m (32 pixel) in length. The model expressed in Eq (4.7) is valid for a reflective flat surface with sticky boundary condition. On the contrary, at an ideal liquid/air interface a perfect slip boundary condition holds and, in addition, the interface shape might be no longer flat. Thus, this model cannot be applied at the liquid/air interface. As a consequence of that, as long as a velocity profile past the liquid/air interface is considered (see inset in Figure 4.12), the fitting curve (red solid line) fails to properly describe the experimental data. Consequently, we reject the fitted values where the measured wall positions $z_{w,i}$ do not correspond to the solid wall and, thus, they don't lie on a straight line. The black empty circles, lying outside the dashed red lines, refer to the interrogation windows whose area falls entirely on the silicon solid wall, while the circles, between the two blue dot-dashed lines, refer to those ROIs whose area falls entirely on the liquid/air interface. The remaining circles correspond to those ROIs falling at the solid/air borders.

Once we identify the discrete wall positions $z_{w,i}$ in the transverse direction, through a linear regression we define the reference silicon solid wall $z_w(x)$ (solid black line). The same procedure for the wall detection is carried out for the experiments A and B, and the results are shown in Figure 4.13. The precision of the wall detection is estimated through the mean squared error of the linear regression, namely

$$\delta z_w = \sqrt{\sum_{i=1}^{N_x} \frac{(z_w(x_i) - z_{w,i})^2}{N_x}}$$

and it ranges from 10 to 30 nanometer depending on the quality of the experimental profiles. In Table 4.3 the averaged positions $\bar{z}_w = \sum_i N_x^{-1} z_{w,i}$ of the silicon walls are reported for the three examined cases.

Global effective slip length

We now proceed to estimate the global effective slip length relative to the known wall position $\bar{z}_w$. We first average all the measured velocities along one period of

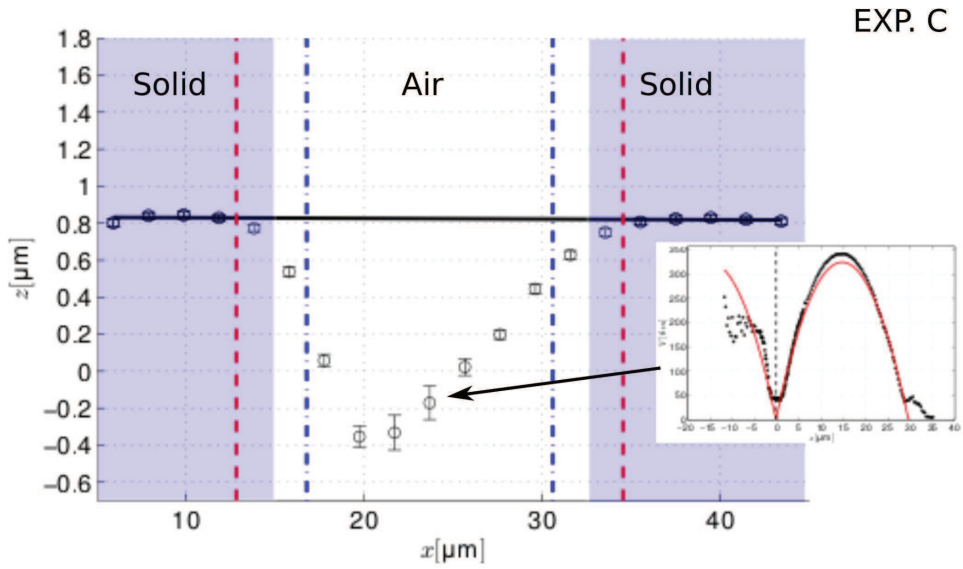

Figure 4.12: Detected wall for the case C along the direction x perpendicular to the microgrooves. The empty circles represent the positions of the axes of symmetry for the measured velocity profiles. The circles lying outside the two red dashed lines correspond to the liquid/solid interfaces, whereas the circles lying inside the two blue dot-dashed lines refers to the liquid/air interface. The black solid line identifies the reference wall obtained as the linear regression of the circles outside the two red dashed lines. In the inset, the velocity profile on a vertical slice past the liquid/air interface and the corresponding fit to 1D Poiseuille profile past a reflective surface.

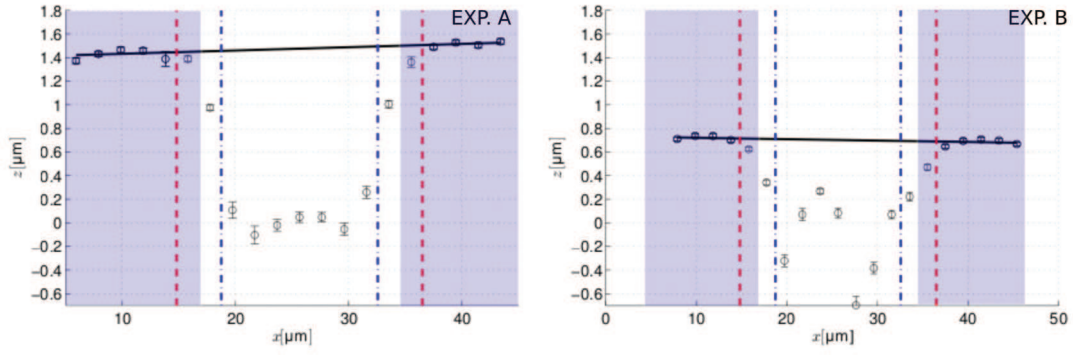

Figure 4.13: Detected walls for the case A and B. The used symbols and signs are the same as in Figure 4.12.

	A	**B**	**C**
$\bar{z}_w \pm \delta z_w$	$1.463 \pm 0.030\ \mu$m	$0.823 \pm 0.013\ \mu$m	$0.700 \pm 0.021\ \mu$m
$b_{glob} \pm \delta b_{glob}$	457 ± 56 nm	186 ± 42 nm	277 ± 70 nm

Table 4.3: Averaged position of the reference solid walls and the global effective slip lengths for the three examined cases.

the roughness transverse profile (that is, $32\,\mu$m in length) and then we fit the result to the model of one-dimensional pressure driven flow with a sticky wall (the cover slip) and a partially slippery wall (the Si-SHS), with finite slip length b_{glob}. The expression of the velocity profile is the following

$$V(z; b_{glob}, z_g, V_{max}) = A \frac{(z - z_g)\left[b_{glob}(z + z_g - 2\bar{z}_w) + (z - \bar{z}_w)(z_g - \bar{z}_w)\right]}{b_{glob} + z_g - \bar{z}_w} \tag{4.8}$$

where

$$A = -4V_{max} \frac{(b_{glob} + z_g - \bar{z}_w)^2}{(z_g - \bar{z}_w)^2(2b_{glob} + z_g - \bar{z}_w)^2}$$

The fitting parameters are b_{glob}, z_g and V_{max}. This time, the reflected part of the experimental profile is not considered for the fit. As an example, in Figure 4.14 we observe that the experimental profile (black solid circles) for the case C and the corresponding fitting curve (red solid line) are in a very good agreement. In Table 4.3, we report the global effective slip length for the three investigated cases. The slip length precision is obtained as the uncertainty of the corresponding fitting parameter $\sigma_b = \sqrt{\mathbf{C}_{bb}}\sigma_\chi$, where σ_χ is the standard deviation of the residues and $\mathbf{C}_{bb}$ is the diagonal element of the covariant matrix corresponding to the parameter b_{glob}. To this value we add the resolution δz_w of the wall detection procedure, and thus the resulting precision $\delta b_{glob} = \sigma_b + \delta z_w$ ranges from 30 to 70 nanometers.

Let's now compare these results to the theoretical prediction for a surface with a periodic pattern of boundary conditions. In particular, Philip (1972) deduced the analytical expression of the effective slip length for a periodic pattern of no slip and

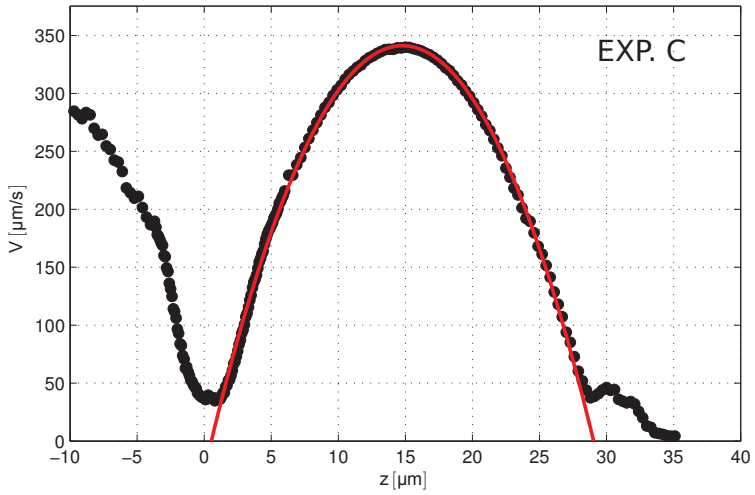

Figure 4.14: Velocity profile (black solid circles) averaged on the transverse direction and the corresponding fitting curve (red solid line) to a 1D pressure driven flow with a sticky wall and a partial slippery wall.

no shear stripes parallel to the flow. The predicted value for a pattern length L and a "no slip" fraction Φ_s is

$$b_{th} = -\frac{L}{\pi} \log \left[\cos \left(\frac{\pi}{2} (1 - \Phi_s) \right) \right] \tag{4.9}$$

For the examined Si-SHS, where $\Phi_s = 0.5$ and L=32 μm, the expected effective slip length is $b = 3.53$ μm. This value is one order of magnitude bigger than what we measured. Moreover, we obtained slip lengths very different from each other even though we adopted the same superhydrophobic surface sample. For instance, the slip length for the case A is about one and a half times bigger than that one of the cases C and even two and a half time bigger than that one of the case B.

This leads us considering the presence of one or more factors, not taken into account by the theoretical model of Philip, that strongly affect the slippery behaviour of the surface. Indeed, since those unknown and uncontrolled factors might changes from one experiment to another, it could be explained the dependence of the global effective slip length on the individual measurement. In order to further investigate those disagreements between the theory and the experiments, in the next paragraph we map the effective slip length onto the transverse direction so that we can judge to what extent the theoretical model assuming a periodic sequence of no slip and no shear stripes can properly describe the actual Si-SHS.

Local effective slip length relative to the solid wall

Instead of averaging the velocities along the transverse direction, we separately fit, to the model of Eq.(4.8), each velocity profile corresponding to a vertical slice, thereby getting an estimate of the effective slip length averaged over a region of 3.94 μm (64 pixels) in width. Indeed, recalling the definition of the effective slip length b and rewriting it in the case of a liquid flowing in the y direction, past an interface parallel to the xy plane, we have

$$\sigma_{yz} = \frac{\eta}{b} V_y \tag{4.10}$$

where σ_{ij} is the stress tensor, V_i the velocity field and η the liquid viscosity. Since in the case of longitudinal grooves, the velocity components V_x, V_y, V_z do not depend on the y coordinate, it results

$$\frac{\partial V_y(x,z)}{\partial z} + \frac{\partial V_z(x,z)}{\partial y} = \frac{\partial V_y(x,z)}{\partial z} = \frac{\eta}{b} V_y(x,z) \tag{4.11}$$

Therefore, the model of Eq.(4.8), used for the calculation of the global effective slip length, is still valid when the local effective slip length has to be determined. Figure 4.15 shows a 3D representation of the experimental velocity profiles (case A) measured at different transverse positions. While the black line represents the detected solid wall, the red line indicates the measured local effective slip length. In Figure 4.16 we plot the local slip lengths for the three cases: A, B and C. It's worth noting that the local slip lengths are computed assuming as the reference wall the straight line $z_w(x)$ (black solid lines), obtained by the linear regression of the discrete wall positions $z_{w,i}$. Considering the local slip lengths b_{loc} as a function of the transverse position x, in all of the three cases they share the same shape, very similar to that one of a Gaussian function. On the other hand, the function peaks are quite different and they are very far away from the infinity value assumed by the

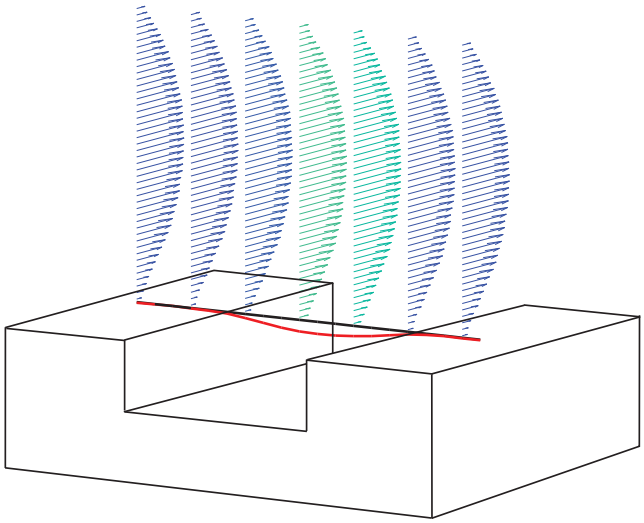

Figure 4.15: 3D reconstruction of the measured velocity profiles for the case A on a series of vertical slices. The black solid line identifies the detected wall position, while the red solid line locates where the velocity profiles extrapolate to zero. The higher is the measured local effective slip length and the brighter is the corresponding velocity profile.

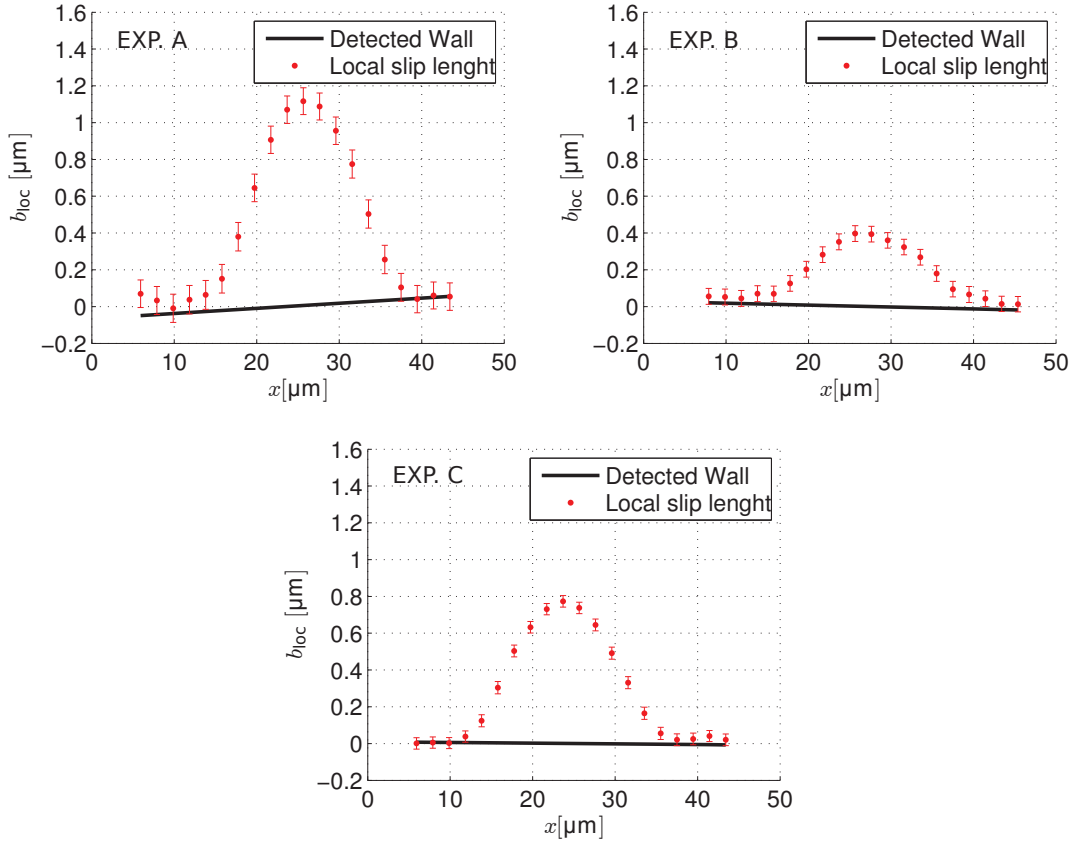

Figure 4.16: Local effective slip length as a function of the transverse coordinate x for all the three cases. The slip lengths are measured assuming the detected liquid/solid interfaces as the reference walls.

theoretical model. Consequently, the theoretical prediction of the global slip length doesn't match the experimental one.

Let's now imagine that the reason of such a mismatch is the uncontrolled shape of the meniscus at the liquid/air interface. In principle, different meniscus curvatures could justify the variability of the measured slip length as well as the strong increase of the whole surface friction, compared to the theoretical predictions. Those assumption was already introduced by Richardson (1973) and Jansons (1988) and then experimentally verified by Steinberger et al. (2007). In the latter study, nanorheology measurements of the boundary flow on a surface with holes filled by microbubbles were performed via a dynamic surface force apparatus. A Newtonian liquid was periodically squeezed and stretched between an oscillating sphere and the microstructured surface, while monitoring the sphere complex force response. The damping part of this response (namely, the imaginary part) is related to the effective hydrodynamic boundary condition on the surface. Both the Wenzel and the Cassie regimes were analyzed and, interestingly, a smaller effective slip length was detected for the latter. Comparing the elastic response (namely, the real part) to a continuous elastohydrodynamic model, the authors determined the stiffness of the trapped microbubbles and, consequently, estimated the protrusion angle of the meniscus, that is the angle formed by the tangent of the meniscus at the three-phase line and the horizontal line. The influence of the meniscus curvature on the effective slip length was then quantified via finite element simulation of a Couette flow between a moving plain surface and a microstructured one. The numerical results showed how a protruding angle deteriorates the surface slippage and for angles larger than 45° the slip length in the Cassie state is even smaller than in the Wenzel state. The experimental results were in good agreement with the simulations so that the observed sticky behaviour of the surface could be explained by the meniscus curvature. Thus, since the trapped gas can also act as anti-lubricant, resulting in high surface friction, the meniscus curvature has to be monitored and controlled. To validate a similar behaviour for the surface geometry we are considering, we need to determine the profile of the liquid/air interface for the examined cases. Accordingly, in the next paragraph we present an easy and effective method for the meniscus detection, based on an appropriate post-processing of the same PIV images adopted for the velocity field measurements.

Detection of the air/liquid interface

Let's consider a scan close to the Si-SHS, made of sets of N images recorded at M evenly spaced focal planes. Every frame is divided in S slices parallel to the flow direction y, as schematically shown by the dotted lines in Figure 4.17. Considering the image n, belonging to one stack of N images at the position z, we detect the maximum intensity pixel values $I_{n,s}(z)$ in every slice $s \in [1; S]$. Then, we compute the average intensity $I_s(z)$ over the N images, that is

$$I_s(z) = \sum_{n=1}^{N} I_{n,s}(z) \tag{4.12}$$

In Figure 4.17 we plot the function $I_s(z)$ for a specific slice (the red one in Figure). That function is very well fitted by a shifted error function (red solid line). The shift value z_0 can be considered as the position of the centers of the colloids closest to the liquid/air or solid/air interface opposite the examined slice. That position can also

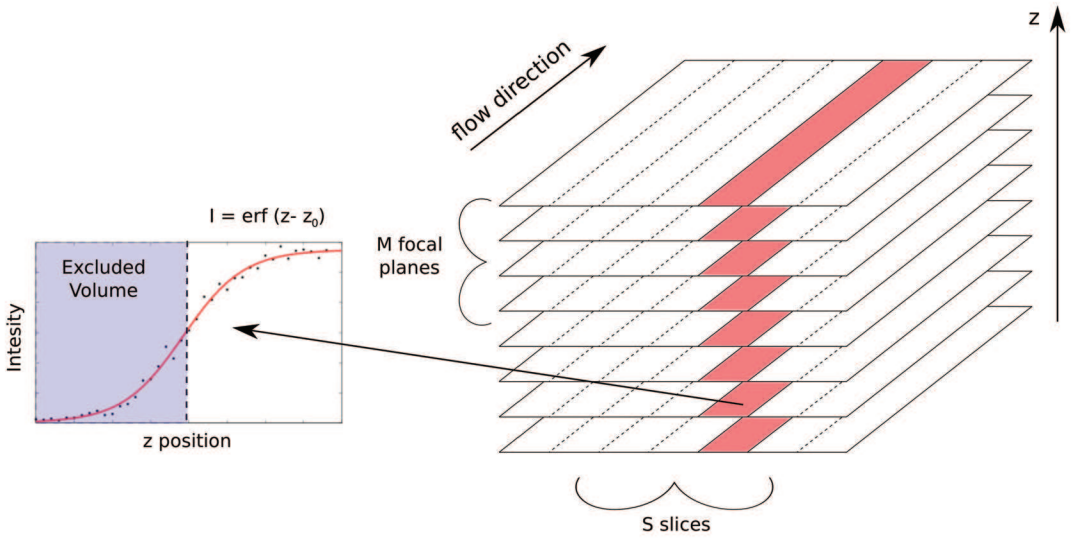

Figure 4.17: Scheme of the algorithm used to detect the liquid/solid and air/solid interfaces. For each image, we determine the maximum pixel intensity in each slice parallel to the flow direction and, then, we average it over the N frames corresponding to the same focal plane position. The resulting intensity profile is fitted to a shifted error function and the shift value z_0 detects the border of the excluded volume, that is the region close to the solid/liquid or air/liquid interface where no colloids have been detected.

be regarded as the upper limit of the excluded volume, that is the region close to the silicon interface where no colloids have been detected. Iterating the procedure for all the slices, we can detect the excluded volume along the transverse direction. It's worth noting that before computing the intensity $I_{n,s}(z)$, a background noise reduction has been performed by subtracting to the frames their mean value computed over the N images belonging to the same focal plane. Therefore, the colloids stuck to the solid wall are no longer present in the analysed images and, hence, only moving colloids are detected.

Figure 4.18 shows those excluded volume profiles (red empty circles) for the three cases. The slice width is 1.97 μm (16 pixels) and an overlap between consecutive slices of 50% has been set. Assuming that the Si-SHS surface is approximately located at $z = 0$, the scanned focal planes lie in a volume between $z = -4\,\mu$m and $z = 6\,\mu$m and are evenly spaced 100 nm apart (see Table 4.2). The red dashed lines are obtained by a linear regression of those points corresponding to the solid walls. In the same Figure, we compare these results to the positions of the silicon wall (black solid line) detected by the reflective surface properties. In the experiment C, where the flow rate is very stable and the reflected velocity profile has a very good quality (see Figure 4.11), the thickness of the excluded volume is about 250 nm on liquid/solid interfaces and that is in a good agreement with the nominal particle radius of 150 nm. Therefore, we can conclude that the detected excluded volume only accounts for the fact that the particles cannot go through the silicon wall, due to their solid nature. A similar behaviour can be assumed also at the liquid/air interface, due to the particle hydrophilicity. Hence, other hydrodynamics effects that might influence the excluded volume, as the Saffman lift, have to be excluded. Indeed, as discussed by Wereley and Meinhart (2005) the Saffman effect induces a migration slip V_m in the direction of the velocity gradient G, as long as the particle move with a relative velocity V_s with respect to the fluid. The ratio of the V_m and

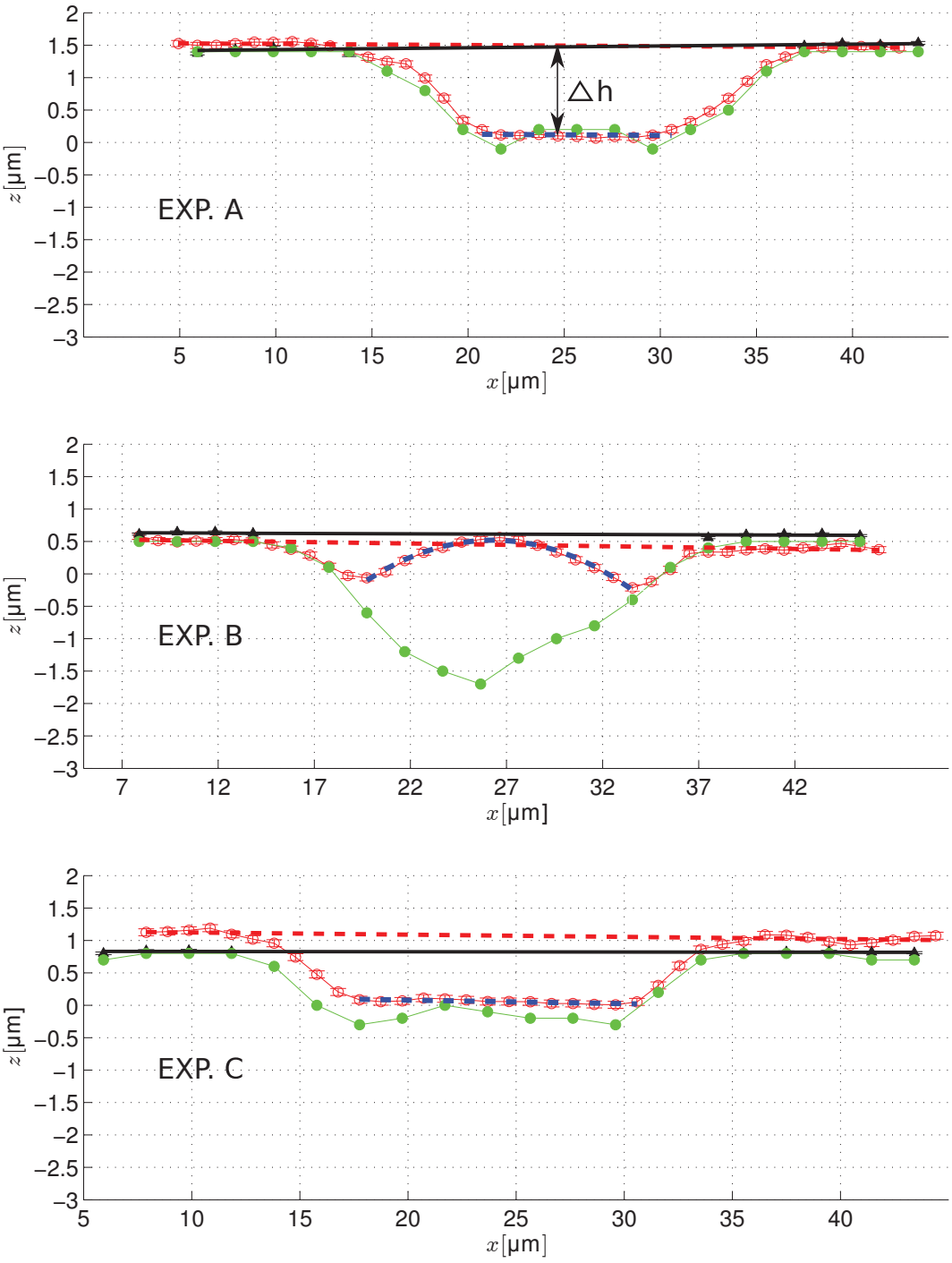

Figure 4.18: Comparison between the interface profiles detected by different methods for all the three cases.

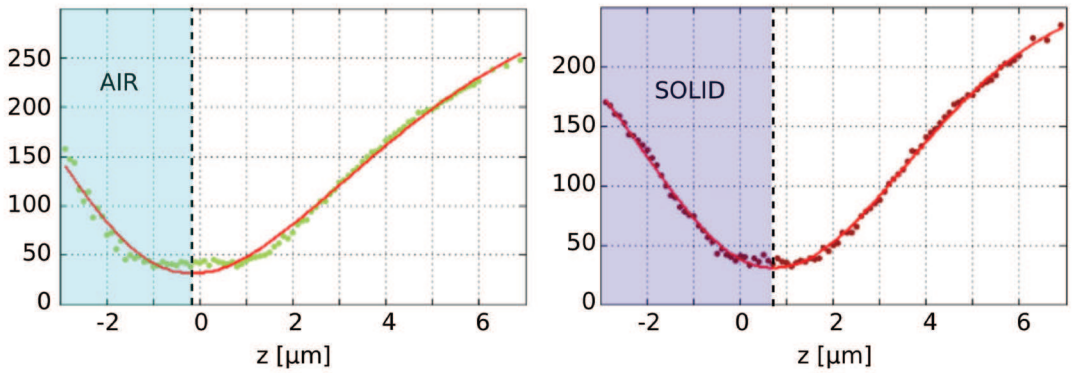

Figure 4.19: Velocity profiles $V_x(z)$ close to the air/liquid (on the left) and solid/liquid (on the right) interfaces and the corresponding fitting curves to Eq.(4.14). The black dashed lines identifies the position of the minimum detected velocity, that can be assumed as the position of the interface.

V_s can be estimated as

$$\frac{V_m}{V_s} = 0.343a\sqrt{\frac{G}{\eta}} \tag{4.13}$$

that is less than $2 \cdot 10^{-5}$ in our case. In the other two cases (A and B), there is not a sensitive different between the detected wall and the upper limit of the excluded volume. This might be the consequence of a low quality of experimental data that results in an offset of the localization of the reflective solid interface.

Finally, we also tested another approach that directly determines the liquid/air and liquid/solid interfaces rather than locating the colloids closest to those interfaces. This method is based on the assumption that the relative minimum of the velocity profile close to the Si-SHS identifies the position of the reflective surface irrespective of the surface shape. Even if this method is quite crude, it provides us with reliable results and it can also be applied at the liquid/air interface, where the measured reflected profile is difficult to model because of the complex geometry the meniscus can assume. Instead of detecting the smallest recorded velocity, we fit a small slice, few microns in width and centered at the Si-SHS interface, of the velocity profiles $V_x(z)$ to a guess function $f(z)$, arbitrarily defined as

$$f(z) = A_1 \left[1 - A_2 \exp\left(-\frac{(z - A_3)^2}{A_4^2}\right)\right] \left[1 + \mathrm{erf}\left(A_5 \frac{z - A_3}{A_4}\right)\right] \tag{4.14}$$

where A_i, $i \in [1, \cdot, 5]$ are the fitting parameters. The choice of $f(z)$ is due to the fact that it is in very good agreement with the experimental data, as shown by the quality of the fit in Figure 4.19. However it's worth noting that this expression is not based on a physical model accounting for the reflections at the solid and air interfaces. Once the relative minimum of the fitting curve $f(z)$ is located, the procedure is iterated for the different transverse position x and, thus, the profile of the minimum velocity positions is traced. In Figure 4.18, the detected interface profiles for the three cases are represented by the green solid circles. The presented method gives results in agreement with both the solid wall detection based on the fit to the 1D Poiseuille velocity profile and the meniscus detection based on the excluded volume. Only in the case B, the method fails to detect the liquid/air interface since the objective was not able to collect the light reflected by the interface. The reason might be the

marked curvature of the meniscus that results in a very distorted reflection at the liquid/air interface.

Discussion

Regarding the measured interface shapes, two important aspects have to be underlined. First, the meniscus curvature assumes a finite value in the case B and fitting to a circle (blue dashed line in Figure 4.18) reveals a curvature radius of $35 \pm 1\,\mu$m, that corresponds to an angle between the tangent of the meniscus at the three-phase line and the horizontal line of $\theta = 13.2^\circ \pm 0.4^\circ$. On the other hand, in the cases A and C the liquid/air interfaces are totally flat. Secondly, there is a finite distance Δh between the position of the colloids closest to the liquid/solid interface and those closest to the liquid/air interface. This length is represented in Figure 4.18 by the distance between the red dashed lines and the blue dashed lines (see Exp. A). When the meniscus is not flat, as in the case B, Δh is evaluated as the vertical distance between the red dashed line and the extremities of the blue dashed line. As already discussed, we can assume that the thickness of the excluded volume is the same at the liquid/solid and liquid/air interfaces. As a consequence of that, Δh is also a good estimate of the vertical shift between the silicon solid wall and the liquid/air meniscus. Such distance assumes different values in all of the three experiments and they are surely responsible for the changing in the global slip lengths. In Table 4.4 we report the measured interface distances Δh as well as the radii of curvature R (the angle θ) and we compare them to the global slip lengths, while in Figure 4.20 we show a three-dimensional plot of those quantities. For sake of clarity, we also plot the projections (empty circles) of the 3D points on the coordinate planes. According to finite element analysis reported by Teo and Khoo (2010) (see figure 12.b in that work), for the specific case of a 1D pressure driven flow in a channel with a superhydrophobic wall consisting of alternating grooves and ribs parallel to the flow direction with a solid fraction of 0.5 and a channel height comparable to the period of the surface pattern, the dependence of the global effective slip length on slight positive or negative curvatures of the meniscus are negligible. Those results are in agreement with the theoretical predictions of Sbragaglia and Prosperetti (2007). Unfortunately, we have measured only three points of the two variables function $b_{glob}(\Delta h, \theta)$ and, thus, further experiments with varying meniscus curvatures would be needed to confirm their theoretical and numerical predictions. Conversely, by our experiments it is evident that the slip length b_{glob} increases proportionally to the vertical shift between the solid/liquid and air/liquid interfaces Δh, as shown in Figure 4.21. That's quite surprising since for a no shear interface the global slip length b_{glob} decays with the distance Δh, as shown in the semi-analytical solution by Ng and Wang (2009), whereas it increases with Δh in the case of a no-slip interface. Therefore, this behaviour suggests the presence of a no-moving liquid/air interface. In addition, the distances Δh are comparable to the local effective slip length measured on the liquid/air interfaces, once the solid wall is assumed as the reference wall (see Figure 4.16). Thus, we conclude that the liquid velocity at the liquid/air interface is almost zero and the measured global slip length is essentially due to the partial water filling of the grooves rather than a perfect slip interface, as assumed in the theoretical model.

What might be the reason causing the air/liquid interface to be immobilized as it were a solid interface? A similar behaviour in a quite different context has already been reported in literature by Ybert and Di Meglio (1998), experimentally

	A	**B**	**C**
Δh	1.38 ± 0.09 μm	0.684 ± 0.07 μm	1.00 ± 0.075 μm
R	0.0 ± 1 μm	35.0 ± 1 μm	0 ± 1 μm
θ	$0.0 \pm 0.4°$	$13.2 \pm 0.4°$	$0.0 \pm 0.4°$
b_{glob}	457 ± 56 nm	186 ± 42 nm	277 ± 70 nm

Table 4.4: Parameters of the liquid/air interfaces for the three cases.

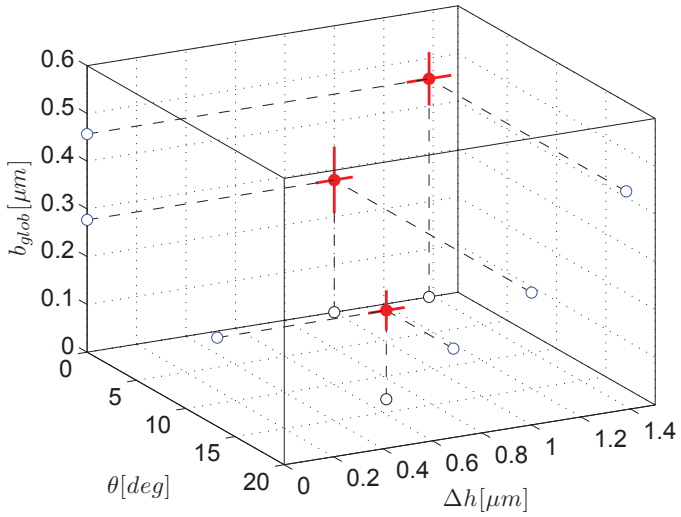

Figure 4.20: Plot of the global effective slip length (red solid circles) as a function of the vertical shift of the meniscus Δh and its slope at the three-phase line. The empty circles are the projections on the coordinate planes.

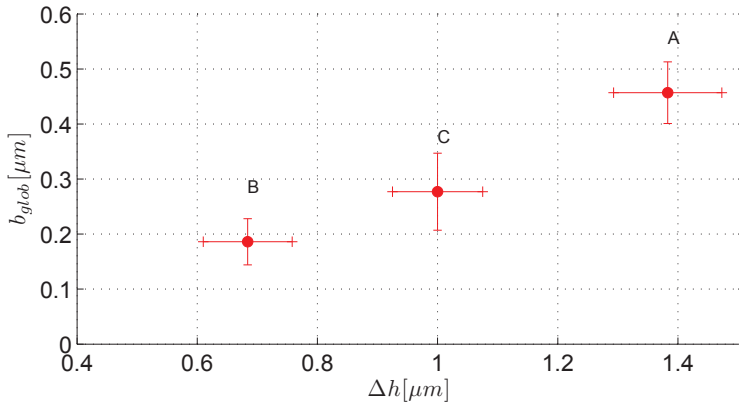

Figure 4.21: Global effective slip length vs the meniscus vertical shift.

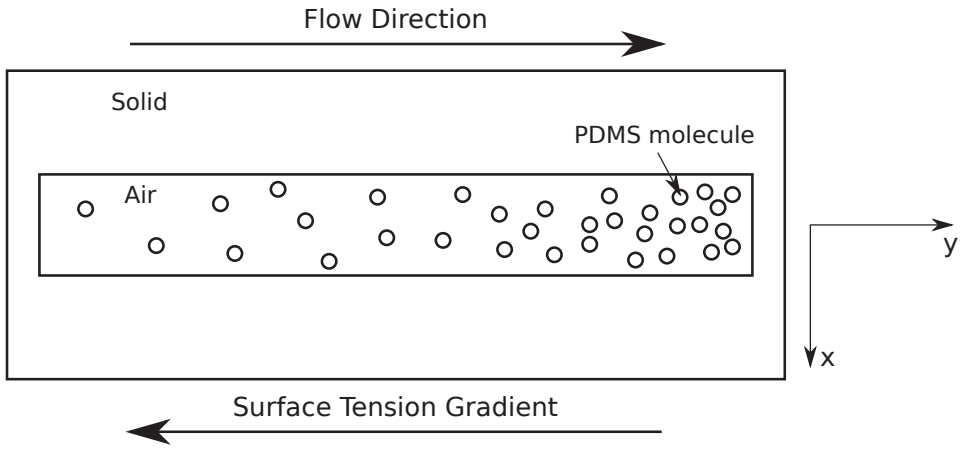

Figure 4.22: Scheme of the contamination of the meniscus by PDMS molecules. The onset of a surface tension gradient contrast the slippage at the liquid/air interface.

investigating the ascending velocity of air bubbles in BSA (bovine serum albumin) protein water solutions. As the bubbles rise in the water volume, their velocities decrease until a lower limit is reached. The authors demonstrated as this phenomenon is due to the absorption of proteins at the liquid/air interface and the higher concentration, promoted by the external flow, of BSA particles at the rear part of the bubbles. The onset of a surface concentration gradient and, hence, a surface tension gradient along the air/liquid interface results in a surface stress which opposed the flow (Marangoni effect). Accordingly, the overall friction is enhanced and the bubbles' speed decreases. The limit is achieved when the concentration gradient hamper the interface motion and the bubbles become hydrodynamically equivalent to rigid spheres. We conjecture that a similar phenomenon might occur at the meniscus of the examined Si-SHS sample, the PDMS molecules being the contaminant particles affecting the liquid/air surface mobility. Indeed, the liquid/air interface is confined in a rectangular region, 1 mm in length and 16 μm in width, as shown in Figure 4.22. Since a part of the channel is made of a manually cut PDMS film, PDMS molecules are dispersed in the water solution at a finite homogeneous concentration. Due to the liquid flow, the PDMS molecules, adsorbed at the liquid/air interface, might be pushed against the downstream transverse wall and a concentration gradient could be established. Clearly, the PDMS contamination of the interface cannot exceed a certain threshold, as the low solid surface tension of the polymer ($\gamma_{s,PDMS} = 19.8$ mN/m) would destabilize the Cassie state. The Wenzel transition rarely occurred in our experiments and, thus, to valid the PDMS contamination as a possible explanation of the low measured global slip length, we should calculate what is the PDMS concentration needed to sensitively reduce the surface mobility and verify that it is not critical for the superhydrophobic state of the silicon sample. As proved by Ybert and Di Meglio (1998), a simple estimate can be carried out by balancing the viscous stress τ_v with the surface tension gradient along the liquid/air interface

$$\tau_v \simeq \frac{\Delta\gamma}{l} \tag{4.15}$$

where $l = 1$ mm is the longitudinal size of the groove. The viscous stress determined by the fitted profiles is about 0.05Pa, hence a surface pressure of $\Delta\gamma \simeq 5{\times}10^{-2}$mN/m may be sufficient to immobilize the interface. Thus the variation in the surface ten-

sion would be weak enough to do not threat the stability of the Cassie state. Referring to the measurements of surface pressures at the water/air interface for various PDMS concentrations, performed by Mann and Langevin (1991), the estimated $\Delta\gamma$ corresponds to a PDMS concentration difference between the grooves' extremities of about $10^{-3}\mathrm{mg/m^2}$.

At the present state of the research, the PDMS contamination is a possible explanation but further investigation are needed to corroborate it. For instance, before the channel is assembled, the PDMS film can be covered by a Teflon layer preventing the PDMS molecules to be released in the water solution. Alternatively, the μ-PIV analysis of the flow past Si-SHS with transverse grooves may also shed a new light on the reported phenomenon.

2.6 Conclusions

In this chapter, we presented the results of the direct measurements of water flow past a superhydrophobic surfaces made of ribs, 16 μm in width, parallel to the flow direction and evenly separated by grooves, 16 μm in width as well. Adopting the micro particle image velocimetry technique, we obtained the velocity profiles along the channel height, averaged on a series of vertical slices 3.95 μm in thickness at several transverse positions. Exploiting the reflective properties of the flat silicon wall and measuring the velocities of both the real and virtual images of the fluorescent colloids, we determined the position of the solid/liquid interface with a precision of tens of nanometers. The improved resolution of the wall detection, compared to other existing methods, allows more accurate measurements of the effective slip length. In addition, the presented method is not affected by the uncertainty of the individual colloid size, due to particle polydispersity, as in Joseph et al. (2006), and it can also detect possible misalignment between the solid walls and the horizontal line.

Averaging the velocity profiles on both the spanwise and streamwise directions, we fitted to a pressure driven flow in a one-dimensional channel with one sticky and one slippery walls. The global effective slip length was a fitting parameter and its value was determined for three different channel scans, using the same silicon sample. The resulting slip lengths were one order of magnitude less than the theoretical prediction of Philip (1972) and they assumed different values through the three examined cases. To further investigate this discrepancy, we calculated the local effective slip length as a function of the transverse coordinate, assuming the detected silicon flat surface as the reference wall. At the liquid/solid interface the local slip length vanished identically as expected. On the contrary, a finite local slip length was measured at the liquid/air interface, with a peak value at the center of the meniscus, barely exceeding 1 μm. Assuming the meniscus shape to be the responsible of an apparent finite shear stress, we devised a procedure to post-process the PIV images in order to detect the excluded volume, that is the region close to the silicon surface where no moving particle were visualized. We compared it to the position of the solid silicon wall and we verified that the thickness of the excluded volume is compatible with the particle size. Assuming that such a thickness was constant along the transverse direction, the shape of liquid/solid and liquid/air interfaces were determined. A method to measure the meniscus shape has already been presented by Ou et al. (2004), relying on a confocal surface metrology system. Herein, we only used the recorded PIV images and thus no further measurements are needed to detect the liquid/air interface. Moreover, the discussed method is computationally

fast and very easy-to-implement. As long as we use the same images to measure the flow velocities and the interface shapes, we can also directly relate one to the other. Indeed, if two separate measurements were conducted, we could not guarantee the meniscus shape has been kept constant in the elapsed time between the two measurements.

Finally we related the measured meniscus shape and its relative position to the global slip length. Even though only three different meniscus shapes were examined, the results suggested that the liquid/air interfaces were immobilized and the effective slip lengths were due to the partial protrusion of water inside the grooves. As an explanation of this behaviour, we conjecture that the PDMS molecule adsorption at the liquid/air interface could be responsible of this apparent effective high friction at the Si-SHS. However, further investigations are needed to verify or reject such an hypothesis.

References

Bocquet, L., Tabeling, P., and Manneville, S. (2006). Comment on large slip of aqueous liquid flow over a nanoengineered superhydrophobic surface. *Physical review letters*, 97(10):109601.

Byun, D., Kim, J., Ko, H., and Park, H. (2008). Direct measurement of slip flows in superhydrophobic microchannels with transverse grooves. *Physics of Fluids*, 20:113601.

Cassie, A. and Baxter, S. (1944). Wettability of porous surfaces. *Transactions of the Faraday Society*, 40(5):546–551.

Choi, C. and Kim, C. (2006). Large slip of aqueous liquid flow over a nanoengineered superhydrophobic surface. *Physical review letters*, 96(6):66001.

Choi, C., Ulmanella, U., Kim, J., Ho, C., and Kim, C. (2006). Effective slip and friction reduction in nanograted superhydrophobic microchannels. *Physics of Fluids*, 18:087105.

Coghill, W. and Anderson, C. (1923). 262:47.

Davies, J., Maynes, D., Webb, B., and Woolford, B. (2006). Laminar flow in a microchannel with superhydrophobic walls exhibiting transverse ribs. *Physics of fluids*, 18:087110.

Gao, X. and Jiang, L. (2004). Biophysics: water-repellent legs of water striders. *Nature*, 432(7013):36–36.

Garrod, R., Harris, L., Schofield, W., McGettrick, J., Ward, L., Teare, D., and Badyal, J. (2007). Mimicking a stenocara beetle's back for microcondensation using plasmachemical patterned superhydrophobic-superhydrophilic surfaces. *Langmuir*, 23(2):689–693.

Guo, Z., Zhou, F., Hao, J., Liang, Y., Liu, W., and Huck, W. (2006). "stick and slide" ferrofluidic droplets on superhydrophobic surfaces. *Applied physics letters*, 89:081911.

Huang, D., Cottin-Bizonne, C., Ybert, C., and Bocquet, L. (2008). Massive amplification of surface-induced transport at superhydrophobic surfaces. *Physical review letters*, 101(6):64503.

Jansons, K. (1988). Determination of the macroscopic (partial) slip boundary condition for a viscous flow over a randomly rough surface with a perfect slip microscopic boundary condition. *Physics of Fluids*, 31:15.

Joseph, P., Cottin-Bizonne, C., Benoit, J., Ybert, C., Journet, C., Tabeling, P., and Bocquet, L. (2006). Slippage of water past superhydrophobic carbon nanotube forests in microchannels. *Physical review letters*, 97(15):156104.

Lee, C., Choi, C., and Kim, C. (2008). Structured surfaces for a giant liquid slip. *Physical review letters*, 101(6):64501.

Lee, C. and Kim, C. (2011). Underwater restoration and retention of gases on superhydrophobic surfaces for drag reduction. *Physical Review Letters*, 106(1):14502.

Li, X., Reinhoudt, D., and Crego-Calama, M. (2007). What do we need for a superhydrophobic surface? a review on the recent progress in the preparation of superhydrophobic surfaces. *Chem. Soc. Rev.*, 36(8):1350–1368.

Lu, C., Xie, Y., Yang, Y., Mark, M., Koh, C., Bai, Y., Lee, L., and Juang, Y. (2007). New valve and bonding designs for microfluidic biochips containing proteins. *Analytical chemistry*, 79(3):994–1001.

Mann, E. and Langevin, D. (1991). Poly (dimethylsiloxane) molecular layers at the surface of water and of aqueous surfactant solutions. *Langmuir*, 7(6):1112–1117.

Maynes, D., Webb, B., and Davies, J. (2008). Thermal transport in a microchannel exhibiting ultrahydrophobic microribs maintained at constant temperature. *Journal of Heat Transfer*, 130:022402.

Mock, U., Förster, R., Menz, W., and Rühe, J. (2005). Towards ultrahydrophobic surfaces: a biomimetic approach. *Journal of Physics: Condensed Matter*, 17:S639.

Neinhuis, C. and Barthlott, W. (1997). Characterization and distribution of water-repellent, self-cleaning plant surfaces. *Annals of Botany*, 79(6):667.

Ng, C. and Wang, C. (2009). Stokes shear flow over a grating: Implications for superhydrophobic slip. *Physics of Fluids*, 21:013602.

Ollivier, H. (1907). *Annales de Chimie et Physique*, 10:229.

Ostuni, E., Chen, C., Ingber, D., and Whitesides, G. (2001). Selective deposition of proteins and cells in arrays of microwells. *Langmuir*, 17(9):2828–2834.

Otten, A. and Herminghaus, S. (2004). How plants keep dry: a physicist's point of view. *Langmuir*, 20(6):2405–2408.

Ou, J., Moss, G., and Rothstein, J. (2007). Enhanced mixing in laminar flows using ultrahydrophobic surfaces. *Physical Review E*, 76(1):016304.

Ou, J., Perot, B., and Rothstein, J. (2004). Laminar drag reduction in microchannels using ultrahydrophobic surfaces. *Physics of fluids*, 16:4635.

Ou, J. and Rothstein, J. (2005). Direct velocity measurements of the flow past drag-reducing ultrahydrophobic surfaces. *Physics of Fluids*, 17:103606.

Parker, A. and Lawrence, C. (2001). Water capture by a desert beetle. *Nature*, 414(6859):33–34.

Philip, J. (1972). Flows satisfying mixed no-slip and no-shear conditions. *Zeitschrift für Angewandte Mathematik und Physik (ZAMP)*, 23(3):353–372.

Richardson, S. (1973). On the no-slip boundary condition. *Journal of Fluid Mechanics*, 59(04):707–719.

Roach, P., Shirtcliffe, N., Farrar, D., and Perry, C. (2006). Quantification of surface-bound proteins by fluorometric assay: Comparison with quartz crystal microbalance and amido black assay. *The Journal of Physical Chemistry B*, 110(41):20572–20579.

Rothstein, J. (2010). Slip on superhydrophobic surfaces. *Annual Review of Fluid Mechanics*, 42:89–109.

Sbragaglia, M. and Prosperetti, A. (2007). A note on the effective slip properties for microchannel flows with ultrahydrophobic surfaces. *Physics of Fluids*, 19:043603.

Shi, F., Niu, J., Liu, J., Liu, F., Wang, Z., Feng, X., and Zhang, X. (2007). Inside front cover: Towards understanding why a superhydrophobic coating is needed by water striders (adv. mater. 17/2007). *Advanced Materials*, 19(17):n–a.

Steinberger, A., Cottin-Bizonne, C., Kleimann, P., and Charlaix, E. (2007). High friction on a bubble mattress. *Nature Materials*, 6(9):665–668.

Stroock, A., Dertinger, S., Ajdari, A., Mezić, I., Stone, H., and Whitesides, G. (2002). Chaotic mixer for microchannels. *Science*, 295(5555):647.

Sun, T., Tan, H., Han, D., Fu, Q., and Jiang, L. (2005). No platelet can adherelargely improved blood compatibility on nanostructured superhydrophobic surfaces. *Small*, 1(10):959–963.

Takeda, K., Nakajima, A., Hashimoto, K., and Watanabe, T. (2002). Jump of water droplet from a super-hydrophobic film by vertical electric field. *Surface science*, 519(1-2):L589–L592.

Teo, C. and Khoo, B. (2010). Flow past superhydrophobic surfaces containing longitudinal grooves: Effects of interface curvature. *Microfluidics and Nanofluidics*, pages 1–13.

Toes, G., Van Muiswinkel, K., Van Oeveren, W., Suurmeijer, A., Timens, W., Stokroos, I., and Van den Dungen, J. (2002). Superhydrophobic modification fails to improve the performance of small diameter expanded polytetrafluoroethylene vascular grafts. *Biomaterials*, 23(1):255–262.

Torkkeli, A., Saarilahti, J., Haara, A., Harma, H., Soukka, T., and Tolonen, P. (2001). Electrostatic transportation of water droplets on superhydrophobic surfaces. In *Micro Electro Mechanical Systems, 2001. MEMS 2001. The 14th IEEE International Conference on*, pages 475–478. IEEE.

Truesdell, R., Mammoli, A., Vorobieff, P., van Swol, F., and Brinker, C. (2006). Drag reduction on a patterned superhydrophobic surface. *Physical review letters*, 97(4):44504.

Tsai, P., Peters, A., Pirat, C., Wessling, M., Lammertink, R., and Lohse, D. (2009). Quantifying effective slip length over micropatterned hydrophobic surfaces. *Physics of Fluids*, 21:112002.

Washizu, M. (1998). Electrostatic actuation of liquid droplets for micro-reactor applications. *Industry Applications, IEEE Transactions on*, 34(4):732–737.

Wenzel, R. (1936). Resistance of solid surfaces to wetting by water. *Industrial & Engineering Chemistry*, 28(8):988–994.

Wereley, S. and Meinhart, C. (2005). Micron-resolution particle image velocimetry. *Microscale Diagnostic Techniques*, pages 51–112.

Ybert, C. and Di Meglio, J. (1998). Ascending air bubbles in protein solutions. *The European Physical Journal B-Condensed Matter and Complex Systems*, 4(3):313–319.

Zhai, L., Berg, M., Cebeci, F., Kim, Y., Milwid, J., Rubner, M., and Cohen, R. (2006). Patterned superhydrophobic surfaces: toward a synthetic mimic of the namib desert beetle. *Nano letters*, 6(6):1213–1217.

Zhang, X., Shi, F., Niu, J., Jiang, Y., and Wang, Z. (2008). Superhydrophobic surfaces: from structural control to functional application. *Journal of Materials Chemistry*, 18(6):621–633.

Chapter 5

Porous silicon superhydrophobic surfaces

In the last decades, several technologies have been proposed to fabricate superhydrophobic surfaces. In this respect, a complete review on the progress in the preparation of such surfaces is provided by Li et al. (2007). Very recently, the porous silicon technology has demonstrated to be one of the most simple and economical way to obtain superhydrophobic surfaces.

In this chapter, we present a preliminary study of the fabrication and characterization of the wetting properties of macroporous silicon surfaces, obtained by anodization in hydrogen fluoride solution of p-type silicon wafers. After briefly recalling the few works that have been currently published on the superhydrophobic porous silicon technology (Section 1), we describe our procedure for superhydrophobic sample preparation, displaying the obtained results through scanning electro microscope images (Section 2.2). The water repellency of the surfaces is measured by static contact angle measurements (Section 2.3) and the dependence of the surface wettability on the fabrication process parameters is also investigated. In Section 3.1, we analysed the results in term of the Cassie and Wenzel models. On the basis of the obtained results, we propose a mixing behavior where the water only partially fills in the surface micropores. Relying on numerical simulations for equivalent surface geometries, reported in literature, we finally predict the expected slip length on the examined superhydrophobic samples (Section 3.2).

1 Fabrication of SHSs via silicon porosification: state of the art

Since the seminal papers of Canham (1990) and Lehmann and Gosele (1991), porous silicon (pSi) has been one of the most studied materials in the field of material sciences and has triggered intense developments in the nanotechnology research. The first observation of pSi layers traces back at the middle of the 20th century, thanks to the experimental works of Uhlir (1956) and Turner (1958), where silicon porosification was obtained by electrochemical dissolution of silicon wafers in aqueous or ethanoic HF solutions. The morphology of pSi can be effectively controlled and, depending on the process parameters, spans from 2 nanometers (nanoporous/microporous silicon) up to tens of micrometers (macroporous silicon). The strong interest of the scientific and technological community in pSi can be explained by several factors: an easy-to-implement fabrication process; a high surface area-to-volume ratio; a pore geometry and morphology as well as optical properties that can be easily tuned; biocompatibility and biodegrability. Thus, pSi has wide range of applications in photonic and optoelectronics, see Cullis et al. (1997), MEMS technology and microelectronics, see Bomchil et al. (1989); Bell et al. (1996), quantum electronics, see Read et al. (1992), fuel cells technology, see Aravamudhan et al. (2005), medical therapy, see Rajaraman and Henderson (2005), and biosensors, see Ressine et al. (2007). For a comprehensive review on the different pSi fabrication technique, we refer the interested reader to the work of Korotcenkov and Cho (2010).

Despite the huge amount of work on this subject, it's only six years ago that the superhydrophobic potentiality of pSi has been reported for the first time by Ressine et al. (2005). In the scientific research, it is quite usual that one can unexpectedly find out very interesting phenomena, even if they were not foreseen and were not the main focus of the original study. Similarly, during the development of protein microarray technology based on pSi, Ressine et al. (2005) found the superhydrophobic state to be possible on both nanoporous and microporous silicon surfaces. One year later, porous silicon superhydrophobic surfaces (pSi-SHSs) with contact angles up to 160° were obtained by Cao et al. (2006). Investigating the dependence of the wettability and reflectivity on the etching method and the surface morphology, the authors found that not all the examined porous structures led to the superhydrophobic state.

Introducing a 2-step method, consisting of a electrochemical surface modification followed by a wet etching, Wang et al. (2007) fabricated a pSi-SHS with contact angle of 160° and a sliding angle less than 1°. Afterward Ressine et al. (2008) demonstrated that appropriately selecting the fabrication process of the pSi yields to very different wetting properties, ranging from highly wetting (nanoporous morphologies) to superhydrophobic (macroporous morphologies) surfaces. By silanizing the macroporous structures, contact angles as high as 176° were achieved. The authors also investigated the possible application of those surfaces for protein microarray realization. A gold-assisted electroless etching process was adopted by Cao et al. (2008) to get a hierarchical porous structure, made of micrometer sized asperities and superimposed onto a network of nanometer sized porous. That resulted in a superhydrophobic phenomenon and, as long as an oleophilic self-assembled monolayer is deposited on the pSi surface, in a superoleophobic phenomenon, with contact angles exceeding 160°. The wetting properties as well as the tribological properties of pSi-SHSs coated by a fluorocarbon alkylsilane molecular layer have been studied

by Liu et al. (2009). A contact angle exceeding 160° and a reduction in the friction coefficient have been reported.

In this Chapter, we explore the feasibility of an easy-to-implement and economical microfabrication technique for realizing macroporous silicon superhydrophobic surfaces. A preliminary study of the wetting properties of those surfaces is conducted through contact angle measurements. We compare the experimental results with classical wetting models, in order to get insight into the physical phenomenon. In addition, we use the empirical formulas of Ng and Wang (2010) to provide an estimate of the slip length on the presented geometry.

2 Experimental investigations of pSi-SHSs

2.1 Introduction

In this Section, we examine a microfabrication technique based on porous silicon as means for producing inexpensive superhydrophobic surfaces. The morphology of a p-type silicon wafer is modified by a electrochemical dissolution to produce pores with controlled size and distribution; surfaces are then coated with a silane layer. Large contact angles are observed on such surfaces and the results are compared with classical wetting models (Cassie and Wenzel) suggesting a mixed Wenzel-Cassie behaviour. In addition, in the light of slip length estimates, we discuss further improvements for the use of such surface in microfluidic applications.

2.2 Surface preparation

The pSi-SHSs are realized from 10-20 Ωcm resistivity p-type silicon wafers with {100} orientation. A macroporous silicon layer of 20 μm thickness is obtained by anodization in a solution of hydrogen fluoride and dimethyl sulfoxide (HF:DMSO, 10 : 46) solution at 10 $\mathrm{mA\,cm^{-2}}$ for 30 minutes. During the anodization process, only a circular area of 1 $\mathrm{cm^2}$ is exposed to the solution. Hence, on the same wafer, both smooth and porous regions are present. Figure 5.1 and Figure 5.2 show a top view and a cross section of a representative porous silicon sample obtained with the described process. The macroporous silicon layer is characterized by a porosity $n = 0.55$ and average pore Feret diameter (or caliper diameter) of $0.86 \pm 0.46\mu$m. Porosity is measured from the gray scale top view scanning electron microscope (SEM) images, see Figure 5.1, by counting the percentage of pixels whose intensity exceeds a set threshold. This figure accounts for the fully developed pores, corresponding to the darker regions of Figure 5.1, as well as the partially developed ones, see Figure 5.2 and explanation therein.

The wafers are then coated with 1H,1H,2H,2H-Perfluorooctyltrichlorosilane; 97% (ABCR) via physical vapour deposition (PVD). We adopt the following procedure. Immediately after anodization the samples are rinsed in deionized (DI) water and dried in N_2. The surface is then activated by exposition to an oxygen plasma in a reactive ion etching (RIE) chamber. Finally the samples are coated with a silane layer via low pressure PVD. The effect of acetone washing on silanized samples is also investigated, by performing a 4 min sonication on part of the samples.

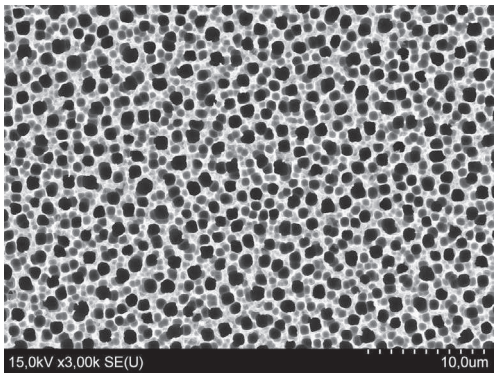

Figure 5.1: Top view SEM image of a macroporous silicon sample. Pores correspond to the black areas, while gray areas are the interpores, pits in the silicon surface that have not reached full depth. Air trapped within the pores may be exploited to reduce the wall friction.

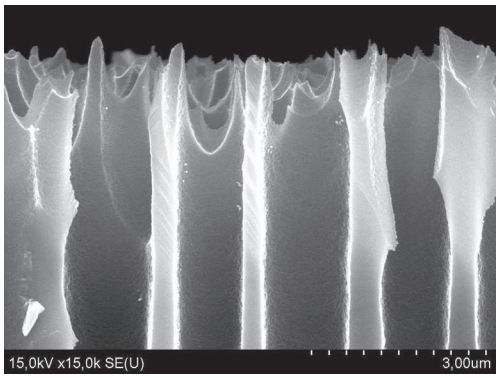

Figure 5.2: Section of the macroporous silicon layer near the surface. Superficial roughness, due to pore walls dissolution and interpores is also evident from this section. The low energy silane coating prevents water from filling in the pores, thus creating a mixed solid-air boundary for the flow.

2.3 Contact angle measurements

We adopt the sessile drop method to measure contact angles (CA) over the porous silicon samples. Figure 5.3 shows a schematic view of the contact angle measurement system. A Nikon D7000 camera, equipped with a Micro-Nikkon 60mm $f2.8/D$ objective, records images of millimeter size sessile DI water drops, at rest over horizontal surface samples. Those surfaces are placed on a moving stage, fitted with three linear step motors, driven by a PC, to adjust along three orthogonal directions the drop position with respect to the camera focal plane. We use a freely available software, *DropSnake*, developed by Stalder et al. (2006), to process images and measure contact angles. In Figure 5.4, we show some representative results of image analysis. In particular, the top panel shows a sessile drop on a smooth silane coated silicon wafer. The bottom panel, instead, reports a drop on the porous silane-coated portion of the wafer. The software requires a user-defined detection of the drop boundary (the blue solid line in the Figures), which is used as initial guess for the B-spline fitting of the drop boundary. The red solid line is the final computed boundary whence the left and right contact angles are measured. For

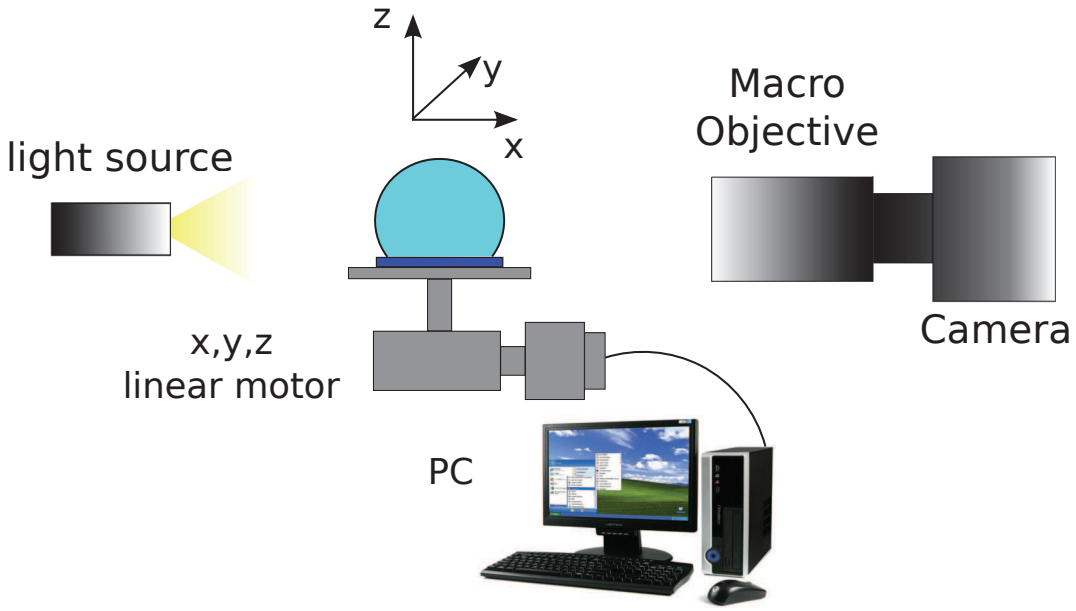

Figure 5.3: Schematic view of the of the contact angle measurement system.

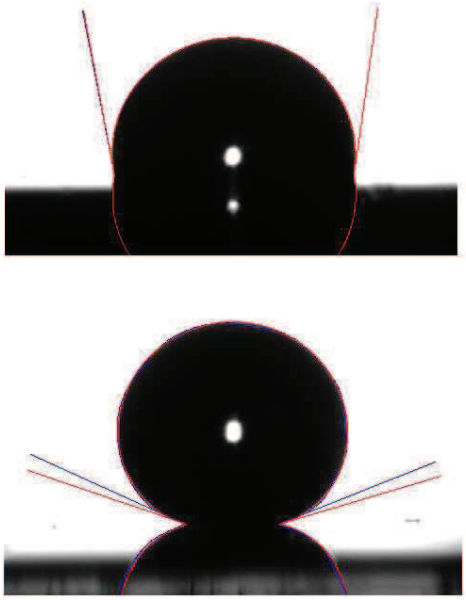

Figure 5.4: Top panel: water drop on smooth silicon surface coated with silane (case C in Table 5.1). Bottom panel: water drop on porous silicon surface coated with silane (case A in Table 5.1). The contact angles are measured using the *DropSnake* plugin for *ImageJ*. The blue lines represent the initial guess drop boundary while the red one the final drop profile as calculated by the software.

	Time [min]	Current [mA cm^{-2}]	Porous	Acetone sonication	Contact Angle [°]
A	30	10	YES	NO	154.5 ± 1.5
B	-	-	NO	NO	98.5 ± 0.6
C	30	10	YES	YES	152.8 ± 1.1
D	-	-	NO	YES	101.8 ± 2.3
E	15	15	YES	NO	160.8 ± 1.6
F	30	5	YES	NO	156.0 ± 1.6

Table 5.1: Summary of the experimental results, along with the fabrication parameters (anodization time and current). Average values between the left and right contact angles are reported. The effect of acetone sonication is also shown.

further details on the software implementation and accuracy, the interested reader is referred to the work of Stalder et al. (2006). The contact angles extracted with *DropSnake* are found to be robust to small changes in the user-defined definition of the drop boundary.

The average contact angles are reported in Table 5.1. We compute the averages by analyzing at least five images of a sessile drop on the same sample, recorded after moving the drop on different positions of the observed region. In this way we aim at averaging the effect of local morphology on the contact angle, that is one of the causes of contact angle hysteresis. For the same reason, we average right and left contact angles.

3 Results and discussion

In Table 5.1 we summarize the contact angle measurements under different experimental conditions, with the aim of investigating the effect of *(i)* surface morphology and *(ii)* low energy coating. We preliminarily note that non-coated samples are hydrophilic, presenting contact angles of 75° on smooth samples and lower on porous ones. Only contact angles after silanization are reported in Table 5.1. Case A refers to silanized porous surfaces obtained by anodization at 10 mA cm^{-2} for 30 minutes. The resulting contact angle of $154.5° \pm 1.5°$ shows that the presented method is successful in providing highly hydrophobic silicon surfaces. The evidence that an effective surface energy modification is prompted by the silane PVD is provided by the contact angle of $98.5° \pm 0.6°$ measured over silanized smooth silicon surfaces (Case B). This value is in line with the experimental contact angle values reported in Janssen et al. (2006) for surfaces coated with various silane types. This value is also compatible with that reported in the molecular dynamics simulations of Chinappi and Casciola (2010) for OTS coated flat silicon. The influence of surface morphology on the contact angle is reflected in the largely different values reported in the cases A and B, and is immediately evident from the images reported in Figure 5.4.

The effect of organic solvent washing of the coated samples is tested by performing an acetone sonication of the samples. The cleaning procedure is applied to both porous and smooth silicon surfaces, corresponding to Cases C and D of Table 5.1, respectively. Though not quantified, some benefits are expected from acetone washing, based on what reported by Chen and Brauer (1982). We only detect slight variations in contact angles, possibly due to the cleaning from surface contaminants

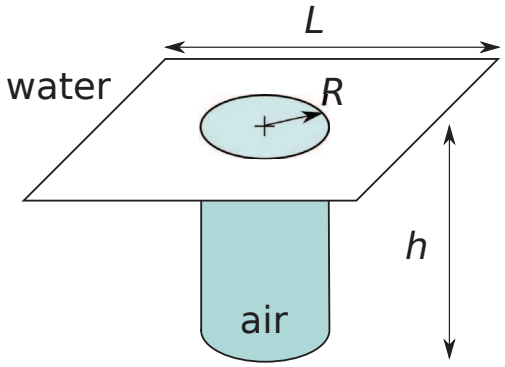

Figure 5.5: Illustration of the idealized lattice used to model the SHS of Figure 5.1 and Figure 5.2 in the calculations. The square lattice is characterized by its length L. Air is trapped within the cylindrical pore of radius R and height h. Water is in contact with the whole periodic cell having area L^2.

obtained with the acetone wash.

Furthermore, we performed preliminary studies on the sensitivity to process parameters such as current density and process time. We report in Table 5.1 the contact angle values for samples anodized at $15\,\mathrm{mA\,cm^{-2}}$ for 15 minutes (case E) and $5\,\mathrm{mA\,cm^{-2}}$ for 30 minutes (case F). In the presented configuration, case E corresponds to the highest value of current density attainable before electropolishing takes place. From the analysis of SEM sections analogous to Figure 5.2, we find that pore morphology shows low sensitivity to current density. Accordingly, anodization parameters affect only weakly the obtained surface water repellency, see Table 5.1.

3.1 Comparison to the theoretical models

We now appeal to two classical models in order to interpret the reported experimental data in relation to the surface morphology. In particular, the increase of contact angle between the porous silicon and the smooth surfaces is analyzed in view of the Cassie and the Wenzel models, presented in Section 1.1 of Chapter 4. We just recall that according to the Wenzel model, the liquid is assumed to fill in totally the surface roughness profile, thereby increasing by a factor r the actual wetted area, when compared to the case of a flat wetted surface. On the other hand, in the Cassie model air pockets are assumed to be trapped within the surface pores and the liquid is in contact with the solid only at a reduced surface fraction Φ_s.

Informed by the analysis of the SEM images in Section 2.2, it is possible to provide an estimate for r and ϕ_s. In particular, ϕ_s coincides with the complement to unity of the surface porosity, that is, $\phi_s = 1 - n = 0.45$. The estimate of r is less straightforward. We consider an idealized surface having the same solid fraction ϕ_s and the pore radius R of our pSi-SHS. Each pore is perfectly circular and pores are regularly distributed on a square lattice of size L, see the sketch in Figure 5.5. Within this scheme, the following relation between L, ϕ_s and R is valid:

$$L^2(1 - \phi_s) = \pi R^2 \tag{5.1}$$

that, after some manipulations, leads to:

$$r = \phi_s + (1 - \phi_s)(2h/R + 1) \tag{5.2}$$

This expression is still valid if the pores are not on a regular lattice. However, Eq.(5.2) is not appropriate in the case of pore overlap. Overlaps actually happen as apparent in Figure 5.1 and the surface morphology is more complicated of the ideal case we are considering. Nevertheless Eq. (5.2) still provides a rough estimation of r. For $\phi_s = 0.45$ and $h/R \simeq 20$, Eq. (5.2) yields $r \simeq 27$. This value of r, combined with the average contact angle value measured on smooth silicon computed from Cases B and D in Table 5.1, that is $\theta = 100°$, leads to a left hand side of Eq. (4.2) smaller than -1. While this value has no direct physical meaning, we can note that the closest physically significant case of $\cos\theta_W = -1$ corresponds to the perfectly hydrophobic state, where the surface is not wetted. These considerations suggest that the Wenzel model is not adequate to explain the phenomenology on the considered morphology, and that reasonably the roughness profile is not fully wetted. In a similar case, the failure of the Wenzel model to predict the contact angle on pSi was already pointed out by Dattilo et al. (2006). By coating pSi surface with a hydrophilic layer of fulleropyrrolidine (contact angle 85°) through a thermal hydrosilylation protocol, the authors found that the porous structure promoted higher contact angles (105°). That is in clear contrast to the Wenzel model, according to which the roughness reinforces the hydrophilic character of the corresponding flat surface.

In respect of the Cassie model, Eq.(4.3), along with the roughness value $\phi_s = 0.45$ and the experimental value $\theta = 100°$, yields $\theta_C \simeq 129°$. The experimental contact angles on porous surfaces coated with silane are however larger than the Cassie estimate, while smaller than the perfectly hydrophobic surface towards which the Wenzel model tends. A possible explanation of the discrepancies between the experimental data and the Wenzel and Cassie models may be found in the partial filling of the pores. This phenomenology is intermediate between the limiting cases of the fully wetted surface and the "fakir" state, embodied by the Wenzel and Cassie models, respectively.

A simple model for this scenario is now presented. Let us suppose that the pores on the regular lattice of Figure 5.5, are filled up to a certain depth d. The contact angle is then given by the weighed average of the contact angles, see Rothstein (2010):

$$\cos\theta^* = \sum_i c_i \cos\theta_i = \phi_s \cos\theta + (r' - 1)\cos\theta - (1 - \phi_s) \tag{5.3}$$

Here r' has the same expression of Eq. (5.1), where the wetted depth d is substituted to the pore height h. Substituting in Eq. (5.3) the experimental data $\theta = 100°$ and $\theta^* = 155°$ we can provide an estimate for the wetted depth $d = 1.3\,\mu$m. This value appears reasonable in view of the SEM images reported in Figure 5.2, but provides only a consistency check on the model. Further investigations of the pore filling of water on hydrophobic rough surfaces is needed to gain a better insight in the phenomenon.

3.2 Slip length models

Following the numerical results of Ng and Wang (2010), we are able to compute the expected slip length for the realized pSi-SHS based on its geometrical characteristics. We first note that the surface shown in Figure 5.1, with connected pore walls, corresponds to the *hole* geometry described in Ybert et al. (2007) and in Ng and Wang (2010), the other one being *pillar*. For the same square lattice of cylindrical

holes sketched in Figure 5.5, Ng and Wang (2010) provide the following empirical formula, based on a fit of numerical data:

$$\beta = -0.134 \ln \phi_s - 0.023 \tag{5.4}$$

where $\beta = b/L$ is the slip length adimenionalized with the square lattice size L. This formula provides an estimate of the solid fraction versus slip length relation within the range $0.22 < \phi_s < 0.75$, based on a semi-analytical solution of a Stokes shear flow with mixed boundary conditions reproducing the lattice of Figure 5.5. Plugging in Eq. (5.4) the measured value $\phi_s = 0.45$, we obtain $\beta = 0.084$. Using Eq. (5.1) and half the Feret diameter $R = 0.43\,\mu$m, we give a figure for the idealized lattice size yielding the experimental solid fraction $\phi_s = 0.45$, that is, $L = 1.0\,\mu$m. The final estimate for slip length for a Stokes shear flow on a hole pattern having the same average characteristics of the SHS is therefore $b = 84$ nm, in line with the experimental findings of Choi et al. (2006).

We note, however, that this estimate is a rough one, and actual experimental values may vary significantly. One limit in applying the analysis of Ng and Wang (2010) to the present surface is that it neglects the effects of curvature of the meniscus, that can be decisive in determining the effective slip length, particularly on hole geometries, as discussed by Steinberger et al. (2007); Ybert et al. (2007). Another issue lies in the observed discrepancy between experimental values of the contact angle from the Cassie model estimates. However, it is interesting to report possible modifications to the surface geometry based on the analysis of Ybert et al. (2007); Ng and Wang (2010) that can boost the friction-reduction capabilities of the surface. The most important consideration comes from the limitations intrinsic to the hole geometry, which is less favourable than the post geometry. We are currently exploring the fabrication parameters for enhanced interpore dissolution, in order to obtain isolated posts while decreasing the solid fraction. Another improvement may come from a prepatterning of the silicon wafer, so to obtain an ordered pore formation, as suggested by Lehmann and Ronnebeck (1999).

The effect of microslip, that is, the presence of intrinsic slip l on the solid fraction, may also be accounted for in the calculation of the effective slip b, proposed by Ng and Wang (2010). However, the increase in effective slip is proportional to the dimensionless intrinsic slip $\lambda = l/L$ according to $\Delta\beta \simeq \lambda/\phi_s$. Therefore, a significant increase in b is observed either when l is of the same order of magnitude of L, or in case of vanishing solid fraction $\phi_s \to 0$. The former case has little technological interest, at least in microscale applications, since it has been shown by Cottin-Bizonne et al. (2005) that typical values of intrinsic slip l are at most of the order of tens of nm. On the other hand, the limit of very low solid fractions poses problems with respect to the mechanical resistance of the surface and to the stability of the Cassie state.

4 Conclusions

We presented and characterized an economical microfabrication technique for superhydrophobic surfaces, based on porous silicon. The pSi-SHS is realized on a p-type silicon wafer, compatible with CMOS technology, allowing for a potential integration of microfluidics with electronics, in view of the development of lab-on-chip applications. The silane coating proved effective in stabilizing the superhydrophobic Cassie state, resulting in persistent air trapped within the pores. Measured contact angles

exceeded 150°. The resistance of the coating to organic solvents was also tested, showing good characteristics. Comparison of contact angle measurements with the available wetting models for heterogeneous surfaces suggested a partial filling of the pores, probably connected to the presence of interpore pitting. The slip length was estimated from numerical results available in literature, yielding $b = 84$ nm.

References

Aravamudhan, S., Rahman, A., and Bhansali, S. (2005). Porous silicon based orientation independent, self-priming micro direct ethanol fuel cell. *Sensors and Actuators A: Physical*, 123:497–504.

Bell, T., Gennissen, P., DeMunter, D., and Kuhl, M. (1996). Porous silicon as a sacrificial material. *Journal of Micromechanics and Microengineering*, 6:361.

Bomchil, G., Halimaoui, A., and Herino, R. (1989). Porous silicon: The material and its applications in silicon-on-insulator technologies. *Applied Surface Science*, 41:604–613.

Canham, L. (1990). Silicon quantum wire array fabrication by electrochemical and chemical dissolution of wafers. *Applied Physics Letters*, 57(10):1046–1048.

Cao, L., Price, T., Weiss, M., and Gao*, D. (2008). Super water-and oil-repellent surfaces on intrinsically hydrophilic and oleophilic porous silicon films. *Langmuir*, 24(5):1640–1643.

Cao, M., Song, X., Zhai, J., Wang, J., and Wang, Y. (2006). Fabrication of highly antireflective silicon surfaces with superhydrophobicity. *The Journal of Physical Chemistry B*, 110(26):13072–13075.

Chen, T. and Brauer, G. (1982). Solvent effects on bonding organo-silane to silica surfaces. *Journal of Dental Research*, 61(12):1439.

Chinappi, M. and Casciola, C. (2010). Intrinsic slip on hydrophobic self-assembled monolayer coatings. *Physics of Fluids*, 22:042003.

Choi, C., Ulmanella, U., Kim, J., Ho, C., and Kim, C. (2006). Effective slip and friction reduction in nanograted superhydrophobic microchannels. *Physics of Fluids*, 18:087105.

Cottin-Bizonne, C., Cross, B., Steinberger, A., and Charlaix, E. (2005). Boundary slip on smooth hydrophobic surfaces: Intrinsic effects and possible artifacts. *Physical Review Letters*, 94(5):56102.

Cullis, A., Canham, L., and Calcott, P. (1997). The structural and luminescence properties of porous silicon. *Journal of Applied Physics*, 82:909.

Dattilo, D., Armelao, L., Maggini, M., Fois, G., and Mistura, G. (2006). Wetting behavior of porous silicon surfaces functionalized with a fulleropyrrolidine. *Langmuir*, 22(21):8764–8769.

Janssen, D., De Palma, R., Verlaak, S., Heremans, P., and Dehaen, W. (2006). Static solvent contact angle measurements, surface free energy and wettability determination of various self-assembled monolayers on silicon dioxide. *Thin Solid Films*, 515(4):1433–1438.

Korotcenkov, G. and Cho, B. (2010). Silicon porosification: State of the art. *Critical reviews in solid state and materials sciences*, 35(3):153–260.

Lehmann, V. and Gosele, U. (1991). Porous silicon formation: A quantum wire effect. *Applied Physics Letters*, 58(8):856–858.

Lehmann, V. and Ronnebeck, S. (1999). The physics of macropore formation in low-doped p-type silicon. *Journal of the Electrochemical Society*, 146(8):2968.

Li, X., Reinhoudt, D., and Crego-Calama, M. (2007). What do we need for a superhydrophobic surface? a review on the recent progress in the preparation of superhydrophobic surfaces. *Chem. Soc. Rev.*, 36(8):1350–1368.

Liu, Y., Wang, X., Luo, J., and Lu, X. (2009). Fabrication and tribological properties of super-hydrophobic surfaces based on porous silicon. *Applied Surface Science*, 255(23):9430–9438.

Ng, C.-O. and Wang, C. Y. (2010). Apparent slip arising from Stokes shear flow over a bidimensional patterned surface. *Microfluidics and Nanofluidics*, 8(3):361–371.

Rajaraman, S. and Henderson, H. (2005). A unique fabrication approach for microneedles using coherent porous silicon technology. *Sensors and Actuators B: Chemical*, 105(2):443–448.

Read, A., Needs, R., Nash, K., Canham, L., Calcott, P., and Qteish, A. (1992). First-principles calculations of the electronic properties of silicon quantum wires. *Physical review letters*, 69(8):1232–1235.

Ressine, A., Finnskog, D., Marko-Varga, G., and Laurell, T. (2005). Superhydrophobic and hydrophilic states on porous silicon. In *Proceedings of microTAS 2005 Conference*, volume 1, pages 256–258.

Ressine, A., Finnskog, D., Marko-Varga, G., and Laurell, T. (2008). Superhydrophobic Properties of Nanostructured–Microstructured Porous Silicon for Improved Surface-Based Bioanalysis. *NanoBiotechnology*, 4(1):18–27.

Ressine, A., Marko-Varga, G., and Laurell, T. (2007). Porous silicon protein microarray technology and ultra-/superhydrophobic states for improved bioanalytical readout. *Biotechnology Annual Review*, 13:149–200.

Rothstein, J. (2010). Slip on superhydrophobic surfaces. *Annual Review of Fluid Mechanics*, 42:89–109.

Stalder, A., Kulik, G., Sage, D., Barbieri, L., and Hoffmann, P. (2006). A snake-based approach to accurate determination of both contact points and contact angles. *Colloids and Surfaces A: Physicochemical and Engineering Aspects*, 286(1-3):92–103.

Steinberger, A., Cottin-Bizonne, C., Kleimann, P., and Charlaix, E. (2007). High friction on a bubble mattress. *Nature Materials*, 6(9):665–668.

Turner, D. (1958). Electropolishing silicon in hydrofluoric acid solutions. *Journal of the Electrochemical Society*, 105:402.

Uhlir, A. (1956). Electrolytic shaping of germanium and silicon. *Bell Syst. Tech. J*, 35(2):333.

Wang, M., Raghunathan, N., and Ziaie, B. (2007). A nonlithographic top-down electrochemical approach for creating hierarchical (micro-nano) superhydrophobic silicon surfaces. *Langmuir*, 23(5):2300–2303.

Ybert, C., Barentin, C., Cottin-Bizonne, C., Joseph, P., and Bocquet, L. (2007). Achieving large slip with superhydrophobic surfaces: Scaling laws for generic geometries. *Physics of Fluids*, 19(12):123601.

Chapter 6

Conclusions and perspectives

1 Towards a novel experimental technique for local measurements of effective slip length

As mentioned in the preface, this thesis is part of a wider project for setting up an innovative technique to investigate the fluid-solid slippage on superhydrophobic surfaces by means of optical tweezers. The original idea came up at the beginning of the collaboration between the three research groups that I have worked with during my international joint Ph.D. studentship. Those groups are the Fluid Dynamics group at the Department of Mechanical and Aerospace Engineering of the University of Rome, the microPhysics group of National Research Council (CNR) at the Department of Physics of the University of Rome and the Liquids and Interfaces group at the Laboratory of Physics of Condensed Matter and Nanostructures of University Claude Bernard Lyon 1. The knowledge and expertise of those research units in different scientific fields as computational fluid dynamics (Fluid Dynamics group), optical trapping (μ-Physics group) and experimental microfluidics (Liquids and Interfaces group) are joined together for the development of a novel experimental technique that involves several disciplines.

The main idea of the project originates from the theoretical work of Lauga and Squires (2005), where the authors addressed the problem of the several and contrasting experimental results reported in literature for the quantification of fluid/solid slip on hydrophobic and superhydrophobic surfaces. As extensively reviewed by Lauga et al. (2006), the apparent violation of the no-slip condition has been investigated for several experimental conditions (namely, wetting, partial wetting, non-wetting surfaces, flat and rough surfaces, etc.) and effective slip lengths ranging from nanometers to microns have been reported. The published results show a strong dependence on the experimental techniques employed. Moreover, experimental data could be easily misinterpreted when apparent slip is affected by physical mechanisms other than liquid/solid slippage. Existing experimental techniques for the characterization of fluid/solid slippage on both hydrophobic and super-hydrophobic surfaces can be classified in five categories, as reported by Lauga et al. (2006). (i) The reduced hydrodynamic resistance in a channel equipped with a hydrophobic or super-hydrophobic surface has been detected by measuring at the same time the channel flow rate and pressure drop, as proposed by Cheng and Giordano (2002). Comparing the experimental results with the theoretical prediction for the

hydrodynamic resistance, an indirect measurement of the slip length is obtained. (ii) Probing the force drag experienced by a small probe that squeezes flow in a confined geometry is the working principle of slip measurements through surface force apparatus and atomic force microscope, as reported, among others, by Craig et al. (2001), Bonaccurso et al. (2002), Cottin-Bizonne et al. (2002) and Cottin-Bizonne et al. (2005). (iii) Conversely, one can directly measure the velocity profiles tracing the motion of passive tracers dispersed in water, as we described in Chapter 4. (iv) The flow can also be directly measured only in a limited region close to the examined wall via fluorescence correlation spectroscopy, as reported by Lumma et al. (2003), or (v) near field laser velocimetry where photobleached molecular probes are tracked using evanescent optical waves, as presented by Pit et al. (2000) and Hervet and Leger (2003).

All of those techniques have in common the fact of requiring an externally-forced flow or motion that adds experimental uncertainties (namely, accurate flow measurement, flow stability, etc.). To eliminate this and other drawbacks, Lauga and Squires (2005) have proposed a simple method to infer the slip length at the liquid/solid interface, based on the diffusivity of a single mesoscopic particle immersed in a fluid at rest and located close to the wall. In that work, they presented the solution of the Stokes equations in term of an image system for point forces (Stokeslets) oriented parallel and perpendicular to a surface with a finite slip length. Afterwards, they determined the drag force exerted on a spherical particle and, consequently, the diffusion coefficient of the colloid as a function of the finite slip length. Thus, tracking the Brownian motion and comparing the diffusivity in the parallel and perpendicular directions to the theoretical prediction, the colloid can be regarded as a local probe of the boundary conditions at the slipping surface. It's worth noting that the presented method works if the flow induced by the colloid is described only with the lowest order singularity (i.e. the Stokeslet), neglecting the higher order terms. This leads to good approximation when the distance h between the particle and the wall is at least one order of magnitude larger than the particle radius a. Nevertheless, more complicated schemes, as one or more colloids placed near the wall ($h/a < 10$), can be studied via boundary-integral methods, relying on the fundamental solutions proposed in the cited work.

As remarked by Lauga and Squires (2005), for accurate slip measurements the probe size has to be comparable with the expected slip length at the examined interface. Therefore, $1\,\mu$m diameter particles are good candidates to probe the slip length on superhydrophobic surfaces. This is the typical size of the colloidal particles we used in Part I of this thesis for three-dimensional manipulation and visualization. Consequently, the nanometric accuracy of digital holographic tracking and its sizing capabilities (demonstrated in Chapter 3) coupled with three-dimensional accurate positioning of holographic tweezers (shown in Chapter 1) gave us the opportunity to periodically trap and release several colloids with a specific initial configuration (for instance at the vertices of a square as in Section 2 of Chapter 3) and to measure with high accuracy the individual mobilities (namely, the diffusivities) as well as the hydrodynamic couplings of those probes (as we performed for the two aligned microrods in Section 2 of Chapter 1). This is the central idea for the development of the new technique to characterize fluid/solid slippage on superhydrophobic surfaces. Indeed, once we compare the experimental values of mobilities and coupling terms with the theoretical or numerical predictions we can infer the slip length of superhydrophobic surfaces.

The hydrodynamic interactions between several trapped colloids or between one or more trapped colloids and a solid wall have already been performed, as reported by Leach et al. (2009) and Di Leonardo et al. (2007), but those experiments have never been extended to the case of a superhydrophobic surface. Nevertheless, we firmly believe that holographic tweezers together with holographic microscopy has great potentialities for the investigation of the slippage behaviour on patterned surfaces. Tracking the free Brownian motion of individual colloids close to an interface drastically simplify the measurements with respect to other existing techniques, avoiding the presence of possible artifacts and/or external factors that could affect the slip length estimate. On the other hand, using the holographic manipulation and trapping require two optical accesses to the sample, namely one from the top and one from the bottom. Thus, only microfluidic chip that are transparent to trapping and illuminating laser light can be used. This is not a strict constraint, since transparent materials as Polydimethylsiloxane (PDMS) and glass are very common in lab-on-a-chip technology. Conversely, the superhydrophobic surfaces made of silicon, as the ones examined in Chapter 4 and Chapter 5, are opaque to visible light. This problem can be overcome by replacing the holographic microscope with a standard bright field microscope in reflection-mode or with a fluorescence microscope. Even though in such configurations the axial tracking is no longer available, the two-dimensional tracking of the probes is enough to determine the diffusivities in the directions parallel to the surface. Those diffusivities are more affected by the presence of a partially slipping wall with respect to the perpendicular diffusivity, as demonstrated by Lauga and Squires (2005). Consequently, an accurate determination of the slip length is still possible when holographic microscopy can not be used.

In conclusion, the presented studies on holographic visualization, optical trapping and superhydrophobicity pave the way for the realization of a novel and complementary experimental technique for the characterization of the fluid/solid slippage that will play an important role in the future advances in the technological and scientific domain of superhydrophobic surfaces.

References

Bonaccurso, E., Kappl, M., and Butt, H. (2002). Hydrodynamic force measurements: boundary slip of water on hydrophilic surfaces and electrokinetic effects. *Physical review letters*, 88(7):76103.

Cheng, J. and Giordano, N. (2002). Fluid flow through nanometer-scale channels. *Physical Review E*, 65(3):031206.

Cottin-Bizonne, C., Cross, B., Steinberger, A., and Charlaix, E. (2005). Boundary slip on smooth hydrophobic surfaces: intrinsic effects and possible artifacts. *Physical review letters*, 94(5):56102.

Cottin-Bizonne, C., Jurine, S., Baudry, J., Crassous, J., Restagno, F., and Charlaix, E. (2002). Nanorheology: an investigation of the boundary condition at hydrophobic and hydrophilic interfaces. *The European Physical Journal E: Soft Matter and Biological Physics*, 9(1):47–53.

Craig, V., Neto, C., and Williams, D. (2001). Shear-dependent boundary slip in an aqueous newtonian liquid. *Physical review letters*, 87(5):54504.

Di Leonardo, R., Keen, S., Leach, J., Saunter, C., Love, G., Ruocco, G., and Padgett, M. (2007). Eigenmodes of a hydrodynamically coupled micron-size multiple-particle ring. *Physical Review E*, 76(6):061402.

Hervet, H. and Leger, L. (2003). Flow with slip at the wall: from simple to complex fluids. *Comptes Rendus Physique*, 4(2):241–249.

Lauga, E., Brenner, M., and Stone, H. (2006). Microfluidics: The no-slip boundary condition. *Perspective*, 17:1.

Lauga, E. and Squires, T. (2005). Brownian motion near a partial-slip boundary: A local probe of the no-slip condition. *Physics of Fluids*, 17:103102.

Leach, J., Mushfique, H., Keen, S., Di Leonardo, R., Ruocco, G., Cooper, J., and Padgett, M. (2009). Comparison of Faxéns correction for a microsphere translating or rotating near a surface. *Physical Review E*, 79(2):26301.

Lumma, D., Best, A., Gansen, A., Feuillebois, F., Rädler, J., and Vinogradova, O. (2003). Flow profile near a wall measured by double-focus fluorescence cross-correlation. *Physical Review E*, 67(5):056313.

Pit, R., Hervet, H., and Leger, L. (2000). Direct experimental evidence of slip in hexadecane: solid interfaces. *Physical Review Letters*, 85(5):980–983.

APPENDIX

Appendix A

Diffusion-driven flow on superhydrophobic surfaces

1 Surface driven-flows and superhydrophobicity

One of the major issue in experimental microfluidics and lab-on-a-chip technology is the huge increase in hydrodynamic resistance due to the reduced size of the channel networks. In such devices characterized by a very high surface to volume ratio, the pressure gradient is no more effective to drive the flow inside geometries where the adherence condition applies at the liquid/solid interfaces (namely, almost everywhere). Instead, in a surface-driven flow the fluid transport is due to dynamical processes occurring within the interfacial region, whose thickness λ is one or more orders of magnitude smaller than the channel characteristic length L. The fluid flow is generated in the interfacial layer by application of a macroscopic gradient on the channel length scale L. In such interfacial processes, as opposed to pressure-driven flows, the increased surface to volume ratio of microfludic devices turns in a crucial factor to generate fluid flow enough intense to be used in both fundamental research and applications.

As an example, electro-osmosis (that is the flow generation by an electric field) is one the most widespread of all surface-driven phenomena for microfluidics, see Stone et al. (2004). As reported by Anderson (1989), other well-known surface-driven flows are diffusio-osmosis and thermo-osmosis where the solvent flow is induced by gradients of solute concentration and temperature, respectively. In all those processes, the interaction of the external field with a diffuse solid/fluid interface results in an apparent slip velocity V_s at the boundary of the interfacial layer (the inner region) that affects the flow throughout the fluid outside the interfacial layer (the outer region). At the length scale L, the resulting slip velocity can be interpreted as a violation of the adherence condition.

Similarly, the same concept applies when, instead of the channel wall, we consider the liquid/surface interface at the surface of colloidal particles. The flow induced at the interfacial layer close to particles propel them in the fluid, resulting in the so-called phoretic transport. This technique has been exploited in several domains. For example, in biology the double stranded DNA electrophoretic transport dynamics through nanpores has been investigated, see Chen et al. (2004). In colloid science, the attraction induced by thermophoresis has been used to drive the spontaneous

assembly of ordered structures (namely, colloidal crystals) that are very important for applied and fundamental research in statistical mechanics, as reported by Weinert and Braun (2008) and Di Leonardo et al. (2009). Relying on diffusio-phoresis and appropriately devising the microfluidic chip, Abécassis et al. (2008) has demonstrated the ability to strongly enhance the migration of large particles, otherwise driven by a very slow Brownian diffusive process, by coupling their dynamics to that of a fast carrier species, as a dilute salt. The authors proved this technique to be effective for both filtering and concentrating operations and they highlighted the wider perspective this transport mechanism has, spanning several research areas from chemotaxis-like transport in biology to sediments and pollutants dispersion in oceanography.

Very promising results can be obtained when two techniques, as the surface-driven flows and superhydrophobic surfaces (SHSs), are coupled together. In this respect, Ajdari and Bocquet (2006) have conducted analytical and numerical studies to demonstrate that even weak slip lengths b of a few ten nanometers (which is the slip length for high hydrophobic flat surfaces, as measured (among others) by Cottin-Bizonne et al. (2005), Joseph and Tabeling (2005) and Huang et al. (2006)) can result in a large enhancement of up to two orders of magnitude of the aforementioned interfacially driven phenomena. This synergetic effect is basically due to the fact that the hydrodynamic slip length b increases the slip velocity V_s by a factor of $(1 + b/\lambda)$, which can practically be of order ten to hundreds. For flat surfaces, such amplification does not depend on the nature of external field (electric potential, solute concentration, temperature) which promotes the transport. Conversely, when this process takes place on patterned hydrophobic surfaces in Cassie state the nature of the physical quantity varying on the macroscopic length scale along the flow direction is crucial. Huang et al. (2008) have studied via molecular dynamic simulations and hydrodynamic theory the flow of aqueous electrolytes at grooved SHSs in both electro and diffusio-osmosis regimes. In the former case, the driving force at the interfacial layer derives from the interaction of the external electric field and the positive and negative ions, attracted at the liquid/solid interface by the ζ potential at the solid surface. Consequently, at the charge-neutral air-water interfaces the electrical driven force vanishes and, thus, the high slip length of the SHSs do not translate in an enhanced surface transport. On the other hand, the diffusio-osmosis driven force is related to the osmotic pressure gradient that persists even on the liquid/air interface, letting be possible a flow amplification of $(1 + b/\lambda)$ that can be even more than one thousand for SHSs.

Despite Huang et al. (2008) have proposed a practical realization to exploit the synergy of diffusio-osmosis and SHSs, the experimental verification of the expected massive amplification has never been performed so far. Consequently, we decided to adapt the microfluidic chip described in Chapter 4 to experimentally demonstrate these giant transport effects. As a preliminary test, we used the same channel geometry proposed by Abécassis et al. (2008), replacing the cover slip with a silicon SHS (Si-SHS) with transverse grooves at the bottom of the channel. Basically, the microfluidic chip consisted of a channel, $400\,\mu$m in width, supplied with liquid water via three inlets in a Ψ-shape geometry. An aqueous solution of Lithium Chloride salt was injected in the channel through the two lateral inlets, whereas ultrapure Milli-Q water fed with fluorescent 200 nm diameter silica particles was introduced in the system via the central inlet. That configuration resulted in a non-vanishing gradient salt in the transverse direction of the channel. However those were not the

best conditions to achieve high amplification of the surface-transport effects. Indeed, the adopted Si-SHS had a solid fraction of 0.5 which is not enough to effectively enhance the surface transport, see Huang et al. (2008). Moreover the salt gradient was perpendicular to the main flow and thus we didn't detect sensitive surface-transport amplification. Nevertheless, in the field of scientific research, quite often one can hit on unexpected and interesting phenomena one would have never been able to anticipate at the beginning of the study. That is exactly what happened when the described system was monitored after the SHS had been collapsed to the Wenzel state. In such conditions, a combination of diffusion driving forces and hydrodynamic motion pushed and trapped the colloids in the surface grooves, which quickly accumulated therein. This phenomenon was completely reversible since ceased to exist when the gradient salt was removed and the trapped colloids diffused out of the grooves. In this Appendix, we report the experimental methods and the preliminary results of this study, highlighting the main features of the phenomenon. This introductive work will be followed in the next future by more accurate quantitative measurements and hopefully by a theoretical model being able to clarify the mechanisms of the massive colloids' trapping in surface roughness.

2 Particle trapping induced by diffusion transport processes on patterned surfaces: a preliminary study

Monitoring the fluid flow in a Ψ-shape channel via fluorescence microscopy, we qualitatively characterize the phenomenon of particle trapping inside surface grooves induced by a salt concentration gradient parallel to the grooves' axis.

The microfluidic chip is very similar to the one described in Chapter 4 for μ-PIV measurements. We replaced the hand-cut PDMS film coated cover slip with an all-PDMS channel, fabricated via soft-lithography. A SU8 mold was obtained on a silicon wafer through a standard photo-lithography process. Once the mold was accurately cleaned through ethanol and DI water rinsing and plasma oxygen exposure, liquid PDMS was poured on it and let polymerize for three hours at 75°. The right panel in Figure A.1 schematically shows the top view of the PDMS slice. The channel (black lines) has a Ψ-shape geometry with three branches joining together. The main channel is 400 μm in width, while the inlet lateral (central) branches are 100 μm (200 μm) in width. The height of the channel is 35 μm. The thickness of the PDMS substrate is 6 mm and, thus, the channel inlets and outlet can be connected to the pumping system via metallic tubes passing through the lateral walls of the

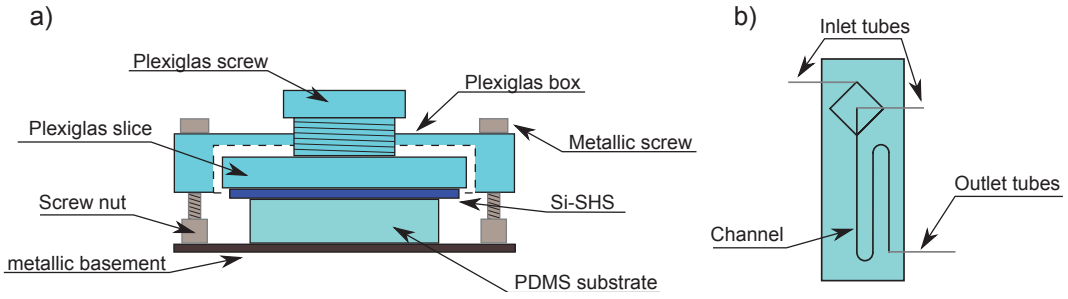

Figure A.1: Scheme of the microfluidic chip inside the sealing device (on the left) and top view of the PDMS substrate (on the right).

Experiment	Sequence	State
1	$S^C S^C S^C \rightarrow WS^C W \rightarrow SW^C S$	Cassie
2	$W^C W^C W^C \rightarrow WW^C W \rightarrow SW^C S \rightarrow WWW$	Wenzel
3	$SS^C W \rightarrow SW^C S \rightarrow SS^C S$	Wenzel

Table A.1: Summary of the experiments. For each one of them, we report the sequence of the injected solutions and the state of the superhydrophobic surface.

PDMS substrate (see Figure A.1b). As opposed to the device adopted in the μ-PIV measurements, such a configuration allows us not to drill the Si-SHS that would have been quite difficult considering the small distance between the two inlet holes. The rhombus shape at the entrance of the channel lets one metallic tube feed simultaneously the two lateral branches of the channel while the second metallic tube supplies the central one. The PDMS channel and the Si-SHS are finally assembled together through the Plexiglas device described in Section 2.2 of Chapter 4. Since the PDMS channel is 6 mm in height, the Plexiglas box does not touch the metallic basement, as shown in the left panel of Figure A.1, but this does not prevent the microfluidic chip to be effectively sealed. The Si-SHS is very similar to the one presented in Chapter 4, except for the orientation of the micro-grooves that are now perpendicular to the flow direction. The pitch of the roughness pattern is $32\,\mu$m and the solid fraction is $\Phi_s = 0.5$. The two inlet tubes are connected to two independent syringes that are actuated by a syringe pump system, which imposes the same flow on both tubes.

Two liquid solutions are adopted in the experiments. The first is ultrapure Milli-Q water, to which we refer as the letter W, whereas the second is an aqueous solution of pure Milli-Q water and 10 mM of Lithium Chloride (LiCl), denoted by the letter S. In both cases we added 1 mM TRIS buffer (pH=9). When the solutions W and S are mixed with fluorescent 200 nm diameter silica colloids (Kisker) at a mass fraction of 0.005% (pH=9), we refer to them as W^C and S^C, respectively. We investigate several cases by supplying the channel inlets with different combinations of those aqueous solutions. For the sake of brevity, we use the abbreviation XYX to refer to the case of solution X injected in the lateral branches of the channel and solution Y supplied in the central one. We first examine the behaviour of the system as long as the Si-SHS is in Cassie state. Then, we study the system when the surface grooves are filled with water (Wenzel state). The flow is monitored through a fluorescence microscope (LEICA), fitted with a 20x objective. At the beginning of any experiment, the PDMS substrate and Si-SHS are well cleaned in ethanol using an ultrasonic bath, to reduce as much as possible the contamination by colloids and the surface absorption of the salt. We now report three typical experiments that draws a general picture of the phenomenon, pointing out the main trends. A summary of the experiments is reported in Table A.1, denoting the sequence of solutions injected in the channel and the state of the superhydrophobic surface.

2.1 Experiment 1

The flow rate of the two syringes is set to $2\,\mu$l/min, which is slow enough to maintain the Cassie state. At the beginning, the channel is totally filled with solution S^C. The fluorescence microscopy image for this configuration is reported in the top panel of Figure A.2. Then, the so-called focus configuration is reached by replacing in the

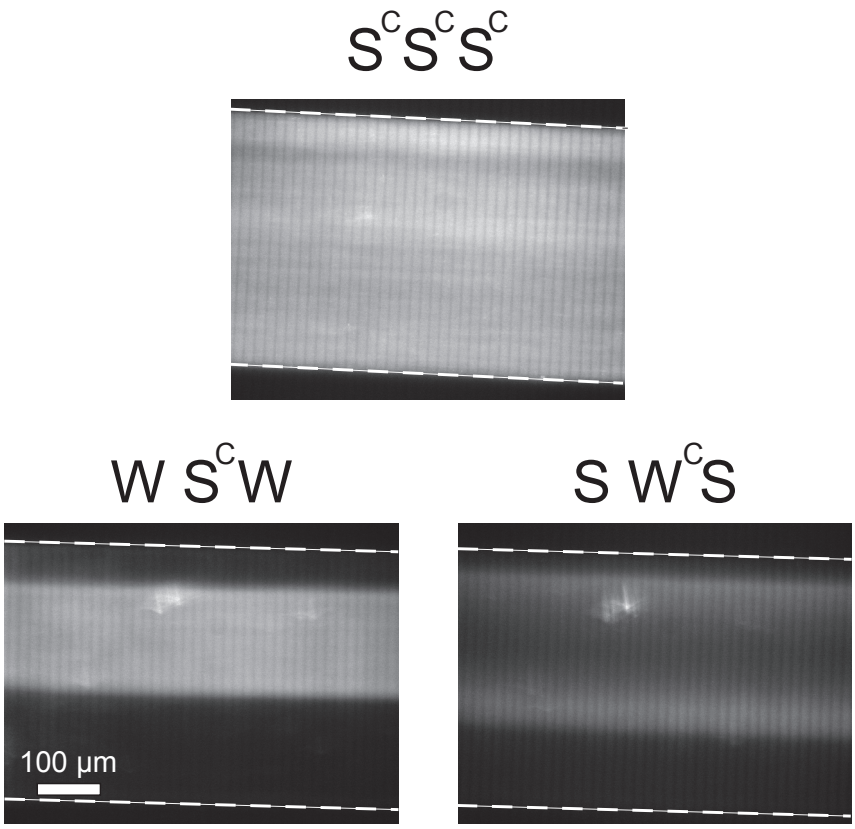

Figure A.2: Experiment 1. The channel is initially filled with the salt solution S (top panel). The white dashed lines represent the boundaries of the PDMS channel. The flow rate is small enough to maintain the Cassie state. Then, the focus configuration WS^{C}W (left bottom panel) and the spreading configuration (right bottom panel) are set.

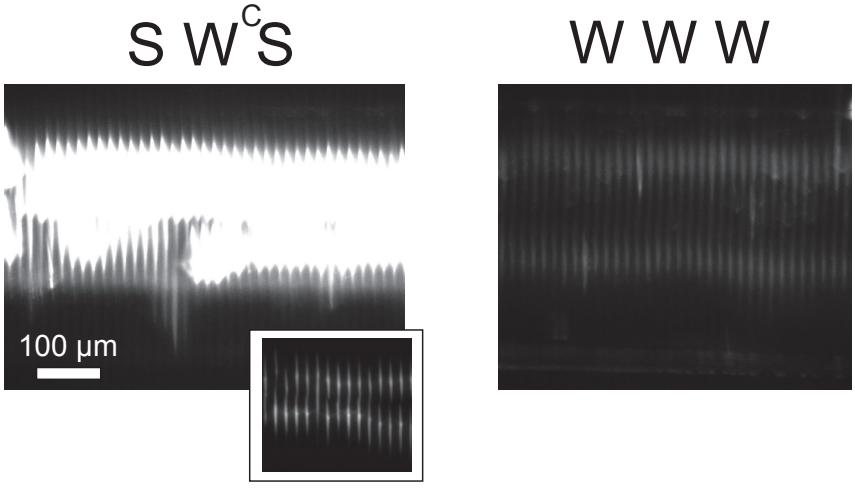

Figure A.3: Experiment 2. When a salt concentration gradient is established (SW^{C}S), the colloids quickly accumulate in the surface microgrooves (left panel). To avoid camera pixel saturation, the exposure time has to be reduced. The inset shows a crop (centered on the trapped colloids) of a frame recorded with an exposure time of 0.14 s, instead of 3.7 s as in the other images. As long as we pass to the configuration WWW, the salt concentration gradient vanishes, the colloids' trapping ceases and the particles slowly diffuse out of the surface roughness (right panel).

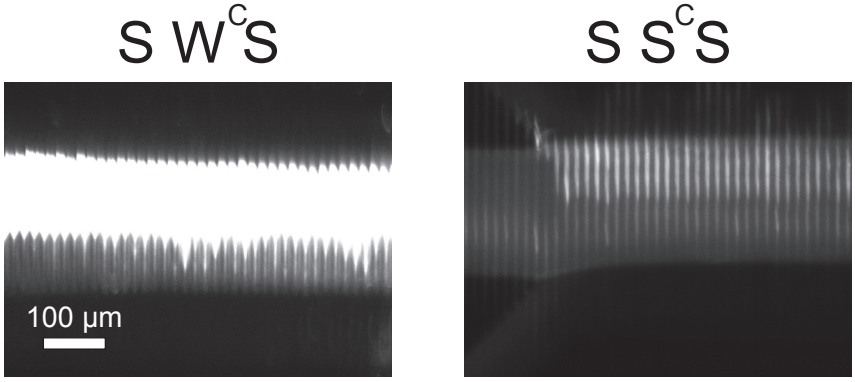

Figure A.4: Experiment 3. When the Wenzel transition is obtained with the salt solution S, instead of the water solution as in the previous experiments, the colloids, forced by the salt gradient, accumulate inside the microgrooves with a different spatial distribution compared to the experiment 2 (left panel). Nevertheless, after few minutes, a similar pattern for the distribution of the trapped colloids is recovered. At the end, the channel is totally filled with salt solution and the colloids, driven by the Brownian motion, move out of the microgrooves.

lateral inlets the solution S^C with pure water W. The term "focus configuration" refers to the fact that, driven by a diffusio-phoretic process, the silica particles are attracted to the region with higher salt concentration and, thus, in WS^CW configuration they tend to focus in the center of the channel. Finally, the spreading configuration is set, namely SW^CS. In this case, following the salt concentration gradient, the colloids spread toward the lateral walls of the channel, as shown in the right bottom panel of Figure A.2. The behaviour of the system is qualitatively comparable to that one reported by Abécassis et al. (2008) for a flat surface and, thus, no giant amplification of surface transport effects are remarked.

2.2 Experiment 2

In the second experiment, we completely fill the channel with solution W^C at low flow rate, namely 2μl/min. We then force the transition to the Wenzel state by raising the flow rate up to $20\,\mu$l/min. In both configurations $W^CW^CW^C$ and WW^CW, there is no accumulation of colloids inside the surfaces grooves. Conversely, as we establish a salt concentration gradient passing to the configuration SW^CS, the colloids are massively attracted inside the surface roughness, resulting in intense bright lines at the center of the channel in correspondence of the transverse grooves, as shown in the left bottom panel in Figure A.3. The colloid focusing is so strong that the camera pixel values saturate almost everywhere. Thus, to correctly visualize the focused colloids we reduce the exposure time from 3.7 s to 0.14 s. A crop of a frame recorded with a reduced exposure time is shown in the inset of Figure A.3. Since the particle trapping is triggered by the salt concentration gradient, it disappears when we pass to the configuration WWW. As long as the salt gradient vanishes, the colloids slowly diffuse out of the grooves, as it is shown in the right bottom panel of Figure A.3.

2.3 Experiment 3

We conduct an experiment similar to the previous one, except for the fact that the transition from Cassie state to Wenzel state is performed with a constant concen-

tration of salt in the channel (configuration SS^CS). When we pass to the spreading configuration (SW^CS), the colloids are still attracted to the surface roughness but apparently they arrange inside the grooves in a different manner, see left panel of Figure A.4. This could be the effect of filling the grooves with salted water instead of pure water as in the previous case. Nevertheless after few minutes, the pattern of bright lines produced by the focused colloids change and move towards the same pattern we obtained in experiment 2. Again, when the salt concentration gradient vanishes, the colloids slowly move out of the roughness cavities, as shown in the right panel of Figure A.4, where the configuration SS^CS is considered.

3 Conclusions

In this Appendix, we examined the combined effects of surface-transport due to a solute concentration gradient and the pressure-driven flow in a Ψ-channel fitted with a superhydrophobic surface in Wenzel state. Even if the phenomenon is still clear, we experimentally verified that a salt (Lithium Chloride) concentration gradient is able to promote a massive particle trapping inside the transverse grooves of the surface (experiments 2 and 3). The particle focusing was monitored via fluorescence microscopy but at this stage neither quantitative data nor theoretical model are presented. In the next future work, we plan to perform the same experiment in a channel geometry that lets us monitor the flow through a confocal microscope, equipped with a high magnification objective, so that the concentration profiles of the fluorescent colloids can be traced along the optical axis direction. Further investigations of the presented phenomenon are very interesting in view of the important potential applications that can be conceived. For instance, since the colloids are massively accumulated in the surface roughness even with a relative low salt concentration, such a particle focusing could be exploited to effectively filter a solution seeded with contaminant particles. If the quick focusing can be converted in a quick spreading, the filtered particles can be subsequently released into the channel. As an example, this system could be used to recover particles used in a previous process occurred in a different area of the lab-on-a-chip. Moreover, once the dependence of the surface attraction on the colloids' size has been investigated, it could be possible to appropriately design the surface roughness to sort different particles mixed in the flowing solution.

References

Abécassis, B., Cottin-Bizonne, C., Ybert, C., Ajdari, A., and Bocquet, L. (2008). Boosting migration of large particles by solute contrasts. *Nature materials*, 7(10):785–789.

Ajdari, A. and Bocquet, L. (2006). Giant amplification of interfacially driven transport by hydrodynamic slip: Diffusio-osmosis and beyond. *Physical review letters*, 96(18):186102.

Anderson, J. (1989). Colloid transport by interfacial forces. *Annual Review of Fluid Mechanics*, 21(1):61–99.

Chen, P., Gu, J., Brandin, E., Kim, Y., Wang, Q., and Branton, D. (2004). Probing single dna molecule transport using fabricated nanopores. *Nano letters*, 4(11):2293–2298.

Cottin-Bizonne, C., Cross, B., Steinberger, A., and Charlaix, E. (2005). Boundary slip on smooth hydrophobic surfaces: intrinsic effects and possible artifacts. *Physical review letters*, 94(5):56102.

Di Leonardo, R., Ianni, F., and Ruocco, G. (2009). Colloidal attraction induced by a temperature gradient. *Langmuir*, 25(8):4247–4250.

Huang, D., Cottin-Bizonne, C., Ybert, C., and Bocquet, L. (2008). Massive amplification of surface-induced transport at superhydrophobic surfaces. *Physical review letters*, 101(6):64503.

Huang, P., Guasto, J., and Breuer, K. (2006). Direct measurement of slip velocities using three-dimensional total internal reflection velocimetry. *Journal of Fluid Mechanics*, 566(447-464):5.

Joseph, P. and Tabeling, P. (2005). Direct measurement of the apparent slip length. *Physical Review E*, 71(3):035303.

Stone, H., Stroock, A., and Ajdari, A. (2004). Engineering flows in small devices. *Annu. Rev. Fluid Mech.*, 36:381–411.

Weinert, F. and Braun, D. (2008). Observation of slip flow in thermophoresis. *Physical review letters*, 101(16):168301.

Index

PUBLICATIONS

Journals

Bolognesi G., Bianchi S., Di Leonardo R., *Digital holographic tracking of microprobes for multipoint viscosity measurements*, Optics Express, Vol 19 No. 20, (2011)

Cavallini L., Bolognesi G., Di Leonardo R., *Real-time digital holographic microscopy of multiple and arbitrarily oriented planes*, Optics Letters, Vol. 36, No. 17, (2011)

Di Leonardo R., Cammarota E., Bolognesi G., Schäfer H., and Steinhart M., *Three-Dimensional to Two-Dimensional Crossover in the Hydrodynamic Interactions between Micron-Scale Rods*, Physical Review Letters, Vol. 107, 044501 (2011)

Nenzi P., Giacomello A., Bolognesi G., Chinappi M., Balucani M., Casciola C.M., *Superhydrophobic Porous Silicon Surfaces*, Sensors & Transducers Journal, Special Issue, Vol. 13, pp 62-72 (2011)

Conference Proceedings

Belfiore N.P., Bolognesi G., Verotti M., Scaccia M., Cappa F., D'Annibale A., Lazzari S., Rudas I.J., *Methods for Surgical Serial Manipulators Isotropy Indexing*, RAAD 2008, Ancona, Italia (2008)

Balucani M., Bolognesi G., Casciola C.M., Chinappi M., Giacomello A., Nenzi P., *Superhydrophobic porous silicon surfaces*, TechConnect Word 2011, Boston, USA, (2011)

Giacomello A., Nenzi P., Bolognesi G., Chinappi M., Balucani M., Casciola C.M., *Superhydrophobic states on porous silicon*, AIMETA 2011, Bologna, Italia, (2011)

Chinappi M., Gentili D., Bolognesi G., Casciola C.M., *Liquid water slippage on hydrophobic rough surfaces*, AIMETA 2011, Bologna, Italia, (2011)

CONFERENCES

Introduction to Optofluidics

International Centre of Theoretical Physics, June 2009 ,Trieste, Italy

Trends in Optical Micro-manipulation

Universitätszentrum Obergurgl, April 2010, Obergurgl, Austria

SPIE Optics and Photonics 2010

San Diego Convention Centre, August 2010, San Diego, USA

2th European Conference on Microfluidics

Meteo-France Internarional Centre, December 2010, Toulouse, France

GDR micro et nanofluidique 2010

Université Claude Bernard Lyon, May 2011, Lyon, France

TechConnect Word 2011

Hynes Convention Centre, June 2011, Boston, USA

XX Congresso Aimeta 2011

Complesso Monumentale di Santa Cristina, September 2011, Bologna, Italy

FUNDINGS AND GRANTS

3-years Ph.D. Fellowship, Dipartimento di Ingegneria Meccanica ed Aerospaziale, Università La Sapienza di Roma

2009 Da Vinci Research Grant, Università Franco-Italiana

4-month Research Grant, French Embassy in Italy